Nanostructured Phenol-Formaldehyde based Carbons as Electrodes for Lithium/Oxygen Batteries

by

Gbolahan O. Shitta-Bey

A thesis submitted to the Department of Chemical and Process Engineering, University of Strathclyde, in part fulfilment of the regulations for the **Degree of Doctor of Philosophy**

2012

Acknowledgements

Firstly, I would like to thank God for seeing me through my studies. I would also like to express my most sincere gratitude to my supervisors Prof. P. J. Hall and Dr. M. Mirzaeian for their constant support and advice throughout this study.

My thanks are extended to Brian Dickson for his continuous encouragement. I am also thankful to the Head of Department, Prof. C. J. Schaschke, the departmental lecturers, secretarial staff, and the laboratory technicians for all their assistance. Gratitude to my fellow PhD students and post-doctoral researchers who helped ensure that I had an overall memorable experience over the duration of my project.

Special thanks to my family, Babatunde, Modupeore, Oluwarotimi, Oluwatoyin and Ibiyemi for their support and encouragement. I am also grateful to Dr O. J Ebohon for his guidance and to all my friends and relatives who have been with me every step of the way.

Table of Contents

Abstract

As environmental concerns regarding CO_2 emissions continue to increase and renewable technologies begin to emerge, electrochemical energy storage devices have proven to be crucial for successful implementation of these new energy strategies. The Lithium/air (Li/air) rechargeable battery represents by far one of the most competitive energy storage devices to date. High energy densities which are about 5 – 10 times that of Lithium-ion (Li-ion) batteries are achievable with these devices. However, due to the problems associated with electrode clogging with discharge product, considerable research has been focused on optimizing the porous structure of the electrode.

Studies performed in this work revealed high discharge capacities for Li/air batteries that utilised carbon-based electrodes with high pore volumes. However the number of discharge/charge cycles was relatively low and still require much improvement. The porous properties of the carbon electrodes were dependent on component ratios and synthesis methods of the carbon precursors (phenol-formaldehyde gels). Varying levels of porosity in the corresponding carbons were obtained with different carbonisation temperatures. Subsequent physical activation considerably increased porous properties of the carbons.

Sol-gel polymerisation was used in the synthesis of low cost phenol-formaldehyde gels as carbon precursors for electrode preparation. By varying various synthesis parameters such as phenol/catalyst ratio (P/C), phenol/formaldehyde ratio (P/F), solvent exchange liquid, and drying methods, maximised pore volumes for these gels were obtained. The most desirable gel reactant ratios were a P/C ratio of 8 and a P/F ratio of 0.4. Furthermore, freeze drying with t-butanol showed the best porous properties in the phenol-formaldehyde (PF) gel. The corresponding gel possessed total pore and mesopore volumes of ~1.16 and 1.15 cm^3/g respectively.

An investigation of the effect of carbonisation temperatures on the aforementioned gel revealed 1050 ^oC as the optimum. Further enhancement of porous structure was achieved by physical activation. Both O_2 and CO_2 activation were carried out. The highest total pore and mesopore volumes of activated carbons obtained in this work were approximately 2.01 and 1.87 cm^3/g, corresponding to a CO_2 activated carbon. Surface characterisation of both O_2 and CO_2 activated carbons showed similar levels of surface functionality.

Electrochemical measurements showed that discharge capacity increased with mesopore volume, with the highest discharge capacity of 1852 mAh/g corresponding to the highest mesopore volume of 1.87 cm^3/g. Furthermore the discharge capacities normalised to the mesopore volumes of the carbons in the electrodes, showed an increase with increasing average pore size. Power capabilities of the batteries were tested by varying discharge rates where it was found that the discharge capacity decreased with increasing discharge rates.

List of figures

List of tables

Chapter 1

Introduction

The major drivers for electrochemical energy storage systems, as well as a comparison of different technologies are described in this section. Furthermore, the fundamental mechanisms governing various energy storage devices including the consequences of such mechanisms in terms of energy and power capabilities are presented. An introduction to battery technology and a brief look at the importance of nanostructured carbon electrodes for Li/air batteries is also included.

1.1 Reasons for Energy Storage

Fossil fuel (coal, oil, natural gas) based energy is fast becoming out of date due to the associated environmental concerns along with the requirements to meet CO_2 emissions reduction targets. Furthermore, as the ever increasing world demand for energy is placing increased pressure on fossil fuel reserves, with energy demand forecasted to be doubled by the year 2050 and tripled by the end of the century, alternative energy sources are gaining more attention [1]. Renewable energy sources such as solar and wind, have therefore attracted significant interest. As shown in Figure 1.1, there has been a drastic increase in wind installations between the years 1980 – 2005 [2]. However, due to the intermittent nature of such renewable energy sources, effective energy storage systems need to be in place, to ensure continuity of supply to meet an ever growing consumer demand. Figure 1.2 illustrates variations in wind speed and therefore wind power output from a wind turbine [3].

Another major area for reducing the dependency on fossil fuels is by switching to electric vehicles (EVs) especially if they are used in conjunction with renewable energy sources. Furthermore, as consumer electronics continue to become more portable, concurrent with increasingly modern lifestyles, there is a greater demand from power sources in terms of being more light weight and compact while still being able to provide considerable amounts of energy. High energy density (energy output per unit weight [4]) electrochemical energy storage devices such as batteries are very attractive in this respect, with rechargeable lithium/air batteries emerging as one of the most competitive worldwide.

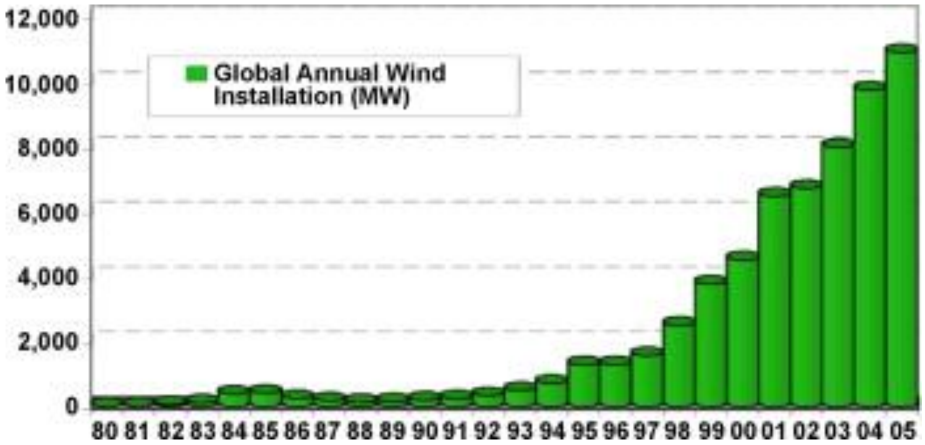

Figure 1.1: Global annual wind installations (MW) 1980 – 2005 [2]

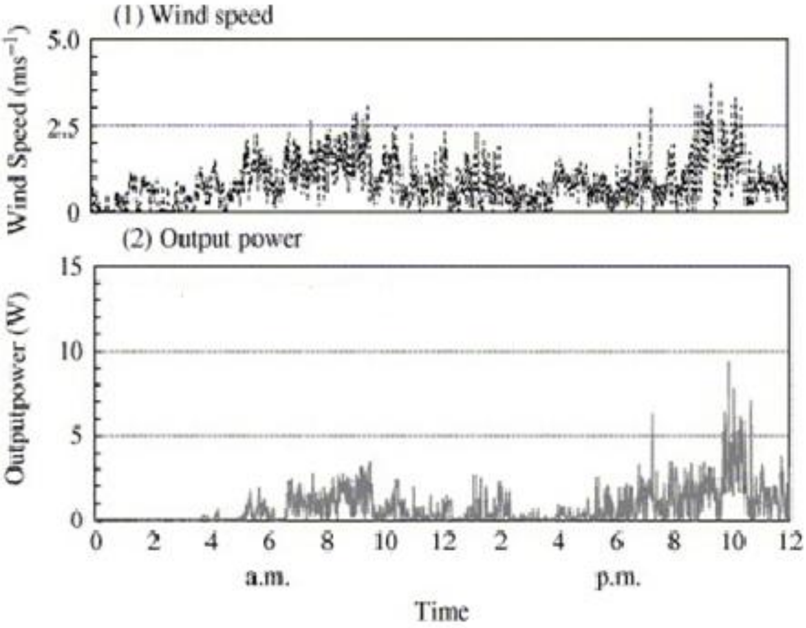

Figure 1.2: Variations in wind speed and wind power output from a wind turbine [3]

In addition to lithium being an extremely light metal, the high operative voltage and high specific energy (mAh/g) of rechargeable lithium based batteries, renders them particularly attractive. The theoretical maximum energy density obtainable from Li electrode based cells operating at a voltage of 2.91 – 2.96 V approaches values of over 11 000 Wh/kg (on the basis of the weight of lithium), and is considerably higher than any advanced rechargeable battery technology [5].

1.2 Energy Storage Systems and Mechanisms

Two major types of electrical energy storage systems are batteries and electrochemical capacitors. The term electrochemical capacitor (EC) is a generic one that encompasses both the electrochemical double layer capacitor (EDLC) and the pseudocapacitor. The aforementioned systems are distinguishable based on the associated mechanisms of energy storage, which include Faradaic processes involving electron transfer across the electrode/electrolyte interface, with changes in the oxidation state of electroactive materials, and non-Faradaic processes where no electron transfer takes place across the electrode interface and charge is stored electrostatically [6]. In actual fact, these energy storage systems lie on a continuum of electron transfer between electrode and electrolyte (Figure 1.3a-d), with batteries on one end of the continuum storing energy through electrochemical reactions and dielectric capacitors on the other end storing energy directly as electrostatic charges on two opposing electrodes [6 - 7].

Batteries store energy indirectly by Faradaic oxidation and reduction of electrochemically active reagents that are able to produce charge. This is accompanied with bulk-phase transformations, high voltages, and therefore, high energy densities (see Section 1.3) but with restricted cycle life due to the irreversibility of chemical electrode reagents often encountered during the charge and discharge processes [7]. A further step in the continuum is a transitional state exhibiting traits of Faradaic and non-Faradaic energy storage. This behaviour occurs due to a derivative dq/dV that arises as a result of a dependence of charge passed, q, faradaically by oxidation or reduction across the double layer, on electrode potential, V, and corresponds to a measurable quantity referred to as Pseudocapacitance [6]. It is distinguishable from regular double-layer capacitance as found in EDLCs, where capacitance arises as a result of potential-dependence on the surface density of charges stored electrostatically (i.e. non-faradaically) at the electrode interfaces. Additionally, the Faradaic reactions that occur in pseudocapacitors do not propagate into the bulk material as in batteries, but are restricted to the electrode/electrolyte interface [7]. Due to the potential dependence i.e. capacitive nature, of the Faradaic reactions, pseudocapacitors are viewed as a transitional state between EDLCs and batteries. This phenomenon is encountered in ruthenium oxide (RuO_2) redox systems [6] as described in Figure 1.3b.

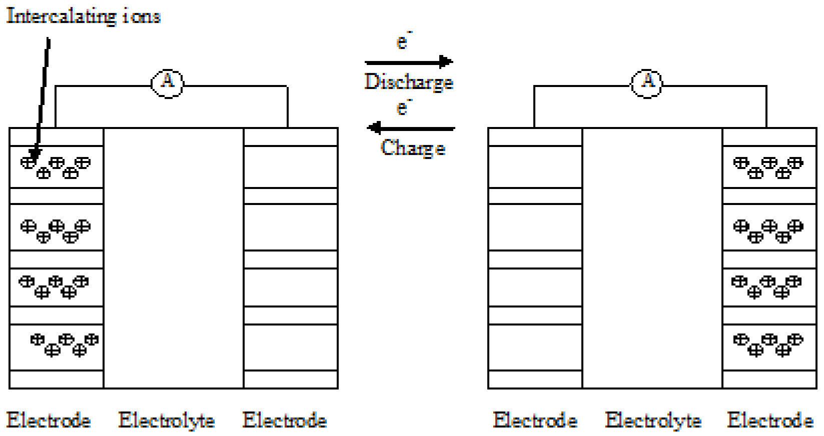

Figure 1.3a: Representation of the charge – discharge process of an intercalation battery where the following occur [6 - 8]; (i) Oxidation and reduction reactions involving the bulk electrodes (ii) Penetrations of ions into the bulk electrodes (iii) Changes in oxidation state and structure of electrode materials (iii) Energy is stored chemically in electrode materials

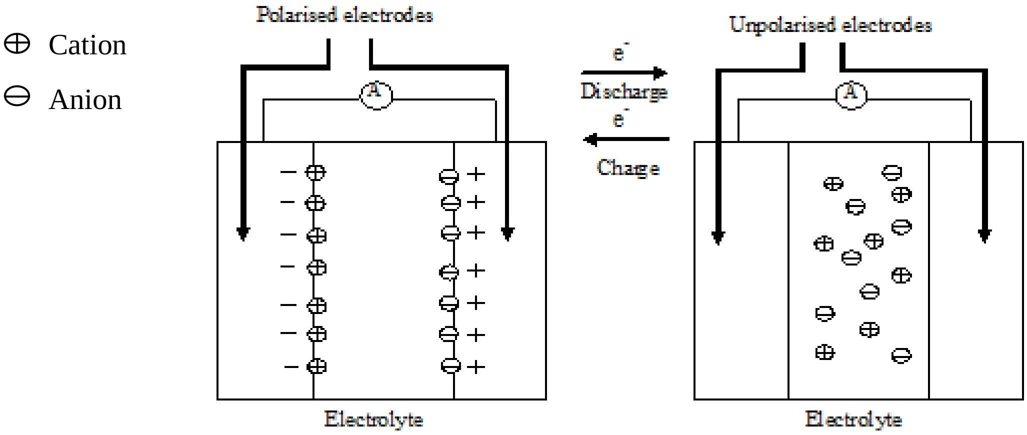

Figure 1.3b: Representation of charge – discharge process of a pseudocapacitor where the following occur [6 - 7], [9]; (i) During charge, the anions migrate to the positively charged electrode (such as that based on a transion metal oxide e.g. RuO_2), causing double layer formation and also charge transfer reactions at the surface of the electrode. This results in changes in oxidation state of the surface atoms of the electrode. (ii) The redox reaction occurs only at the electrode/electrolyte interface, and does not propagate into the bulk

electrode as in batteries (Figure 1.3a) (iii) Energy is stored faradaically (where charge is transferred from the electrode to the electrolyte and vice versa) and non-faradaically (in the double-layer i.e. the electrode/electrolyte interface region)

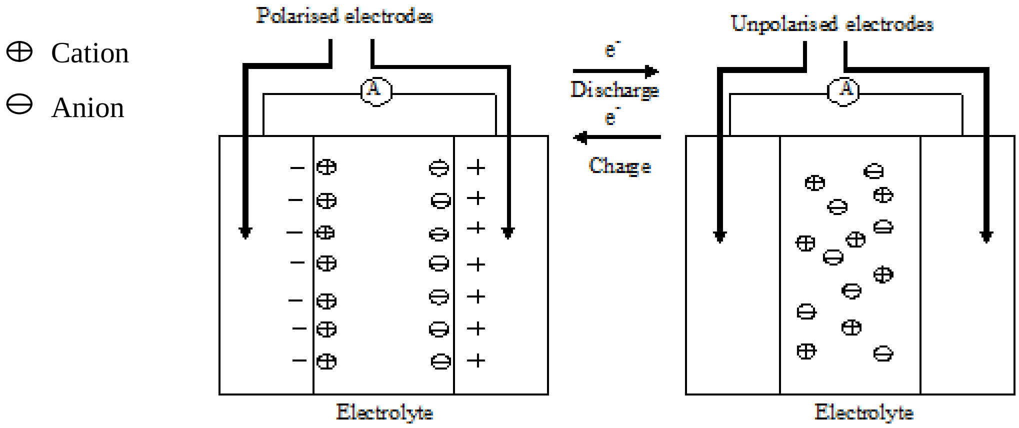

Figure 1.3c: Representation of charge – discharge process of an EDLC, where the following occur [6 - 7], [10]; (i) During charge, both electrodes become polarised and anions are attracted to the positively polarised electrode, whereas cations are attracted to the negatively polarised electrode. (ii) Upon discharge, both anions and cations are removed from the double layer and into the electrolyte. (iii) Energy is stored non-faradaically at the double layer and no reactions are involved during operation.

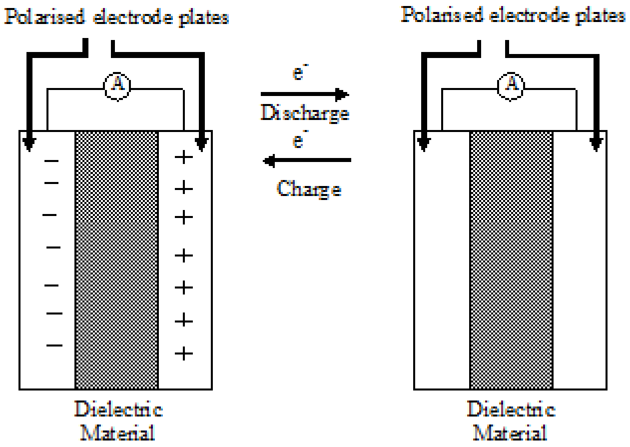

Figure 1.3d : Representation of charge – discharge of a traditional capacitor, where the following occur [6 - 7]; (i) Electrodes are polarised during charge, and energy is

stored in the electric field between negatively and positively polarised electrodes. (ii) The electric field diminishes on discharge and is generated on charge. (iii) No reactions occur and charges are physically separated by a dielectric material

EDLCs store energy in an electrical double layer at the electrode/electrolyte interface. As their operation is non-Faradaic and without any chemical or phase changes, they possess highly reversible energy storage mechanisms with cycle lifetimes greater than 10^6. Completing the continuum are electrostatic capacitors which store energy directly as charge on two plates separated by a dielectric material and differ from EDLCs due to the existence of a double layer in the latter. In EDLCs, cations and anions in the electrolyte are attracted to the electrode surface by equal but opposite charges resulting in two capacitors in series connected by an electrolyte**.** Both systems work on the basis of the removal and addition of electrostatically accommodated charge. The accumulation of charge in a dielectric capacitor is as a result of an excess and deficiency of electron charges on the capacitor plates, whereas in the EDLCs, it is a combination of this effect (however in this case in the region of the double-layer), as well as the counter-balancing of the surface densities of accumulated cations or anions at the interface [6]. Due to the high internal surface area of the electrodes usually used in EDLCs, and the presence of a double layer, their energy densities are significantly higher than in electrostatic capacitors [7]. This can be understood from the viewpoint of the energy stored in a capacitor, E, given by:

$$E = \frac{1}{2}\varepsilon A\frac{V^2}{d} \tag{1.1}$$

where A is the area of the electrode plates, V is the applied voltage, d is the distance between the electrode plates and ε is the permittivity of the material between the plates [11]. Equation 1.1 clearly shows that the energy stored, is directly proportional to the area of the electrode, which in the case of EDLCs, is significantly greater than those used in the parallel plate capacitor. Furthermore, as the double layer region on each electrode surface of the EDLCs can be regarded as equivalent to a parallel plate capacitor, with a thickness on the nanometer scale, there is a drastic increase in the energy storage capabilities of the EDLCs, in comparison to a parallel plate capacitor, where much greater distances exist between the electrode plates [11].

The differences in the mechanisms of energy storage in batteries and ECs, lead to different energy and power capabilities. This is due to the fact that the non-Faradaic reactions that take place in the ECs, occur without any chemical or phase changes, while the opposite is true for batteries. As a result, ECs can perform at higher discharge rates (corresponding to higher power densities), while such high rates of discharge for batteries, reduces their performance significantly, and leads to lower power densities for these batteries [12]. However, the same Faradaic reactions in batteries that lead to bulk phase transformations, also lead to high voltages, which remain essentially constant during discharge, thereby, leading to higher energy densities for these devices, as opposed to ECs, whose voltages are charge dependent, and decline drastically upon discharge, resulting in lower energy densities [6]. Based on these differences, it is likely that these devices will work side by side in order to produce highly functional energy storage systems [7]. Nevertheless, a considerable amount of research is being devoted to increasing the power capabilities of the Li/air batteries and this will be elaborated on further in this work.

1.3 Battery Technology

Batteries possess the ability to store energy chemically which can be converted into electrical energy as required, to power a wide range of applications [13]. The discharge of the battery corresponds to this process of delivering energy. In the case of a primary battery, the end of discharge represents the end of life of the battery, after which the battery is no longer used. However, for the rechargeable battery, the original chemical state of energy can be restored by a reversal in current flow [13 - 14]. However, as mentioned earlier, certain irreversible chemical changes do occur. The extent to which its original condition can be restored is dependent on the battery mechanism and the processes occurring therein.

Applications for rechargeable batteries are vast in number, and are all dependent on their ability to store electrical energy from an external power source. Some of these include portable electronics, electric vehicles and emergency power supplies [15]. In the same context, rechargeable batteries can also be used for load-levelling applications, such as when they are integrated into an electricity supply system for meeting short duration demand peaks, or when they are used in conjunction with renewable energy sources, such as solar and wind power, to ensure continuity in power supply (as described in Section 1.1). In these applications, i.e. load-levelling, the rechargeable battery can be considered as a secondary power source. Another example is in the hybrid electric vehicle (HEV), which uses an internal combustion engine with a rechargeable battery, where the battery handles starting, acceleration, and other peak power demands [14]. In other applications such as portable electronics and electric vehicles (EVs), the rechargeable battery can be considered as the primary or main power source. Restoring a rechargeable battery to its original chemical state is simply a means of putting it back into a position where it can generate energy again.

The energy generated by a battery, depends on the energy produced by the chemical reaction involved in the battery. This is known as the Gibbs free energy, which simply refers to the energy available from a system (or reaction). The maximum amount of energy that can be generated by the reaction, is given by the standard change in Gibbs free energy (ΔG^0),

$$\Delta G^0 = \Delta H^0 - T\Delta S^0 \tag{1.2}$$

where ΔH is the standard change in enthalpy (J/mol), T is the temperature (K), and ΔS is the standard change in entropy of the system (J/mol.K). A process (or a reaction) is spontaneous, if ΔG is negative, which corresponds to a decrease in free energy. It is, therefore, useful in determining whether a reaction will occur spontaneously or not.

The types of reactions that generate energy are redox reactions involving both oxidation at the anode and reduction at the cathode. The electrolyte serves as an ionic conductor and the electrodes as electronic conductors. The aforementioned electrode reactions, called half cell reactions (oxidation and reduction), determine the theoretical operating voltage of the cell; which is the difference in electrode potential between the two electrodes, and represents the driving force for the external current derived from the cell. Current is the number of coulombs of charged passed per second, and has the unit ampere (A) or coulombs per second (C/s) [16]. The standard change in Gibbs free energy (ΔG^0), orginially defined in equation 1.2, can also be given as,

$$\Delta G^0 = -nFE^0_{cell} \tag{1.3}$$

where n is the number of moles of electrons involved in the reaction, and F is the Faraday constant. The faraday constant has a value of 96487 coulombs of charge per mole of electrons [14], [17]. This value can be expressed in ampere-hour units. Since 1 Ah = 3600 C, 96487 coulombs is equivalent to 26.8 Ah. E^0 is the standard cell potential or theoretical voltage of the cell in volts (V) or joules per coulomb (J/C). The negative sign is indicative of a drop in energy of the system, as energy is being delivered [14]. The product 'nF' represents the charge passed during the reaction [18].

The standard cell potential can be calculated from the standard electrode potentials as follows,

$$E^0_{cell} = E^0_C - E^0_A \tag{1.4}$$

where E^0_C and E^0_A are the standard reduction potentials of the cathode and anode, respectively [14]. It can also be calculated, by obtaining the ΔG^0 value from equation 1.2, and substituting into equation (1.3) [19]. Parameters such as ΔH^0 and ΔS^0, are available in thermochemical tables [20], and the number of moles of electrons, n, is obtained from the chemical equation representing the redox reaction being studied.

However, the practical operating voltage does not depend only on the half cell reactions, but also takes into account any side reactions, charge transfer kinetics and internal resistance of the cell components. This is explained in more detail in Section 2.3.

A further consideration is the theoretical capacity or Ampere-hour (Ah) capacity of the cell which is associated with the quantity of electricity obtained from the active materials assuming a complete utilization of these materials [4] and can be expressed as specific capacity (on a per gram basis, taking into consideration the total mass of reactants). This specific capacity can also be defined as the charge output or charge passed per unit weight of active materials and can be given as:

$$Specific\ Capacity\ (Ah/g) = \frac{nF}{m_t} \tag{1.5}$$

where m_t is the total mass of reactants, and all the other terms are as defined in equation (1.3). The theoretical specific energy is representative of the maximum energy output of a battery assuming a complete utilization of the active materials and is given as:

$$Specific\ Energy\ (Wh/g) = Voltage\ (V) \times Specific\ Capacity\ (Ah/g) \tag{1.6}$$

Combining equations (1.5) and (1.6), specific energy can be written as

$$Specific\ Energy\ (Wh/g) = \frac{nFE^{O}_{cell}}{m_t} \tag{1.7}$$

Cell chemistries that yield high specific capacities (Ah/g) and high operating potentials (V) along with the utilization of light weight electrodes are necessary to achieve high specific energies (Wh/g) [14].

1.4 Importance of Nanostructured Carbons for Li/air Batteries

As will be expanded on further in this work, the operation of the Li/air battery involves deposition of discharge product into the pores of the air cathode. It is therefore important for the cathode material (carbon) to possess an appropriate level of porosity. Nanotechnology enables the manipulation of the porous structure of materials. Furthermore, nanostructured carbons facilitate efficient electronic/ionic diffusion due to short diffusions paths, provide active sites and in some cases allow for new reaction mechanisms [21]. In general, the appeal of the carbon based electrode, is due the availability of carbon in a vast array of physical structures (e.g. porous structures), low cost and good electrical conductivity [22]. A more indepth discussion on the subject of carbon electrode materials, shall be presented in section 2.2.5.3. A considerable part of this work focuses on controlling the porosity of the carbon electrode in order to maximise electrochemical performance. Not only does this contribute towards understanding the relationship between electrochemical performance of Li/air cells and porosity, it also sheds some light on, and deepens the understanding of the processes that govern the operation (charge and discharge) of these batteries.

Chapter 2

Literature Review

This chapter deals with the evolution of rechargeable lithium batteries and also provides a review on metal/air batteries. In addition to an in-depth look at various aspects of the Li/air battery including electrodes, electrolytes and electrocatalysts, this section also discusses issues facing other metal/air technologies. Furthermore, topics such as the theoretical and practical energy density of Li/air batteries as well as the challenges facing Li/air batteries are included in this section.

2.1. Rechargeable Lithium Batteries

Batteries have been in use for several decades. However, since the commercialisation of Li-ion batteries by Sony [23] in 1990, Li-ion batteries took up a substantial share of the market particularly in the area of consumer electronics, causing a shift away from previously used low voltage systems such as Nickel-Cadmium (Ni-Cd), Nickel-Metal Hydride (Ni-MH) and Lead-acid (Pb-acid) batteries [24]. Figure 2.1 shows a comparison between Li-ion batteries and other rechargeable batteries in terms of energy density [25].

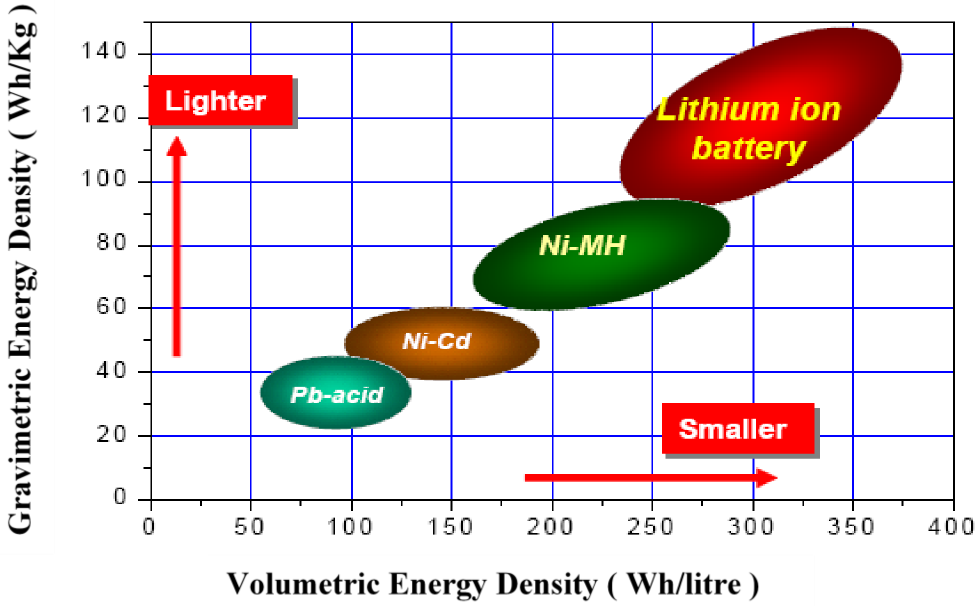

Figure 2.1: Comparison of gravimetric and volumetric energy densities of various rechargeable batteries [25]

Li-ion batteries have attracted a considerable amount of attention due to their high energy density, high operating voltage, flexible and light weight design and as a result are currently being used in laptops, mobile phones, and other portable equipment [26 - 27]. The operation of these batteries (Figure 2.2), involves the exchange of lithium ions between a graphitic anode structure and a redox active cathode material [8]. The electrochemically active electrode species are the lithiated carbon anode and a lithium transition metal oxide cathode. The discharge process involves the oxidation of the anode material (Equation 2.1), and the reduction of the cathode material (Equation 2.2), and involves the de-intercalation of lithium ions from the anode and subsequent intercalation into the cathode. The reverse occurs on charge as shown in equations 2.1 – 2.3 [28 - 29].

Anode:

$$Li_xC_6 \rightarrow xLi^+ + xe^- + 6C \tag{2.1}$$

Cathode:

$$Li_{1-x}CoO_2 + xLi^+ + xe^- \rightarrow LiCoO_2 \tag{2.2}$$

Overall cell reaction:

$$Li_xC_6 + Li_{1-x}CoO_2 \underset{\text{Charge}}{\overset{\text{Discharge}}{\rightleftharpoons}} LiCoO_2 + 6C \tag{2.3}$$

where x represents a stochiometric range of $0 < x < 1$ [28 - 29]. The most common electrolytes used for rechargeable Li-ion cells, are solutions of lithium salts in organic solvents, such as $LiPF_6$ in EC – PC (ethylene carbonate – propylene carbonate) or EC – DMC (ethylene carbonate – dimethyl carbonate) solvent mixtures [15]. The amount of energy that can be stored in these batteries is however limited by the cathode, $LiCoO_2$ [13], [30 - 33], and does not exceed 140 mAh/g [24]**.** Another cathode material that has attracted some interest for Li-ion batteries are those based on lithium iron phosphate ($LiFePO_4$) which possess a relatively higher theoretical capacity (170 mAh/g), in comparison to $LiCoO_2$ [34 - 35].

The research on rechargeable lithium batteries also extends to the use of lithium metal as the anode. Investigations have been carried out using lithium as an anode along with various transition metal compounds as intercalation cathodes, such as MoS_2, MnO_2, TiS_2 etc. The specific capacities based on these cathode materials are in the range of 135 – 260 mAh/g [14]. Notable research has being carried out, using various combinations of electrode materials for Li-ion batteries, typically involving a lithium transition metal nitride anode, and capacities of up to 900 mAh/g have been reported [36 - 39]. Li-ion batteries have already been applied to electric vehicles which are available in the marketplace. However, the driving range is restricted. Extending the driving range would require batteries possessing much higher energy densities [40].

The non-aqueous Li/air battery initially introduced by Abraham *et al.* [19], [41], represents a major advance compared to its predecessor: the Li-ion battery, and has been perceived to be capable of attaining an energy density 5 – 10 times that of commercially available Li-ion batteries [30 - 31]. However, recent work on Li/air batteries has revealed even higher energy densities that exceed this range significantly, with values of around 1500 – 3000 mAh/g [30], [32]. This large increase in energy densities has led to further and more thorough research into Li/air batteries [27], [30 - 32].

In Li/air batteries (Figure 2.3), lithium metal is used directly as an anode to supply lithium ions and therefore the amount of lithium ions that can be supplied is in abundance. Instead of lithium ion intercalation, lithium is allowed to react directly with an infinite supply of oxygen (the active cathode material) from air [31]. The oxygen however does not need to be carried onboard the cell and therefore has no contribution to the overall cell weight making the cell lighter than the Li-ion batteries and also allows for a much higher specific energy [42].

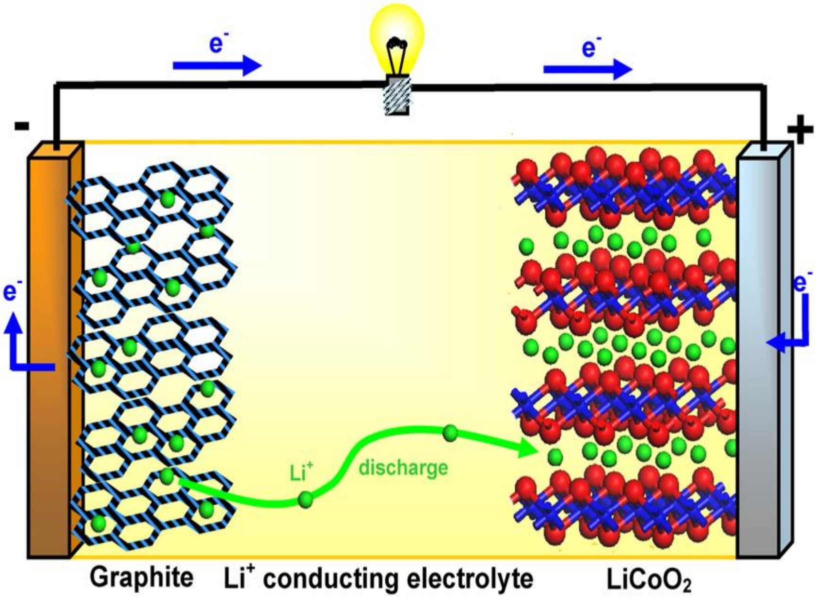

Figure 2.2: Schematic of a lithium ion battery with a graphite anode and $LiCoO_2$ cathode [8]

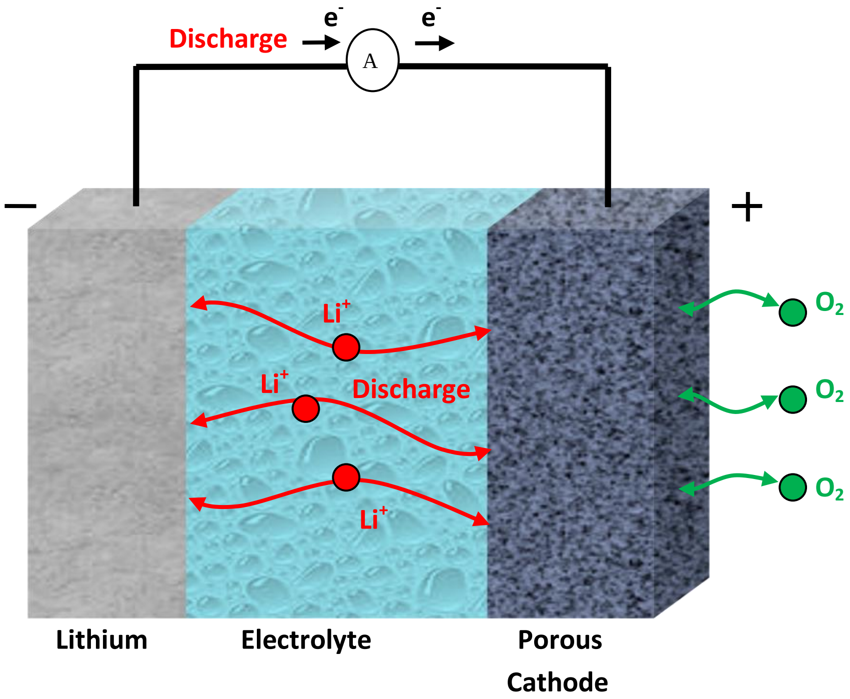

Figure 2.3: Schematic representation of the Li/O_2 battery [31]

2.2 Metal/air Batteries

2.2.1 Introduction

Metal/air batteries are unique in the sense that the active cathode material, oxygen, is obtained from air, and therefore does not need to be carried onboard the cell, and is in abundance. This therefore allows for much higher discharge capacities in comparison with conventional battery systems [14], [43]. The high energy density, light weight along with portability of these batteries makes them very attractive. Primary aqueous Zn/air batteries are now being used as high capacity power source for hearing aids while the electrically rechargeable version of the Zn/air batteries are still being developed [44 - 45]. Nevertheless, the aforementioned properties of metal/air batteries make them potential candidates for use in electric vehicles [46]. The various metal/air systems that have gained considerable attention are the aqueous Fe, Zn, Al and Li/air batteries whilst others such as aqueous Mg/air, Ca/air and Cd/air have gained less attention [47]. A common mechanism in these aqueous systems is the reduction of oxygen to form OH^- anions and the subsequent dissolution of the OH^- anions into the electrolyte. Additionally, the purpose of the air electrode in such systems is only as a reaction site for the catalytic reduction of oxygen [48]. The major determinants of specific capacity of these aqueous systems include the dissolving capacity of the electrolyte and the capacity of the metal anode.

As this work focuses on non-aqueous Li/air batteries, it would be interesting to compare various non-aqueous metal/air batteries. However, most research efforts on these types of batteries have been dedicated to Li/air batteries, and is likely due to the relatively higher amount of electricity that can obtained from lithium in comparison to other typical metal anodes [14]. Nevertheless, for the purpose of gaining a historical background on the kind of issues that have been faced by other metal/air batteries in general, a brief discussion has been included on the aqueous Fe, Zn and Al/air batteries prior to a more detailed discussion on Li/air batteries.

2.2.2 Zn/air batteries

Commercially available Zn/air alkaline batteries using manganese oxide electrocatalysts, Zn powder anode, and carbon air cathodes, are currently used for powering warning lights (navigation aid), remote signals, railroad track circuits and hearing aids [13], [47]. However, the batteries used in these devices are primary Zn/air batteries. Although studies have been carried out to develop electrically rechargeable Zn/air batteries [48] there is still no commercial product available [47]. The major issues facing the development of electrically rechargeable zinc-air batteries are non-uniform zinc deposition which results in shape change of the negative electrode, dendrite formation (which can lead to short circuits), limited solubility of reaction product and deterioration of the air electrode leading to limited charge-discharge cycles [14], [49].

2.2.3 Al/air batteries

Due to their relatively high energy densities (a consequence of the high voltage associated with the dissolution of aluminium in solution [14]) in comparison to other metal/air batteries (apart from Li/air), Al/air batteries have attracted much attention [14]. However, as a result of high corrosion rates of aluminium in the alkaline electrolyte (which is most commonly used) and the associated hydrogen evolution, which lead to a decrease in anodic efficiency, these batteries have not yet been commercialised [50 - 51]. This has led to various research efforts to improve the aluminium anode, most of which focus on developing aluminium alloys and introducing additives into the electrolyte with the aim of reducing the corrosion effects [52]. Although saline electrolytes have been investigated and possess lower corrosion rates of aluminium (about 3-4 orders of magnitude lower than in alkaline electrolytes) [47], [53], Al/air cells using such electrolytes possess lower specific energy, as well as reduced performance of the air electrode, than their alkaline counterparts. Furthermore, aluminium cannot be electrodeposited in aqueous electrolyte and, therefore, electrically rechargeable aqueous Al/air batteries are not feasible [14], [47].

2.2.4 Fe/air batteries

Iron/air batteries have attracted much attention for use as electrically rechargeable batteries, due to the ability of iron to be electrodeposited from aqueous electrolytes [47]. Unlike zinc, iron does not undergo the extensive inhomogeneous redistribution of active material or shape change when subjected to several charge-discharge cycles [14]. However, the Fe/air battery possesses low charge efficiency due to the problem of excessive hydrogen evolution (resulting from the reaction of the metal electrode with water) as charging occurs. Additionally, the hydrogen evolution that occurs on open circuit leads to corrosion of the iron electrode as well as a high self-discharge rate [54]. The aforementioned issues facing iron/air batteries, limits their application in commercial batteries. Most of the work on iron/air batteries has been discontinued [14].

2.2.5 Li/air batteries

This section begins with the historical development of Li/air batteries and the principle of operation. Various aspects of the Li/air batteries including the electrode materials, types of electrolytes and electrocatalysts are discussed. The electrochemical equivalent (which is indicative of the quantity of electricity) of the various metals used in the previously mentioned metal/air batteries (Sections 2.2.2 – 2.2.4) including Li/air batteries is in the order of Li > Al > Fe > Zn. As a result the Li/air batteries represent the most attractive metal/air combination for increased specific capacities.

2.2.5.1 Historical Development of Li/air Batteries

Researchers at Lockheed introduced the Li/air battery concept using an aqueous alkaline electrolyte [55]. These batteries suffered from major safety concerns associated with vigorous reaction of lithium with water and subsequently led to the abandonment of this concept in the late 1980s [1], [14]. An alternative method was proposed by Abraham and Jiang [19] making use of a non-aqueous electrolyte. In this method, however the discharge products lithium peroxide (Li_2O_2) and lithium oxide (Li_2O) are insoluble in the electrolyte and hence are precipitated and deposited within the pores of the electrode (cathode) and the discharge reaction terminates when these pores are choked with the discharge product [56]. Kowalck *et al.* [57] proposed a method using both aqueous and non-aqueous electrolyte, with the former at the cathode and the latter at the anode. Although longer operation life in the battery was the major advantage of this approach, there was still the issue of electrolyte consumption and reduced capacity in comparison to the non-aqueous Li/air batteries [5]. This is due to the fact that in the aqueous electrolyte battery, the electrolyte takes part in the oxidation-reduction reaction (an intrinsic aspect of its operation) and is therefore consumed during discharge of the battery. As a result, a considerably larger amount of electrolyte (increased weight of electrolyte) in comparison to the non-aqueous electrolyte battery is required to compensate for this, leading to a reduced specific capacity for the aqueous electrolyte Li/air battery [5]. However, it has recently come to light that even in the non-aqueous electrolyte battery, some undesired side reactions that involve the reaction between discharge product and electrolyte do occur [12], [58], but the extent of this reaction is likely to be less than in aqueous electrolyte batteries. Rather than being an intrinsic aspect of the reaction mechanism of non-aqueous Li/air batteries, these side reactions are dependent on the ability to maintain an appropriate level of charge transfer kinetics during battery operation [24]. The non-aqueous Li/air battery has attracted a great deal of attention and still represents a preferred alternative to the aqueous electrolyte based battery.

2.2.5.2 Principle of the Li/air Battery

Li/air batteries can also be referred to as lithium/oxygen (Li/O_2) batteries when operated in pure oxygen. The fundamental principles are the same and sometimes 'Li/air and Li/O_2' are used interchangeably. The only difference is that in Li/air cells a membrane would be required to prevent moisture and CO_2 ingress, both of which are detrimental to the electrochemical performance of the cell due to the dangerous reaction of water with Li, and reaction of CO_2 with electrolyte to form insoluble Li_2CO_3 respectively [59]. As a result, most research devoted to improving the electrochemical performance of these batteries is performed on Li/O_2 cells [24], [31 - 32], [42], [56], although, work is being carried out on developing O_2-selective membranes [60].

The Li/O_2 battery consists of an Li metal anode, a catalyst-loaded carbon air cathode and a glass micro-fibre separator soaked with non-aqueous electrolyte. The active cathode material is O_2 obtained from the atmosphere and the carbon acts as the site for the catalytic reduction of O_2 and also for deposition of discharge product [48]. During discharge, the Li^+ ions from the electrolyte along with electrons from the external circuit combine with O_2 from air to form Li_2O_2 within the pores of the porous O_2 cathode [32]. Upon charging, the Li_2O_2 decomposes back to Li and O_2. The overall cell reaction is as follows:

$$2Li_{(s)} + O_{2(g)} \underset{\text{Charge}}{\overset{\text{Discharge}}{\rightleftarrows}} Li_2O_{2(s)} \qquad E^0_{cell} = 2.96\ \text{V} \qquad (2.4)$$

The end of discharge occurs when the porous O_2 cathode is choked with discharge product [61]. Therefore, a highly mesoporous cathode material with appropriate pore size and pore volume to allow for ease of electrolyte diffusion, as well as provide enough space for deposition of discharge product, is required to allow for high discharge capacities [24]. Porous carbon is the cathode material of choice due to the ability to engineer its porous characteristics as appropriate [22]. It is, however, important to note that the cathode material most commonly used is a composite material made up of a binder and catalyst, as well as carbon [30], [42]. The choice and characteristics of the binder [62], carbon [42], catalysts [30], separator [45] and electrolyte [56], play a vital role in determining the electrochemical performance of Li/O_2 batteries, and some of these shall be discussed in more detail. Furthermore, the discharge reaction previously shown represents the simplest version of processes taking place during operation of the battery. As shall be discussed in Section 2.2.5.4 the formation of an additional discharge product Li_2O can also occur [62], the amount of which is dependent on the concentration of oxygen in the electrolyte [56].

$$4Li_{(s)} + O_{2(g)} \underset{\text{Charge}}{\overset{\text{Discharge}}{\rightleftarrows}} 2Li_2O_{(s)} \qquad E = 2.91\ V \tag{2.5}$$

2.2.5.3 Carbon Electrode Materials

Carbon is the most commonly used material for electrodes in electrochemical energy storage devices, due to its availability in a wide range of physical structures, good electrical conductivity and adequate corrosion resistance [22]. They have also demonstrated promising electrochemical performance when used as cathode materials for Li/O_2 batteries [42]. The carbon materials which are used as electrodes in Li/O_2 batteries are porous in nature, which means they consist of an interconnected matrix of small solid particles, which can be filled with electrolyte [13]. The carbon porosity parameters have been shown to significantly influence the electrochemical characteristics of Li/O_2 batteries [42].

2.2.5.3.1 Types of Carbons

The two main naturally occurring forms of carbon include diamond and graphite [63]. Although there exists a variety of other forms of carbons, Marsh *et al.* [64] suggested that in one way or another, these others forms are related to the graphite structure. Diamond (Figure 2.4) has a more dense structure than graphite, consists of closely packed carbon atoms and is non-porous.

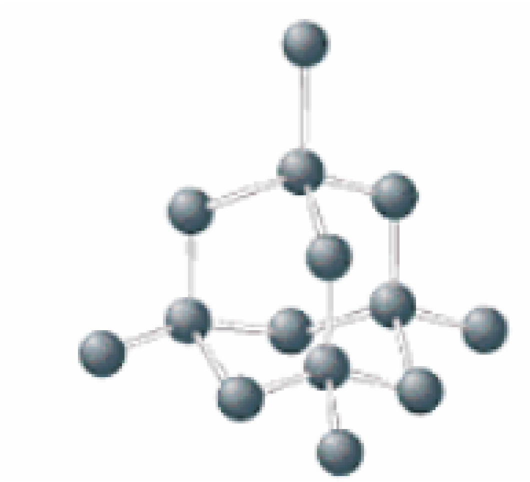

Figure 2.4: Structure of diamond [65]

In diamond (Figure 2.4), each carbon atom is bonded to four other carbons, and as result, these carbon atoms are sp^3 hypridized. On the other hand, each carbon atom in graphite is bonded to three other carbons, resulting in sp^2 hybridization of the carbon atoms (Figure 2.6): the implication of which is the existence of unhybridized p orbitals [17]. Herein lies a significant difference between graphite and diamond. Both graphite and diamond can be viewed as giant networks of carbon atoms. The molecular orbitals in both materials, therefore, result from huge amounts of contributing atomic orbitals, resulting in a virtual continuum of molecular orbital energy levels, called bands [17], [66]. The large energy gap (band gap) between the molecular orbitals of diamond, as a result of its sp^3 bonding, makes the mobility of electrons from one orbital to another, extremely difficult and as such, diamond is regarded as an insulator (unable to conduct electricity). However, the closely spaced molecular orbital energy levels (a consequence of the unhybridized p orbitals) in graphite, allows for easy movement of electrons from one orbital to the next, and accounts for the ability of graphite to conduct electricity [17], [66].

Graphite and graphite related structures such as polymer derived carbons, carbon nanofibres and carbon nanotubes, represent a family of carbons that posses different degrees of structural order. The basic structural unit for these materials is the layer based on the graphitic lattice [67]. It is the variation in the degree of perfection, the extent and the stacking arrangements of these layers that result in a variety of carbon forms. Apart from diamond, and with consideration of varying levels of structural order, carbons can be broadly classified into (i) graphite, (ii) non-graphitisable glass-like carbon (hard carbon) and (iii) soft carbon [26]. A schematic representing these forms of carbon is shown in Figure 2.5.

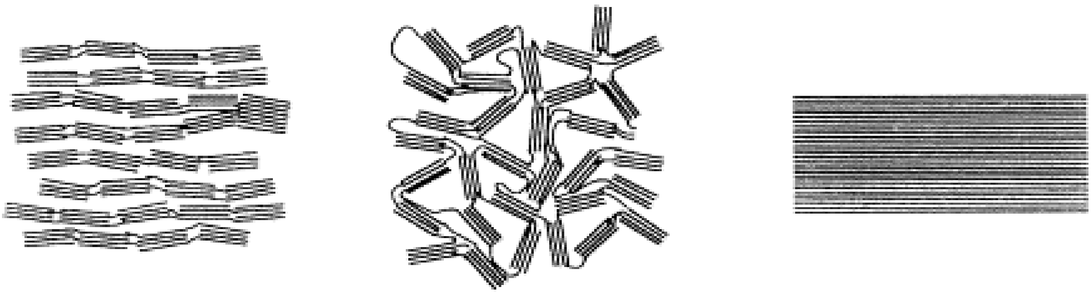

Soft carbon
(or graphitisable carbon)

Hard carbon
(or non-graphitisable carbon)

Graphite

Figure 2.5: Schematic of three types of carbons [26]

The two major forms of graphite include natural and synthetic graphite. Synthetic graphites are more commonly used for electrochemical applications [22]. They are normally synthesised by pyrolysis of organic precursors at extremely high temperatures (2600 ^{o}C – 3000 ^{o}C) [63]. The structure of graphite typically consists of layers of carbon atoms arranged in hexagonal rings (graphene layers), held rather loosely together by van der Waals forces and stacked in a sequence ABAB graphite structure, referred to as hexagonal graphite, or with a sequence ABCABC graphite structure referred to as rhombohedral graphite as shown in Figure 2.6 [14], [65] [66]. The former is the most commonly occurring structure [69].

One of the methods in which the layered structure of graphite has been exploited, is in the lithium ion battery: where it is used as an intercalation electrode, allowing the intercalation of lithium within its layers [8]. It is the ability of graphite to conduct conduction of electricity that makes it suitable as an electrode for various electrochemical energy storage devices [67], [71].

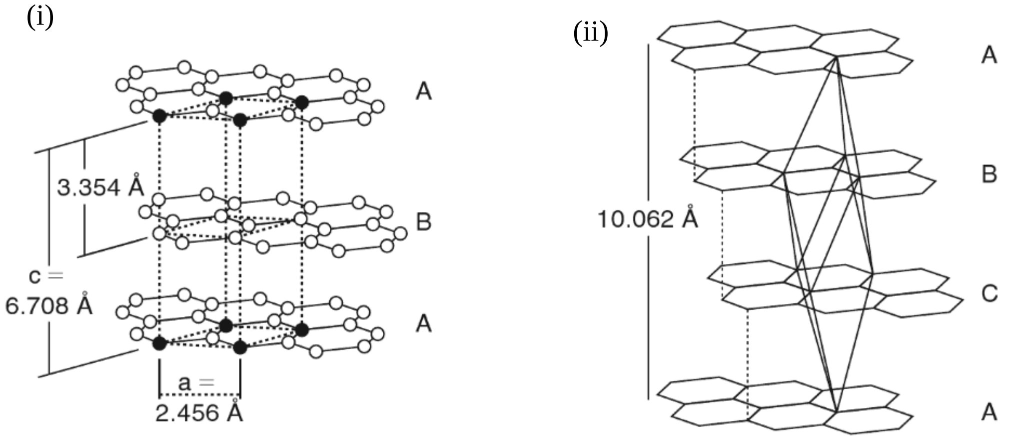

Figure 2.6: (i) Hexagonal unit cell, (ii) Rhombohedral unit cell (interlayer spacing in both structures are the same) [70]

Soft carbons and hard carbons (depicted in Figure 2.5), can be viewed as sections of hexagonal carbon layers of different size which exhibit very little order parallel to the layers. The graphitisation process generally involves the ordering and stacking of these layers upon high temperature treatment [22].

During the pyrolysis of organic precursors under inert atmospheres, volatile decomposition products, such as CO_2, CO, CH_4, and higher hydrocarbon derivatives, are given off [72 - 73]. The remaining carbon atoms are transformed into graphene sheets (planar aromatic structures). If this decomposing precursor forms a semiliquid state (as with petroleum, coaltar pitch and some coals), the planar sheets can become increasingly aligned in parallel, allowing for graphitisation upon heat treatment to 3000 ^{o}C. Such graphitising carbons are referred to as ‘soft carbons’ and possess low surface area and porosity [22].

On the other hand, if the carbon precursor is adequately cross-linked (as with organic gels), a fluid state is not realised during decomposition, preventing the alignment of the planar aromatic structures. The carbons yielded from these materials are difficult to graphitize at any heat treatment temperature and are therefore referred to as ‘hard carbons’. These hard carbons posses considerable surface areas and high pore volumes [22]. An example of such carbons is polymer-derived carbon.

As a result of the aforementioned properties possessed by hard carbons, they are the most suitable candidates to be used as electrode materials for the Li/O_2 battery, in comparison to the other forms of carbons described. Polymer-derived carbons are particularly attractive due to their low cost (in comparison to carbon nanotubes, carbon nanofibres or carbide-derived carbons for example) and ability to manipulate their pore structure as appropriate [7]. One of the most widely used of such materials, for energy storage applications, are Resorcinol-Formaldehyde (RF) carbons [24], [74 - 75]. In terms of the performance of Li/O_2 batteries based on RF carbon electrodes, a discharge capacity as high as 1682 mAh/g and a cycle life of about 25 cycles has been reported [24].

In this work, phenol, a cheaper alternative in comparison to resorcinol [76 - 78], has been used in an attempt to reduce the raw material costs involved in the synthesis of organic gels. A comparison of the costs of PF and RF based electrodes can be seen in the Sigma-Aldrich prices of phenol and resorcinol, shown in Table 2.1 [78]. Much larger quantities of these materials will inevitably be required for large scale fabrication of electrodes, and, therefore, these price differences will be even more pronounced.

Table 2.1: Price comparison of phenol and resorcinol [78]

Raw Material	**Cost (£/Kg)**
Phenol	109.2
Resorcinol	264

Phenol is able to undergo all the typical reactions of resorcinol, such as the sol-gel polymerisation reaction with formaldehyde to produce organic gels, which have been subsequently carbonised to form carbon gels. The chemical differences between phenol and resorcinol, in terms reactivity, will be discussed in more detail, in section 4.1. Although phenol is known to have a slower reaction rate compared to resorcinol, with the appropriate manipulation of reactant ratios, scientists have been able to produce organic gels and carbonised gels possessing appreciable levels of porosity with mesopore (pores size between 2 and 50 nm) volumes ranging from 0.9 – 1.43 cm^3/g and 1.2 – 1.84 cm^3/g for organic and carbonised gels, respectively [76 - 77]. However, a thorough investigation of the control of porosity of PF gels derived via sol-gel polymerisation aimed at demonstrating their applicability to Li/O_2 batteries is yet to be reported.

The properties of the prospective carbon, such as pore volume and pore size, represent major parameters affecting the electrochemical performance of the carbon based electrodes [42]. Various types of pores, including micropores, mesopores and macropores, classified according to their sizes (based on IUPAC classification [79]), are shown in Table 2.2. Electrodes based on mesoporous carbon with high pore volumes are particularly attractive for Li/O_2 batteries as they allow for ease of electrolyte diffusion into the pores of the electrode as well providing enough space for storage of discharge product [42].

Table 2.2: Various types of pores and pore sizes [79]

Pore Classification	**Pore Diameter (D)**
Micropores	$D < 2$ nm
Mesopores	$2 \leq D \leq 50$ nm
Macropores	$D > 50$ nm

2.2.5.3.2 Surface Functionality

The chemical species present on the surface of carbons determine the physicochemical properties of these materials. Various surface functional groups containing oxygen, hydrogen, nitrogen, sulphur and halogens can be introduced on carbon surfaces. The concentration and type of the surface functionalities is highly dependent on the procedure by which the carbons have been prepared [80]. The interest in understanding the surface chemistry of carbons has grown due to the electrochemical importance of various surface groups and as a result the modification of carbon surfaces is indeed an important area of research. Electrolyte wettability and chemical reactivity associated with the carbon surfaces are examples of properties that could be varied in order to influence the electrochemical performance of energy storage devices [80].

One of the most common and most important surface functional groups that influence the physicochemical properties of carbon materials is the carbon-oxygen complex. They are identical to those found in normal organic compounds and are believed in some cases to display similar behaviour towards reactants, to those organic compounds possessing the same surface groups [22]. Gas phase oxidation by means of various oxidizing agents including O_2 and CO_2, and chemical treatment by oxidizing agents in solution such as HNO_3 and $KMnO_4$ are known to introduce oxygen surface functional groups on carbon [22]. Various examples of such groups include the phenolic –OH, carbonyl and carboxyl groups. Lee *et al.* [81] showed that the presence of carbonyl groups on the surface of carbon, improved the electrochemical performance of lithium ion batteries, through a reaction involving lithium ions with these surface oxygen groups.

2.2.5.4 Electrolytes

The electrolyte acts as a medium of ion transfer between the anode and the cathode. Along with good ionic conductivity, the electrolyte must not be electronically conductive i.e. must not allow the passage of electrons as this would allow for short-circuiting in the cell [14]. Other requirements include thermal stability, a wide electrochemical voltage window, and compatibility with other cell components. The choice of electrolyte for Li/O_2 batteries is determined by the aforementioned factors. Electrolytes typically used in batteries are liquid solvent based such as aqueous and non-aqueous electrolytes. However, solid electrolytes have also been used [13], [82]. Aqueous electrolytes are detrimental to the performance of Li/O_2 batteries due to the high reactivity of lithium with water as shown in the reaction below [14]:

$$Li_{(s)} + H_2O_{(l)} \longrightarrow LiOH_{(aq)} + \tfrac{1}{2} H_{2(g)} \qquad (2.6)$$

Upon low-rate discharge and on open-circuit, self-discharge depicted by the above reaction occurs rapidly and eventually destroys the anode [14]. However, work has been carried out on the development of unique materials, such as the Li-ion conducting solid-state glass ceramic plate, which protects the Li anode from contact with water, but is able to conduct Li-ions [57].

Organic electrolytes are most commonly used in Li/O_2 batteries, more specifically lithium salts in organic solvents, as they provide an inherently safer alternative to aqueous electrolytes [24], [41], [56]. Although organic electrolytes have lower conductivities and higher viscosities than aqueous electrolytes, they possess a higher electrochemical stability window (~4.6V) in comparison to aqueous electrolytes (~2V) [13]. Organic solvents such as propylene carbonate [30], 1, 2-dimethoyethane [48], and lithium salts such as $LiPF_6$ [24], $LiAsF_6$ [31], $LiClO_4$ [83] and $LiSO_3CF_3$ [48] have been utilised in lithium/oxygen batteries. The salts are required to provide mobile ions for transport to the electrode surface [14]. As electrolyte solvents with low evaporation rates are preferred for Li/air batteries, Xu *et al.* [59] made a comparison of several electrolyte solvents in terms of their evaporation rates as shown in Figure 2.7; where DME, DEE, DEC, BEE, DPG, DG, EDG, PC and BDG stand for 1,2-dimethoxy/ethane, 1,2-diethoxy/ethane, diethyl-carbonate, 1-tert-butoxy-2-ethoxyethane, dipropylene-glycol-dimethyl-ether (diproglyme), diethylene-glycol-dimethyl-ether (diglyme), diethylene-glycol-diethyl-ether (ethyl diglyme), propylene-carbonate and diethylene-glycol-dibutyl-ether (butyl diglyme), respectively. It can be observed that PC, which is one of the most frequently used electrolyte solvents in Li/air batteries, has one of the lowest evaporation rates of the solvents studied which is due to its high boiling point. The low volatility of PC makes it an attractive electrolyte solvent as it better maintains the electrolyte composition during use [59]. However, properties such as high boiling points and low volatilities are also associated with high viscosities. It has been argued, that an electrolyte with a low viscosity, may result in a slightly higher discharge capacity for the Li/O_2 battery, compared to one with a higher viscosity, as the former enhances the rate of diffusion of oxygen in the electrolyte [84] (which as will be described later in this section, is one of the processes that occurs during the discharge of the Li/O_2 battery). This could explain why some researchers use a combination of PC and other solvents to reduce viscosity [85 - 86]. However, caution should be taken as such mixtures could increase the volatility of the mixed solvent which means there needs to be a fine balance between volatility and viscosity.

Another important issue relating to non-aqueous electrolytes is the wettability of the air cathode. This depends on the contact angle between the electrolyte and the electrode. Due to the relatively high polarity of the PC solvent, the electrolytes based on PC are also of high polarity. The result of this is a lower affinity for the carbon pore surfaces leading to larger contact angles assuming a low polarity of the carbon surface. Thus, such electrolytes are unable to access the surface of the pores in the electrode easily or fully, leaving gaps (contact angle) between carbon surface and the electrolyte. Subsequently, oxygen is able to diffuse quicker through these gaps to get reduced at the triphase (solid/liquid/gas) regions leading to improved discharge capacities [59]. It should noted that access of the electrolyte through the orifice of the pores is highly beneficial for Li/air batteries and is the reason why mesoporous electrodes are attractive; this is different from the issue just discussed regarding wettability which deals with contact between electrolyte and the carbon surface rather than passage of electrolyte through the orifice of the carbon pores.

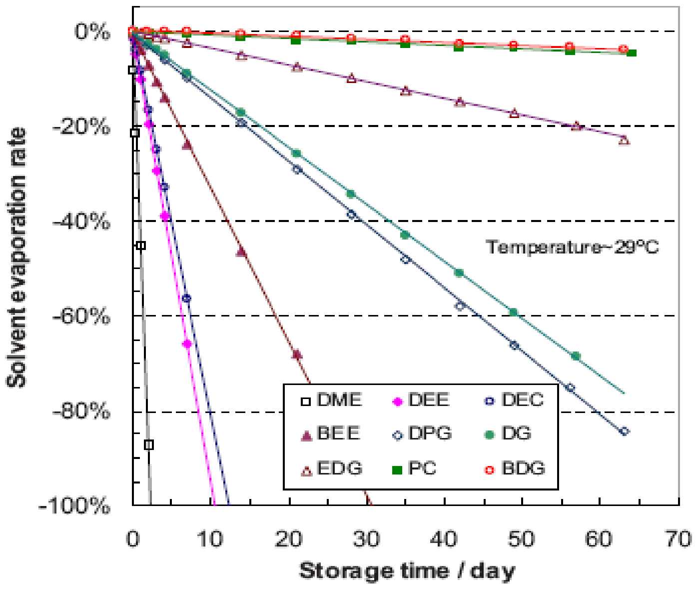

Figure 2.7: Solvent evaporation rates in various electrolyte solvents [59]

Zhang *et al.* [48] suggested that the 3-phase model cannot sustain continuous deposition of discharge product, because the O_2-diffusion channels (gaps) would be easily filled with the discharge product and, therefore, proposed a model (Figure 2.8) consisting of a two-phase (liquid-solid) reaction zone whereby the carbon pores are completely wetted with electrolyte and only dissolved oxygen participates in the charge transfer reactions. In this model, since the pores within the carbon particles are completely wetted, O_2 diffusion begins in gas diffusion channels between the wetted surfaces, and is subsequently dissolved in the electrolyte where it continues to diffuse as dissolved oxygen, towards the electrode/electrolyte region. Thus, in this case, oxygen solubility and diffusivity in the electrolyte become increasingly important as both have a significant effect on the rate of oxygen transport through the electrolyte to the carbon-electrolyte interface [87]. It was suggested [56] that the ability for the electrolyte to wet the carbon surface is crucial for obtaining good discharge capacities. This is understood considering that mainly dissolved oxygen in the electrolyte is taking part in charge transfer reactions and, therefore, an increasing amount of wetted carbon surface implies increased reaction zones and better discharge capacities. Furthermore, it was shown that in the case of the two-phase model, electrolyte formulation also affects the ratio of Li_2O_2/Li_2O formed during discharge. For example, a higher solubility of oxygen in the electrolyte means a greater oxygen concentration. It was suggested that lower concentrations of oxygen would lead to an increase in the formation of Li_2O [56]. Both the 2-phase and 3-phase models have strong points and both are likely to apply to the non-aqueous Li/air battery. However, there is no experimental evidence to quantify the level of contribution of charge transfer reactions based on each model to the overall discharge capacity of the cell.

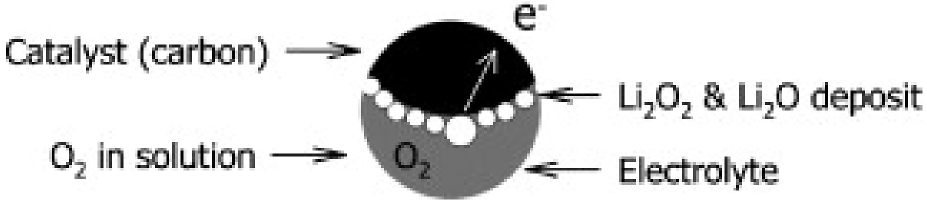

Figure 2.8: Two-phase reaction zone model for the non-aqueous Li/air battery [48]

Hydrophobic room temperature ionic liquid electrolytes (RTILs) have also been investigated for use in Li/O_2 batteries and have been considered to be an attractive alternative since Li/O_2 batteries will eventually work in air which contains moisture [88]. These electrolytes are room-temperature molten salts made up of bulky, asymmetric organic cations and inorganic anions. RTILs are also attractive for use in Li/O_2 batteries due to their high thermal stability, high ionic conductivity, large electrochemical window and also because they are non-flammable and non-volatile in nature [89]. Solid electrolytes have also been successfully applied to Li/O_2 batteries [82]. Batteries containing solid electrolytes possess the benefits of an all solid-state design where safety concerns regarding possible rupture and ignition of liquid electrolyte based cells in high temperature environments, are not present.

2.2.5.5 Electrocatalysts

Traditionally, as for aqueous Li/air batteries for example, the role of the catalyst is primarily to assist in the breakage of the O – O bond [90]. However, in the case of the non-aqueous systems, the role of the catalyst in the formation and decomposition of discharge product, Li_2O_2 [30], [90], which does not involve the breakage of the O – O bond, is yet to be fully understood [30]. However, studies have shown that discharge capacities and capacity retention can be increased while charge voltage can be decreased with the use of the appropriate catalysts suggesting that in the Li/O_2 non-aqueous electrolyte cell, the reduction of O_2 to $O_2{}^{2-}$ and its oxidation back to O_2 is aided by such catalysts [30]. Reducing the charge voltage is important as it increases the efficiency of Li/O_2 batteries and could prevent unwanted side reactions such as electrolyte oxidation at higher voltages. Capacity retention is also required in order to achieve longer cycle life.

Debart *et al*. [32] showed that with the use of α – MnO_2 nanowire catalysts a discharge capacity of over 3000 mAh/g (per gram of carbon) with a charge voltage of ca. 4 V can be achieved. However, drop in capacity upon repeated cycling still remains an issue. This shows that although certain catalysts are more effective than others with regards to capacity retention, the capacity fade that occurs even after the selection of the most preferred catalyst is likely due to the porosity of the electrode [30], [32]. Nevertheless, these studies show that the catalyst can enhance capacity retention. The research undertaken by scientists on electrocatalysts in non-aqueous Li/air batteries, also show that higher surface area catalysts produce better electrochemical performance due to enhanced kinetics [32], [91]. Other catalysts, such as Fe_3O_4, Co_3O_4, CuO and electrolytic manganese dioxide (EMD) have also shown noteworthy electrochemical performance [30 - 31]. Manganese oxides based catalysts are particularly attractive due to their low cost and non-toxicity. In general, it would appear that the main considerations affecting the choice a catalyst include low cost, high surface area, non-toxicity and its ability to lower the charge voltage, increase discharge capacity and capacity retention.

2.3 Theoretical vs Practical Energy Density for Li/O_2 Batteries

The theoretical energy density or specific energy of the Li/O_2 battery is approximately 3456 or 5225 Wh/Kg (including the weight of O_2), according to equation (1.7) and based on the formation of Li_2O_2 or Li_2O, respectively. By recognizing that the 'nFE^0_{cell}' term in equation (1.7), simply refers to the absolute value of the standard change in Gibbs free energy, ΔG^0, the calculation for the aforementioned energy densities was carried out by diving the ΔG^0 value for the formation Li_2O_2 and Li_2O by the mass of reactants involved in each reaction. The ΔG^0 values were obtained from the NIST-JANAF thermochemical tables [20]. However the practical energy density would be much less taking into the account other components of the cell such as the air cathode, electrolyte, current collector, binder, cell casing etc. In fact, these considerations bring up another avenue for research into increasing energy density of Li/O_2 batteries, by looking for ways to remove or reduce the weight of certain battery components, such as the binder and the current collector [92].

Another useful parameter, similar to specific energy in terms of the disparity between theoretical and practical values, used for analysing the electrochemical performance of the Li/O_2 battery, is the specific capacity. The specific capacity of the

Li/O_2 cell, calculated using equation 1.5, is approximately 1168 mAh/g and 1794 mAh/g (including the weight of O_2), for the formation of Li_2O_2 or Li_2O respectively. Most of the published data on Li/O_2 cells normalise the specific capacity to the weight of the carbon in the electrode [41 - 42], [93 - 94]. The deposition of discharge product in the carbon pores of the O_2-electrode is the main driving factor for this method of reporting specific capacity of Li/O_2 cells [1]. Furthermore it provides a platform for comparison between various published data allowing for effective research in the area of Li/O_2 batteries.

Other contributions to a drop in capacity for non-aqueous Li/O_2 systems result from polarisation losses at the electrode (activation and concentration polarisation) as well as ohmic losses from certain cell components [4]. Activation polarisation losses originate from the kinetic limitations to charge transfer processes at the electrode/electrolyte interface while concentration polarisation occurs as a result of slow diffusion of reactants to the active regions in the electrode due to build up of discharge product. The former is an interface phenomenon, which is likely to be associated with a kinetic activation barrier in the oxidation reduction reaction at the cathode [12], while the latter is dependent upon varying levels of porosity of the air cathode and the ease of diffusion through it, in addition to mass transport processes in the electrolyte [4]. Both polarisation losses, also referred to as overpotentials, lead to the drop in voltage of the cell and subsequently a drop in capacity. Ohmic polarisation (also known as IR drop, where I is current and R is resistance), on the other hand, results from resistive losses in the current collectors, electrolyte and active masses. The associated current flow through the internal resistance also leads to a drop in voltage and subsequently the capacity of the cell [4].

The discharge process, which involves deposition of discharge product into the pores of cathode, leads to restraints in the practical specific energy of Li/O_2 batteries and has prompted research in the area of improving the porosity of the electrode both to increase the storage capacity and to allow for proper utilization of the active surface area. Tran *et al.* [95] showed that larger pores are less easily choked with discharge product than smaller ones, implying that the active regions in the wider pores are more effectively utilised.

2.4 Summary of Issues Facing Li/O_2 Batteries

It is evident that Li/O_2 batteries possess an immense potential. However, issues, such as electrode polarisation [24], capacity retention, low cycle life, charge overvoltage, safety [12], and membranes to prevent CO_2 and H_2O penetration [32], need to be addressed before the commercialisation of these batteries. The presence of a lithium metal anode still leads to the likelihood of dendrite formation. A chemically heterogeneous passivation layer known as the solid-electrolyte interface (SEI) is formed when lithium metal is immersed in an organic solvent, and prevents any further corrosion of the lithium metal. The formation of a brittle and morphologically heterogeneous structure due to the chemical heterogeneity of the SEI, can lead to an accumulation of defects upon continuous lithium stripping and plating during discharge and charge respectively. Non-uniform current distributions as a result of the aforementioned defects can arise throughout the SEI, allowing for preferential deposition of lithium metal and leading to dendrite formation [12]. The safety concerns regarding dendrite formation in the non-aqueous Li/air battery is due to the possibility of an aggressive reaction of dendrites with a variety of contaminants [12]. This has led to research into artificial protective layers (or SEI) to minimise dendrite formation [96 – 97].

As mentioned in the previous section, the discharge overpotential leads to the drop in capacity of the Li/air battery. Other important aspects of the Li/air cell are the OCV (open circuit voltage) and the charge overpotential as shown in Figure 2.9 (where the mid-points of the discharge and charge curves are approximated as the working voltages in a hypothetical flat discharge and charge profile, respectively).

An attempt is made here to shed further light on the overpotentials in the Li/air battery (Figure 2.9). However to gain an overall picture on voltage characteristics of the cell, the OCV shall be explained briefly. The OCV represents the cell voltage when there is no net current flow and should ideally correspond to the standard potential of the cell [11]. However it can be observed from Figure 2.9 that this voltage is higher than the standard potential of the cell. This is thought to be due to a mixed potential effect associated with the reaction of Li-ions with impurities as well as the electrochemical catalyst [12].

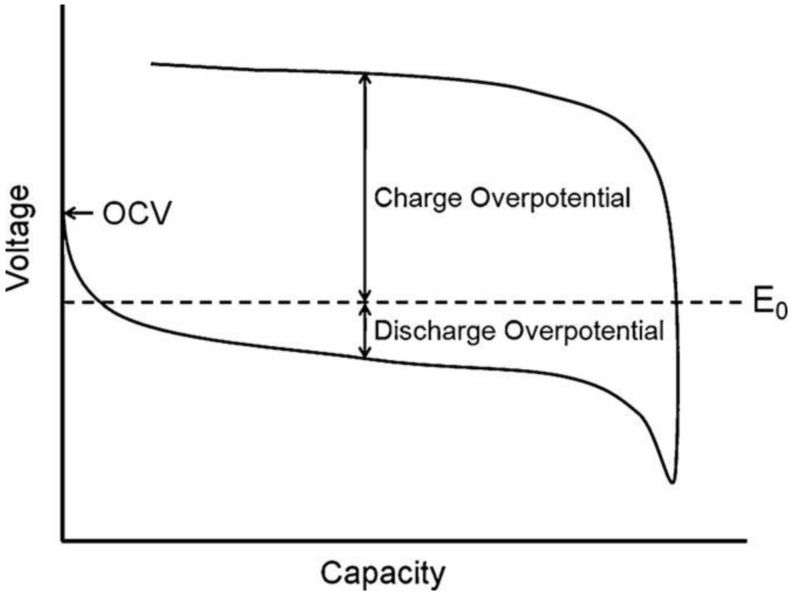

Figure 2.9: Schematic representation of a typical discharge/charge curve for the Li/O_2 battery. E_0 is the standard potential (or thermodynamic potential) and OCV is the open circuit voltage [1]

The discharge overpotential is probably due to various polarisation losses during cell operation as described in Section 2.3. On the other hand, it can be noted that the voltage required upon charging of the cell is substantially higher than the reversible potential for Li_2O_2 formation. As will be explained later in this report, this could be indicative of the presence of other compounds formed by the side reactions which are associated with slow charge transfer kinetics during discharge. As such it can be seen that some of the processes that lead to discharge overpotential subsequently affect the charge voltage. Another possible explanation is that the use of different catalysts leads to variable levels of charge voltage as the catalysts can aid in the decomposition of Li_2O_2 to different extents. The effect of these overpotentials is that they could lead to relatively low electrical energy efficiencies of the discharge-charge cycles. The electrical energy efficiency for a discharge-charge cycle can be related to the ratio of the discharge voltage to the charge voltage, as shown in equation 2.7 [12].

$$Efficency\ (\%) = \frac{discharge\ voltage}{charge\ voltage} \times 100 \tag{2.7}$$

Optimisation of the porous structure of the O_2 cathode to reduce electrode polarisation, a deeper understanding of the fundamental processes governing the operation of the Li/O_2 battery to determine qualitatively and quantitatively the possible reasons for low capacity retention and cycle life, as well as an investigation of the role of the catalyst in reducing charge overvoltage and, therefore, increasing efficiency could increase the commercial viability of these batteries. Additionally, searching for cheaper raw materials in the production of these batteries will also render them more attractive.

Chapter 3

Objectives of Study

3.1 Objectives

The overall objective is to optimise the porosity of phenol-formaldehyde (PF) carbon gels, correlate the electrochemical performance of lithium/oxygen (Li/O_2) batteries using activated PF carbon based electrodes to porosity parameters as well as surface functionalities, and to determine the factors that enhance and impede the performance of Li/O_2 batteries.

3.2 General Objectives

The non-aqueous Li/O_2 battery possesses an energy density 5 – 10 times that of Li-ion batteries and is by far one of the most competitive energy storage devices in recent times. There is, therefore, considerable interest in this device as a means of storing energy from renewable energy sources as well as for use in electric vehicles and portable electronics. As it is particularly vital that this technology becomes commercially viable, cheaper raw materials as well as a thorough understanding of the processes that govern its operation are crucial to its success. The latter could assist in exploiting the full potential of Li/O_2 batteries, allowing them to reach even higher energy densities and attaining longer cycle life.

Due to the relatively inexpensive nature and ease of production of polymeric carbons, they have been thoroughly utilised as electrode materials in the area of electrochemical energy storage with resorcinol-formaldehyde carbons being the most common. Low cost phenol is an attractive alternative to resorcinol as it contributes to the reduction in raw material costs. However, little is known about the effect of various synthesis conditions on the porous structure of PF gels specifically synthesised by the sol-gel polycondensation method. Furthermore, a detailed outline of the optimum conditions beginning from the initial gel synthesis stage to the final electrode, that yields the most desirable properties in terms of porosity and surface functionalities, for use as electrodes in Li/O_2 batteries has not been reported yet. The aim of this work is therefore to investigate the effect of various synthesis parameters on the porous structure of PF gels and carbons with the sole purpose of controlling porosity to maximise electrochemical performance of Li/O_2 batteries using the PF based carbon electrodes, whilst gaining a better understanding of the electrochemical significance of surface properties of the carbons and of the processes that occur during the operation of the Li/O_2 battery.

3.3 Specific Objectives

The specific objectives of this work are listed below and the corresponding block diagram of the specific objectives is shown in Figure 3.1.

- Investigate the effect of reactant ratios, such as phenol/catalyst (P/C) ratio, and phenol/formaldehyde (P/F) ratio, on the porous structure of PF gels, and determine the most suitable combination of these parameters for porosity development.
- Identify a suitable solvent exchange liquid capable of retaining the original porous structure of the PF gels after drying.
- Investigate the effect of drying method on the porous structure of PF gels.
- Examine the effect of carbonisation temperature on the porous structure of PF carbons to identify the temperature that yields the highest level of porosity.
- Compare the effect of O_2 and CO_2 activation on the porous structure of PF carbons in order to identify the most suitable activating reagent for activated carbon production.
- Compare the surface characteristics of O_2 and CO_2 activated PF carbons and the possible implications on electrochemical performance
- Determine the effect of discharge rate on the electrochemical performance of Li/O_2 batteries to gain a better understanding of the power capabilities of these batteries.

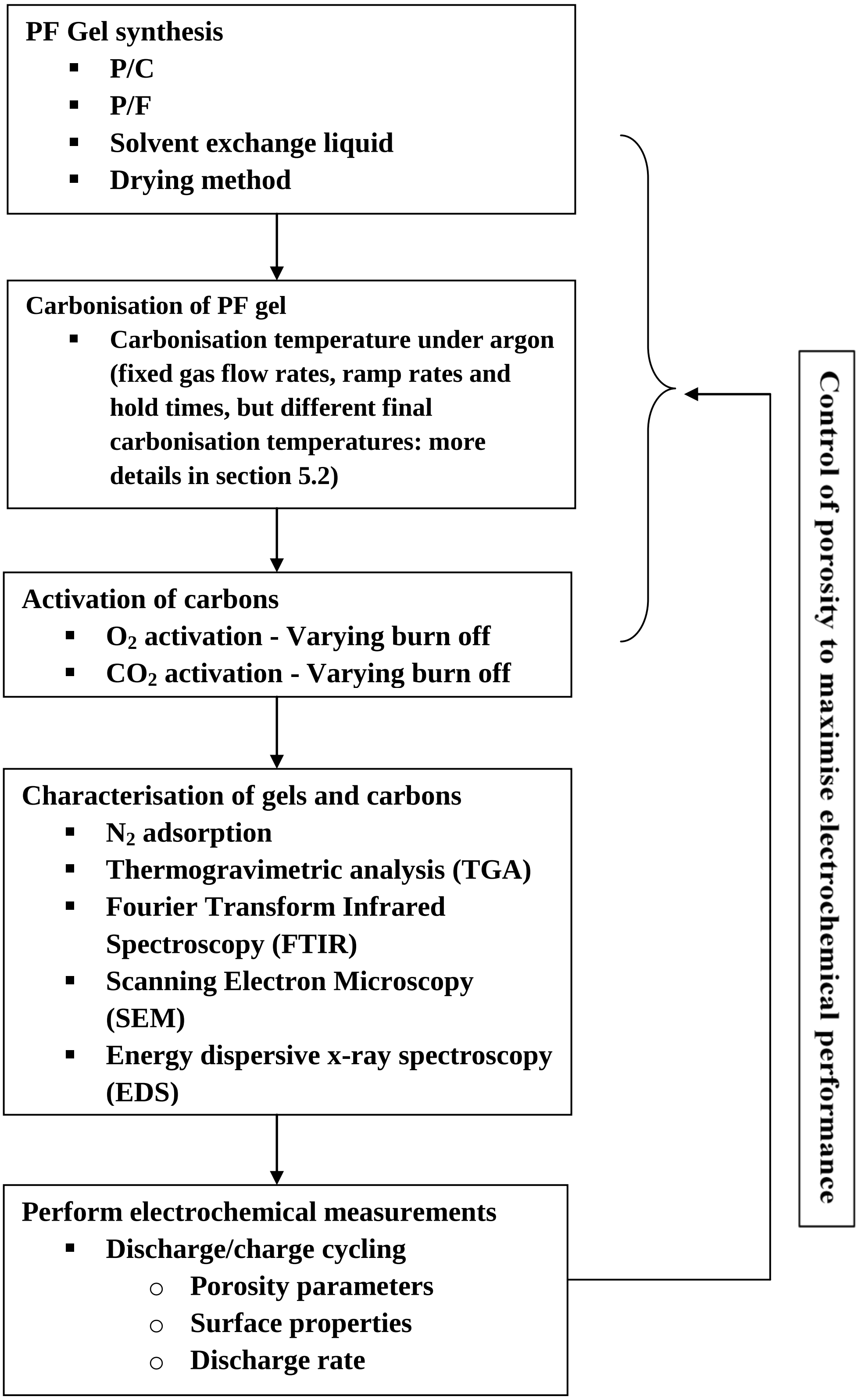

Figure 3.1: Block diagram of specific objectives

Chapter 4

Theory

In addition to discussing the relevant aspects of carbon gel production, this section also deals with various analysis methods that have been used in this work; such as the N_2 adsorption/desorption isotherm analysis using the Barret-Joyner-Halenda (BJH), Brunauer-Emmett-Teller (BET), and t-plot methods; all used to obtain porous properties of the synthesised samples, thermogravimetric (TGA) analysis, which was used to obtain weight loss profiles of the samples with respect to temperature, Fourier Transform Infrared (FTIR) spectroscopy to obtain information about surface functionalities of the samples, Scanning Electron Microscopy to obtain images of the samples, Energy Dispersive X-ray Spectroscopy (EDS) to detect certain species contained in the samples, and the galvanostatic discharge/charge measurement technique, which was used to determine the electrochemical performance of Li/O_2 batteries.

4.1 Carbon Gel Production

Aside from their uses as electrode materials for electrochemical energy storage devices, carbons can also be used as packing materials for chromatography [98], thermal insulators [99], catalyst supports [100], and adsorbents for gas separation [101]. The majority of published works on carbon precursors (organic gels) are based on resorcinol formaldehyde gels. However, in an attempt to reduce raw material costs, resorcinol can be replaced with phenol. Due to the electron density in the 2, 4, 6 ring positions of phenol, it is believed that it undergoes a similar sol-gel polycondensation reaction to resorcinol, however, at a slower rate [77]. The hydroxyl group of phenol is an electron releasing substituent, which activates the positions ortho- and para- to it, by increasing the electron density at these positions [16]. In resorcinol, however, which contains two hydroxyl groups, the previously mentioned active sites on the aromatic ring are doubly activated [102], making resorcinol more reactive towards electrophilic aromatic substitution.

4.1.1 Initial Synthesis Stages

The initial reaction sequence in the synthesis of PF gels, typically begins with the addition of formaldehyde to phenol, in the presence of an alkaline catalyst. This leads to the formation of hydroxymethyl derivates of phenol, which then undergo condensation reactions to form methylene and methylene ether bridged compounds, giving way to chain growth formation [103]. The function of the catalyst is to convert phenol into a phenoxide ion, which is more reactive than phenol itself [16]. However, it has also been suggested that the valence and ionic radius of the metallic ion used in the catalyst, plays a role in the phenol-formaldehye reaction. For example, studies done by Grenier-Loustalot *et al.* [104] suggested that the deprotonated phenol is better stabilized by a divalent cation in comparison to a monovalent one [105]. Futhermore, the dissociation of the catalyst (which allows it to take part in the reaction mechanism) is sensitive to the solvation of the metallic cation [104]. This solvation increases as the ionic radius of the cation decreases, favouring the dissociation of the catalyst. The catalytic reaction between phenol and formaldehyde (sol-gel polymerisation) is depicted in Figure 4.1 and shows methylene and methylene ether linkages, formed by condensation reactions.

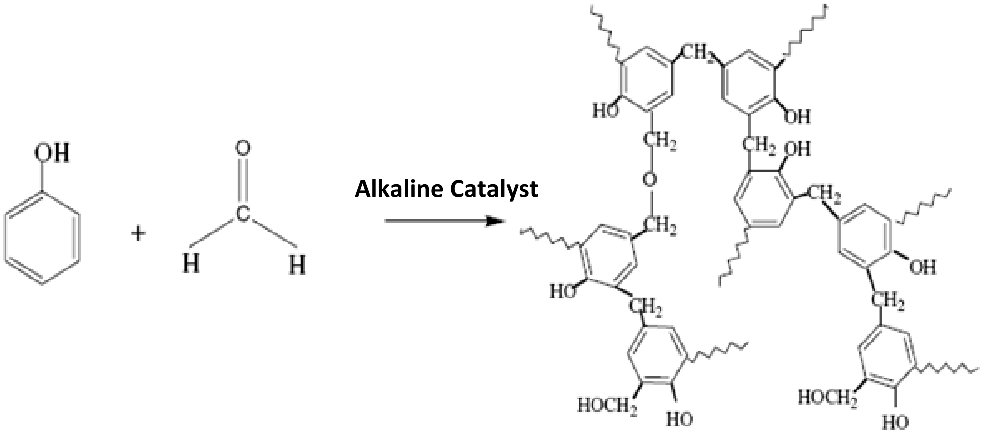

Figure 4.1: Schematic of the reaction between phenol and formaldehyde in the presence of an alkaline catalyst [77]

The amount of reactants and the ratios of reactants present in solution during the initial mixing stages have a significant influence on the final porous structure of the gel. Furthermore, the solvent not only helps to homogenise the precursor but its polarity strongly influences the particle and network forming reactions [106]. The lower electron density, due to the lack of one OH group in phenol, compared to resorcinol (Section 4.1), which results in a lower reactivity for the former [102], implies a need for utilising higher amounts of catalyst, in order to prevent segregation (due to unreacted phenol), and increase reaction rate. The ensuing polymer solution is referred to as the sol [107].

4.1.2 Gelation and Curing

The rate at which the condensation reactions proceed depends on the precursor materials including the type of catalyst, the catalyst concentration, reactant concentration and the type of solvent [108]. However, heating is required to provide sufficient energy for polymerisation to proceed at an appreciable rate [107]. The viscosity of the solution continues to increase until a gel point is reached and a solid is formed that signifies the formation of a three-dimensional continuous network known as the hydrogel. The stiffening of the gel that occurs is due to the cross-linking of the oligomers (molecules composed of too few monomer units to be classified as polymers, but more monomer units than in dimers, trimers, tetramers etc [16]) formed during the initial mixing stages. The term curing refers to the continuous cross-linking of previously formed polymers to form the final porous solid network whose pores are usually filled with solvent from the sol [109].

4.1.3 Solvent Exchange and Drying

The solvent exchange step involves replacing the remaining solvent (usually water) in the gel with an organic solvent such as acetone, t-butanol, isopropanol or amyl acetate [76], [107], through a repetitive washing procedure, and precedes the drying stage.

There are various methods of drying of the wet gel and they typically result in different porous structures of the final dried gel. Evaporative drying, for example, which can be carried out under vacuum or ambient pressure [106], [110], usually leads to a greater level of shrinkage, in comparison to other forms of drying such as supercritical and freeze drying [107], [111]. Important parameters that affect the structure of the final gel during the solvent exchange and the drying process shall be discussed in this section.

The properties of the final dried gel upon evaporative drying, can be associated with the type of solvent used for the prior solvent exchange process. It is important to note that after gelation, chemical transformations are still taking place [106]. Further condensation reactions (aging) continue to occur during the drying stage leading to further stiffening of the gel network by an Ostwald-ripening type process; whereby smaller more soluble particles dissolve and reprecipitate on to larger less soluble ones [106], [112]. Therefore, the greater the solubility of the reactant e.g. phenol or resorcinol, in the solvent exchange liquid, the more rapid the aging rate [109]. It has been suggested that a precise control of the rate of aging (slow aging) can reduce the possibility of large gradients in shrinkage and the subsequent collapse of the gel structure [108].

Additionally, the temperature chosen for the evaporative drying process could affect the rate of evaporation and subsequently the magnitude of the capillary forces exerted on the pore walls resulting in different porous structures in the final dried gel. This can be understood from the viewpoint of the liquid-vapour interactions within the pore. The pore liquid forms a liquid meniscus at the exit of the pore subjecting it to hydrostatic tension. The tensile stress on the pores of the gel during the drying procedure is described by equation 4.1:

$$\sigma_r = \frac{2\gamma \cos\theta}{r_{pore}} \tag{4.1}$$

where γ is the liquid surface tension, θ is the wetting angle with the gel solid network surface and r_{pore} is the gel pore radius [109]. Tamon *et al.* [111] have shown that evaporative drying is not able to maintain the original structure of the wet gel as well as in other forms of drying, such as supercritical and freeze drying (which shall be discussed shortly), due to a relatively increased level of shrinkage owing to the formation of a vapour-liquid interface [107].

Another drying method is supercritical drying. It involves a second solvent exchange process with another liquid of lower surface tension such as liquid CO_2. The extraction of the new pore fluid is performed in its supercritical state and thus avoids the vapour-liquid interface and the associated mechanical stresses and capillary forces on the pore walls [107]. This method of drying is unique in the sense that the liquid contained in the gel, is removed above its critical point i.e. a particular temperature and pressure, where the conversion of liquid to its vapour states, does not occur in the expected way (directly): rather, the liquid goes through an intermediate 'fluid' state, which is neither liquid nor vapour, hence preventing surface tension and effectively keeping the original structure of the gel [17], [113]. Wu *et al.* [77] synthesised PF gels using this method with mesopore volumes of up to 1.43 cm^3/g. Although this method of drying is known to preserve properly the wet gel porous structure, the requirement of high pressure equipment increases the processing costs [76]. A less expensive method also capable of better preservation of the gel structure is freeze drying. In this case the pore liquid is extracted from the gel structure by sublimation and involves exposing the gel to a temperature below the freezing point of the pore liquid and placing under vacuum. Much higher mesoporosity in the gels can be obtained from this method in comparison to evaporative drying but mesopore volumes are not as high as those obtained in supercritical drying. Mukai *et al.* [76] synthesised freeze dried PF gels with mesopore volumes of up to 0.9 cm^3/g. Although there might be energy penalties and subsequently slightly increased costs for freeze dying methods in comparison to evaporative vacuum drying, typically due to the longer times for vacuum pump usage for the former, the global outlook on energy sources is gearing towards renewable supplies, such as solar and wind power, which will inevitably become much cheaper, and more widely available on the long term, therefore, rendering such price differences relatively minimal. Furthermore, as mentioned earlier, freeze drying is more capable of maintaining the gel structure, than evaporative vacuum drying [114].

4.1.4 Carbonisation and Activation

Carbonisation or pyrolysis involves heating the gel in a furnace at temperatures above 500 ^{o}C, in an inert atmosphere, and converting it into carbon [109]. An even more revealing definition is that carbonisation is the process of formation of a material with increasing carbon content from an organic material, usually by pyrolysis, resulting in an "almost" pure carbon residue at temperatures up to approximately 1300 ^{o}C [67]. This suggests that even at this temperature, heteroatoms are still present within its structure. Furthermore, as it is known that synthetic graphite is one of the most chemically pure carbon forms [115], and also that it is normally obtained from graphitisable materials upon heat treatment to about 3000 ^{o}C, it follows that it is only at these temperatures that high purities can be realised.

Due to the fact most of the carbons used in electrochemical applications requiring porous materials, are based on non-graphitisable carbons that are prepared at carbonisation temperatures of 800 – 1050 ^{o}C [14], [42], [67], the word 'carbon' being used in these applications, does not refer to pure carbon, but a carbonised material with an increased relative carbon content, in comparison to the other species (such as oxygen and hydrogen) present in the organic precursor.

Further enhancement of the porous properties of the carbons has been reported to be achievable by physical and chemical activation [42], [116], [117]. Physical activation involves gasification of the carbon at elevated temperatures in gases such as O_2 and CO_2 while chemical activation involves impregnating the organic precursor with chemicals such as KOH, HNO_3, H_3PO_4 which act as oxidising agents during carbonisation of the precursor (carbonisation and activation in this case occurs simultaneously) [7], [22]. These procedures have also been known to introduce electrochemically active functional groups onto the surface of the carbons [81], [116] i.e. the same procedures that lead to the enhancement of porosity, also cause the retention of surface functional groups from the oxidising agents, on the carbon.

Varying the reactant ratios and types of reactants at the synthesis stage, as well as conditions of further stages of processing to form a carbon, can yield materials with different structures and properties. This has enabled scientists to prepare these carbon gels with a range of characteristics to suit the required application [100 - 101]. The characterisation of activated carbons, carbonised gels, and their organic precursors (polymer gels) shall be explained in the following sections.

4.2 N_2 Adsorption/Desorption

This technique is used for the physical characterisation of materials. Properties such as surface area and porosity can be obtained by applying this method. It is based on the introduction of nitrogen gas molecules (adsorbate) to the solid (adsorbent) over a series of controlled pressures. The gas molecules are physically adsorbed by the adsorbent; meaning that it does not involve any chemical reaction as in chemisorption, but occurs as a result of the field forces at the surface of the adsorbent [118]. As the analysis gas is released onto the surface of the solid there is a subsequent drop in pressure of the gas and a corresponding increase in weight of the solid; both of which can be used to calculate the amount of gas adsorbed once an equilibrium pressure is reached. This is then followed by desorption, which is the reverse of the process described above.

The relation at fixed temperature, between the amount of gas adsorbed and the pressure of the gas, produces what is known as an adsorption isotherm [118]. These isotherms are indicative of the nature of the solid in question. Based on IUPAC classification, there are six known adsorption isotherms [119] as shown in Figure 4.2**.** The adsorption isotherms can be analysed using a number of equations or theories, to obtain surface areas and pore size distributions of the adsorbent. Some of the methods include the Brunauer-Emmett-Teller (BET) method [116], which can be used to obtain the surface area of the adsorbent, Barret-Joyner-Halenda (BJH) method to obtain pore size distribution [121] and t-plot method to obtain micropore volume [79]; all of which shall be described in more detail in the following sections.

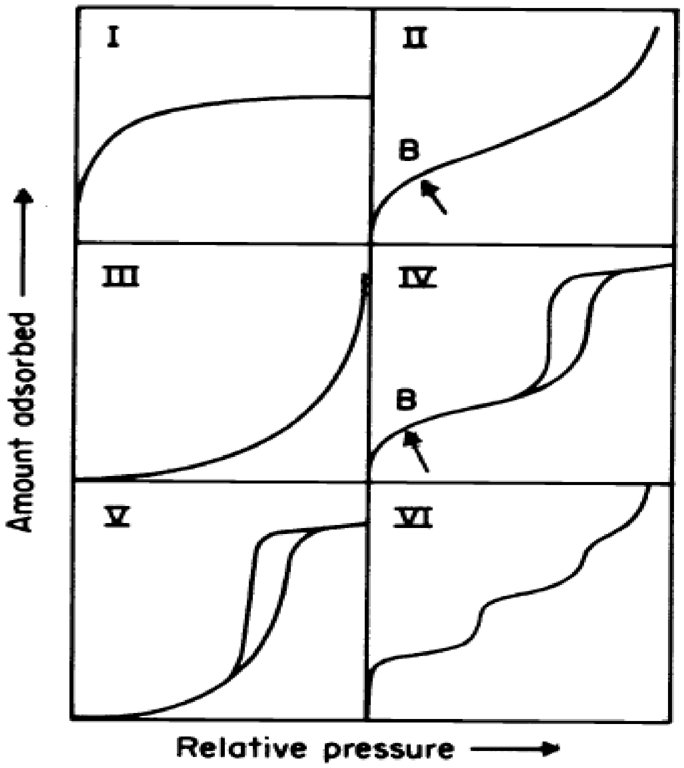

Figure 4.2: Types of adsorption isotherms [119]

Type I – Closely associated with microporous solids.

Type II – Typical of non-porous or macroporous adsorbents. Point B is indicative of the stage at which monolayer coverage is complete and multilayer adsorption is about to begin.

Type III & V – Not very common. Indicative of weak adsorbent-adsorbate interaction but is experienced by certain porous solids and also seen for H_2O adsorption [122]

Type IV – Typical of mesoporous solids and exhibits a hysteresis loop representative of capillary condensation in the mesopores. Point B is similar to that for Type II.

Type VI – Rarely found [123]. Indicative of step-wise multilayer adsorption on uniform non-porous adsorbents.

4.2.1 The Brunauer-Emmett-Teller (BET) Theory

The BET theory [120] is an extension of Langmuir's theory [124] which is based on the assumption that at equilibrium, rate of adsorption is equal to rate of desorption and that adsorption is limited to the monolayer. Brunauer *et al.* [120] extended this theory to multilayer adsorption, and the proposed method, referred to as the BET theory, is now universally accepted as one the best methods for determining the surface area of porous adsorbents [119].

In the physical adsorption process, at low relative pressure, higher energy adsorption sites are filled first and then lower energy sites afterwards. Therefore narrow pores which have higher overlapping potentials are initially filled. However this is not to say that lower energy sites are not filled as well, it only implies that the average residence time of the adsorbate molecule is longer on higher energy sites [125]. Furthermore, upon increase in pressure, and the associated progressive increase in surface coating, there is the likelihood that a gas molecule will be adsorbed by a previously bound molecule. This will therefore allow for multiple adsorbed layers and is representative of the assumption on which the BET theory is based. A schematic representation of the BET model of adsorption is shown in Figure 4.3. A kinetic approach combined with Langmuir assumptions provides a good starting point for the derivation of the BET equation, as it will reveal how the BET theory is an extension of Langmuir's theory.

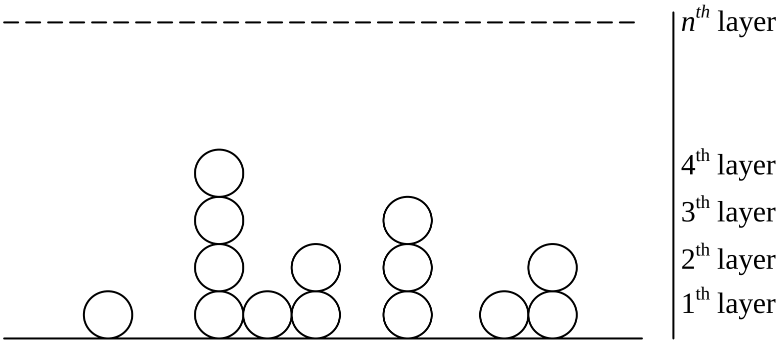

Figure 4.3: BET model for adsorption [118]

According to the kinetic theory of gases, the number of molecules, N, that strikes each square centimetre of the surface of a solid per second is given by

$$N = \frac{\bar{N}P}{(2\pi\bar{M}RT)^{\frac{1}{2}}} \tag{4.2}$$

where $\bar{N}$, P, $\bar{M}$, R and T are the Avogadro's number, adsorbate pressure (mm Hg), adsorbate molecular weight, gas constant (J mol^{-1} K^{-1}) [17], and absolute temperature respectively (K) [125]. If θ_0 is defined as the fraction of the surface unoccupied with adsorbed molecules, then the number of collisions with the uncovered surface per square centimetre of surface per second is

$$N' = kP\theta_0 \qquad where\ k = \frac{\bar{N}P}{(2\pi\bar{M}RT)^{\frac{1}{2}}} \tag{4.3}$$

Thus the number of molecules striking and adhering to each square centimetre of surface is:

$$N_{ads} = kP\theta_0 A_1 \tag{4.4}$$

where A_1 is the condensation coefficient, which is also representative of the probability of a molecule being adsorbed upon collision with the surface. The rate of desorption of adsorbed molecules per square centimetre of surface is given by

$$N_{des} = N_m\theta_1 v_1 e^{-E/_{RT}} \tag{4.5}$$

where N_m, θ_1, E, and v_1, represent the number of adsorbed molecules in a completed monolayer per square centimetre, the fraction of the surface occupied by the adsorbed molecules, the energy of adsorption (in Joules, J) and the vibrational frequency (in s^{-1}) of the adsorbate normal to the surface when adsorbed, respectively.

Based on Langmuir's assumption of equilibrium between the rate of adsorption and desorption in the first layer, it follows that equations (4.4) and (4.5) are equal and the equilibrium can be expressed as

$$N_m \theta_1 v_1 e^{-E/RT} = kP\theta_0 A_1 \tag{4.6}$$

The extension of the Langmuir's kinetic theory to multilayer adsorption by Brunauer *et al*. [120] implies that equation (4.6) can be generalised for the nth layer to the form

$$N_m \theta_n v_n e^{-E_n/RT} = kP\theta_{n-1} A_n \tag{4.7}$$

The BET theory assumes that for the second and higher layers,v, E, and A remain constant. On this basis, a series of equations using L as the heat of liquefaction (in J mol^{-1}) can be written as follows

$$N_m \theta_1 v_1 e^{-E/RT} = kP\theta_0 A_1 \tag{4.6}$$

$$N_m \theta_2 v e^{-L/RT} = kP\theta_1 A \tag{4.8a}$$

$$N_m \theta_3 v e^{-L/RT} = kP\theta_2 A \tag{4.8b}$$

and by generalising for second and higher layers,

$$N_m \theta_n v e^{-L/RT} = kP\theta_{n-1} A \tag{4.8c}$$

From equations (4.6) and (4.8a-c), it follows that

$$\frac{\theta_1}{\theta_0} = \frac{kPA_1}{N_m v_1 e^{-E/RT}} = \alpha\,, \qquad \theta_1 = \alpha\theta_0 \tag{4.9a}$$

$$\frac{\theta_2}{\theta_1} = \frac{kPA}{N_m v e^{-E/_{RT}}} = \beta \,, \qquad \theta_2 = \beta\theta_1 = \alpha\beta\theta_0 \tag{4.9b}$$

$$\frac{\theta_3}{\theta_2} = \frac{kPA}{N_m v e^{-E/_{RT}}} = \beta \,, \qquad \theta_3 = \beta\theta_2 = \alpha\beta^2\theta_0 \tag{4.9c}$$

$$\frac{\theta_n}{\theta_{n-1}} = \frac{kPA_1}{N_m v e^{-L/_{RT}}} = \beta \,, \qquad \theta_n = \beta\theta_{n-1} == \alpha\beta^{n-1}\theta_0 \tag{4.9d}$$

The total number of molecules adsorbed at equilibrium is given by

$$N = N_m\theta_1 + 2N_m\theta_2 + \ldots + nN_m\theta_n = N_m(\theta_1 + 2\theta_2 + \ldots + n\theta_n) \tag{4.10}$$

By substituting for θ values, from equations (4.9a-d), we obtain

$$\frac{N}{N_m} = \alpha\theta_0 + 2\alpha\beta\theta_0 + 3\alpha\beta^2\theta_0 + \ldots + n\alpha\beta^{n-1}$$
$$= \alpha\theta_0(1 + 2\beta + 3\beta^2 + \ldots + n\beta^{n-1}) \tag{4.11}$$

As α and β are constants, we can define the BET constant as

$$C = \frac{\alpha}{\beta} \tag{4.12}$$

Substitution of Cβ for α in equation (4.11) gives,

$$\frac{N}{N_m} = C\theta_0(\beta + 2\beta^2 + 3\beta^3 + \ldots + n\beta^n) \tag{4.13}$$

The summation in equation (4.13) can be expressed as $\beta/(1-\beta)^2$. Thus

$$\frac{N}{N_m} = \frac{C\theta_0\beta}{(1-\beta)^2} \tag{4.14}$$

Also,

$$1 = \theta_0 + \theta_1 + \theta_2 + \ldots + \theta_n \tag{4.15}$$

Therefore,

$$\theta_0 = 1 - (\theta_1 + \theta_2 + \ldots + \theta_n) = 1 - \sum_{n=1}^{\infty} \theta_n \tag{4.16}$$

Substituting for θ_n from equation (4.9d),

$$\theta_0 = 1 - \alpha\theta_0 \sum_{n=1}^{\infty} \beta^{n-1} \tag{4.17}$$

Substituting for α from equation (4.12),

$$\theta_0 = 1 - C\theta_0 \sum_{n=1}^{\infty} \beta^{n} \tag{4.18}$$

Considering the value of the sum of an infinite geometric progression [125],

$$\sum_{n=1}^{\infty} \beta^{n} = \frac{\beta}{1-\beta} \tag{4.19}$$

Equation (4.18) can be expressed as,

$$\theta_0 = 1 - C\theta_0 \left(\frac{\beta}{1-\beta}\right) \tag{4.20}$$

This implies that,

$$\theta_0 = \frac{1}{1 + {}^{C\beta}\!/_{(1-\beta)}} \tag{4.21}$$

By substituting for θ_0 into equation (4.14), we have

$$\frac{N}{N_m} = \frac{C\beta}{(1-\beta)(1-\beta+C\beta)} \tag{4.22}$$

When $\beta = 1$, N/N_m tends to infinity. This occurs upon condensation of adsorbate at $P = P_0$. Under these conditions,

$$\beta = \frac{P}{P_0} \tag{4.23}$$

Substituting for β in equation (4.22), we obtain

$$\frac{N}{N_m} = \frac{C(P/P_0)}{(1-P/P_0)[1-P/P_0+C(P/P_0)]} \tag{4.24}$$

Equation (4.24) can be rearranged to the form,

$$\frac{1}{N[(P/P_0)-1]} = \frac{1}{N_m C} + \frac{C-1}{N_m C}\left(\frac{P}{P_0}\right) \tag{4.25}$$

Plotting $1/N[(P/P_0)-1]$ against P/P_0 will produce a straight line normally in the range of $0.05 \leq P/P_0 \leq 0.35$, as the linear relationship usually exists within this range i.e. equation 4.25 is only valid for the above stated range. At lower relative pressures, the influence of surface heterogeneity becomes more significant, while at higher relative pressures, adsorption by capillary condensation along with physical adsorption also takes place, and the equation loses its validity [126]. The slope and intercept of this plot within the state, however, can be used to determine N_m and C. The specific surface area, S_{BET} (in m^2/g) can be calculated from,

$$S_{BET} = N_m N_{av} \sigma \tag{4.26}$$

where N_{av} and σ represent the Avogrado constant and the average area (in m^2) occupied by each molecule in the completed monolayer respectively [127]. Over the relative pressure range $0.05 \leq P/P_0 \leq 0.34$, the BET theory is applicable and represents a highly effective method for the determination of surface area.

4.2.2 The Barret-Joyner-Halenda (BJH) Theory

The BJH theory [128] is a well established method for determining pore volume distributions for porous substances exhibiting capillary condensation in their mesopores. Capillary condensation occurs when multilayer adsorption has reached a point whereby the pore spaces are filled with liquid separated from the gas phase by menisci [112]. The model considers the desorption that occurs in a system of cylindrical pores (which have undergone capillary condensation) that have been subjected to a stepwise reduction in relative pressure from $(P/P_0)_1$ to $(P/P_0)_2$ to $(P/P_0)_3$ etc. A schematic representation of the assumed desorption mechanism is shown in Figure 4.4.

The model assumes that the relative pressure $(P/P_0)_1$ is equal to unity (which is consistent with the experiments carried out in this work where relative pressures of approximately 0.99 were recorded, as will be seen in several N_2 adsorption isotherms in Chapter 6) and therefore all the pores are filled with liquid. The largest pore (*Pore 1*) has a radius of r_{p1} (nm) and a physically adsorbed layer of molecules of thickness t_1 (nm). This physically adsorbed layer contains within it an inner capillary with radius, r_k, where evaporation occurs upon reduction in P/P_0. The radius of the inner capillary and thickness of the physically adsorbed layer can be calculated using the Kelvin equation and Hasley equation, respectively [125].

Decreasing $(P/P_0)_1$ to $(P/P_0)_2$ leads to the desorption of a measureable volume of adsorbed gas, ΔV_1 (cm^3). This reduction in relative pressure results in the emptying of *Pore 1* of its capillary condensate and a reduction in thickness, Δt_1, of the physically adsorbed layer. The parameters r_{p1}, r_k, Δt_1, and ΔV_1 can be related to the pore volume of *Pore 1* by equation (4.27),

$$V_{p1} = \frac{r_{p1}^2}{(r_{k1} + \Delta t_1)^2} \Delta V_1 = R_1 \Delta V_1 \qquad (4.27)$$

where,

$$R_1 = \frac{r_{p1}^2}{(r_{k1}+\Delta t_1)^2}$$

Upon further reduction in relative pressure from $(P/P_0)_2$ to $(P/P_0)_3$, the associated total desorbed volume, ΔV_2, is a combination of the volume of desorbed liquid adsorbate from *Pore 2* and the desorbed volume related to the second thinning of the physically adsorbed layer in *Pore 1* designated by, $V_{\Delta t_2}$. Therefore,

$$V_{p2} = \frac{r_{p2}^2}{(r_{k2}+\Delta t_2)^2}\left(\Delta V_2 - V_{\Delta t_2}\right) = R_2\left(\Delta V_2 - V_{\Delta t_2}\right) \tag{4.28}$$

where,

$$R_2 = \frac{r_{p2}^2}{(r_{k2}+\Delta t_2)^2}$$

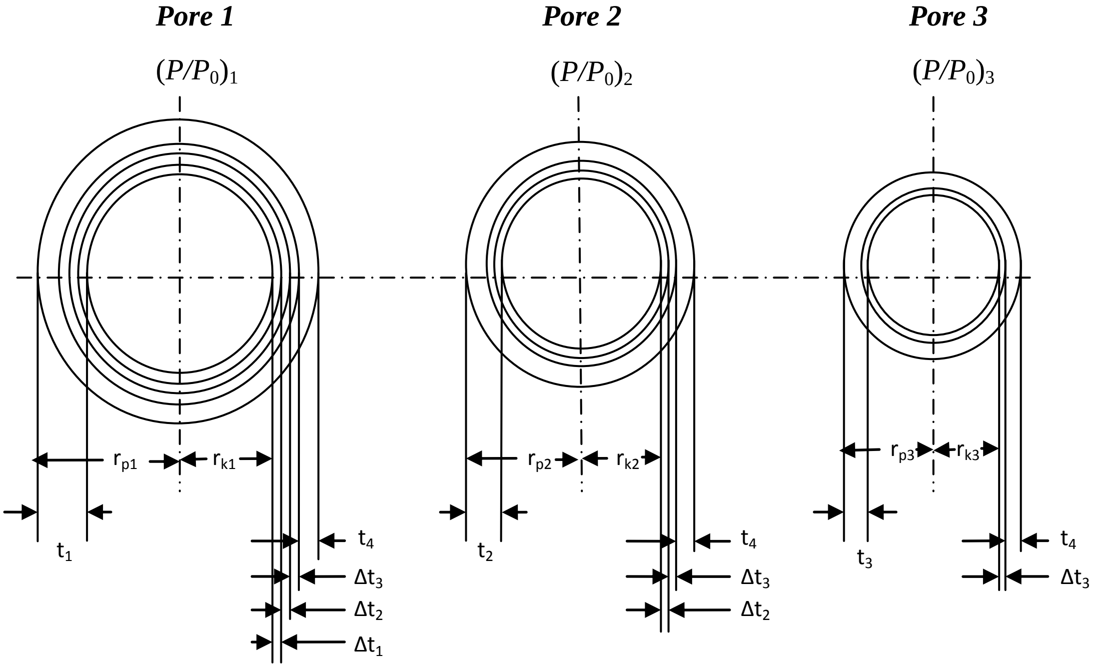

Figure 4.4: Schematic representation of assumed desorption mechanism [128]

It can also be seen from Figure 4.4 that the volume desorbed from the second thinning of the physically adsorbed layer in *Pore 1*, $V_{\Delta t_2}$, can be expressed as,

$$V_{\Delta t_2} = \pi L_1 (r_{k2} + \Delta t_1 + \Delta t_2)^2 - \pi L_1 (r_{k2} + \Delta t_1)^2 \tag{4.29}$$

where L_1 is the length of *Pore 1* (in nanometers, nm).

Applying this same procedure to subsequent reduction in relative pressure will prove difficult as a greater number of pores would be involved and subsequently the number of previously emptied pores in which thinning occurs would be increased making the calculation of $\mathrm{V}_{\Delta \mathrm{t}_2}$ impractical. However by considering an average area from which physically adsorbed gas is desorbed, $\mathrm{V}_{\Delta \mathrm{t}_2}$ can alternatively be expressed as,

$$V_{\Delta t_2} = \Delta t_2 A c_1 \tag{4.30}$$

where Ac_1 is the average area (m^2) from which the physically adsorbed gas is desorbed. In order to represent any one of the steps in the stepwise desorption, equation (4.30) may be generalised and expressed as,

$$V_{\Delta t_2} = \Delta t_n \sum_{j=1}^{n-1} A c_j \tag{4.31}$$

Following the same line of thought, equation (4.28) can also be generalised and written in the form

$$V_{pn} = R_n \Delta V_n - R_n \Delta t_n \sum_{j=1}^{n-1} A c_j \tag{4.32}$$

As *Ac* varies with decreasing relative pressure, equation (4.32) is not suited as a computing device. However, the area of each pore *Ap,* is a constant and as a result, a method of relating this pore area to the average area from which desorption occurs, was developed by Barrett *et al*. [128] and, is shown schematically in Figure 4.5. This method assumes that all capillaries emptied of their condensate during a decrease in relative pressure have an average radius of $\bar{r}_p$. The change in thickness of the physically adsorbed layer of a previously emptied pore of radius, $\bar{r}_p$, during the *n*th desorption step is designated as Δt_n. Prior to desorption, the capillary radius is r_{n-1} and after desorption is r_n. It has an average value of $\bar{r}_c$.

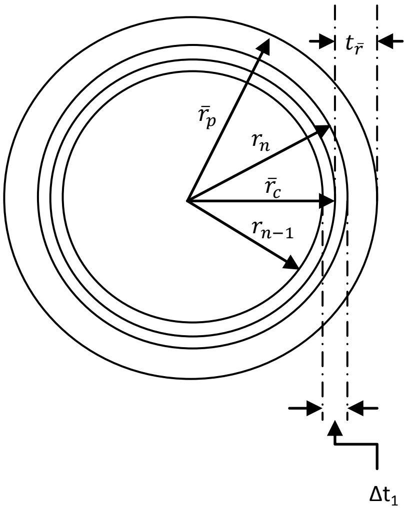

Figure 4.5: Relation between capillary area and actual pore area at nth desorption step

As it has been assumed that the capillary is concentric with the pore, the average area of the capillary that produces Δt_n is expressed as,

$$A_c = A_p\left(\frac{\bar{r}_c}{\bar{r}_p}\right) \tag{4.33}$$

The average capillary radius $\bar{r}_c$ can be expressed as,

$$\bar{r}_c = \bar{r}_p - t_{\bar{r}} \tag{4.34}$$

where $t_{\bar{r}}$ is representative of the thickness of the physically adsorbed layer at the corresponding value of P/P_0. For simplicity, the ratio of the average capillary radius to the average pore radius is designated as *c* as shown below

$$c = \frac{\bar{r}_c}{\bar{r}_p} = \frac{\bar{r}_p - t_{\bar{r}}}{\bar{r}_p} \tag{4.35}$$

Therefore equation (4.32) can be expressed in a usable form as shown in equation (4.36) which is the working form of the BJH equation.

$$V_{pn} = R_n \Delta V_n - R_n \Delta t_n \sum_{j=1}^{n-1} c_j A_{pj} \tag{4.36}$$

The units of all dimensions pertaining to radius, length and thickness for the above derivations, are nanometers, while the unit for area is in m^2 (however, this should not be confused with specific area which is in m^2/g) It is important to note that the Kelvin equation, which works on the basis of capillary condensation, is not applicable at low relative pressures (below 0.3) [125] where adsorption occurs mainly in very small pores, such as micropores. Under such conditions, capillary condensation is unlikely due to the lack of formation of menisci [129 - 130]. This therefore renders BJH equation unusable for the micropore analysis. Section 4.2.3 discusses how such pores can be analysed.

4.2.3 Micropore Analysis

In order to determine micropore volume, the t-plot method proposed by De Boer *et al*. [131] was used. It works by comparison of the isotherm of a microporous material to a standard type II isotherm (representing non-porous materials). The method is based upon the statistical thickness, t (nm), of an adsorbed nitrogen layer on a non-porous solid (the reference material), whose BET constant, C, is known, and is similar to that of the material under study. The statistical thickness can be calculated using the Harkins and Jura equation; which relates it to relative pressure, P/P_0 [132].

$$t = \left[\frac{13.99}{\left(0.034 - \log\left(\frac{P}{P_0}\right)\right)} \right]^{\frac{1}{2}} \tag{4.37}$$

The statistical thickness obtained from the above equation is used to replot the analysis isotherm by replacing P/P_0 with t (i.e. a plot of volume of gas adsorbed versus t rather than P/P_0), yielding what is known as a t-plot. Extrapolation of this plot to the volume axis yields an intercept which upon appropriate conversion gives the micropore volume of the sample being studied [125]. Alternative methods for micropore analysis include the density functional theory (DFT) and Horvath-Kawazoe (HK) methods [72].

4.3 Thermogravimetric Analysis (TGA)

TGA is a technique use to determine the change in weight of a substance with temperature. It can be measured as a function of temperature or time under a controlled temperature program yielding a TGA curve (or weight loss curve). As such changes in weight could be associated with chemical changes in the sample under study, substantial amount of information can be obtained using this technique. An example is the rupture of chemical bonds with increasing temperatures, which leads to the evolution of volatile matter [133]. This technique can also be used to determine the ash content and moisture content of a sample [133]. Furthermore, weight loss data can be presented as a differential TGA curve (or derivative weight loss curve) showing the temperatures at which significant weight losses occur [134]. Both curves work synergistically, where the derivative curve allows for a more effective interpretation of the weight loss curve. An example is shown in Figure 4.6 [135].

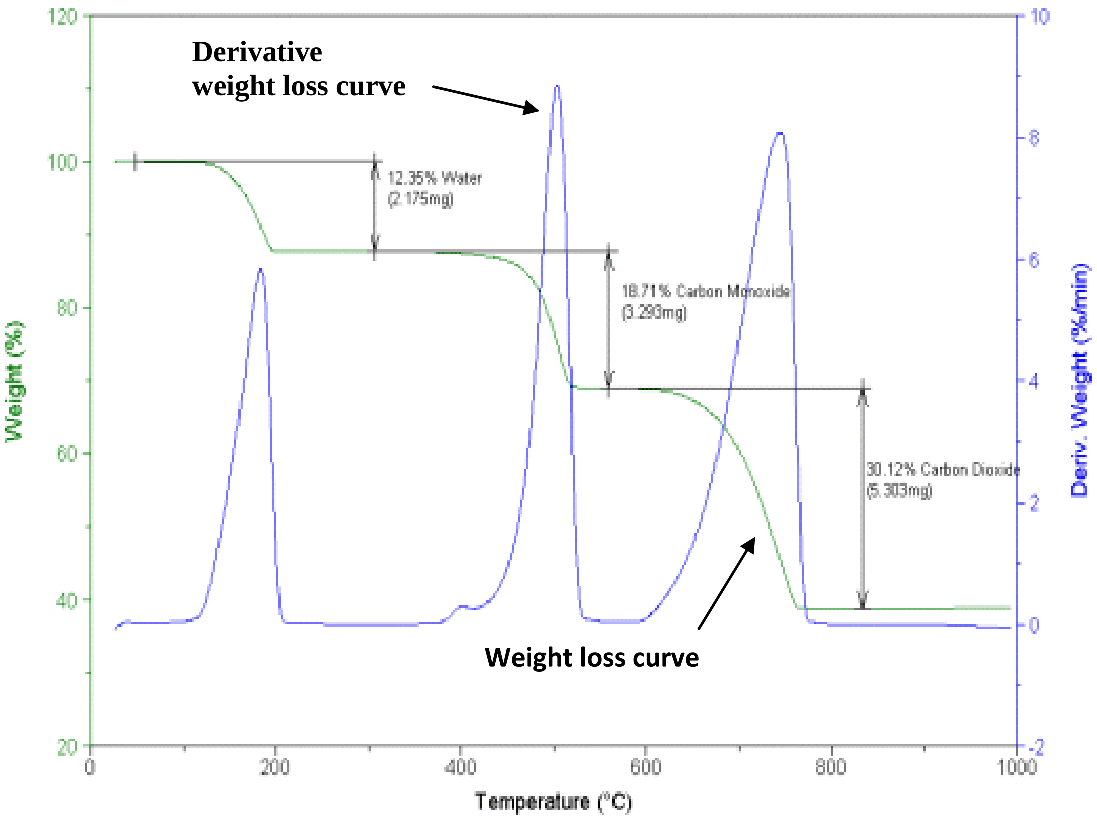

Figure 4.6: Weight loss and derivate weight loss curves for calcium oxalate monohydrate [135]

As shown, the amount of weight loss corresponding to specific regions of the weight loss curve can be calculated. This is made possible because the original weight of the sample is known. Furthermore, the derivative weight loss curve, which is simply the rate of weight change with increasing temperature, makes it possible to easily identify and distinguish those regions on the TGA curve where notable weight losses occur.

4.4 Surface Functional Group Analysis

4.4.1 Fourier Transform Infrared (FTIR) Spectroscopy

Spectroscopic analysis techniques are based on the interaction between matter and electromagnetic radiation [136]. Electromagnetic radiation has a particle-wave character and these particles are called photons. The energy of a photon, E, is directly proportional to its frequency, as given by the equation 4.38,

$$E = hv \tag{4.38}$$

where h is the Planck's constant, 6.63×10^{-34} J.s and v is the frequency in reciprocal seconds (s^{-1}) or hertz (Hz) [16]. Electromagnetic radiation travels at the speed of light ($c = 3 \times 10^{8}$ m/s), which can be given as the product of its frequency, v, and wavelength, λ, as shown in equation 4.39.

$$c = v\lambda \tag{4.39}$$

The range of photon energies, defines the electromagnetic spectrum, which consists of regions such as the gamma ray, X-ray, ultra-violet, visible and infrared regions, corresponding to specific wavelengths or frequencies. Various spectroscopic techniques such as Ultraviolet–Visible (UV-VIS) Spectroscopy, Nuclear Magnetic Resonance (NMR) Spectroscopy, and Infrared (IR) Spectroscopy, are based on the absorption of electromagnetic radiation from the corresponding parts of the spectrum [16]. When a molecule absorbs a photon on exposure to electromagnetic radiation, its energy increases by an amount equal to that of the photon. The specific photon energies absorbed by a molecule, depend on its structure, and can be measured with a spectrometer. The data obtained are highly sensitive indicators of molecular structure, and have made the use of spectroscopic analysis especially relevant to chemical analysis.

Infrared radiation is the segment of the electromagnetic spectrum between microwaves and visible light. However, only the mid-infrared region is of the most use for structure determination [136]. This is the region that lies in the wavelength range of 2.5 × 10^{-6} to 2.5 × 10^{-5} m. The most commonly employed unit in IR spectroscopy is the wave number (reciprocal centimetre, cm^{-1}), so that the range 2.5 × 10^{-6} - 2.5 × 10^{-5} m corresponds to 4000 - 400 cm^{-1}. This unit is useful as it is directly proportional to energy as will be seen in equation 4.41. Substituting for v, from equation 4.39, into equation 4.38, we get,

$$E = \frac{hc}{\lambda} \tag{4.40}$$

with all symbols as previously defined. By recognising that the wavenumber is the reciprocal of the wavelength, and by defining the wavenumber as W, we have,

$$E = hcW \tag{4.41}$$

The most important requirement for the absorption of a photon of infrared radiation, is that the energy of the photon must match the difference in energy between two different vibrational states of the molecule. Only certain vibrational energy states are possible and, as such, these energies are said to be quantized. The absorption of a photon of infrared radiation excites a molecule from its lowest (or ground) vibrational state, to a higher one. These vibrations include stretching and bending modes. A number of distinct vibrations are associated with different types of molecules, therefore allowing the determination of structural features of various substances, making IR spectroscopy suited to qualitative analysis [16] [136]. For example the amount of energy required for the transition from one vibrational state to another, in a carbon-carbon single bond, would be less that a similar transition in a carbon-carbon double bond, as the latter has a lower potential energy (i.e. it is more stable). Therefore, the signal (which is represented as an absorption peak on an IR spectrum) corresponding to the change in vibrational state of the carbon-carbon double bond will exist at the higher wave number end of the IR spectrum, relative to the carbon-carbon single bond [16].

Differing from traditional dispersive-IR spectroscopy methods which were only able to determine infrared frequencies individually by employing a prism or grating, FTIR spectroscopy makes use of an interferometer capable of obtaining all frequencies at the same time (i.e. in one scan) [22].

The FTIR spectrometer (Figure 4.7) makes use of an infrared beam radiated from an IR source. The light goes through a beamsplitter which splits it into two optical beams; one reflecting off a fixed mirror and the other off a moving mirror. The path travelled by the beam is of fixed length in the former and of a variable length in the latter. Both beams return to the beamsplitter where they recombine and travel towards the sample compartment and through to the detector. By this time the interferometer has analysed the two beams as a function of the moving mirror position producing an interferogram. The ensuing interferrogram is converted into an IR spectrum by Fourier transform. FTIR spectroscopy is the preferred method for IR spectral analysis as it represents a non-destructive technique, with increased accuracy, speed, sensitivity and optical throughput [22], [137].

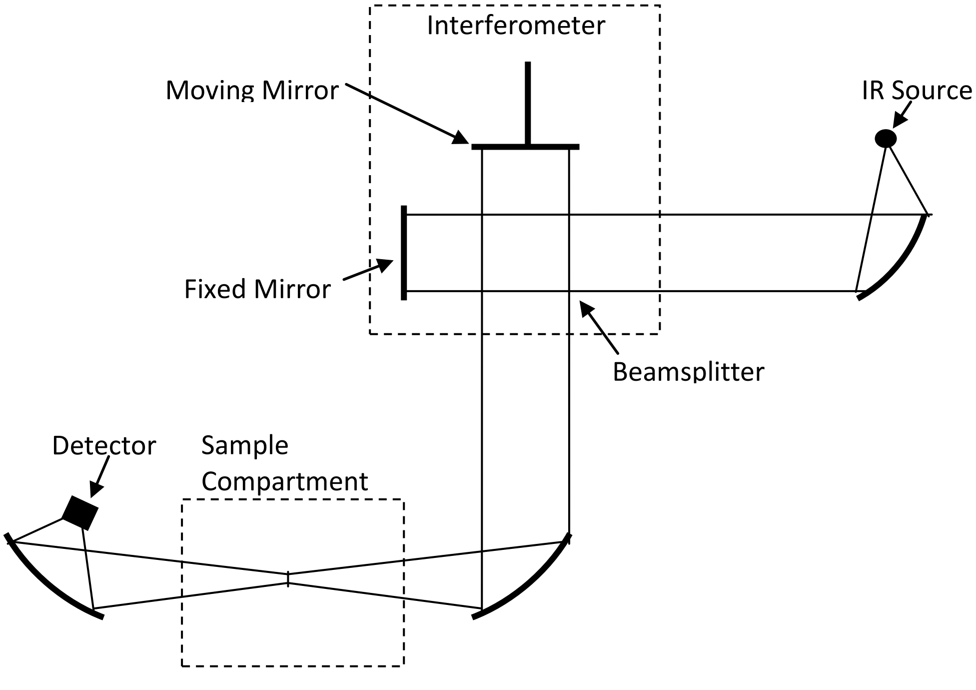

Figure 4.7: Schematic representation of an FTIR spectrometer [138]

It is quite common to display the IR spectra as a plot of percentage transmittance against wavenumber [77], [136], [139]. However, the percentage transmittance, which is the amount of light transmitted by the specimen, is not linearly proportional to the concentration of the functional group under study, and although suitable for qualitative analysis, represents a relatively complex method of obtaining quantitative information [136]. On the other hand, replacing the percentage transmittance with absorbance, which is the amount of light absorbed by the sample, allows the ensuing spectrum to be used both qualitatively and quantitavely (due to the linear proportionality between absorbance and concentration). The absorbance, A, is related to the concentration of the functional group under study [140], as given by Beer's law, which is stated as follows,

$$A = \varepsilon l c \tag{4.42}$$

where ε is the absorptivity of the functional group, l is the path length travelled by the beam through the sample (thickness of the sample), and c is the concentration of the functional group. The absorbance, is given by the area under the peak of the signal under study, and is directly proportional to concentration [136].

4.4.2 Alternative Methods for Surface Functional Group Analysis

4.4.2.1 X-ray Photoelectron Spectroscopy (XPS)

This is another useful surface analysis technique which depends on the emission of core electrons (inner electrons) from an atom, due to the absorption of photons from the x-ray region of the electromagnetic spectrum [141]. When radiation of energy (known energy) in excess of the binding energy of an electron (i.e. the energy required to remove an electron from an atom [17]) is absorbed, electrons of a measurable kinetic energy are emitted. A schematic of the XPS experimental setup is shown in Figure 4.8. The characteristic binding energy of the emitted electron, E_b is given by,

$$E_b = hv - E_k \tag{4.43}$$

where, h, is the Planck's constant, v is photon frequency, and E_k is the kinectic energy of the electron. The 'hv' term is the energy of the characteristic x-ray [142]. The X-ray Photoelectron (XP) spectrum is simply a plot of the electron intensity versus the binding energy. These binding energies are a direct representation of orbital energies and are characteristic of each element. Published tables of binding energies are available, and can be used for the assignment of peaks in the XP spectrum.

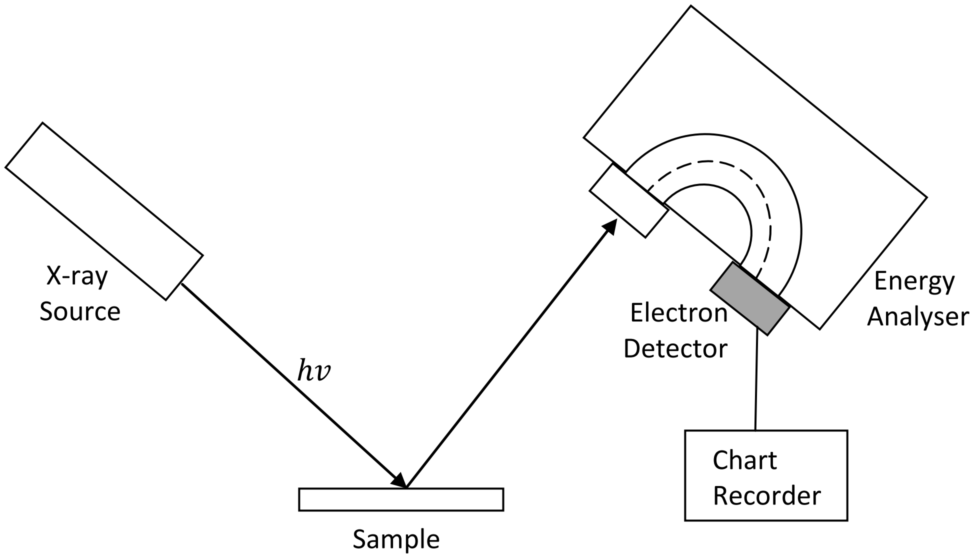

Figure 4.8: Schematic representation of XPS experimental setup [141]

Different bonding environments around an atom result in variations in the binding energies of the core electrons, known as chemical shifts (which are well documented for instant reference) [141]. In addition to obtaining qualitative information from characteristic peaks on the XP spectrum, the peak intensities represent a measure of the concentration of various surface functional groups, making this technique a valuable tool for quantitative analysis [22].

4.4.2.2 Temperature Programmed Desorption with Mass Spectrometry (TPD-MS)

This technique typically involves heating a specimen at a programmed heating rate, to induce thermal desorption of gaseous species, which are then analysed by a mass spectrometer [22]. The mass spectrometer ionizes the gaseous products by way of electron impact, and subsequently passes the ions through a magnetic field, leading to the deflection of the ions from their original trajectory, and causing them to adopt a circular path, the radius of which is indicative of their mass-to-charge ratio (m/z) [16]. Scanning all the m/z values for the different ions, yields a mass spectrum characteristic of a particular compound, the quantity of which can also be obtained from the mass spectrometer [22], [143].

The data obtained by TPD-MS is represented as a plot of the amount of desorbed species versus desorption temperature, known as a thermogram, typically exhibiting one or more desorption peaks. The peaks are associated with certain types of functional groups, and can be very useful in identifying and distinguishing between different samples, in terms of the concentration and the type of their surface groups. The correlation between surface oxides on carbon and the gases evolved during thermal desorption for example, is well documented [22]. It has been shown that at low and intermediate temperatures, CO_2 is the desorption product from carboxyl groups, and CO is the desorption product from aldehyde groups. A notable application of this method was demonstrated in the investigation of the effect of oxidation (with nitric acid) on the surface functional groups of carbon black, where a drastic increase in surface oxygen functionality was observed for the oxidised carbon in comparison to the original sample [22].

4.5 Scanning Electron Microscopy (SEM) and Energy Dispersive X-ray Spectroscopy (EDS)

To deepen our understanding of nanosystems, it is necessary to characterize such structures on a nanometer level. Scanning Electron Microscopy allows for the observation of organic and inorganic materials on a nanometer or micrometer scale [144]. The scanning electron microscope represents one of the most widely used electron beam instruments, for reasons such as high levels of automation, as well as the relatively straight forward interpretation of acquired images [145]. Aside from being able to determine the size and shape of nanoparticles, as well as surface topography, this technique also enables the determination of chemical composition of the sample under study when combined with Energy Dispersive X-ray Spectroscopy.

When a specimen is irradiated with an electron beam, a variety of electrons and photons of various energies are produced [144 - 145]. The emitted electrons range from secondary electrons, auger electrons (those produced by the decay of excited atoms) to backscattered electrons, as shown in Figure 4.9. These signals can be used to produce images of the studied samples. The secondary electrons for example, can produce images which contain information such as surface topography. The de-excitation of atoms originally excited by the electron bombardment, also produce characteristic x-rays (Figure 4.9), which can be used to obtain quantitative and qualitative information regarding chemical composition of the specimen. This is made possible with the use of Energy Dispersive X-ray Spectroscopy. Most scanning electron microscopes sold today, are equipped with EDS capabilities.

A notable example of the benefit of using this technique in nanotechnology, is the ability to determine the shape and size of pores in a structure, which can then further be used as a method to optimize the porous structure for electrochemical applications. SEM images typically posses regions of varying brightness, due to the intensity of the secondary electrons detected once electron bombardment has occurred i.e. more electrons are emitted from high points (corresponding to bright regions of the SEM image) than from low points (corresponding to dark regions of the SEM image) [146]. The internal reflections that occur within the lower regions, which are embedded between particles (representing the pores), result in only a fraction of the secondary electrons being able to escape, so as to be detected [144].

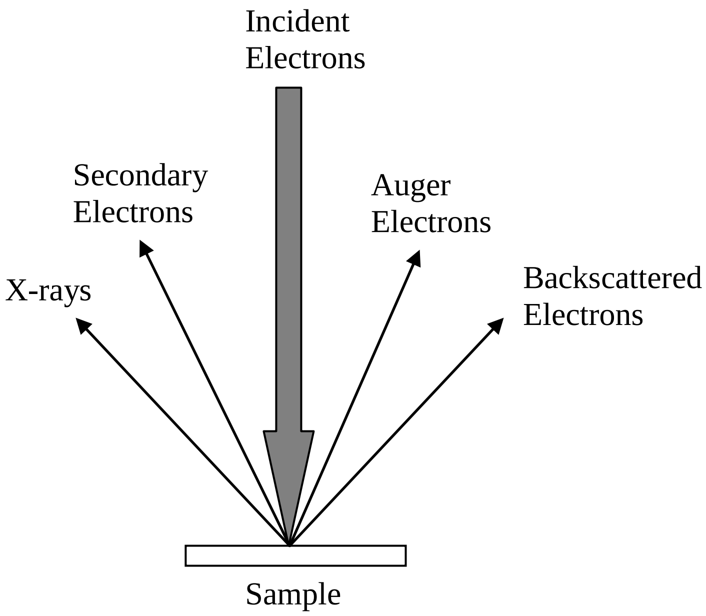

Figure 4.9: Schematic representation of signals generated in a scanning electron microscope when an electron beam interacts with a specimen [145]

4.6 Electrochemical Measurements

4.6.1 Galvanostatic Discharge/Charge Cycling

Galvonstatic discharge/charge cycling is a straightforward method to determine the discharge capacity of a battery as well as its cycle life. It works by applying a constant current to a cell and monitoring the voltage response either for a fixed duration of time or until a specified voltage is reached [147]. The discharge capacity is measured as follows

$$Discharge\ Capacity\ (mAh/g) = Current\ density (mA/g) \times time(h) \qquad (4.44)$$

where ‘Current density’ is the applied current per gram of active material, ‘time’ represents the time for discharge.

It can be observed from equation (4.44) that the capacity of a cell is dependent on the discharge current applied. Other parameters include the voltage limits as well as the state of charge (the fraction of the capacity of the battery that is still available for further discharge [4], [148]. The information obtained from the charge-discharge curves can be very useful for analysing the electrochemical performance of a cell. Deviations from the thermodynamic potential of cell reactions during discharge and charge, corresponding to discharge overpotential and charge overpotential, respectively, could also be obtained, by the difference between the actual voltage and the thermodynamic or theorectical voltage (as described in Figure 2.9).

Chapter 5

Experimental

The section covers the description of chemical reagents used in gel synthesis in addition to experimental methods. The initial part of this chapter deals with the synthesis methods for preparing phenol-formaldehyde gels as well as subsequent carbonisation and activation. It then continues with the procedures involved in material characterisation of the gels and the carbonised materials, including N_2 adsorption, FTIR and TGA, for porosity analysis, surface functionality and weight loss analysis, respectively, as well as SEM for sample imaging and EDS for detecting certain species contained in the samples. The final part covers the experimental methods involved in cell fabrication and also the procedures involved in testing the electrochemical performance of the cells. In addition to the experiments described in this section, further experiments were carried out to confirm the reliability of the synthesis procedures for the gels, the carbonised materials, as well as the electrochemical measurements. More details of these experiments and the corresponding error calculation methods, applied for the measured parameters, shall be included with the tables of parameters throughout the results and discussion section (Chapter 6).

5.1 Synthesis of Phenol-Formaldehyde (PF) Gels

The chemicals used for the synthesis of the PF gels are shown in table 5.1.

Table 5.1: Description of chemicals used for PF gel synthesis

Materials	Formula	Company/Source
Phenol (99%)	C_6H_5OH	Sigma-Aldrich
Formaldehyde (37% weight in water, stabilized by 10-15 % weight methanol)	CH_2O	Sigma-Aldrich
Sodium carbonate anhydrous (≥ 99.5%)	Na_2CO_3	Sigma-Aldrich
Tertiary-butyl alcohol (t-butanol) (99.5 %)	$(CH_3)_3COH$	Sigma-Aldrich
Acetone (99.5%)	C_3H_6O	Sigma-Aldrich
Deionised water	H_2O	University Laboratory (deionised water obtained by filtration, using ion exchange resins)

5.1.1 Gel Preparation

PF gels were synthesised by the sol-gel polycondensation of phenol (P) and formaldehyde (F), catalysed by sodium carbonate, Na_2CO_3 (C), according to a procedure described elsewhere [76]. Measured quantities of phenol, sodium carbonate, formaldehyde and deionised water were used according to the description below.

In a typical synthesis procedure, phenol, P, and sodium carbonate, C, were initially dissolved in 94 ml of deionised water, W, in a beaker under magnetic stirring. After dissolution for 5 min, formaldehyde solution, F, was added to the mixture which was then stirred vigorously for 45 min at room temperature. The molar ratio of phenol/catalyst, (P/C), and phenol/formaldehyde, (P/F), were varied during the synthesis of the gels, and the concentration of phenol in water, P/W (mol/l), was fixed at approximately 1.06 mol/dm^3. Tables 5.2 and 5.3 show the different reactant ratios and typical weights that were used during synthesis. The values for both P/F and P/W (mol/l) were chosen, as these reactant ratios have been used to obtain highly mesoporous gels with mesopore volumes ranging from 0.9 – 1.43 cm^3/g [76 - 77].

Table 5.2: Synthesis of phenol-formaldehyde gels with different P/C

P/C (g/g)	**P/F (g/g)**	**P/W (mol/l)**	**P_{wt} (g)**	**C_{wt} (g)**	**F_{vol} (l)**	**W_{vol} (l)**
3	0.5	1.06	$9.40 \leq \mathbf{P_{wt}} \leq 9.44$	$3.5330 \leq \mathbf{C_{wt}} \leq 3.5334$	$16.2 < \mathbf{F_{vol}} < 16.3$	0.094
6	0.5	1.06	$9.40 \leq \mathbf{P_{wt}} \leq 9.44$	$1.7670 \leq \mathbf{C_{wt}} \leq 1.7674$	$16.2 < \mathbf{F_{vol}} < 16.3$	0.094
8	0.5	1.06	$9.40 \leq \mathbf{P_{wt}} \leq 9.44$	$1.3250 \leq \mathbf{C_{wt}} \leq 1.3254$	$16.2 < \mathbf{F_{vol}} < 16.3$	0.094
10	0.5	1.06	$9.40 \leq \mathbf{P_{wt}} \leq 9.44$	$1.060 \leq \mathbf{C_{wt}} \leq 1.064$	$16.2 < \mathbf{F_{vol}} < 16.3$	0.094
12	0.5	1.06	$9.40 \leq \mathbf{P_{wt}} \leq 9.44$	$0.8830 \leq \mathbf{C_{wt}} \leq 0.8834$	$16.2 < \mathbf{F_{vol}} < 16.3$	0.094

P_{wt} and C_{wt} refer to the weights of phenol and catalyst, respectively. F_{vol} and W_{vol} refer to the volumes of formaldehyde and water, respectively. ‘l’ refers to litres.

Table 5.3: Synthesis of phenol-formaldehyde gels with different P/F

P/F (g/g)	P/W (mol/l)	P/C (g/g)	$\mathbf{P}_{wt}$ (g)	$\mathbf{C}_{wt}$ (g)	$\mathbf{F}_{vol}$ (litres)	$\mathbf{W}_{vol}$ (l)
0.3	1.06	8	$9.40 \leq \mathbf{P}_{wt} \leq 9.44$	$1.3250 \leq \mathbf{C}_{wt} \leq 1.3254$	27	0.094
0.4	1.06	8	$9.40 \leq \mathbf{P}_{wt} \leq 9.44$	$1.3250 \leq \mathbf{C}_{wt} \leq 1.3254$	$20.2 < \mathbf{F}_{vol} < 20.3$	0.094
0.5	1.06	8	$9.40 \leq \mathbf{P}_{wt} \leq 9.44$	$1.3250 \leq \mathbf{C}_{wt} \leq 1.3254$	$16.2 < \mathbf{F}_{vol} < 16.3$	0.094
0.6	1.06	8	$9.40 \leq \mathbf{P}_{wt} \leq 9.44$	$1.3250 \leq \mathbf{C}_{wt} \leq 1.3254$	13.5	0.094
0.7	1.06	8	$9.40 \leq \mathbf{P}_{wt} \leq 9.44$	$1.3250 \leq \mathbf{C}_{wt} \leq 1.3254$	$11.5 < \mathbf{F}_{vol} < 11.6$	0.094
0.8	1.06	8	$9.40 \leq \mathbf{P}_{wt} \leq 9.44$	$1.3250 \leq \mathbf{C}_{wt} \leq 1.3254$	$10.1 < \mathbf{F}_{vol} < 10.2$	0.094

P_{wt} and C_{wt} refer to the weights of phenol and catalyst, respectively. F_{vol} and W_{vol} refer to the volumes of formaldehyde and water, respectively. ‘l’ refers to litres.

The resultant solutions were transferred to sealable glass bottles (with screw caps that can be used to close them tightly) and kept in an oven at 90 ^{o}C and at atmospheric pressure. After 4 days, gelation was complete with the formation of hydrogels. The samples were removed from the oven and allowed to cool for approximately 1.5 hrs. The procedure followed for the synthesis of these gels is consistent with similar procedures reported in literature, for the preparation of PF gels [76].

5.1.2 Solvent Exchange

Prior to the addition of the solvent exchange liquid, the samples were sliced (using a spatula) into smaller pieces (roughly to the same degree for each experiment) to allow for a more effective solvent exchange process. The hydrogels were then solvent exchanged with t-butanol or acetone by soaking in the aforementioned solvents, and transferring to a shaker for 3 days at 30 ^{o}C to replace residual water in the samples prior to drying (both acetone and t-butanol were chosen as solvents, as they have been successfully applied in the preparation of highly mesoporous polymeric gels [76], [110]). The temperature of 30 ^{o}C in the shaker was particularly important in the case of the t-butanol exchange process as this liquid solidifies at ≤ 25.6 ^{o}C [149]. Following this, the samples were removed and drained of all liquid by a sieve filtration process. This was aided by the use of a BALSTON

9955-12 pump to force the liquid through the filter and, therefore, quicken the process.

5.1.3 Drying

5.1.3.1 Evaporative Vacuum Drying

The hydrogels were dried in an oven set at 70 ^{o}C for 2 days or 40 ^{o}C for 3 days, and under vacuum (approximately -1 bar) throughout. The vacuum was applied using and Edwards XDS 5 pump. A glass cold-trap immersed in a flask filled with ice cubes (Figure 5.1), was used to collect and condense the acetone or t-butanol vapour, and was emptied frequently (every 20 mins) to prevent suction of the solvent exchange liquid back into the oven or into the pump.

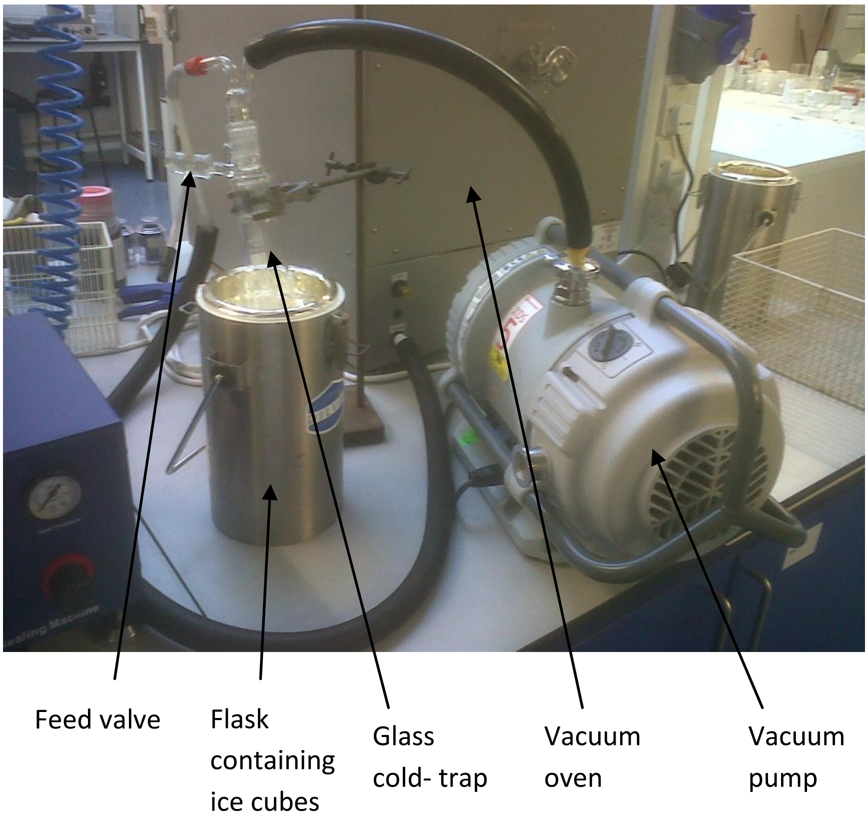

Figure 5.1: Picture of cold-trap set up

5.1.3.2 Freeze Drying

PF cryogels were prepared by freeze drying under a pressure of 0.003 bar, at -40 ^{o}C for 3 days. The hydrogels were placed in a Lyotrap Plus freeze drier specimen chamber and fitted with a temperature probe. A freezing temperature of -40 ^{o}C was used, to ensure that all pore liquid contained in the sample was completely frozen; this process ran for about 6 hrs. Following this, the freezing process was halted, and an ULVAC GLD – 136 vacuum pump attached to the freeze drier, was switched on, in order to begin the drying procedure (sublimation of the frozen solvent). The vapour released at this stage was trapped in the freeze drier condenser chamber which was set to about – 45 ^{o}C. After approximately 3 days, dried gels (cryogels) were obtained. The freeze drying procedure was based on the work done by Mukai et al [76] for the synthesis of PF gels.

5.2 Carbonisation

PF gels were carbonised in a carbolite tubular furnace (schematic shown in Figure 5.5). Approximately 2 g of sample was loaded in a silica boat and placed carefully at the centre of the furnace. Argon was introduced into the furnace at a flowrate of 250 ml/min in order to maintain an inert atmosphere. The gels were carbonised at 600 ^{o}C, 700 ^{o}C, 800 ^{o}C, 900 ^{o}C, 1000 ^{o}C and 1050 ^{o}C in order to determine the temperature that produced the most desirable porous properties in the ensuing carbons and would therefore be used for subsequent carbonisation procedures. A typical program for the carbonisation process is represented in Figure 5.2, which shows carbonisation at 1050 ^{o}C. The isothermal steps (150 ^{o}C and 400 ^{o}C) were determined by TGA analysis of the PF gels under argon (Section 6.2.1)

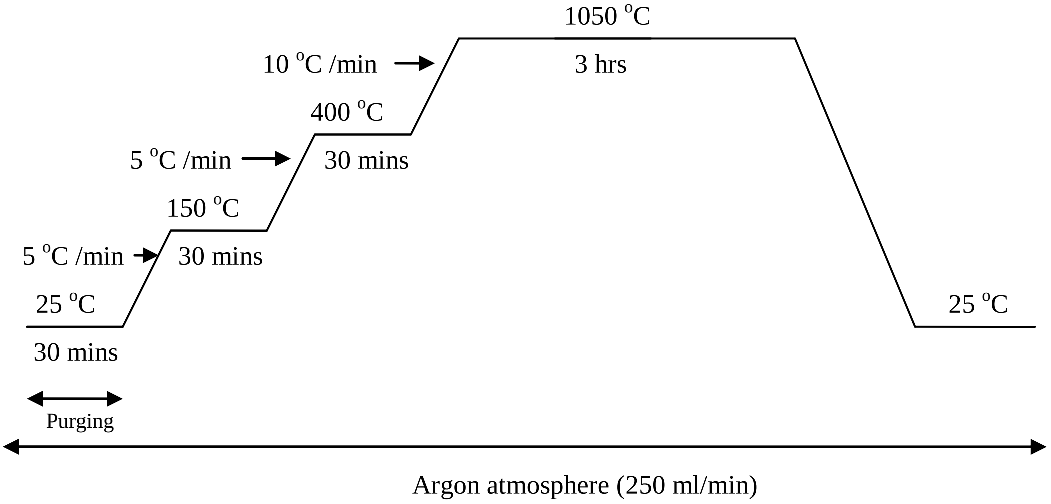

Figure 5.2: Heating program for carbonisation in the carbolite furnace

5.3 Activation

5.3.1 O_2 Activation

PF carbons were subject to fast oxidation with O_2 in order to determine the effect on the porosity of the activated carbons. Using the carbolite tubular furnace (Figure 5.5), activation to different degrees of burn-off was attained by varying temperature (300 – 500 °C), time (20 – 30 mins) and gas flowrate (100 to ~ 370 ml/min). The activation temperatures were chosen based on a TGA analysis of PF carbon gels under O_2 (Appendix A). The temperature where significant weight loss was observed, was taken as the initiation point for the activation process, and was subsequently used as a basis for the range of temperatures investigated for O_2 activation. The sample was initially purged with argon at room temperature for 30 mins, to ensure the sample was under inert atmosphere. The sample was then heated up to the activation temperature and the flow of argon was switched off and replaced with O_2 to commence the activation process. Upon completion of this stage, the gas was switched back to argon and the heating process was halted in order to allow the furnace to cool to room temperature. A program for one of the O_2 activation runs is shown in Figure 5.3.

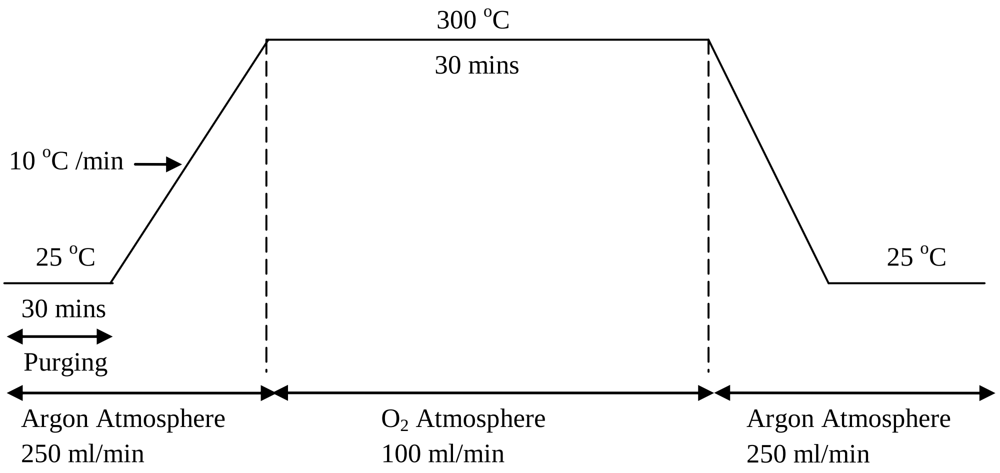

Figure 5.3: Heating program for O_2 activation in the carbolite furnace

5.3.2 CO_2 Activation

Mild activation in CO_2 atmosphere was carried out on PF carbons also using the carbolite furnace (Figure 5.5). By keeping temperature constant at 800 °C and varying activation times from 30 – 120 mins, various degrees of burn off (activation induced carbon removal) were obtained in the CO_2 activated PF carbons. The activation temperature was based on previous studies where effective porosity development was observed in polymer derived carbons upon activation at 800 °C [110]. The program for one of the CO_2 activation runs is shown in Figure 5.4.

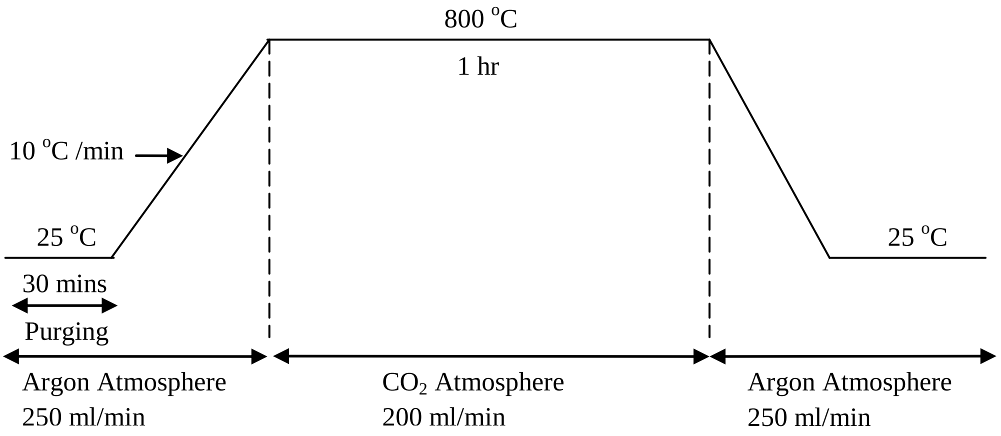

Figure 5.4: Heating program for CO_2 activation in the carbolite furnace

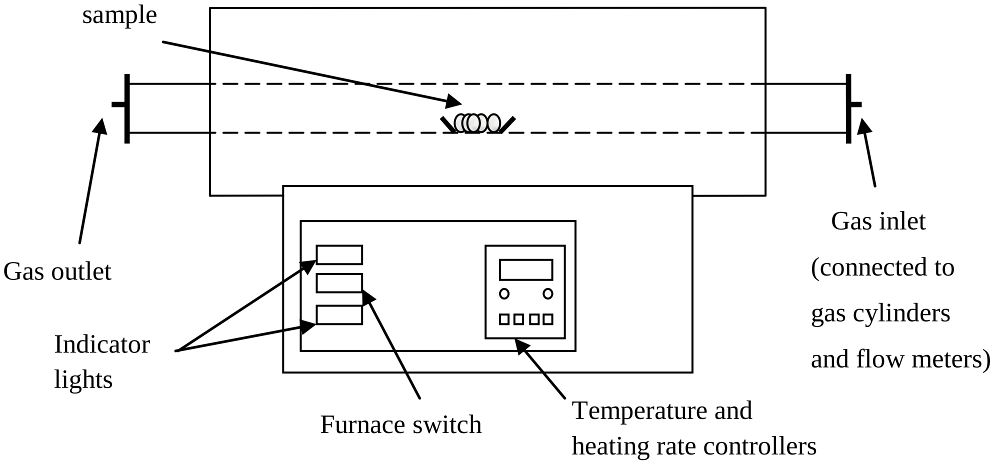

Figure 5.5: Schematic of tube furnace set up.

5.4 Material Characterization

5.4.1 N_2 Adsorption/Desorption

A Micrometrics ASAP 2420 adsorption analyzer (Figure 5.6) was used for the determination of the porous structure of the PF gels and carbons by analysing the nitrogen adsorption/desorption isotherms measured at 77 K. Prior to the adsorption measurements, the samples were partially degassed by heating at 50 ^{o}C in an oven overnight.

The samples were then transferred to the degassing port (Figure 5.6), where in the case of the gels, they were kept at 90 ^{o}C for 3 hours under vacuum (10 µm Hg), and in the case of the carbonised materials, they were kept at 120 ^{o}C for 4 hours under vacuum (10 µm Hg), to remove any unwanted physically adsorbed gases. Following this, the samples were transferred to the sample analysis port, where the nitrogen gas was introduced to the samples for porosity measurements. The BJH method was used for mesoporosity analysis, the t-plot method for micropore analysis, and the BET method for determination of surface area. The calculations for total pore volumes were based on the adsorbed volume of nitrogen at $P/P_0 = 0.99$ [110], [150]. By applying the BJH method to the desorption isotherms, pore size distributions were determined, consistent with similar analysis reported in the literature [128].

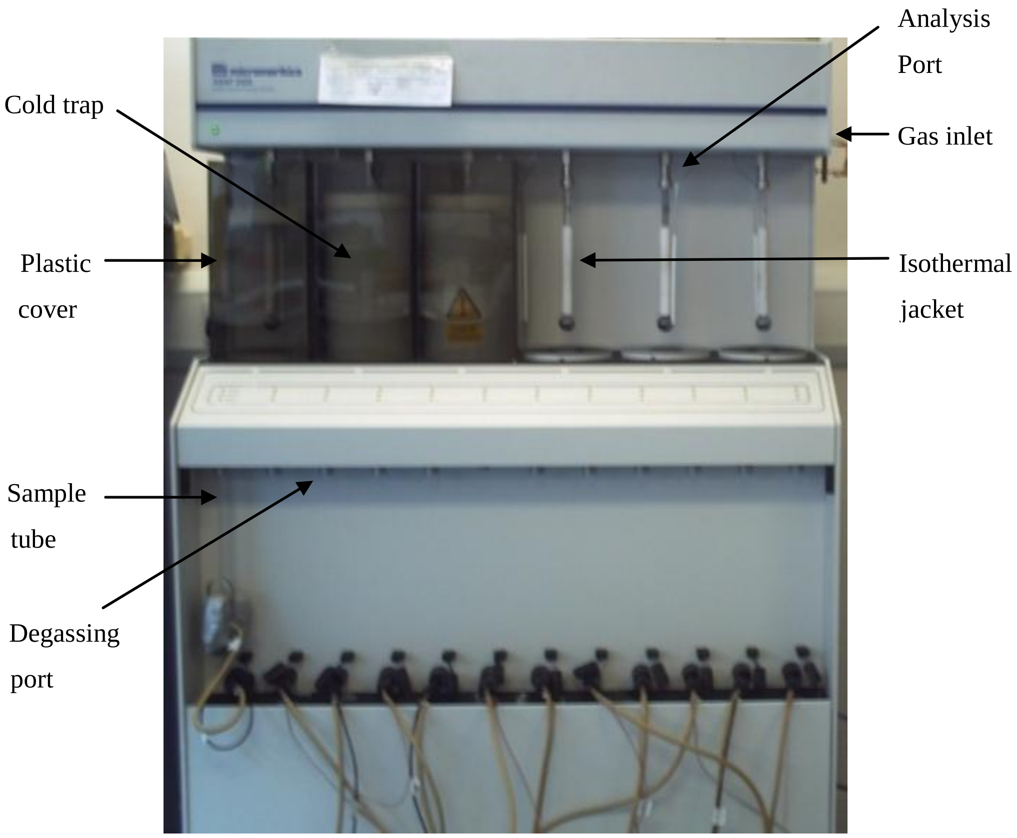

Figure 5.6: Micrometrics Accelerated Surface Area Porosity System ASAP 2420 (equipment used for N_2 adsorption/desorption measurements)

5.4.2 Fourier Transform Infrared Spectrometry (FTIR)

FTIR analysis was carried out on the gel, carbon, and activated carbon materials, for qualitative and quantitative analysis of surface functionalities present in the structure. The samples were mixed with KBr at a ratio of 1:1500 (sample/KBr). The weights of the samples and KBr were approximately 1.5 mg and 1500 mg, respectively, in order to obtain clear pellets and to avoid complete absorption of the IR beam (which may occur when too high a concentration of sample is used) [151]. Both KBr and the sample were ground together with a pestle and mortar for 5 minutes and were subsequently subject to a pressure of 10 bar for another 5 minutes, to form KBr discs (about 200 mg of the sample/KBr mixture was used for making the discs). The thickness of each disc was approximately 0.5 mm. The KBr discs where then placed under vacuum in a vacuum oven at 100 ^{o}C, and a pressure of approximately – 1 bar, to remove any adsorbed moisture. This was then followed by running a background spectrum on the FTIR equipment. For the analysis of each sample, 12 scans were run at a resolution of 4 cm^{-1}, and the spectrum was obtained between 4000 - 450 cm^{-1}, consistent with similar procedures reported in literature [152].

5.4.3 Thermogravimetric Analysis

A Mettler TGA/DSC 1 STARe system (Figure 5.7) was used for the thermal analysis of the PF gels and PF carbon, to examine temperatures at which considerable weight loss occurs during thermal treatment of these samples. The samples were weighed in an alumina pan and placed on a horizontal microbalance connected to the TGA. The sample weights were typically about 10 mg. The program for the thermal analysis started with purging of the sample at 25 ^{o}C for 30 mins under argon flowing at 50 ml/min, to remove oxygen from the system. This was then followed by heating the gel to 1050 ^{o}C at 10 ^{o}C/min under argon (50 ml/min) and allowed for the determination of the variation of weight loss with temperature. The same procedure was followed for the PF carbon but, in this case, the sample was heated to 500 ^{o}C under O_2 (50 ml/min), and at a heating rate of 10 ^{o}C/min after which the gas was switched back to argon and sample allowed to cool.

Figure 5.7: Mettler TGA/DSC system

5.4.4 Scanning Electron Microscopy (SEM) and Energy Dispersive Spectroscopy (EDS)

SEM images of gels, carbons and activated carbons were obtained using an FEI Sirion 200 field-emission gun scanning electron microscope (FEGSEM), with a 5 kV accelerating voltage and a beam current of approximately 100 pA. Secondary electron images were obtained using an in-lens detector. Gel samples were gold coated (a conductive coating) using an Edwards S150 sputter – coater.

A Hitachi SU6600 field emission scanning electron microscope equipped with EDS was used to determine the concentration of specific chemical species in the structure of gels and carbons, using an 20 kV accelerating voltage electron beam, and a beam current of 40 nA. X-rays were detected using an X-MAX 20 X-ray detector.

5.5 Electrode Fabrication and Cell Construction

5.5.1 Electrode Fabrication

The cathode was prepared by initially mixing the carbon cryogel, electrolytic manganese dioxide (EMD), Kynar Flex 2801 binder (polyvinyl-lidene difluoride/hexafluoropropylene; PVDF/HFP; 88/12 by weight) and propylene carbonate (PC), with approximately 11 wt % carbon, 15 wt % kynar, 19 wt % EMD and 55 % wt propylene carbonate, and is consistent with procedures reported in literature[27] [31]. Typical weights of the materials used include: 44 mg of carbon, 60 mg of kynar, 76 mg of EMD and 220 mg of propylene carbonate. The aforementioned materials, along with added acetone, were mixed in a small glass bottle under magnetic stirring for 4 hrs, after which a paste was formed. The resultant paste was then spread into a 200 µm thick film using an applicator (Figure 5.8). Prior to any further stages, the film was left unaltered to allow for evaporation of acetone. Following this, the thick film was then cut to form circular disk-like electrodes of 1.3 cm diameter [42], by using a fixed diameter punch, screwed to a punch handle (Figure 5.9), as it provides a quick and effective method of making several electrodes of the same diameter.

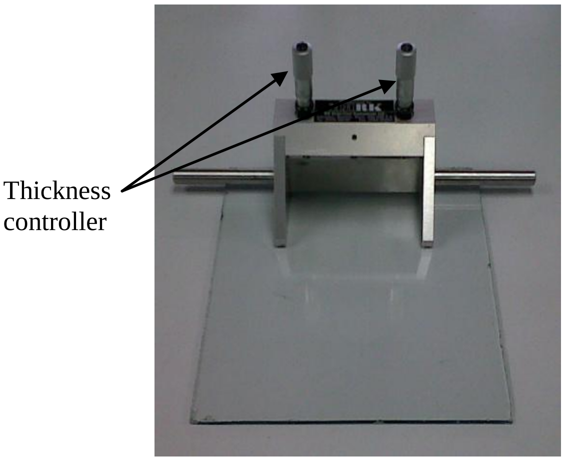

Figure 5.8: Picture of the applicator used for controlling the electrode thickness

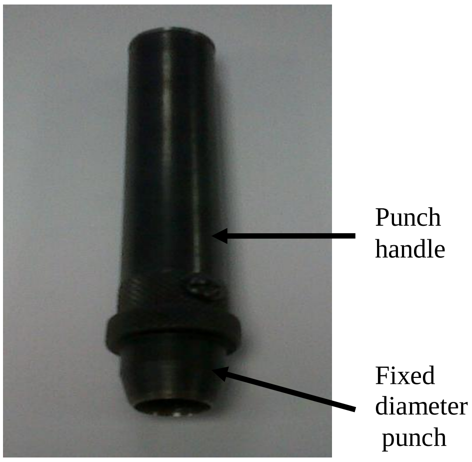

Figure 5.9: Picture of punch kit

5.5.2 Cell Construction

Construction of the electrochemical cell was carried out in an argon atmosphere Saffron Omega glove box (< 1 ppm moisture, < 1 ppm oxygen), shown in Figure 5.10 in order to prevent corrosion of the Li metal foil and the contact of electrolyte with air moisture (due to the hygroscopic nature of $LiPF_6$) [14], [31]. The cell components consisted of a stainless steel bar which functions as the anode current collector, a lithium metal foil (also in circular disc form), a glass micro-fibre separator soaked with electrolyte (1 M $LiPF_6$ in propylene carbonate), a cathode electrode (carbon composite cathode) and an aluminium mesh, with a spring and a hollow aluminium bar on top of it, functioning as a current collector as shown in Figure 5.11. The hollow aluminium also functions as the entry point for O_2 into the cathode side of the cell.

The aforementioned cell components were then stacked in the order depicted in Figure 5.11. The stainless steel bar was inserted into the union and lithium metal was then placed on top of it. The separator was then added and soaked in electrolyte. This was followed by carefully placing the cathode on top of the separator and then adding the aluminium mesh. The aluminium mesh was then pressed down to ensure good contact between the cell components. The hollow aluminium bar was then inserted into the union. Both the hollow aluminium bar and stainless steel bar were pressed together simultaneously while tightening the nuts on both ends of the cell. The cell construction is consistent with methods described in the literature [62]. The cell was then placed into a cell casing (Figure 5.12) and sealed with Parafilm to prevent CO_2 and moisture ingress prior to introducing oxygen into the cell and during cell operation.

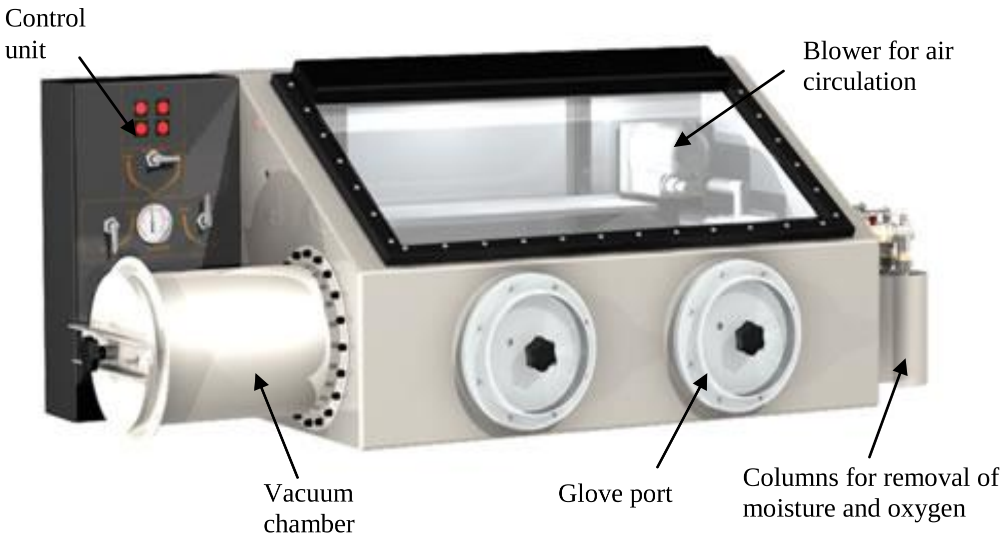

Figure 5.10: Saffron glove box [153]

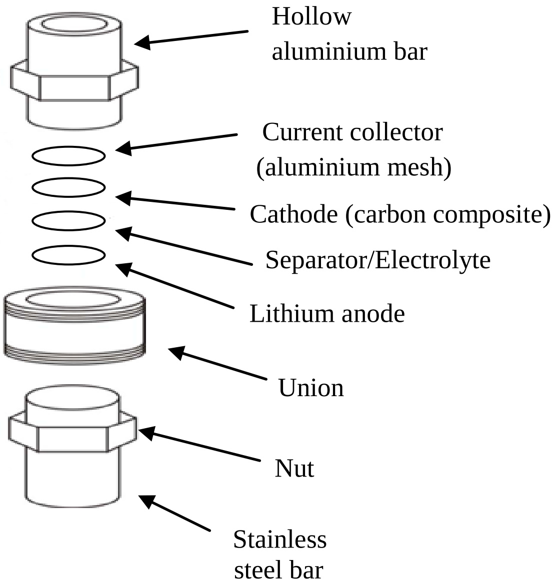

Figure 5.11: Schematic representation of cell construction and components [62]

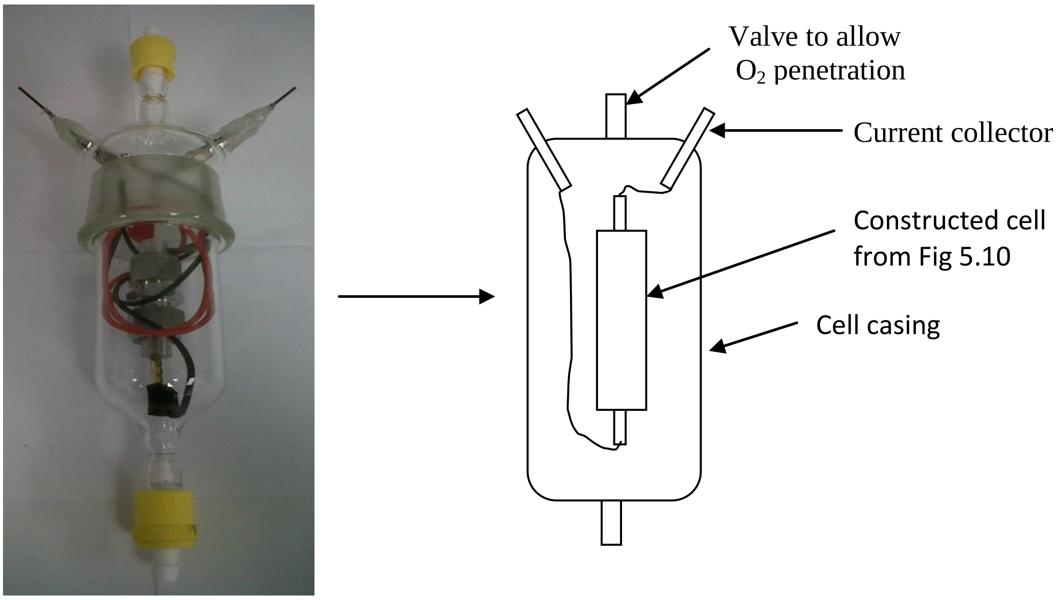

Figure 5.12: Picture of cell placed inside the cell casing

5.6 Electrochemical Measurements

5.6.1 Galvanostatic Discharge/Charge Cycling

Prior to electrochemical tests, the cell was exposed to an O_2 atmosphere at room temperature for 30 mins (O_2 dosing) and then sealed tightly on both ends of the cell casing (using the yellow valves pictured in Figure 5.12). Galvanostatic discharge/charge measurements were carried out on the cell using a Solartron 1470E potentiostat, with a constant current at a discharge/charge rate of 70 mA/g in the voltage range between 2 and 4.5 V. These parameters were used, so as to enable the comparison with other work on Li/O_2 batteries [32], [42]. The amount of current that was passed through and drained from the Li/O_2 cell was based on the weight of carbon in the electrode and the chosen discharge rate. Safety limits were set as: Potential range of – 5 V to + 5 V and a current range of – 4 A to + 4 A, in order to ensure that cell operation was restricted to safe values. For the analysis of the effect of discharge rate, the cells were discharged at 20, 50, 70 and 100 mA/g.

Chapter 6

Results and Discussion

6.1 Control of Gel Porosity

In this section an investigation into the effect of various synthesis parameters on the porous structure of the phenol-formaldehyde (PF) gels was carried out. Reactant ratios such as phenol/catalyst (P/C) and phenol/formaldehyde (P/F) were varied. The effect of different solvent exchange liquids was investigated using acetone and t-butanol and subsequently analysing the porous structure of the corresponding gels. Furthermore a study on the effect of different drying methods was performed using freeze drying, low temperature and high temperature vacuum drying.

6.1.1 Effect of P/C Ratio on the Pore Structure of PF Gels

An investigation of the effect of phenol/catalyst ratio (P/C) was carried out in order to optimise the porous structure of PF gels. With a fixed P/F ratio of 0.5 and a fixed concentration of phenol in water of 1.06 mol/dm^3, the P/C ratio was varied in the range of 3 – 12 (Table 5.2 in section 5.1.1, shows the weights of reactants and accuracy of measurements). Both the P/F ratio and a similar concentration of phenol in water, have been used by previous researchers to produce highly mesoporous gels, with mesopore volumes ranging from 0.9 – 1.43 cm^3/g [76 - 77]. In these studies, P/C ratios of 3, 8.5 and 10.5 allowed for gel formation [77]. However at considerably higher P/C ratios (very low catalyst concentration), such as P/C = 50 and above, no gelation occurred. This is likely due to the relationship between catalyst content and crosslinking as will be explained in this section, as well as the general importance of crosslinking in the gelation process a described in section 4.1.2. Furthermore, Mukai et al [76], suggested that high catalyst concentrations (low P/C ratios) favour gel formation. Taking these factors into consideration, in addition to the fact that other P/C ratios have not been reported, P/C ratios of 3 - 12 were chosen for this work, to cover the whole range of reactant ratios that have been known to produce PF gels and also investigate higher and untested P/C ratios.

The results of the N_2 adsorption/desorption analysis for PF gels with varying P/C ratios which were subject to freeze drying at -40 ^oC are displayed in Figure 6.1.

Only three N_2 adsorption/desorption isotherms are displayed for clarity. The porous characteristics of corresponding PF gels are shown in Table 6.1. The shape and properties of the isotherms in Figure 6.1 indicate that they are of type IV, exhibiting hysteresis loops, which are representative of the mesopores present in the structure of the gels [118]. This corresponds well to isotherms obtained by similar gels reported in the literature [76]. The lower and upper sections of the aforementioned hysteresis loops are indicative of capillary condensation and evaporation, respectively, in the mesopores of the PF gels [118]. Furthermore, the presence of an interconnected porous network of polymer particles in the gel structure, is verified in the SEM image of a PF gel synthesised in this work (Figure 6.2), and is consistent the porosity detected for PF gels by nitrogen adsorption/desorption analysis, and also with SEM images of similar gels reported in the literature [76].

It can be seen from Figure 6.1 that there is an initial increase in quantity of N_2 adsorbed with P/C ratio for $P/C \leq 8$ and a subsequent decrease for $P/C \geq 8$. This shows that for P/C ratios above 8, there is a decline in porosity while for $P/C \leq 8$, a development in mesoporosity in the structure of the PF gels occurs. This is also confirmed in Table 6.1 which shows an initial increase in total pore and mesopore volumes as P/C ratio increases from 3 – 8 and a subsequent decrease thereafter. The highest mesopore volume of approximately 1.28 cm^3/g in the PF gels was obtained with a P/C ratio of 8.

It is evident that the P/C ratio has a significant effect on the porous structure of the gels. In the reaction of phenol with formaldehyde, the catalyst deprotonates phenol to form a more reactive phenoxide ion, which then reacts with formaldehyde to form hydroxymethyl derivates of phenol [103]. This is followed by the condensation of the hydroxymethyl derivates to form methylene and methylene ether bridged compounds, which permit chain growth. It is the interaction of these polymer chains that leads to an interconnected network of polymer particles [154]. Increasing the catalyst concentration, leads to an increase in the concentration of phenoxide ions, resulting in the formation of more hydroxymethyl derivates, more highly branched polymer chains and increased crosslinking. This allows for smaller and more interconnected polymer particles and, therefore, smaller pores. On the other hand, a lower concentration of catalyst gives way for a less branched system, which subsequently leads to the formation of larger particles, larger pore size and increased pore volume [154]. This could explain the increase in pore volume as the P/C ratio increases from 3 – 8 (which corresponds to a progressive decrease in the concentration of catalyst). The observed drop in pore volume with a further increase in P/C ratio (decrease in the amount of catalyst) for P/C > 8, is believed to be due to a collapse in the porous structure of the PF gels resulting from the lack of sufficient catalyst to foster the formation of a completely three dimensional cross-linked gel matrix during gelation.

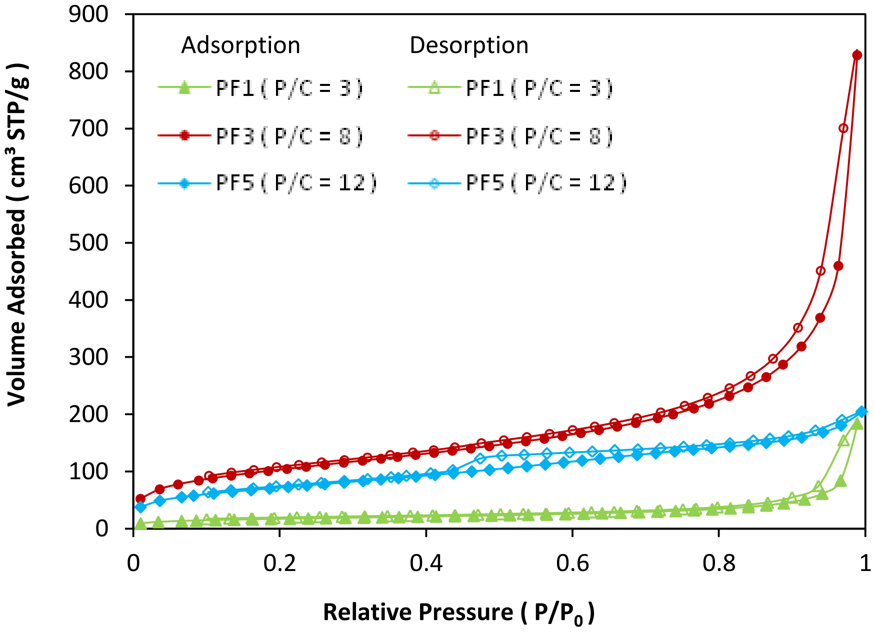

Figure 6.1: N_2 adsorption/desorption isotherms at 77K for PF cryogels with different P/C ratios freeze dried at -40 ^{o}C

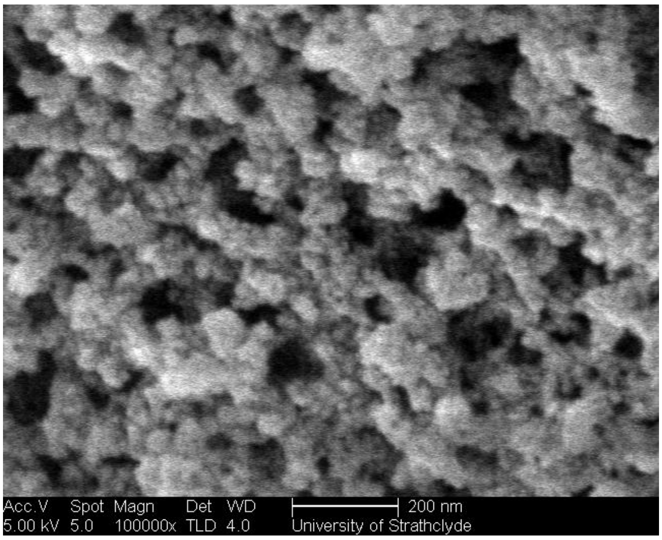

Figure 6.2: SEM image of PF3 showing an interconnected porous network of polymer particles

Pore size distribution (PSD) curves for the freeze-dried PF gels with varying P/C ratios are displayed in Figure 6.3a. A magnified version of the PSD curves for the pore size range of 2 – 5nm is shown in Figure 6.3b. It can be observed in Figure 6.3b, that for P/C ratios above 8 (P/C:10 and 12), the PSD curves possess peaks in the range of 3.5 – 4.5 nm indicative of the presence of small mesopores in the porous structure of the gels.

Considering PF gels prepared with P/C ≤ 8, the PSD curves for gels with P/C ratio of 6 and 8 exhibit two peaks in the small and large pore diameter regions representative of the contribution of small mesopores (Figure 6.3b) and of large mesopores (Figure 6.3a) to the structure of the gels. Furthermore, the volumetric measurements on these gels (P/C: 6 and 8) shown in Table 6.1, indicate a dominance of mesopores in their structure and also the relatively higher pore volumes they possess in comparison to the other gels shown in Figure 6.3a; P/C ratio 8 showing the highest mesopore volume of ~ 1.28 cm^3/g.

In the case of the PF gel synthesised with a P/C ratio of 3, it can be observed from the PSD curves in Figure 6.3a that the gel structure consist entirely of large mesopores with an average pore diameter of 19.4 nm given in Table 6.1. Its mesopore volume of 0.28 cm^3/g is significantly lower that the mesopore volume of the gel synthesised with a P/C ratio of 8.

Elucidating the effect of P/C ratio on pore size, from the pore size distribution curves, might seem quite complex, because some of the PSD curves are unimodal, while others are bimodal. However, when considering the peak diameter corresponding the largest pore size, one can spot an increase in this pore size from P/C = 3 to P/C = 8, and a corresponding decrease, with a further increase in the P/C ratio as shown by the D_{peak} values in Table 6.1. The average pore diameter, D_{avg} on the other hand, reflects the presence of small and large mesopores. For example, although the peak in the large mesopore region for P/C = 6 corresponds to a pore size larger than that in a similar region for P/C= 3, the sample with P/C = 6, has a lower average pore diameter than P/C =3. This is due to the presence of a small mesopore peak in P/C =6 and its absence in P/C=3. Therefore, the PSD curves, D_{avg} and D_{peak} values, work synergistically to give a full picture of the pore size distribution in PF gels.

These results indicate the variation of P/C ratio represents an effective method for controlling the porous structure of PF gels. It also shows that under the experimental conditions used in this work, such as the reactant ratios, temperatures and time for gelation, the preparation of highly mesoporous gels with maximised pore volumes, can be achieved at a P/C ratio of 8 (which also represents the optimum phenol/catalyst ratio). However, in order to ensure that each stage of the gel preparation process represents the most favourable in terms of porosity development, further experiments have been carried out, as shown in the next section, which deals with the effect of different solvent exchange liquids used in the solvent exchange step, on the porous structure of PF gels.

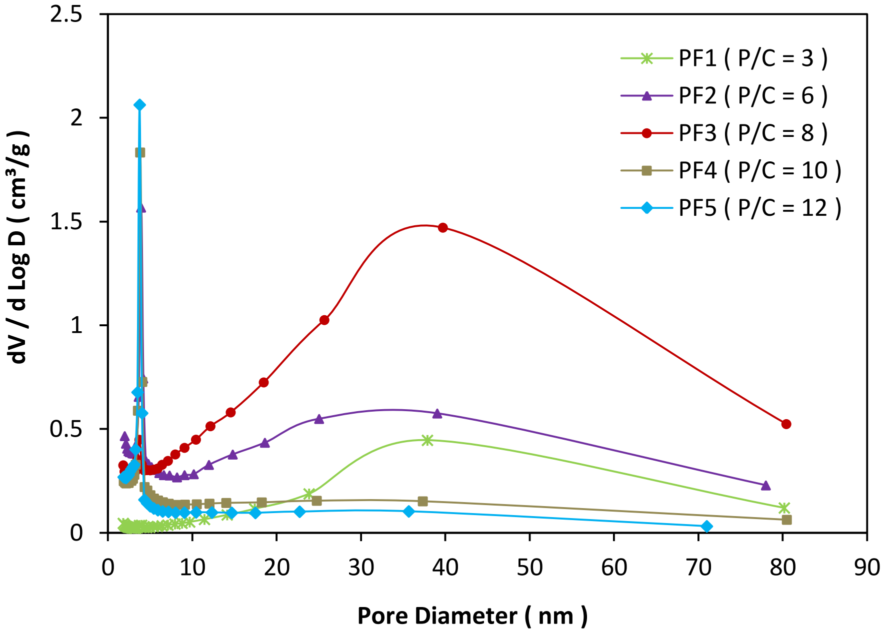

Figure 6.3a: Pore size distribution of freeze dried PF gels with different P/C ratios

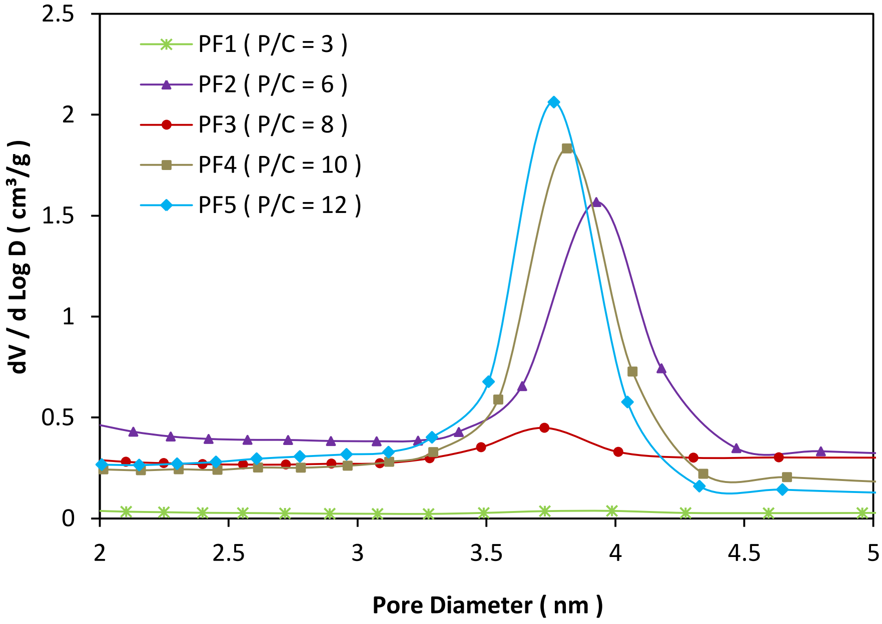

Figure 6.3b: Expanded pore size distribution curves of freeze dried PF gels with different P/C ratios

***Table 6.1:** Pore characteristics of PF gels with different P/C ratios freeze dried at -40 ^{o}C

Sample	**P/C**	**S_{BET} (m^2/g)**	**ΔS_{BET} (m^2/g)**	**V_{total} (cm^3/g)**	**ΔV_{total} (cm^3/g)**	**V_{micro} (cm^3/g)**	**V_{meso} (cm^3/g)**	**ΔV_{meso} (cm^3/g)**	**% V_{micro}**	**% V_{meso}**	**D_{avg} (nm)**	**ΔD_{avg} (nm)**	**D_{peak} (nm)**
PF1	3	59 ± 1.0 %	$S_{BET(PF1)}$ ± 2.9 %	0.2847	$V_{total(PF1)}$ ± 5.2 %	0.0029	0.2818	$V_{meso(PF1)}$ ± 5.5 %	1.02	98.98	19.2	$D_{avg(PF1)}$ ± 7.1 %	37.8
PF2	6	380 ± 0.8 %	$S_{BET(PF2)}$ ± 2.9%	0.7613	$V_{total(PF2)}$ ± 5.2 %	0.0115	0.7497	$V_{meso(PF2)}$ ± 5.5 %	1.52	98.48	8.0	$D_{avg(PF2)}$ ± 7.1 %	39.0
PF3	8	369 ± 0.7 %	Av. $S_{BET(PF3)}$ ± 5.5 %	1.2814	Av.$V_{total(PF3)}$ ± 13.4 %	0.0023	1.2791	Av.$V_{meso(PF3)}$ ± 13.4 %	0.18	99.82	13.9	Av. $D_{avg(PF3)}$ ± 17.6 %	39.7
PF4	10	249 ± 0.6 %	$S_{BET(PF4)}$ ± 5.5 %	0.3554	$V_{total(PF4)}$ ± 13.4%	0.0034	0.3520	$V_{meso(PF4)}$ ± 13.4 %	0.96	99.04	5.7	$D_{avg(PF4)}$ ± 17.6 %	4.0
PF5	12	258 ± 0.5 %	$S_{BET(PF5)}$ ± 5.5%	0.3165	$V_{total(PF5)}$ ± 13.4%	0.0000	0.3165	$V_{meso(PF5)}$ ± 13.4 %	0.00	100.00	4.9	$D_{avg(PF5)}$ ± 17.6 %	3.8

*All parameters are as defined in Appendix B. The errors under the column heading, S_{BET}, refer to the errors associated with the Micrometrics ASAP 2420 software. ΔS_{BET}, ΔV_{total}, ΔV_{meso}, and ΔD_{avg}, refer to reproducibility errors calculated using the average deviation method [155]. The abbreviation, Av (shown for PF3 parameters) refers to an average based on three synthesis experiments of PF3. The average deviation shown for PF3 was also applied to samples PF4 and PF5, due to the similarity in their structures. The aforementioned samples i.e. PF3 – PF5, were prepared using a relatively lower amount of catalyst, which may be resulted in some unreacted phenol to precipitate at the bottom of the flask in which they were gelled, leading to a two layer structure of the type shown in Figure 6.11. On the other hand, when a higher amount of catalyst or formaldehyde (section 6.1.4) was used, a uniform gel structure emerged. One such sample is PF9 (to be introduced in later sections). As PF1 and PF2 also possessed uniform gel structures, the average deviation shown for these samples in Table 6.1, were obtained based on reproducibility tests performed on a similarly structured sample, namely, PF9. PF3 and PF9 have been used to represent the two types of structures obtained for the gels, and all other gels can be grouped under theses representative structures. It has, therefore, been assumed that the deviation from the average of measured parameters for these representative gels (PF3 and PF9) would apply to others within their respective categories and can also be applied to the experimental values (raw data).

6.1.2 Solvent Exchange Analysis

The effect of solvent exchange liquid on the pore structure of both freeze-dried and vacuum dried (evaporative) PF gels, is the subject of this section. Prior to the analysis and discussion of the results obtained in this work, a clarification of the considerations affecting the choice of the solvents used here, will be presented, both for the freeze drying and evaporative vacuum drying aspects of effect of solvent exchange.

6.1.2.1 Solvents used for Freeze Drying

In this work, t-butanol has been used with the freeze-drying method. A variety of solvents have been successfully utilised by scientists, for the solvent exchange procedure [78], [107], [139], [156]. These solvents are shown in Table 6.2 [157]. However out of all these solvents, only t-butanol has been used for freeze drying [76], [111], [158 - 159]. Furthermore, most of the solvents listed, have freezing points lower than the minimum temperature of the freeze drier used in this work (approx. - 40 ^{o}C).

Table 6.2: Normal freezing points of different solvents used for solvent exchange [157]

Solvent	Freezing Point (^{o}C)
Acetone	- 94.7
t-butanol	25.7
Methanol	- 97.5
Isopropanol	- 87.9
Ethanol	-114.1
Amyl acetate	- 70.8

The non-exchanged gel which contains the remnant solvent, water, from the polycondensation reaction, as the pore liquid [77], [111], [158], may seem to be another alternative to the solvent exchanged gel with t-butanol, considering that water has a relatively higher freezing point than the other solvents (acetone, methanol, isopropanol and amyl acetate) listed in Table 6.2. However, studies performed by Tamon *et al.* [111], show that the increase in volume (decrease in density) upon freezing is significantly larger for water, in comparison to t-butanol, as shown in Table 6.3, and this could potentially destroy the pore structure of the gel with water as the pore fluid.

Table 6.3: Change in density upon freezing for t-butanol and water [111]

Solvent	**$\Delta\rho$ (g/cm^3)**
t-butanol	$- 3.4 \times 10^{-4}$
Water	$- 7.5 \times 10^{-2}$

$\Delta\rho$ represents change in density. The negative sign indicates a decrease in density

Furthermore, pore structure characterisation studies performed by Tamon *et al.* [160], showed that a more porous structure was obtained when t-butanol was used as the pore fluid in comparison to water, prior to freeze drying. The porosity parameters from the aforementioned studies are shown in Table 6.4.

Table 6.4: Porosity parameters of gels synthesised with t-butanol and water as the pore liquids [160]

Solvent	**V_{meso} (cm^3/g)**	**V_{micro} (cm^3/g)**	**r_{peak} (nm)**
t-butanol	1.02	0.02	6.20
Water	0.44	ND	1.96

V_{meso} = mesopore volume, V_{micro}= micropore volume, r_{peak} = dominant pore radius, ND (not detected)

6.1.2.2 Solvents used for Evaporative Vacuum Drying

Both t-butanol and acetone have been used with evaporative vacuum drying in this work. Any of the other solvents mentioned in Table 6.2 can also be tested.

However, there wouldn’t be any comparison with the freeze drying technique since those solvents cannot be used in the freeze dryer. The non-exchanged gel which contains water as the pore fluid, could again seem to be an alternative, since in this case, both drying techniques can be applied. The issues with having water as the pore liquid in evaporative drying are quite different from those associated with freeze drying.

During evaporation, there is tension in the pore liquid [109]. The magnitude of the tensile stress, σ_r, on the pore walls is given by

$$\sigma_r = \frac{2\gamma \cos\theta}{r_{pore}} \tag{4.1}$$

where γ is the liquid surface tension, θ is the wetting angle of the liquid in contact with the gel solid network surface, and r_{pore} is the pore radius [109]. In order to balance the liquid tension, the solid network is subjected to compressive stresses, which cause the gel to shrink [109]. Equation 4.1 shows that a liquid with high surface tension will lead to increased tensile stresses and, therefore, more shrinkage in the pore structure. It has been suggested that using liquids with lower surface tension, helps to minimise shrinkage [107], [109], [161].

Weiner *et al.* [161], performed experiments that demonstrated the effect of this relationship, using a non-exchanged gel with water as the pore fluid, and an acetone exchanged gel. Figure 6.4 shows the effect of these different pore fluids on the average pore diameter of the ensuing dried gels. In each pair of samples S6:S10, S7:S11, S8:S12, S9:S13, the same synthesis conditions were used, with the only difference being that one was solvent exchanged with acetone and the other wasn’t. For example, sample S6 represents an acetone exchanged gel and sample S10 represents a non-exchanged gel; both were synthesised using the same conditions. Similarly, sample S7 and S11 represent exchanged and non-exchanged gels respectively. However, the synthesis conditions for the S7:S11 pair differ from that of the S6:S10 pair. For each synthesis route (each pair of samples), it can be seen that the average pore diameters of the non-exchanged gels are lower, in comparison to the acetone exchanged gels.

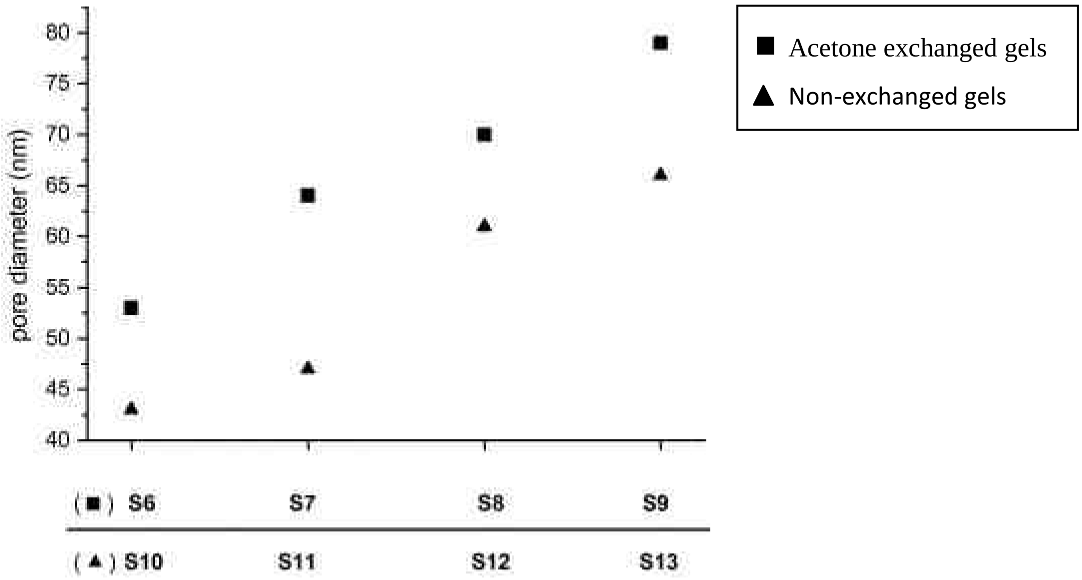

Figure 6.4: Effect of pore fluid on pore diameter of gels [161] (the reactant ratios for the all the gels are the same, but the gelation times and temperatures for each pair of samples were varied as follows: 'S6:S10' – 24 hrs at 90 °C, 'S7:S11' – 24 hrs at 50 °C and 24 hrs at 90 °C, 'S8:S12' – 24 hrs at 22 °C and 24 hrs at 90 °C, 'S9:S13' – 24 hrs at 22 °C, 24 hrs at 50 °C and 24 hrs at 90 °C)

This shift to smaller pore diameters experienced for the non-exchanged gels (with water as the pore fluid) is due to increased shrinkage in these gels, as a result of the significantly higher surface tension of water (~ 72×10^{-3} N/m), in comparison to acetone (~ 23×10^{-3} N/m) [157].

The surface tension values for the solvents mentioned in Table 6.2, including that of water, are shown in Table 6.5. Methanol, isopropanol and amyl acetate, have considerably lower surface tension values than water, and could represent suitable candidates for solvent exchange prior to evaporative drying. However, as mentioned earlier these solvents cannot be used in the freeze dryer equipment, due to their very low freezing points (lower than the minimum temperature of the freeze dryer), and would hinder the comparison of the two drying techniques.

Table 6.5: Normal surface tension values for various solvents [157]

Solvent	**Surface tension (10^{-3} N/m)**
Water	71.99
Acetone	22.72
t-butanol	19.96
Methanol	22.07
Isopropanol	20.93
Ethanol	21.97
Amyl acetate	25.17

It is important to note that the surface tension values of the solvents shown in Table 6.5 are dependent on temperature. However, since there is a drastic difference between the surface tension of water and the other solvents, it is likely that regardless of the temperature, the surface tension of water will still be significantly higher [157]. A study carried out by Kumar *et al*. [162], compared the effect of different solvent exchange liquids on the pore structure of silica gels after evaporative drying. In the study, and under the conditions used, the surface tensions (γ) of the liquids tested were as follows: $\gamma_{isopropanol} < \gamma_{ethanol} < \gamma_{acetone} < \gamma_{methanol}$. Porosity measurements on the corresponding gels, showed that as the surface tension increases, the pore volume decreases (consistent with the earlier discussion on this subject), resulting in the isopropanol exchanged gel, showing the highest pore volume. Although the difference in the pore volumes are quite modest (0.764 cm^3/g, 0.715 cm^3/g, 0.651 cm^3/g and 0.578 cm^3/g for the isopropanol, ethanol, acetone and methanol exchanged gels, respectively), the results demonstrate the possibility of other solvents outperforming acetone for the evaporative drying process and could also explain why some scientists employ the use of isopropanol and ethanol as solvent exchange liquids [156], [163].

6.1.2.3 Effect of Solvent Exchange Liquid on the Pore Structure of PF Gels

A further step in determining optimum conditions for obtaining maximised porosity in PF gels was analysing the effect of different solvent exchange liquids.

Out of all the publications on PF gels derived by the sol-gel polymerisation process [76 - 77], [164 - 165], none of them has discussed the effect of solvent exchange liquids on the gel pore structure. Here, an in-depth study has been carried out on the aforementioned subject and published [114]. The details shall be discussed as follows.

Since the analysis of the effect of P/C ratio on pore structure, showed that a P/C ratio of 8 represents the optimum for maximised porosity, the effect of solvent change, was based on this formulation i.e. P/C =8, P/F = 0.5, and P/W = 1.06 mol/l. For this investigation, lower boiling and higher boiling solvents; t-butanol and acetone, respectively, were used during the solvent exchange step in the synthesis of PF gels as both solvents have been successfully applied in the preparation of highly mesoporous polymeric gels [76], [110]. N_2 adsorption/desorption isotherms for t-butanol and acetone exchanged PF gels synthesised with a P/C ratio of 8 are shown in Figure 6.5. The porosity parameters as well the description of the aforementioned samples are given in Table 6.6.

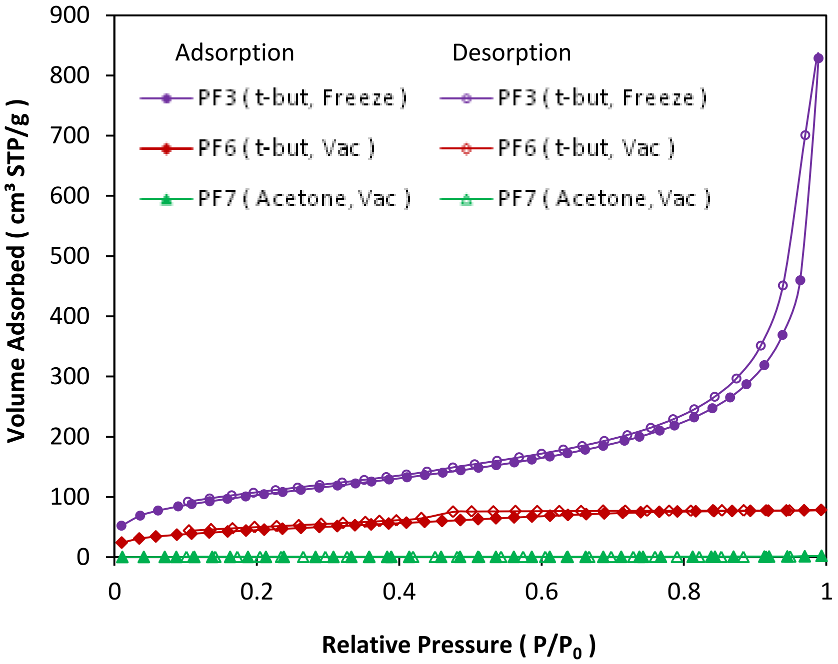

Figure 6.5: N_2 adsorption/desorption isotherms at 77K for t-butanol and acetone exchanged PF gels prepared with P/C ratio of 8

Figure 6.5 shows a considerably higher amount of N_2 adsorbed by the t-butanol exchange samples in comparison to the acetone exchanged sample. This is indicative of higher levels of porosity in the former. Table 6.6 shows that when t-butanol is being used as the solvent exchange liquid to remove water from the wet gel structure, the ensuing gels, after further processing, exhibit considerably higher specific surface areas and larger pore volumes. PSD curves for the t-butanol and acetone exchange samples are shown in Figure 6.6a. Magnified PSD curves for the pore size range of 2 – 20 nm are shown in Figure 6.6b.

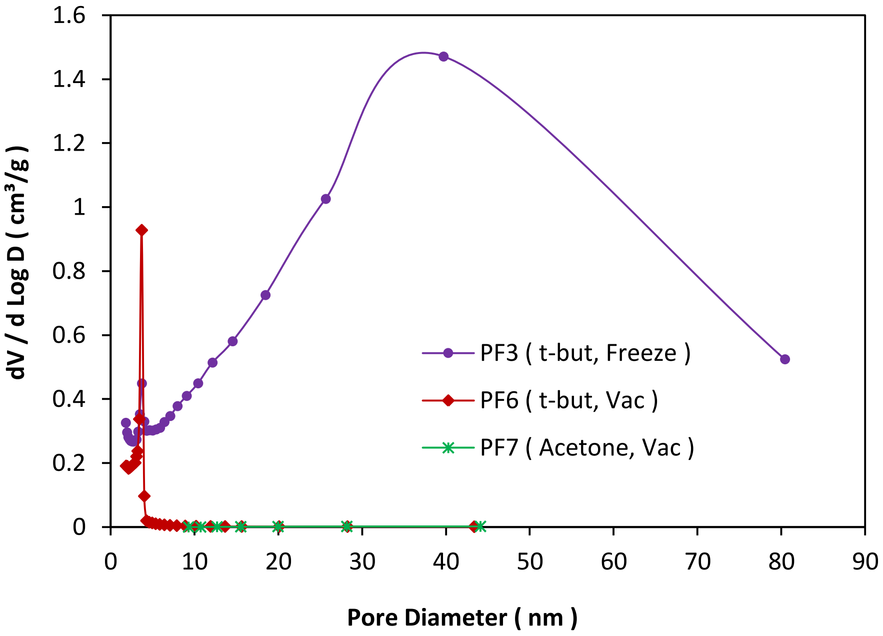

Figure 6.6a: Pore size distribution of gels prepared with different solvent exchange liquids

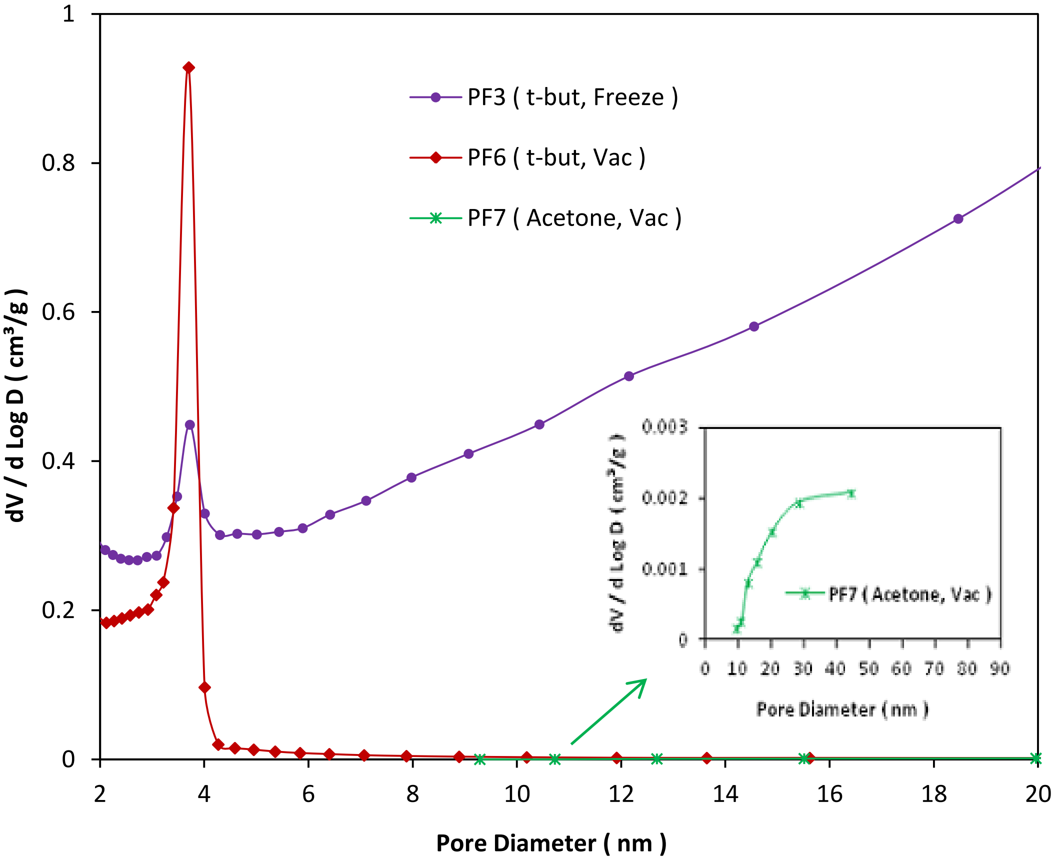

Figure 6.6b: Expanded pore size distribution curves of gels prepared with different solvent exchange liquids

***Table 6.6:** Porous characteristics of PF gels with P/C ratio of 8 prepared with different solvent exchange liquids

Sample	**S. E. Liq.**	**D. Met.**	**S_{BET} (m^2/g)**	**ΔS_{BET} (m^2/g)**	**V_{total} (cm^3/g)**	**ΔV_{total} (cm^3/g)**	**V_{micro} (cm^3/g)**	**V_{meso} (cm^3/g)**	**ΔV_{meso} (cm^3/g)**	**% V_{micro}**	**% V_{meso}**	**D_{avg} (nm)**	**ΔD_{avg} (nm)**	**D_{peak} (nm)**
PF3	t-but	F.D	369 ± 0.7 %	Av. $S_{BET(PF3)}$ ± 5.5 %	1.2814	Av. $V_{total(PF3)}$ ± 13.4 %	0.0023	1.2791	Av. $V_{meso(PF3)}$ ± 13.4 %	0.18	99.82	13.9	Av.$D_{avg(PF3)}$ ± 17.6 %	39.7
PF6	t-but	V.D	159 ± 0.8 %	$S_{BET(PF6)}$ ± 5.5 %	0.1211	$V_{total(PF6)}$ ± 13.4 %	0.0057	0.1154	$V_{meso(PF6)}$ ± 13.4 %	4.71	95.29	3.0	$D_{avg(PF6)}$ ± 17.6 %	3.7
PF7	Acet.	V.D	0.97 ± 2.5 %	$S_{BET(PF9)}$ ± 5.5 %	0.0034	$V_{total(PF7)}$ ± 13.4 %	0.0002	0.0032	$V_{meso(PF7)}$ ± 13.4 %	5.88	94.12	13.9	$D_{avg(PF7)}$ ± 17.6 %	N/A

*All parameters are as defined in Appendix B. Vacuum drying was carried out at 40 ^{o}C. See caption for Table 6.1 for general information about error analysis. Samples PF6 and PF7 have been grouped under the PF3 structure type, and their errors have been obtained from the errors associated with PF3.

Both Figures 6.6a and b indicate that the acetone exchanged PF gel corresponding to PF7, exhibits an almost non-porous structure having a very low total pore volume of 0.0034 cm^3/g (Table 6.6). It is therefore evident that acetone is not capable of preserving the PF hydrogel structure upon drying and as such is not appropriate for use as a solvent exchange liquid for this type of gel. The extremely low porous characteristics of the vacuum dried acetone exchanged PF gel is believed to be a result of a higher extent of capillary forces exerted on the pore walls in the gel structure leading to a collapse of the porous matrix. Some of the processes occurring during gels synthesis could have led to this, and shall be discussed below.

The tensile stress on the pores within the gel structure is dependent on the pore radius, liquid surface tension and wetting angle with the gel solid network surface, as described in Equation 4.1 (Section 4.1.3). It can be deduced from this relation that the levels of tensile stress in pores of varying dimensions, would differ from one another. Due to the existence of a wide range of pore diameters in the gel network, it follows that varying levels of stresses would be exerted on different parts of the gel structure. These non-uniform stresses are responsible for the collapse of the porous matrix [106]. The lower boiling point of acetone implies a quicker rate of evaporation during the vacuum drying process and therefore the rate of stress change exerted on the network is larger [166]. It can therefore be inferred from the experimental results that the gel network cannot withstand the elevated stress rates in comparison to a process involving slower evaporation such as when t-butanol is used, and as a result, a collapse of the porous network occurs.

Additionally, since chemical transformations in the form of further condensation reactions, which lead to the stiffening the gel network by an Ostwald-ripening type process, continue to occur through the drying stage, it can only imply that slower evaporation allows more time for the strengthening of the gel network or continued gelation [167]. The rate at which these transformations occur is proportional to the solubility of phenol in the pore fluids (acetone and t-butanol). Therefore as long as phenol possesses a similar solubility in both pore fluids, the slower rate of evaporation of t-butanol would result in longer times for aging and subsequently less or slower compaction of the wet gel structure, allowing for better preservation of the original hydrogel structure [108].

For the vacuum drying process of the t-butanol exchanged gel at 40 ^{o}C, the slower evaporation and the associated reduced rates of stress change exerted on the network in comparison to that obtained during the evaporation of acetone [166], results in a higher pore volume of the vacuum dried t-butanol exchanged gel as opposed to an extremely low pore volume for the vacuum dried acetone exchange gel at the same temperature.

As the freeze dried t-butanol exchanged sample had been subjected to a drying temperature of -40 ^{o}C, which is sufficiently lower than the freezing point of t-butanol, 25.6 ^{o}C [149], the formation of a vapour-liquid interface on the pore walls during solvent removal is avoided and this results in a highly mesoporous dried gel structure due to an improved capability of maintaining the original porous characteristics of the wet gel. A more detailed discussion on different drying methods is shown in the next section.

6.1.3 Effect of Drying Method on the Pore Structure of PF Gels

For the investigation of drying methods, PF hydrogels were dried by low and high temperature vacuum drying, and freeze drying of t-butanol exchanged gels. The N_2 adsorption/desorption isotherms at 77 K for PF gels dried with different drying methods is shown in Figure 6.7. Table 6.7 shows a description of the drying methods that correspond to each sample. It can be observed from Figure 6.7 that a considerably higher amount of N_2 is adsorbed with the freeze dried gel, PF3, in comparison to the low and high temperature vacuum dried gels PF6 and PF8, respectively. Furthermore, data given in Table 6.7 show that PF3, possesses a considerably higher specific surface area, total pore volume, mesopore volume and average pore size.

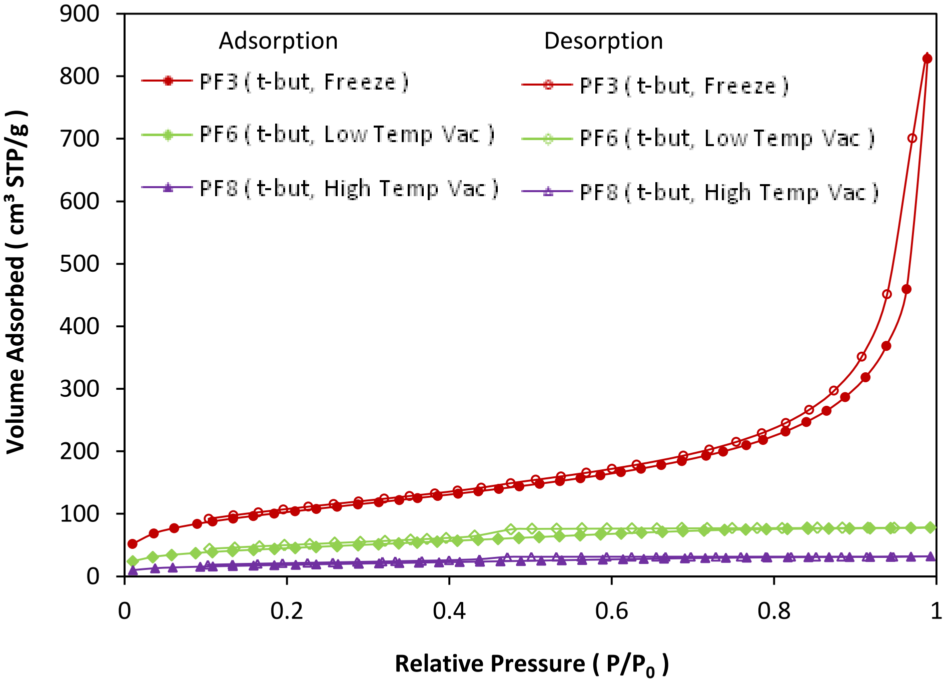

Figure 6.7: N_2 adsorption/desorption isotherms for PF gels with different drying methods

The PSD curves for the aforementioned samples are shown in Figure 6.8a. An expanded version of the PSD for the low pore diameter range is displayed in Figure 6.8b. Porosity parameters of the gels are given in Table 6.7. The PSD curves in Figures 6.8a and 6.8b show that the low and high temperature vacuum dried gels exhibit low levels of porosity. These gels posses total pore volumes of ~ 0.12 cm^3/g and 0.05 cm^3/g, respectively, with mean pore sizes of around 3 nm. On the other hand, the PSD curve for the freeze dried gel shown in Figure 6.8a is indicative of a gel possessing a highly mesoporous structure with a total pore volume of 1.28 cm^3/g representative of the highest pore volume of all gels and an average pore size of 13.9 nm. These experimental results do indeed show that freeze drying is the preferred drying method for the synthesis of highly meosporous PF gels.

Vacuum drying leads to the formation of a vapour-liquid interface as the liquid in the pores of the gel is removed by evaporation. Mechanical stresses on the pores of the gel can occur due to the surface tension between the vapour and the liquid at this interface, resulting in the collapse of the porous structure [107]. Conversely, the freeze drying technique involves a removal of the residual liquid in the hydrogel directly as vapour from its frozen state [107], [159], [168]. In this case, the vapour-liquid interface is avoided [168] and the original porous structure of the solvent exchanged gel is preserved much better in comparison to the vacuum drying method [111].

Comparing both low and high temperature vacuum dried gels, the corresponding N_2 adsorption/desorption isotherms shown in Figure 6.7, suggest that low temperature drying results in higher levels of porosity possibly due to the decrease in rate of evaporation [166]. This prevents collapse of the porous structure to some extent due to less shrinkage, allowing for the original wet gel structure to be better maintained in the final structure of the dried gel. Furthermore the PSD curves in Figure 6.8b along with the data given in Table 6.7 show that PF6 exhibits a greater pore volume than PF8. These results demonstrate the immense influence of drying methods on the porous structure of PF gels.

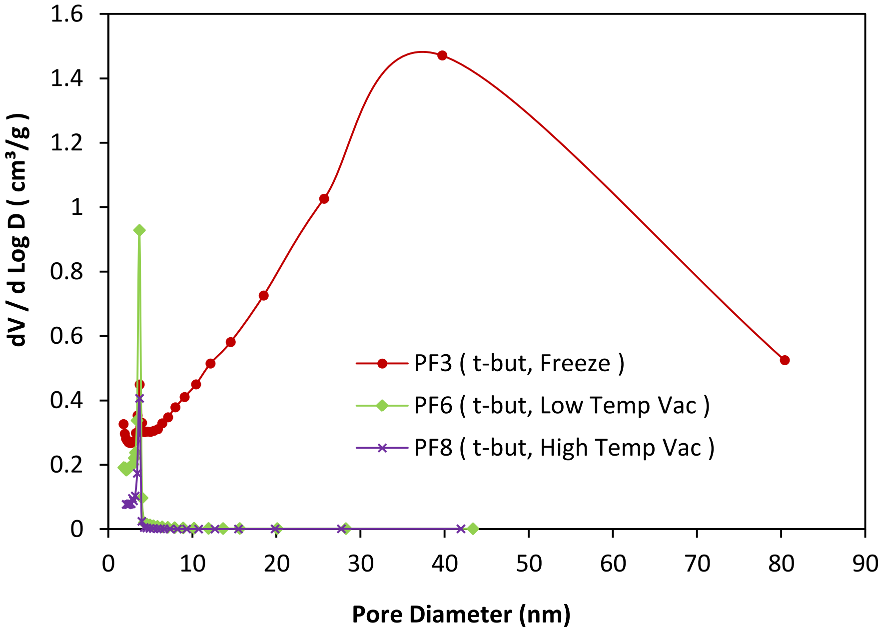

Figure 6.8a: Pore size distribution of PF gels prepared with different drying methods

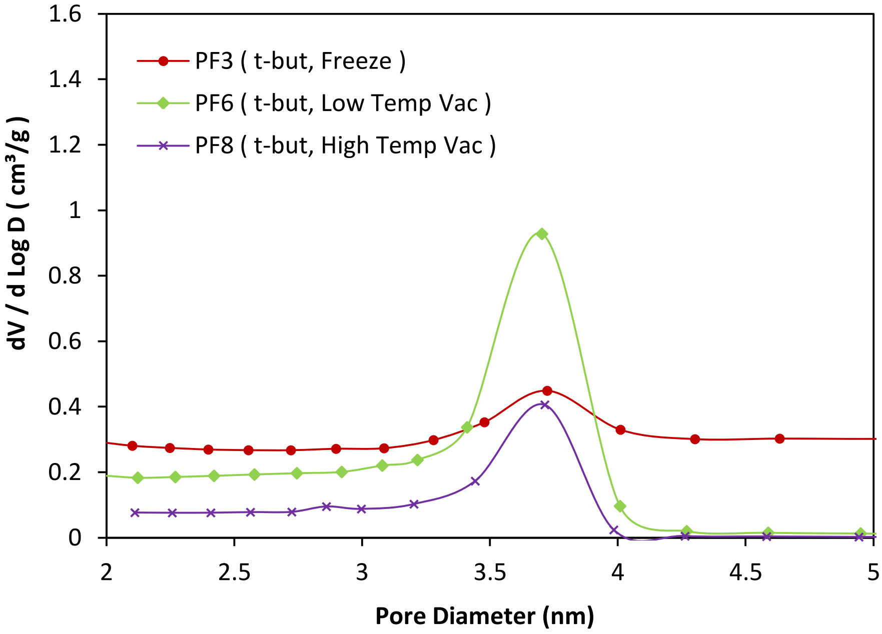

Figure 6.8b: Expanded pore size distribution curves of PF gels prepared with different drying methods

***Table 6.7:** Porous characteristics of PF gels with P/C ratio of 8 prepared with different drying methods (Solvent exchange liquid for all samples was t-butanol)

Sample	**D. Met.**	**S_{BET} (m^2/g)**	**ΔS_{BET} (m^2/g)**	**V_{total} (cm^3/g)**	**ΔV_{total} (cm^3/g)**	**V_{micro} (cm^3/g)**	**V_{meso} (cm^3/g)**	**ΔV_{meso} (cm^3/g)**	**% V_{micro}**	**% V_{meso}**	**D_{avg} (nm)**	**ΔD_{avg} (nm)**	**D_{peak} (nm)**
PF3	F.D at -40 °C	369 ± 0.7 %	Av. $S_{BET(PF3)}$ ± 5.5 %	1.2813	Av. $V_{total(PF3)}$ ± 13.4 %	0.0023	1.2790	Av. $V_{meso(PF3)}$ ± 13.4 %	0.18	99.82	13.9	Av. $D_{avg(PF3)}$ ± 17.6 %	39.7
PF6	V.D at 40 °C	159 ± 0.8 %	$S_{BET(PF6)}$ ± 5.5 %	0.1211	$V_{total(PF6)}$ ± 13.4 %	0.0057	0.1154	$V_{meso(PF6)}$ ± 13.4 %	4.71	95.29	3.0	$D_{avg(PF6)}$ ± 17.6 %	3.7
PF8	V.D at 70 °C	65 ± 0.8 %	$S_{BET(PF8)}$ ± 5.5 %	0.0497	$V_{total(PF8)}$ ± 13.4 %	0.0030	0.0467	$V_{meso(PF8)}$ ± 13.4 %	6.04	93.96	3.1	$D_{avg(PF8)}$ ± 17.6 %	3.7

*All parameters are as defined in Appendix B. See caption for Table 6.5 for general information about error analysis. Samples PF6 and PF7 have been grouped under the PF3 structure type, and their errors have been obtained from the errors associated with PF3.

6.1.4 Effect of P/F Ratios on the Pore Structure of PF Gels

Section 6.1.1 showed that at a P/F ratio of 0.5, the P/C ratio of 8 is the optimum for porosity development. It is assumed that a similar trend exists for other P/F ratios. PF gels with P/F ratios of 0.4, 0.5, 0.6, 0.7, and 0.8, were synthesised using a fixed P/C ratio 8 and P/W of 0.1 g/ml. As a P/F ratio of 0.5 has been shown to produce porous materials [76], the aim here was to investigate ratios above and below this value. At P/F ratios of 0.7 and 0.8, no gelation occurred. This is likely due to the lack of adequate cross-linking to allow for gelation.

The formation of methylene and methylene ether bridged compounds by the condensation of hydroxymethyl derivates of phenol (Sections 4.1.1 and 6.1.1) is an important step in PF gel synthesis, as this is the mechanism responsible for crosslinking in the PF gel [103]. Since the 2,4,6 positions of phenol represent the active sites for electrophilic aromatic substitution [16], the reaction of phenol with formaldehyde should lead to a trihydroxymethyl derivate of phenol, which will then allow all three hydroxymethyl groups to be involved in the condensation/crosslinking reactions. However, during the reaction of formaldehyde with phenol, condensation reactions also occur simultaneously, leading to chain growth formation, which could sterically hinder or prevent access to the other reactive sites of phenol from reaction with formaldehyde [103]. As a result, excess formaldehyde is typically used for the PF gel synthesis to allow for increased access to these reactive sites. The lack of gelation for P/F ratios, 0.7 and 0.8, could suggest an insufficient supply of formaldehyde to allow for effective crosslinking. A similar situation, where lack of gelation occurs, due to low amounts of formaldehyde, has been reported in resorcinol-formaldehyde gel synthesis [169], and could also be due to the steric effects just described.

Figure 6.9 shows N_2 adsorption/desorption isotherms at 77 K for freeze-dried PF gels synthesised with different P/F ratios. All porosity parameters are displayed in Table 6.8. The samples are predominantly mesoporous with over 95 % mesoporosity in all samples indicating that the majority of the pore volume in the samples originates from the mesopores. It can be observed from Figure 6.9 that the sample with P/F ratio 0.5 (PF3) adsorbs the highest amount of nitrogen. This is consistent with Table 6.8, which shows that this sample also has the highest total pore and mesopore volumes. The aforementioned porosity parameters are at their lowest at a P/F ratio of 0.6 (PF10). These findings could also be due to the steric effects discussed earlier in this section, and it is believed that the low amount of formaldehyde used in the synthesis of PF 10 (P/F = 0.6), although capable of leading to gel formation, was inadequate to allow for sufficient cross link density in the gel, leading to excessive shrinkage of its porous structure during gelation and resulting in low pore volume.

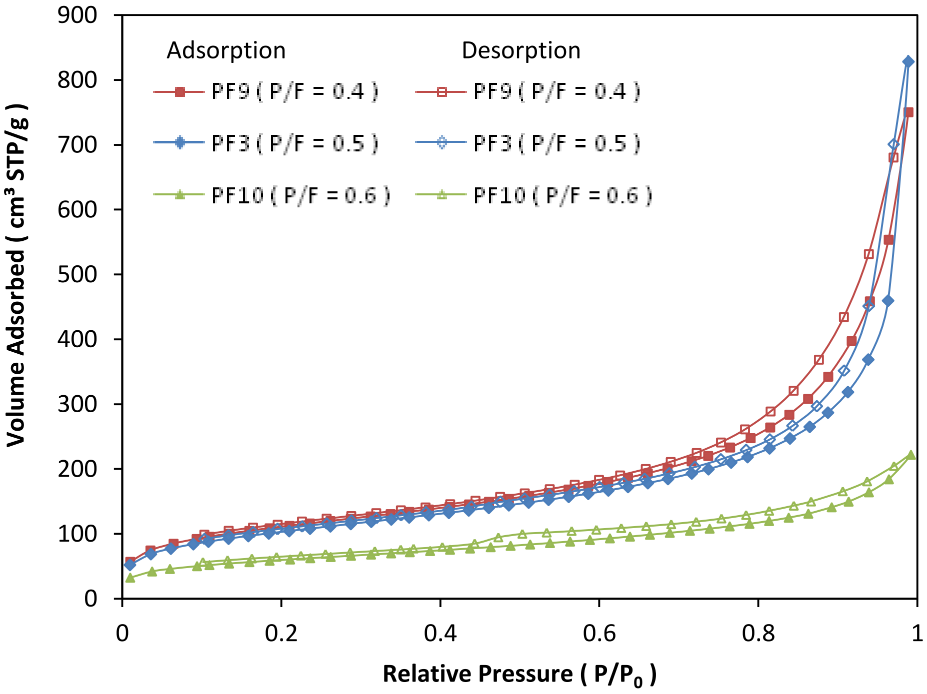

Figure 6.9: N_2 adsorption/desorption isotherms for freeze dried PF gels with different P/F ratios

Additionally, Figure 6.9 and Table 6.8 indicate that the sample PF9 (P/F = 0.4) possesses lower pore volumes than PF3 (P/F=0.5). This suggests that in terms of porosity, the P/F ratio of 0.5 represents the optimum ratio. Out of all three samples, PF9, which possesses the lowest P/F ratio of 0.4, has the highest amount of formaldehyde. This can only imply that this sample possesses much higher crosslink densities in the gel network, which leads to a structure containing pores of smaller dimensions and relatively lower pore volumes (as described in Section 6.1.1). On the other hand, at a P/F ratio of 0.5, the lower formaldehyde content, allows for reduced crosslinking, resulting in higher levels of porosity. The aforementioned effects of formaldehyde content on the porous propereties of PF9 (P/F = 0.4), is an example of where too high a crosslink density could have a somewhat undesired effect on porosity, although there is only a subtle difference between total pore and mesopore volumes, as well as pore size between the samples with P/F = 0.4 and P/F = 0.5.

Figure 6.10a shows the PSD curves of PF gels synthesised with different P/F ratios. The PSD curves for pore diameter in the range of 2 – 5 nm is magnified and shown clearly in Figure 6.10b. It is evident that PF10 (P/F = 0.6) shows a dominant peak in the small mesopore region between 2 – 5 nm while both PF3 and PF9 possess dominant peaks in the large mesopore regions within the range of approximately 20 – 40 nm. This is consistent with the results of the volumetric calculations displayed in Table 6.8, which show that the total pore volume of PF10 is considerably less than both PF3 and PF9.

A comparison between the appearance and texture of the gels with P/F ratios of 0.4 and 0.5 shows that the structure of the former is more uniform, while in the latter, a hard layer of gel forms at the bottom of the flask with a slightly different coloration of the gel. This is depicted in Figure 6.11. Due to the relatively low amount of formaldehyde used in the synthesis of PF3 (P/F=0.5), it is believed that some unreacted phenol precipitates to the bottom of the flask forming the observed hard layered structure [76]. The slightly different coloration shown in Figure 6.11 with P/F 0.5 possibly corresponds to the sections of the gel that have only been partly cross-linked. Removing the gel from the flask (for P/F=0.5), involves carefully scraping off what appears to be the properly cross-linked spongy pink gel, while in the case of P/F = 0.4, the whole gel can be used. This implies that the sample with the P/F ratio of 0.4, represents a more efficient use of raw material (higher yield) although at the expense of some porosity, whereas a P/F ratio of 0.5 represents the optimum conditions for porosity. From a typical amount of 9.4 g of phenol, used in the gel synthesis procedure, the ensuing gels, PF3 and PF9 gave a yield of 2.3 g and 13 g respectively. The amount corresponding to PF3 (2.3 g) is significantly low because only a small amount of the whole gel could be used. This clearly demonstrates the inefficient use of raw material for this gel.

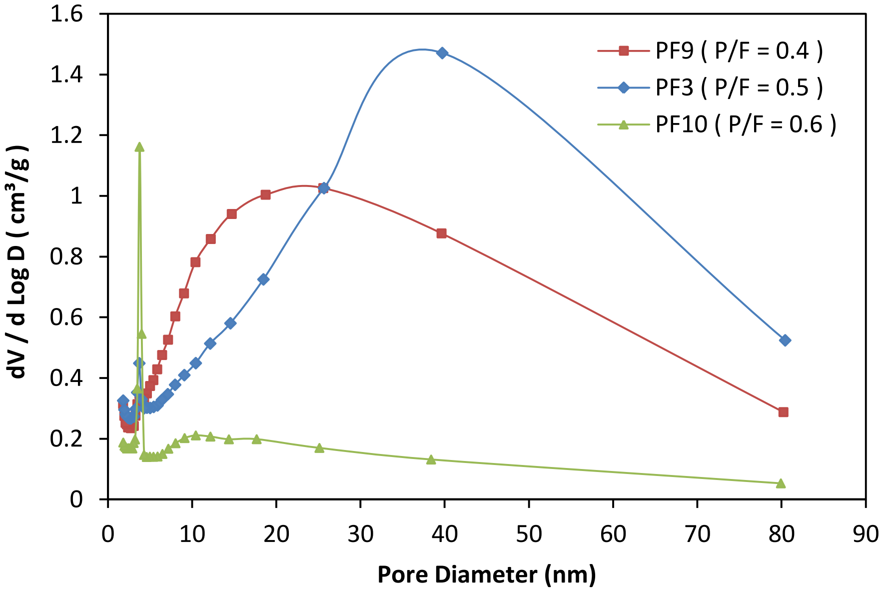

Figure 6.10a: Pore size distribution of PF gels prepared with different P/F ratios

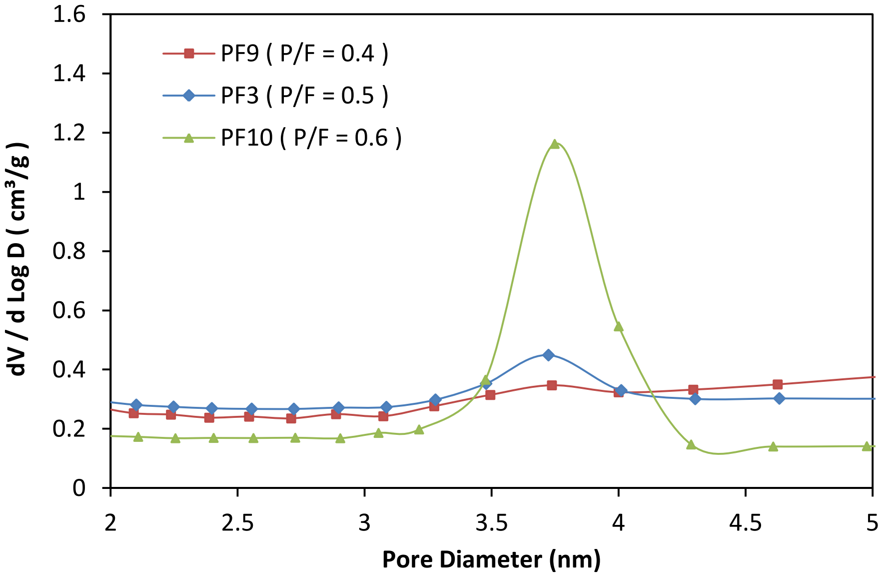

Figure 6.10b: Expanded pore size distribution curves of PF gels prepared with different P/F ratios

***Table 6.8:** Pore characteristics of PF gels with different P/F ratios (at P/C = 8)

Sample	**P/F**	**S_{BET} (m^2/g)**	**ΔS_{BET} (m^2/g)**	**V_{total} (cm^3/g)**	**ΔV_{total} (cm^3/g)**	**V_{micro} (cm^3/g)**	**V_{meso} (cm^3/g)**	**ΔV_{meso} (cm^3/g)**	**% V_{micro}**	**% V_{meso}**	**D_{avg} (nm)**	**ΔD_{avg} (nm)**	**D_{peak} (nm)**
PF9	0.4	394 ± 0.8 %	Av. $S_{BET(PF9)}$ ± 2.9 %	1.1608	Av. $V_{total(PF9)}$ ± 5.2 %	0.0096	1.1512	Av. $V_{meso(PF9)}$ ± 5.5 %	0.83	99.17	11.4	Av. $D_{avg(PF9)}$ ± 7.1 %	25.7
PF3	0.5	369 ± 0.7 %	Av. $S_{BET(PF3)}$ ± 5.5 %	1.2814	Av. $V_{total(PF3)}$ ± 13.4 %	0.0023	1.2791	Av. $V_{meso(PF3)}$ ± 13.4 %	0.18	99.82	13.9	Av. $D_{avg(PF3)}$ ± 17.6 %	39.7
PF10	0.6	210 ± 0.8 %	$S_{BET(PF10)}$ ± 5.5 %	0.3432	$V_{total(PF10)}$ ± 13.4 %	0.0090	0.3342	$V_{meso(PF10)}$ ± 13.4 %	2.62	97.38	7.8	$D_{avg(PF10)}$ ± 17.6 %	3.7

* PF11 and PF12 could not be formed into gels. All parameters are as defined in Appendix B. See caption for Table 6.5 for general information about error analysis. PF10 has a similar structure to PF3 and its errors have been obtained from the errors associated with PF3.

Furthermore, upon reproducibility tests for both P/F = 0.4 and P/F = 0.5 based samples, the porosity parameters such as S_{BET}, V_{total}, V_{meso}, and D_{avg}, varied more significantly in the sample with a P/F ratio of 0.5. This is likely due to the possibility of removing some of the bottom layer structure along with the top layer, when scraping the gel off for further treatment and analysis. Therefore, along with the increased yield for gels based on a P/F = 0.4, a greater level of reproducibility was observed.

The results obtained from the control of gel porosity (section 6.1), reveal an immense potential of PF gels, in terms of the highly mesoporous structures that have been obtained. The highest mesopore volume obtained for the PF gel, is ~ 1.28 cm^3/g, and compares well with typical values for RF gels, synthesised under similar conditions, reported in the literature [111], [158 - 159], were mesopore volumes ranging from 1.1 – 1.3 cm^3/g, have been achieved.

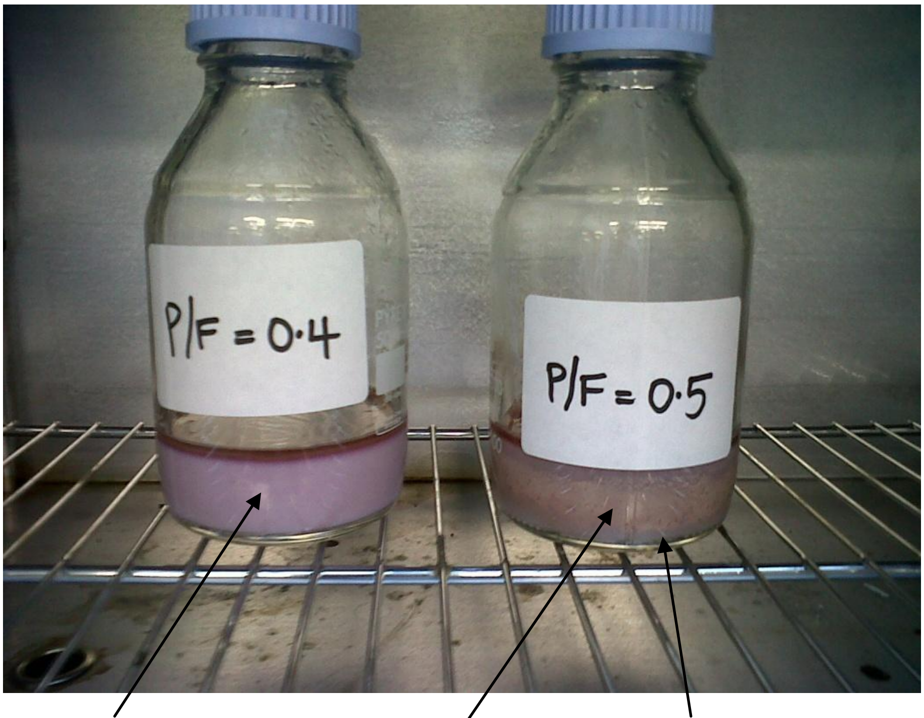

Uniform gel structure

Slightly different colouration

Hard layer formed at bottom of the flask

Figure 6.11: Appearance of PF gels with different P/F ratios

6.2. Control of Carbon Porosity

This section deals with the effect of various carbonisation temperatures on the porous structure of PF carbons. Additionally an investigation into the effect of activation on the structure of the carbons was carried out in both O_2 and CO_2 by varying the degree of burn-off.

6.2.1 Effect of Carbonisation Temperature

The N_2 adsorption-desorption isotherms are shown in Figure 6.12. For clarity, only 4 isotherms have been displayed.

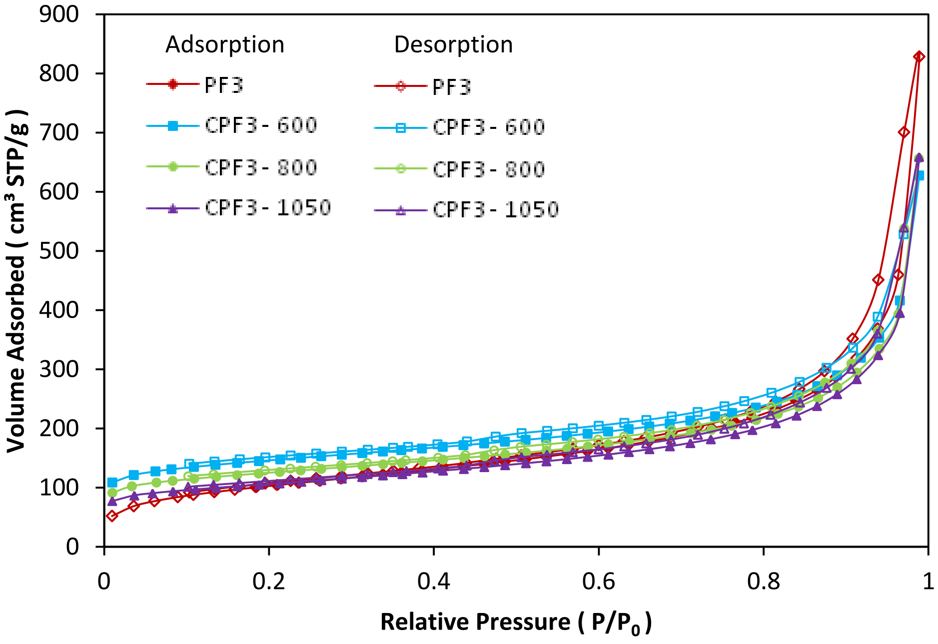

Figure 6.12: N_2 adsorption/desorption isotherms for PF3 gels and CPF3 carbons

The porosity properties of the PF gel and carbon gels are shown in Table 6.9. The N_2 adsorption/desorption isotherms are typical of type IV isotherms with hysteresis loops representing capillary condensation in the mesopores [118]. It is evident that the amount of nitrogen adsorbed by the PF gel is higher than that adsorbed by the carbons. This is indicative of an overall loss of porosity upon carbonisation which could be due to shrinkage of some pores. On the other hand, Table 6.9 shows that although there is an overall loss in porosity of the PF gel upon carbonisation, there is also an increase in micropore volumes, indicative of the development of microporosity upon pyrolysis. It other words it shows the carbons exhibit higher micropore volumes than the PF gel. As would be verified by FTIR measurements in section 6.3, pyrolysis leads to the cleavage of C-O and C-H bonds from methylene ether and methylene bridges linking the phenol molecules in the PF gel, and the subsequent removal of small molecular species, such as CO, CO_2, CH_4 etc. [170]. This leads to a significant amount of mass loss (about 50 %) and also the creation of a certain amount of new porosity [110].

Figure 6.13a shows the PSD curves for the PF gel and carbonised samples (600 ^{o}C, 800 ^{o}C and 1050 ^{o}C). PSD curves for a pore diameter range of 2 – 5 nm are magnified and shown in Figure 6.13b. The PSD curve for the PF gel appears to stand out from those of the carbonised samples in Figure 6.13a. In fact there is a downward shift of the curves (when comparing the gel and the carbons) in the large mesopore region between approximately 30 – 40 nm, and this is indicative of a drop in mesopore volume over that range. There is also an upward shift in the PSD curves in the small mesopore region between 2 – 5 nm in Figure 6.13b, when moving from PF gel to carbonised gels. Table 6.9 suggests that the increase in porosity based on this peak, is masked by the drop in mesopore volume in the large mesopore region leading to lower mesopore volumes of the carbonised samples in comparison to the PF gel.

The pore volume measurements of the samples displayed in Table 6.9, show that along with the increase in micropore volume there is a slight drop in mesopore volume and total pore volume when the gel is carbonised to 600 ^{o}C. The development of porosity that occurs due to the removal of methylene and methelyne ether linkages that connect the phenol molecules, also leads to the shrinkage of the bulk gel structure. This can be understood from the viewpoint of the formation of aromatic multi-ring structures that are more closely packed than the previous structures containing methylene and methylene ether bridges [170]. Therefore, the increase in microporosity, as a result of carbonisation reactions, can also be due partly to the shrinkage of mesopores to form smaller pores, as a result of bulk structure shrinkage. The shrinkage of mesopores during carbonisation is consistent with previously reported investigations on similar gels [110], and agrees well with the overall drop in total pore volume upon carbonisation.

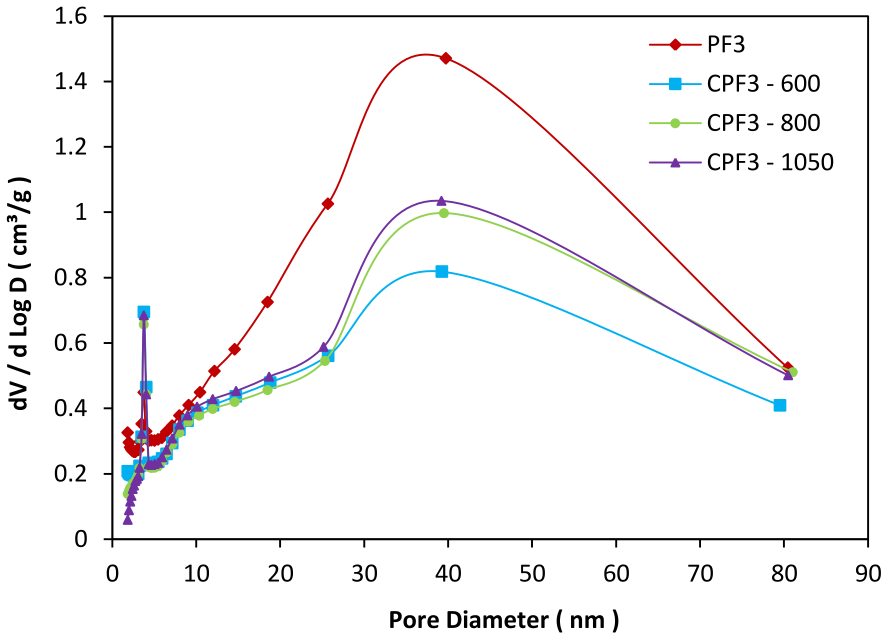

Figure 6.13a: Pore size distribution of PF3 gel and CPF3 carbons

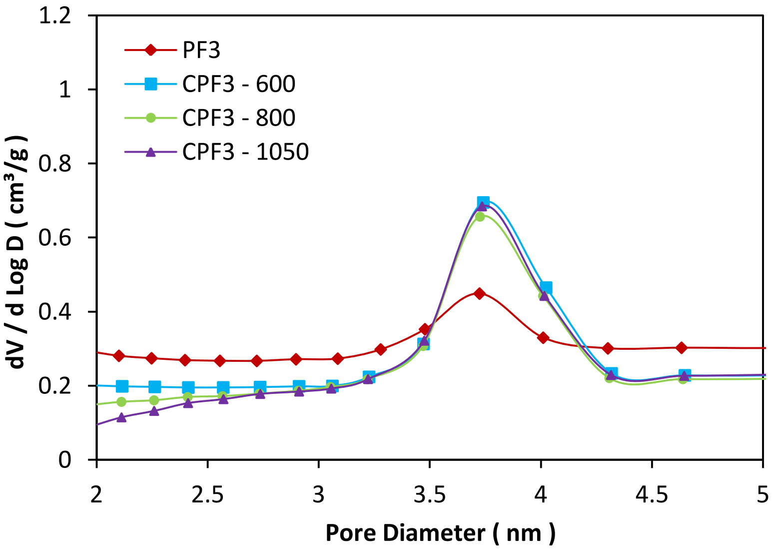

Figure 6.13b: Expanded pore size distribution curves for PF3 gel and CPF3 carbons

*Table 6.9: Textural characteristics of PF3 gel and CPF3 carbons

Sample	S_{BET} (m^2/g)	ΔS_{BET} (m^2/g)	V_{total} (cm^3/g)	ΔV_{total} (cm^3/g)	V_{micro} (cm^3/g)	ΔV_{micro} (cm^3/g)	V_{meso} (cm^3/g)	ΔV_{meso} (cm^3/g)	% V_{micro}	% V_{meso}	D_{avg} (nm)	ΔD_{avg} (nm)	D_{peak} (nm)
PF3	369 ± 0.7 %	Av. $S_{BET(PF3)}$ ± 5.5 %	1.2814	Av. $V_{total\ (PF3)}$ ± 13.4 %	0.0023	N/A	1.2791	Av. $V_{meso(PF3)}$ ± 13.4 %	0.18	99.82	13.9	Av. $D_{avg\ (PF3)}$ ± 17.6 %	39.7
CPF3-600 ^{o}C	480 ± 1.5 %	$S_{BET(CPF3\text{-}600)}$ ± 3.4 %	0.9706	$V_{total\ (CPF3\text{-}600)}$ ± 5.5 %	0.1070	$V_{micro(CPF3\text{-}600)}$ ± 7.4 %	0.8636	$V_{meso(CPF3\text{-}600)}$ ± 5.9 %	11.0	89.0	8.0	$D_{avg\ (CPF3\text{-}600)}$ ± 4.2 %	39.2
CPF3-700 ^{o}C	413 ± 1.3 %	$S_{BET(CPF3\text{-}700)}$ ± 3.4 %	0.9853	$V_{total\ (CPF3\text{-}700)}$ ± 5.5 %	0.0799	$V_{micro(CPF3\text{-}700)}$ ± 7.4 %	0.9054	$V_{meso(CPF3\text{-}700)}$ ± 5.9 %	8	92	9.5	$D_{avg\ (CPF3\text{-}700)}$ ± 4.2 %	38.8
CPF3 - 800 ^{o}C	414 ± 1.4 %	$S_{BET(CPF3\text{-}800)}$ ± 3.4 %	1.0151	$V_{total\ (CPF3\text{-}800)}$ ± 5.5 %	0.0835	$V_{micro(CPF3\text{-}800)}$ ± 7.4 %	0.9316	$V_{meso(CPF3\text{-}800)}$ ± 5.9 %	8.2	91.8	9.8	$D_{avg\ (CPF3\text{-}800)}$ ± 4.2 %	39.5
CPF3-900 ^{o}C	363 ± 1.2 %	$S_{BET(CPF3\text{-}900)}$ ± 3.4 %	0.8802	$V_{total\ (CPF3\text{-}900)}$ ± 5.5 %	0.0631	$V_{micro(CPF3\text{-}900)}$ ± 7.4 %	0.8171	$V_{meso(CPF3\text{-}900)}$ ± 5.9 %	7.2	92.8	9.7	$D_{avg\ (CPF3\text{-}900)}$ ± 4.2 %	39.0
CPF3-1000 ^{o}C	372 ± 1.1 %	$S_{BET(CPF3\text{-}1000)}$ ± 3.4 %	0.9343	$V_{total\ (CPF3\text{-}1000)}$ ± 5.5 %	0.0623	$V_{micro(CPF3\text{-}1000)}$ ± 7.4 %	0.8720	$V_{meso(CPF3\text{-}1000)}$ ± 5.9 %	7	93	10.0	$D_{avg\ (CPF3\text{-}1000)}$ ± 4.2 %	39.9
CPF3-1050 ^{o}C	357 ± 1.1 %	$S_{BET(CPF3\text{-}1050)}$ ± 3.4 %	1.0194	$S_{BET(CPF3\text{-}1050)}$ ± 5.5 %	0.0602	$V_{micro(CPF3\text{-}1050)}$ ± 7.4 %	0.9592	$V_{meso(CPF3\text{-}1050)}$ ± 5.9 %	5.91	94.09	11.4	$D_{avg\ (CPF3\text{-}1050)}$ ± 4.2 %	39.2

*All parameters are as defined in Appendix B. See caption for Table 6.5 for information about error analysis for PF3 and also the method of error calculation. The errors associated with the carbons are based on three carbonisation experiments carried out at 1050 ^{o}C [CPF9-1050 ^{o}C (to be introduced shortly)]. It is assumed that the deviation from the average of measured parameters would be similar for other temperatures.

Table 6.9 shows that upon further increase in carbonisation temperature above 600 °C, there is an overall drop in micropore volume and increase in mesopore volume, although with some slight deviation. The trend in both mictopore and mesopore volume with increasing carbonisation temperature, is shown in Figure 6.14.

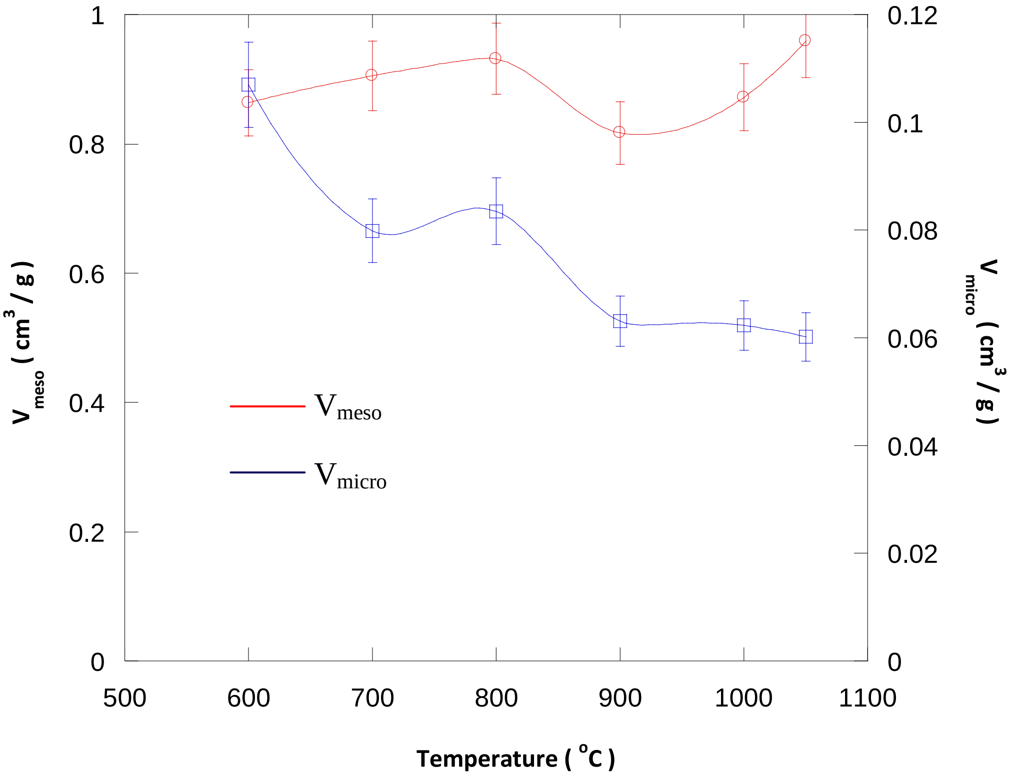

Figure 6.14: Variation of micropore and mesopore volumes of CPF3 carbons with carbonisation temperature (the lines connecting the data points represent trend lines)

The TGA measurement carried out on the PF gel is displayed is in Figure 6.15 and includes weight loss versus temperature and derivative curves. The former shows that during carbonisation, the change in weight of the sample with temperature at temperatures approaching 1000 °C and beyond, is much less than at lower temperatures. Furthermore, the derivative weight loss curve, shows that rate of weight change is small at these temperatures. An explanation of this shall be given shortly. Firstly, it is also important to note that at temperatures below 600 °C, the derivate curve shows significant levels of weight loss and these could be attributed to the release of most of the volatile matter [110]. The peaks on the derivative curve, could be due to the desorption of adsorbed water at 120 ^{o}C, and carbonisation reactions involving the breakage of C-O bonds at 400 ^{o}C, and C-H at 530 ^{o}C [110]. These various steps of the carbonisation process, have been identified by researchers using a combination of mass spectrometry with TGA [171], to reveal gaseous species such as CO_2, CO, CH_4 and higher hydrocarbon derivatives. Additional evidence of the aforementioned carbonisation reactions shall be presented in the FTIR analysis section (section 6.3, Figure 6.28), which shows the disappearance of peaks associated with the methyelene ether (C-O-C) and methylene ($-CH_2-$) linkages from the organic precursor upon carbonisation. It is important to note here, that although as mentioned earlier, significant weight loss corresponding to the release of most of the volatile matter is observed at temperatures below 600 ^{o}C, weight loss, continues to occur even at temperatures above 1000 ^{o}C (though much smaller). This is consistent with the work done by Darne *et al*. [172], which suggests that it is only upon graphitisation, that heteroatoms, such as oxygen and hydrogen are completely removed from carbon structure, which in this case, as expected for hard carbons, may not occur even at temperatures as high as 3000 ^{o}C. As such, the continuous weight loss observed in the TGA measurement in Figure 6.15 is likely due to the continuous release of volatile matter, although, on a smaller scale relative to the lower temperatures. Similar weight loss profiles for organic gels have been observed [110].

Previous studies have shown that as carbonisation proceeds, both surface area and micropore volume increase, reaching a limiting value at 600 ^{o}C [173]. This is consistent with the porosity parameters for the carbonised samples obtained here, which show a maximum micropore volume at 600 ^{o}C. One might assume that the corresponding decrease and increase in micropore and mesopore volume respectively, at higher temperatures, could be due to reactions taking place in the neighbouring regions, encompassing the micropores, namely, a reaction of the carbon material with oxygen (from the chemical transformations taking place during carbonisation), causing the removal of the carbon atoms surrounding the micropores, and resulting in the widening of these pores [170]; a topic which shall be expanded further in section 6.2.2.

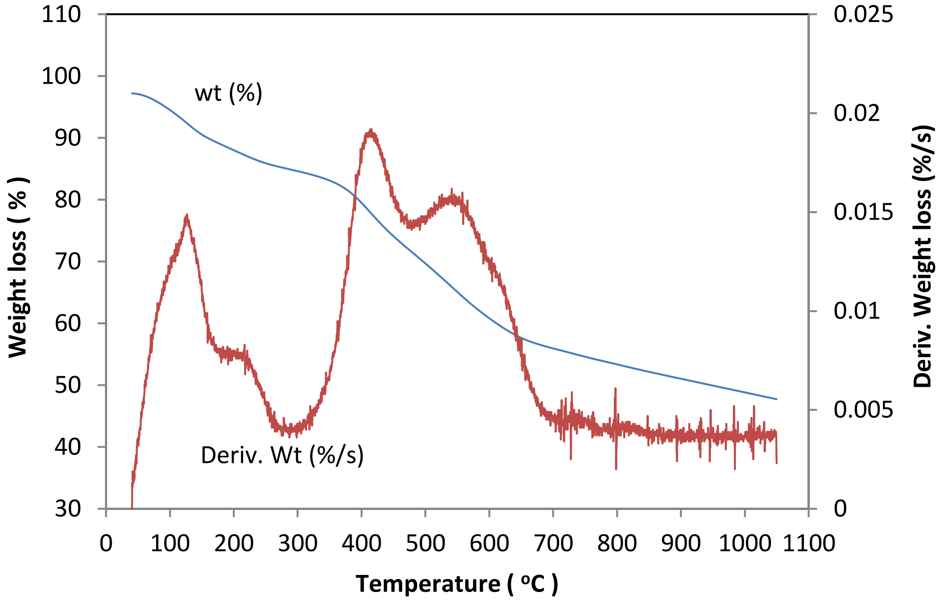

Figure 6.15: TGA measurement for PF3 under argon (wt (%) refers to the weight loss curve and Deriv. Wt (%/s) refers to the derivative weight loss curve)

Although the carbonisation of the PF gel leads to a slight drop in total pore and mesopore volumes, the results suggest that of all carbonised samples, CPF-1050 ^{o}C shows the most favourable porous properties with a total pore volume, mesopore volume and pore size of approximately 1.02 cm^{3}/g, 0.96 cm^{3}/g and 11.4 nm, respectively.

The effect of carbonisation temperature was also performed on PF9 as this was shown to be the preferred gel for use in this work due to its more uniform structure and ease of reproducibility. Similar carbonisation temperatures were used ranging from 600 – 1050 ^{o}C. However the samples that were carbonised at temperatures < 1000 ^{o}C, displayed a self ignition behaviour upon removal from the inert atmosphere of the furnace and exposure to air at ambient conditions, whereas this was not observed at temperatures of 1000 ^{o}C and 1050 ^{o}C. With respect to the samples that displayed self-ignition: initially the samples were at room temperature for about a minute, and suddenly the carbon started to self heat and burn slightly, eventually converting the whole sample to ash. This, however, did not occur with the PF3 samples and the reason for this behaviour is not fully understood. However, some reports in literature give a slight indication as to what might be responsible. As stated in Section 4.1.1, higher amounts of catalysts (Na_2CO_3) are required in the sol-gel polymerisation of PF gels in comparison to RF gels. Scherdel *et al.* [165] showed that the amount of Na_2CO_3 used in RF gel synthesis is lower by a factor of 100 – 1000 than that for PF gels; indicating that PF gels require much higher quantities of catalysts for synthesis. Both the cost implications and electrochemical significance of increased catalyst content shall be discussed in section 7.3. EDS measurements carried out by Scherdel *et al.* [165], also showed that sodium impurities of about 3.5 wt% were found in PF carbon samples. Such impurities could include elemental sodium as described below [174 - 175].

Wigmans *et al.* [174]**,** showed that in the presence of carbon, and at temperatures greater than 527 ^oC, sodium carbonate decomposes according to the following equation:

$$Na_2CO_3(s) \longrightarrow Na_2O(s) + CO_2(g) \qquad (6.1)$$

This investigation also showed that a further increase in temperature above 627 ^oC leads to the reaction of sodium oxide with carbon as follows,

$$Na_2O(s) + C(s) \longrightarrow 2Na(s) + CO(g) \qquad (6.2)$$

The self ignition observed for carbonised PF9 gels between 600 – 900 ^oC, could be due to the presence of elemental sodium, which is known to spontaneously ignite upon exposure to air [175]. This could suggest that the weight loss observed in the TGA curve in Figures 6.15 and 6.19 between 500 ^oC and 700 ^oC, could, in addition to the previously mentioned carbonisation reactions, also be due to the decomposition of sodium carbonate and the subsequent decomposition of sodium oxide.

Identical amounts of catalyst, Na_2CO_3, were used in the synthesis of PF3 and PF9. However, in order to determine the variation in the concentration of Na_2CO_3, within different regions of the gel structure after the synthesis procedure, energy dispersive

X-ray spectroscopy (EDS) was carried out on both gels. Concentrations of up to 2.85 and 2.82 wt % of sodium species for PF3 and PF9 were obtained respectively. As the gels had not be subject to high temperature treatment (> 500 °C), these sodium species are most likely to be in the form of sodium carbonate as described earlier. Furthermore, these concentrations, appear to be somewhat similar, and still do not account for the self ignition of PF9 as opposed to PF3. This may suggest that higher concentrations of sodium metal are required to produce the observed spontaneous combustion. One consideration could be the presence of L-shaped pores of the type depicted in Figure 6.16 [67], where regions of elevated sodium metal concentrations exist. Such regions might be difficult to detect using an electron beam, as is the case with EDS, because a charged particle such as an electron, can be repelled by electrons already present in the carbon, before reaching the sodium containing region.

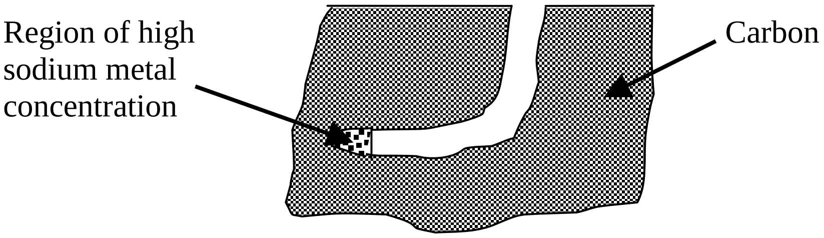

Figure 6.16: Schematic of an L-shaped pore [65]

One might assume that such regions of high sodium metal concentration, were present in the self-igniting PF9 carbons, and not in the PF3 based carbons, due to differences in the pore geometries, imposed by different formaldehyde concentrations. In which case, this could be responsible for the observed self-ignition at carbonisation temperatures between 600 – 900 °C, and changes in the pore geometry upon further increase in temperature may have resulted in greater dispersal of sodium metal species within the carbon structure. Some evidence of this could be found in the drop in concentration of sodium species upon carbonisation, from 2.82 wt % (for PF9) to 1.65 wt % (CPF9 -1050).

As a result of the self-ignition behaviour of PF9 samples carbonised between 600 – 900 °C, and the subsequent conversion of the bulk sample to ash, these materials could not be analysed. However, for PF9 carbonisation temperatures of 1000 °C and 1050 °C, stable carbons were formed and were subject to porous structure analysis. The N_2 adsorption/desorption isotherms for PF9 gel and CPF9 carbons are shown in Figure 6.17. Table 6.10 shows the porous characteristics of the gel and the corresponding carbons. It can be seen from Figure 6.17, that the quantity of N_2 adsorbed in the gel is higher than that adsorbed by the carbons. This is similar to the PF3 experiments as explained earlier. Furthermore, as carbonisation temperature increases from 1000 °C to 1050 °C there is a corresponding increase in amount of N_2 adsorbed, indicating an increase in pore volume of the carbon with increasing temperature. This is confirmed in Table 6.10 which shows that CPF9 - 1050 °C possesses a higher pore volume than CPF9 - 1000 °C.

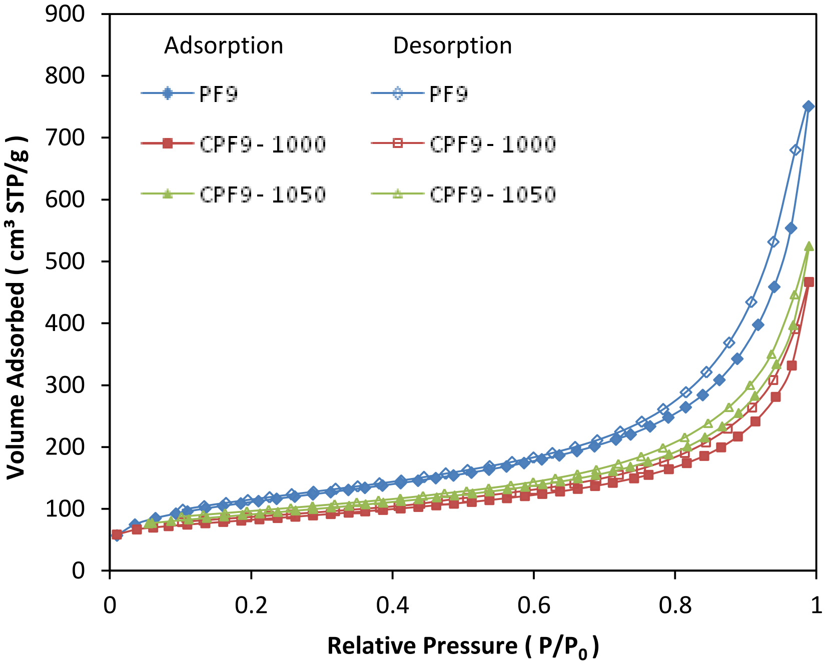

Figure 6.17: N_2 adsorption/desorption isotherms for PF9 gel and CPF9 carbons

The PSD curves for PF9 gel and CPF9 carbons are shown in Figure 6.18a. PSD curves for pore sizes in the range of 2 – 5 nm are magnified and shown in Figure

6.18b. It can be observed that all the PSD curves possess peaks in the small mesopore and large mesopore regions. There is a significant shift downwards in the large mesopore peak when moving from gel to carbon as displayed in Figure 6.18a. Whereas the differences in the peaks in the small mesopore region for all samples shown in Figure 6.18b are not as drastic. This is consistent with an overall drop in pore volume upon carbonisation of the PF gel. In the case of CPF9 -1000 ^{o}C and CPF9 – 1050 ^{o}C, there is an upward shift in the large mesopore peak with increasing temperature as shown in Figure 6.18a, and to a similar extent a downward shift in the small mesopore peak as shown in Figure 6.18b. The volumetric measurements, shown in Table 6.10, suggest that the decrease in mesopore volume associated with the downward shift in the small mesopore peak is masked by the increase in pore volume attached to the large mesopores resulting in a net increase in mesopore volume of the carbon with increasing carbonisation temperature.

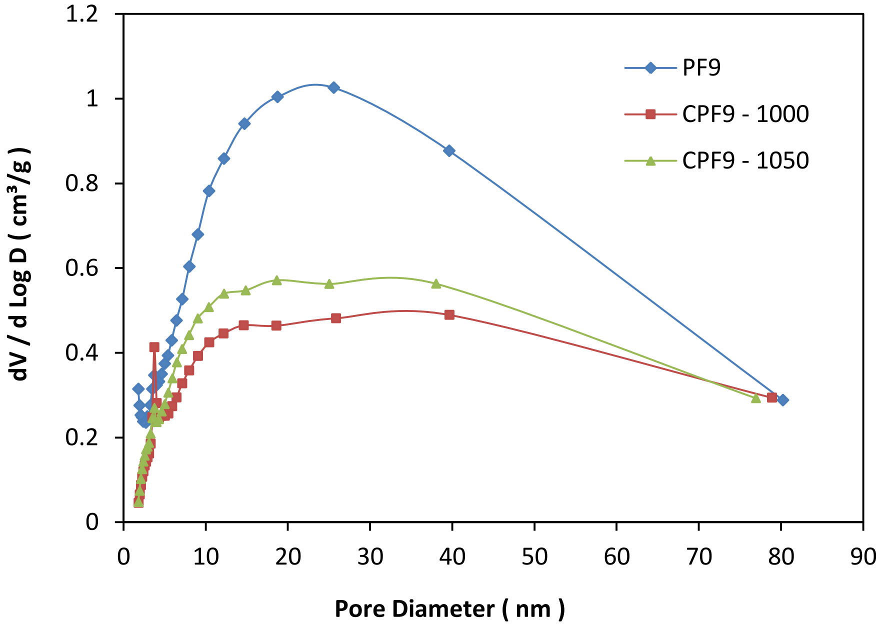

Figure 6.18a: Pore size distribution of PF9 gel and CPF9 carbons

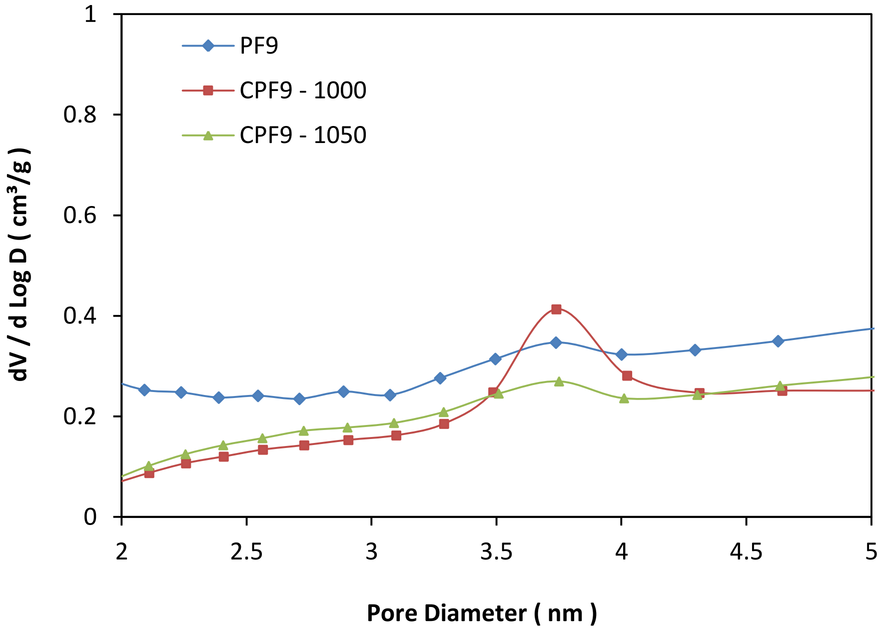

Figure 6.18b: Expanded pore size distribution curves for PF9 gel and CPF9 carbons

A generally similar trend of an increase in porosity with increasing carbonisation temperature, as was found with PF3, is observed for PF9, and is consistent with the mechanism of carbonisation, which typically involves the rearrangement of carbon atoms upon removal of volatiles, with the subsequent formation of new porosity, as well as the widening of pores by reaction of the carbon material with emitted gaseous species from carbonisation reactions. The results obtained for PF9 show that 1050 ^{o}C is the optimum carbonisation temperature for PF9 in terms of yielding the most desirable porous properties.

The TGA measurements for PF9 are shown in Figure 6.19. It can be observed that the curves exhibit somewhat similar peaks to PF3, as well as a continuous decline (although small) of the weight loss vs. temperature curve at temperatures approaching 1000 ^{o}C and beyond, indicating the continuous loss of volatile matter as discussed earlier.

***Table 6.10:** Pore characteristics of PF9 and CPF9 carbons

Sample	**S_{BET} (m^2/g)**	**ΔS_{BET} (m^2/g)**	**V_{total} (cm^3/g)**	**ΔV_{total} (cm^3/g)**	**V_{micro} (cm^3/g)**	**ΔV_{micro} (cm^3/g)**	**V_{meso} (cm^3/g)**	**ΔV_{meso} (cm^3/g)**	**% V_{micro}**	**% V_{meso}**	**D_{avg} (nm)**	**ΔD_{avg} (nm)**	**D_{peak} (nm)**
PF9	394 ± 0.8 %	Av. $S_{BET(PF9)}$ ± 2.9 %	1.1608	Av. $V_{total\ (PF9)}$ ± 5.2 %	0.0096	N/A	1.1512	Av. $V_{meso(PF9)}$ ± 5.5 %	0.83	99.17	11.4	Av. $D_{avg\ (PF9)}$ ± 7.1 %	25.6
CPF9-1000 °C	278 ± 1.0 %	$S_{BET(CPF9-1000)}$ ± 3.4 %	0.7219	$V_{total(CPF9-1000)}$ ± 5.5 %	0.0422	$V_{micro(CPF9-1000)}$ ± 7.4 %	0.6797	$V_{meso(CPF9-1000)}$ ± 5.9 %	5.85	94.15	10.4	$D_{avg\ (CPF9-1000)}$ ± 4.2 %	$15 \leq D_{peak} \leq 40$
CPF9-1050 °C	310 ± 0.9 %	Av. $S_{BET(CPF9-1050)}$ ± 3.4 %	0.8117	Av. $V_{total\ (CPF9-1050)}$ ± 5.5 %	0.0450	Av. $V_{micro(CPF9-1050)}$ ± 7.4 %	0.7667	Av. $V_{meso(CPF9-1050)}$ ± 5.9 %	5.50	94.50	10.5	Av. $D_{avg\ (CPF9-1050)}$ ± 4.2 %	$15 \leq D_{peak} \leq 40$

*All parameters are as defined in Appendix B. See caption for Table 6.5 for information about error analysis for PF9. See caption for Table 6.9 for information about error analysis of the carbons.

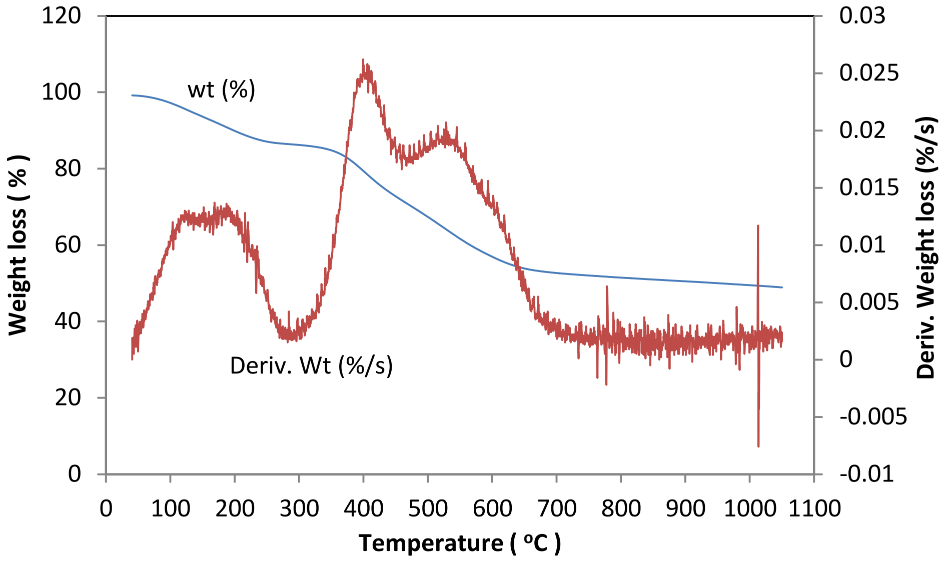

Figure 6.19: TGA measurement for PF9 under argon (wt (%) refers to the weight loss curve and Deriv. Wt (%/s) refers to the derivative weight loss curve)

The results obtained in this section show that pyrolysis of PF gels at varying temperatures produces carbons with different levels of porosity. The initial total pore volume and mesopore volumes of the gel drop slightly upon conversion to carbon. However, comparing the carbons, there is an overall increase in aforementioned pore volumes with carbonisation temperature. Furthermore, the results show that micropores contribute to approximately 5 – 10 % of the overall pore volume, indicating that the PF carbons are predominantly mesoporous. Overall, the mesopore volumes of the PF based carbons prepared, range from about 0.77 – 0.96 cm^3/g, and is slight lower than those that have been obtained for RF based carbons, where values ranging between approximately 1.0 – 1.5 cm^3/g have been obtained [111], [158]. However, as will be seen in the following sections, the activation experiments increase the mesopore volumes drastically, making the activated PF based carbons (the materials being used as electrodes), comparable with similarly activated RF based carbons, in terms of attainable mesopore volumes.

6.2.2 Effect of Activation

6.2.2.1 Effect of O_2 Activation on the Pore Structure of PF Carbon Gels

To determine the effect of fast oxidation [176] on the porous structure of carbonised PF gels, oxygen activation was carried out at different flowrates, temperatures, and varying times, corresponding to various degrees of burn off. The rate of the gasification reaction with carbon (Figure 6.20) depends on reaction temperature as well as the rate of diffusion of the reacting gas to the carbon surface [64]. The reaction itself corresponds to the removal of carbon atoms. This initially starts with the formation of surface oxygen complexes, which then desorb as CO_2, removing carbon atoms in the process, and generation pores, as shown in the overall process below,

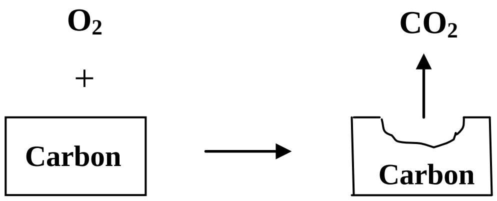

Figure 6.20: Schematic representation of the carbon-oxygen gasification reaction and pore generation [67]

The term burn-off simply refers to carbon removal, and it was calculated as follows [177]:

$$Burn\ off(\%) = \left(\frac{W_{final} - W_{inital}}{W_{inital}}\right) \times 100 \tag{6.3}$$

where W_{final} refers to the weight of the activated carbon (i.e. after treatment) and $W_{initial}$ refers to the weight of the untreated carbon. As a result, the flowrate (corresponding to the rate of diffusion of oxygen to the carbon surface), and the temperature, were varied, to allow for different rates of reactions and varying levels of burn-off. The duration of activation was also varied, to allow more time for activation and therefore increased burn-off.

Preliminary experiments were carried out on CPF9 – 1000 ^{o}C based carbons. Herein referred to as CPF9-1 and the corresponding O_2-activated as ACPF9-1-O_2/x/y, where x is the temperature (^{o}C), and y is the time in minutes. Time of activation and gas flowrate were kept constant at 20 mins and 100 ml/min, respectively. Activation temperatures of 300 ^{o}C and 450 ^{o}C were used. Figure 6.21 shows the N_2 adsorption/desorption isotherms at 77 K for the CPF9-1 and the associated O_2-activated carbons with different degrees of burn-off.

The isotherms are of type IV with hysteresis loops indicating the presence of mesopores [118]. The lower and upper parts of the hysteresis loop are representative of capillary condensation and evaporation in the mesopores of the carbon structure respectively [118]. Table 6.11 shows the porosity parameters of the carbons as well as the description of each sample that corresponds to the various degrees of burn off. Figure 6.21 shows an increase in amount of gas adsorbed with an increase in the extent of burn-off from 8 – 20 %, indicative of the development of porosity in the porous structure of the carbon. Table 6.11 shows an increase in total pore and mesopore volumes with increasing burn-off. This characteristic increase in pore volumes with increasing extent of burn-off is consistent with previous work reported on similar carbon gels [116]. The rise in pore volumes could be due to the creation of pores and widening of existing pores by selective gasification of certain structural components or by opening of previously inaccessible pores [116].

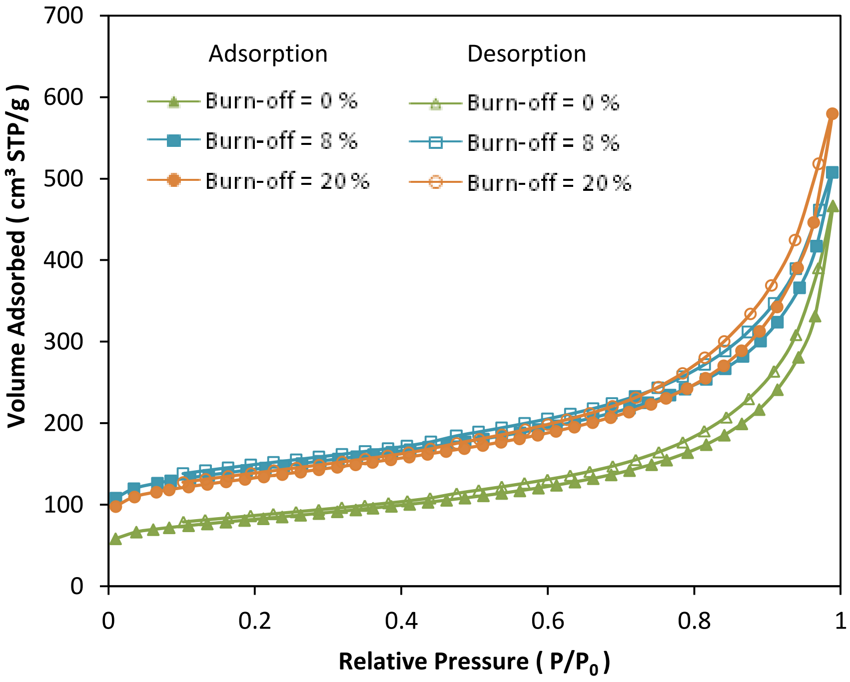

Figure 6.21: N_2 adsorption/desorption isotherms at 77K for CPF9-1 (Burn off = 0%), ACPF9-1-O_2 /300/20 (Burn-off = 8 %) and ACPF9-1-O_2/450/20 (Burn-off = 20 %).

The PSD curves of CPF9-1 and the corresponding O_2-activated carbons with different burn-offs are shown in Figure 6.22a. The PSD curves for pore diameters in the range of 2 – 5 nm are magnified and shown in Figure 6.22b. It can be seen from Figures 6.22a and b that all PSD curves possess two peaks in the small and large pore diameter regions confirming the contribution of small and large mesopores to the structure of the samples. Additionally, the volumetric measurements displayed in Table 6.11 show that the activated samples are predominantly mesoporous, with pore sizes ranging between 6.7 – 8.1 nm.

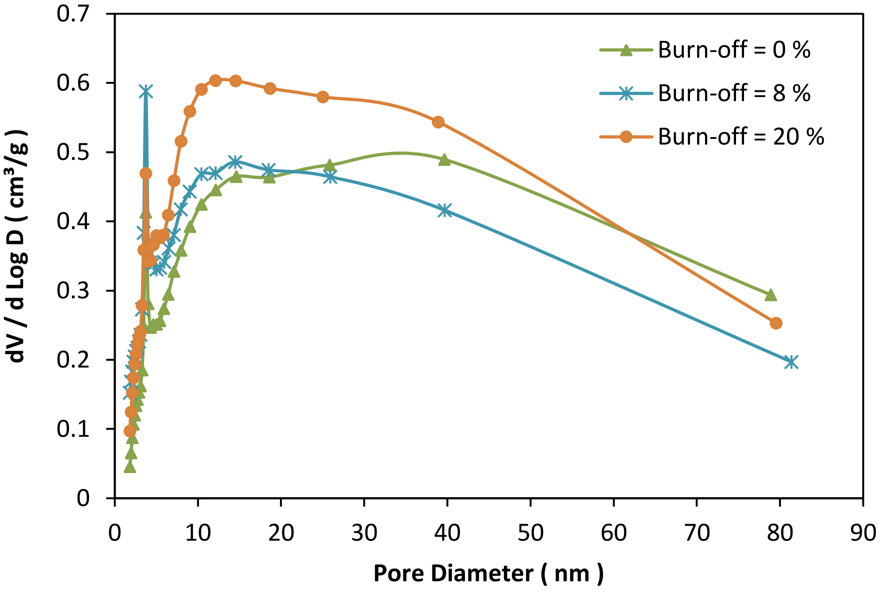

Figure 6.22a: Pore size distribution of CPF9-1 (Burn off = 0%), ACPF9-1-O_2 /300/20 (Burn-off = 8 %) and ACPF9-1-O_2/450/20 (Burn-off = 20 %).

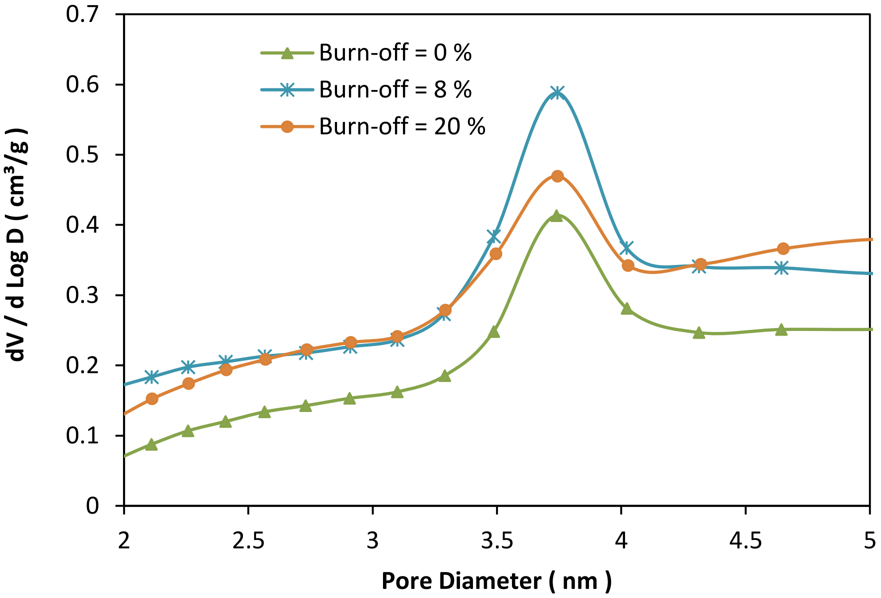

Figure 6.22b: Expanded pore size distribution curves for CPF9-1 (Burn off = 0%), ACPF9-1-O_2 /300/20 (Burn-off = 8 %) and ACPF9-1-O_2/450/20 (Burn-off = 20 %).

***Table 6.11:** Pore characteristics of CPF9-1 and ACPF9-1-O_2 based carbons

Sample	**Burn off (%)**	**S_{BET} (m^2/g)**	**ΔS_{BET} (m^2/g)**	**V_{total} (cm^3/g)**	**ΔV_{total} (cm^3/g)**	**V_{micro} (cm^3/g)**	**ΔV_{micro} (cm^3/g)**	**V_{meso} (cm^3/g)**	**ΔV_{meso} (cm^3/g)**	**% V_{micro}**	**% V_{meso}**	**D_{avg} (nm)**	**ΔD_{avg} (nm)**	D_{peak} (nm)
CPF9-1	0	278 ± 1.0 %	$S_{BET(CPF9-1)}$ ± 3.4 %	0.7219	$V_{total\ (CPF9-1)}$ ± 5.5 %	0.0422	$V_{micro\ (CPF9-1)}$ ± 7.4 %	0.6797	$V_{meso(CPF9-1)}$ ± 5.9 %	6	94	10.4	$D_{avg\ (CPF9-1)}$ ± 4.2 %	$10 \leq D_{peak} \leq 40$
ACPF9-1-O_2/300/20	8	472 ± 1.4 %	$S_{BET(ACPF9-1-O2/300/20)}$ ± 3.4 %	0.7856	$V_{total\ (ACPF9-1-O2/300/20)}$ ± 5.5 %	0.1047	$V_{micro\ (ACPF9-1-O2/300/20)}$ ± 7.4 %	0.6809	$V_{meso\ (ACPF9-1-O2/300/20)}$ ± 5.9 %	13	87	6.7	$D_{avg\ (ACPF9-1-O2/300/20)}$ ± 4.2 %	$10 \leq D_{peak} \leq 40$
ACPF9-1-O_2/450/20	20	442 ± 1.2 %	$S_{BET(ACPF9-1-O2/450/20)}$ ± 3.4 %	0.8968	$V_{total\ (ACPF9-1-O2/450/20)}$ ± 5.5 %	0.0851	$V_{micro\ (ACPF9-1-O2/450/20)}$ ± 7.4 %	0.8117	$V_{meso\ (ACPF9-1-O2/450/20)}$ ± 5.9 %	9	91	8.1	$D_{avg\ (ACPF9-1-O2/450/20)}$ ± 4.2 %	$10 \leq D_{peak} \leq 40$

*Gas flowrate was 100 ml/min. All parameters are as defined in Appendix B. See caption for Table 6.9 for information about error analysis of the carbons. These errors (i.e. for the carbons) have also been applied to the activated carbons, as the preparation of both of these materials, is furnace-based.

The next stage of experiments was carried out on the CPF9 – 1050 ^oC based carbons as they showed improved porosities based on the effect of carbonisation temperatures performed on the PF gels. However, using the information obtained from the preliminarily experiments, the aim here was to increase further, the level of porosity, than was obtained in the initial experiments. Therefore, activation was carried out for longer times at higher gas flow rates and also higher temperatures to obtain increased levels of burn-off. The starting carbon in this case is referred to as CPF9-2 (the differences in the pore structure for CPF9-1 and CPF9-2, are shown in table 6.10, as CPF9 – 1000 ^oC and CPF9 – 1050 ^oC, respectively) and corresponding O_2 activated carbons as ACPF9-2-O_2/x/y, where x is the temperature (^oC), and y is the time in minutes. Time of activation and gas flowrate were kept constant at 30 mins and ~ 370 ml/min, respectively. Activation temperatures of 300 ^oC and 500 ^oC were used.

The N_2 adsorption/desorption isotherms for CPF9-2 and the associated O_2-activated carbons are shown in Figure 6.23. Table 6.12 shows the porous characteristics of the aforementioned samples. It can be observed from Figure 6.23 that there is an initial increase in quantity of N_2 adsorbed with a burn off of 65 %. However, for higher a burn-off (84 %), there is a corresponding decrease. The initial increase as explained earlier is due to the development of porosity in the structure of the carbon, as a result of the removal of carbon atoms during gasification (Figure 6.20). The subsequent decrease could be related to the rate of oxidation of carbon by oxygen, which is known to be very fast (about 100 times faster than CO_2 for example), and exothermic [64]. Further increase in temperature to 500 ^oC, may have caused an increase in the rate of an intrinsically rapid reaction, thereby resulting in the rapid burning of the carbon sample and subsequent destruction of its porous structure.

The PSD curves for the CPF9-2 and the corresponding O_2-activated carbons are shown in Figure 6.24. All the PSD curves appear to be identical in profile, apart from their positions on the y - axis. It can be observed there is an initial upward shift of the curve from a burn off of 0 to 65 %. However, for a higher degree of burn off, there is a corresponding downward shift. Both observations are indicative of an increase and decrease in pore volumes, respectively. This is also confirmed in Table 6.12 which shows that as the burn off increases to 65 %, there is a significant increase in pore volume, which upon further increase in burn off, decreases drastically.

These experiments show that O_2 activation is a good method for increasing the mesoporosity of PF carbons. However, experimental conditions such as temperature, gas flowrate and time should be adjusted accordingly. For the CPF9-2 carbon, a substantial increase in pore volume from ~ 0.81 to 1.24 cm^3/g upon O_2-activation was observed.

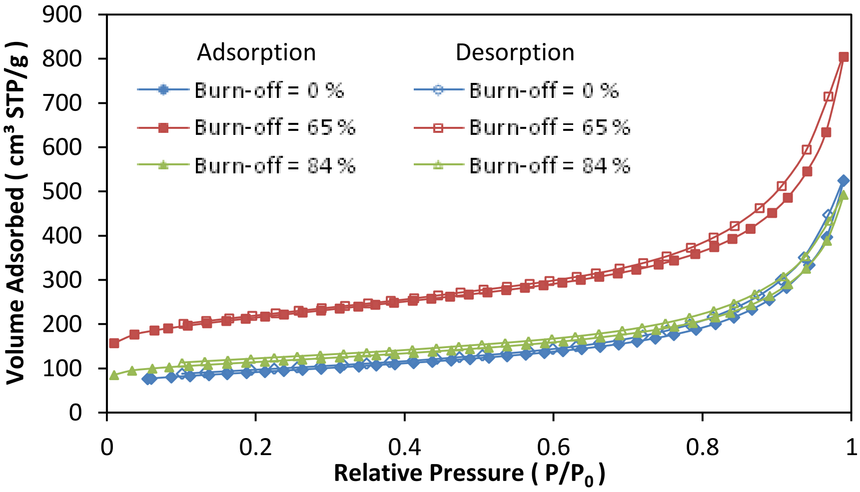

Figure 6.23: N_2 adsorption/desorption isotherms at 77K for CPF9-2 (Burn-off = 0%), ACPF9-2-O_2/300/30 (Burn-off = 65%) and ACPF9-2-O_2/500/30 (Burn-off = 84%)

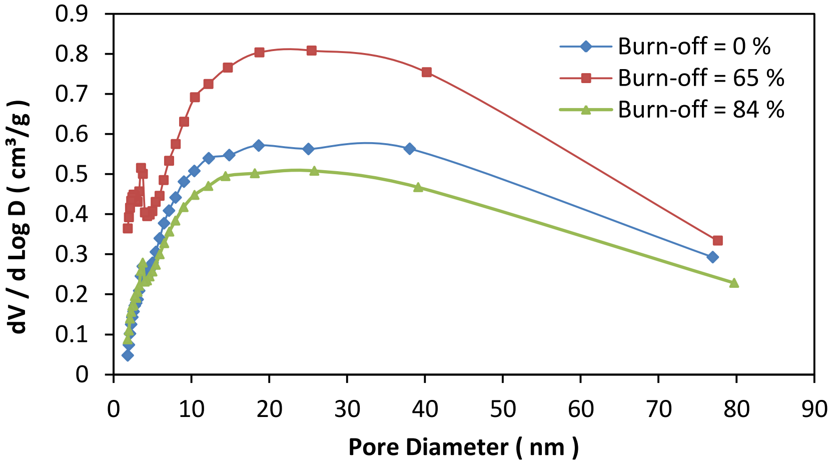

Figure 6.24: Pore size distribution of CFP9-2 (Burn-off = 0%), ACPF9-2-O_2/300/30 (Burn-off = 65%) and ACPF9-2-O_2/500/30 (Burn-off = 84%) carbons

***Table 6.12:** Pore characteristics of CPF9-2 and ACPF9-2-O_2 based carbons

Sample	**Burn off (%)**	**S_{BET} (m^2/g)**	**ΔS_{BET} (m^2/g)**	**V_{total} (cm^3/g)**	**ΔV_{total} (cm^3/g)**	**V_{micro} (cm^3/g)**	**ΔV_{micro} (cm^3/g)**	**V_{meso} (cm^3/g)**	**ΔV_{meso} (cm^3/g)**	**% V_{micro}**	**% V_{meso}**	**D_{avg} (nm)**	**ΔD_{avg} (nm)**	D_{peak} (nm)
CPF9-2	0	310 ± 0.9 %	Av. $S_{BET(CPF9-2)}$ ± 3.4 %	0.8117	Av. $V_{total\ (CPF9-2)}$ ± 5.5 %	0.0450	Av. $V_{micro\ (CPF9-2)}$ ± 7.4 %	0.7667	Av. $V_{meso(CPF9-2)}$ ± 5.9 %	5.50	94.50	10.5	Av. $D_{avg\ (CPF9-2)}$ ± 4.2 %	20≤ D_{peak} ≤40
ACPF9-2-O_2/300/30	65	715 ± 1.3 %	$S_{BET(ACPF9-2-O2/300/30)}$ ± 3.4 %	1.2444	$V_{total\ (ACPF9-2-O2/300/30)}$ ± 5.5 %	0.1376	$V_{micro\ (ACPF9-2-O2/300/30)}$ ± 7.4 %	1.1068	$V_{meso\ (ACPF9-2-O2/300/30)}$ ± 5.9 %	11.06	88.94	7.0	$D_{avg\ (ACPF9-2-O2/300/30)}$ ± 4.2 %	20≤ D_{peak} ≤40
ACPF9-2-O_2/500/30	84	377± 1.3 %	$S_{BET(ACPF9-2-O2/500/30)}$ ± 3.4 %	0.7619	$V_{total\ (ACPF9-2-O2/500/30)}$ ± 5.5 %	0.0799	$V_{micro\ (ACPF9-2-O2/500/30)}$ ± 7.4 %	0.6820	$V_{meso\ (ACPF9-2-O2/500/30)}$ ± 5.9 %	10	90	8.1	$D_{avg\ (ACPF9-2-O2/500/30)}$ ± 4.2 %	20≤ D_{peak} ≤40

*Gas flowrate was ~ 370 ml/min. All parameters are as defined in Appendix B. See caption for Table 6.11 for information about error analysis.

6.2.2.2 Effect of CO_2 Activation on the Pore Structure of PF Carbon Gels

To investigate the effect of a mild oxidation procedure [176] on the porous structure of carbons, they were subject to gasification with CO_2: the experimental conditions of which, shall be explained shortly. Firstly, the term ‘mild oxidation’ has been used here as a way of distinguishing between the reaction of oxygen with carbon, which is about a 100 times faster than that with CO_2 [64]. However, the general mode of removal of carbon atoms (burn off), by the reaction of the oxidising gas with the carbon surface, follows a similar format to that in Figure 6.20, but with the evolution of CO instead of CO_2.

CO_2 activation was carried out at a fixed temperature of 800 °C and flowrate of 200 ml/min for varying times. For these experiments, the CPF9-1050°C was used and is referred to as CPF9-2 and the corresponding CO_2 activated carbons as ACPF9-2-CO_2/x/y, where x is the temperature (°C) and y represents duration of activation in minutes (similar naming format to the O_2 activated samples). Figure 6.25 shows the N_2 adsorption/desorption isotherms at 77 K for CPF9-2 and ACPF9-2-CO_2 based carbons with different degrees of burn-off. There is a steady increase in the amount of gas adsorbed with increasing burn-off even at high extents of burn-off, and this is suggestive of the development of porosity in the carbon structure.

The porous characteristics of the samples as well as sample names that correspond to the various degrees of burn off are shown in Table 6.13. Table 6.13 shows that there is an increase in total pore and mesopore volumes with increasing burn off. This shows that longer periods of gasification under CO_2 at fixed temperature leads to further porosity development resulting in larger pore volumes.

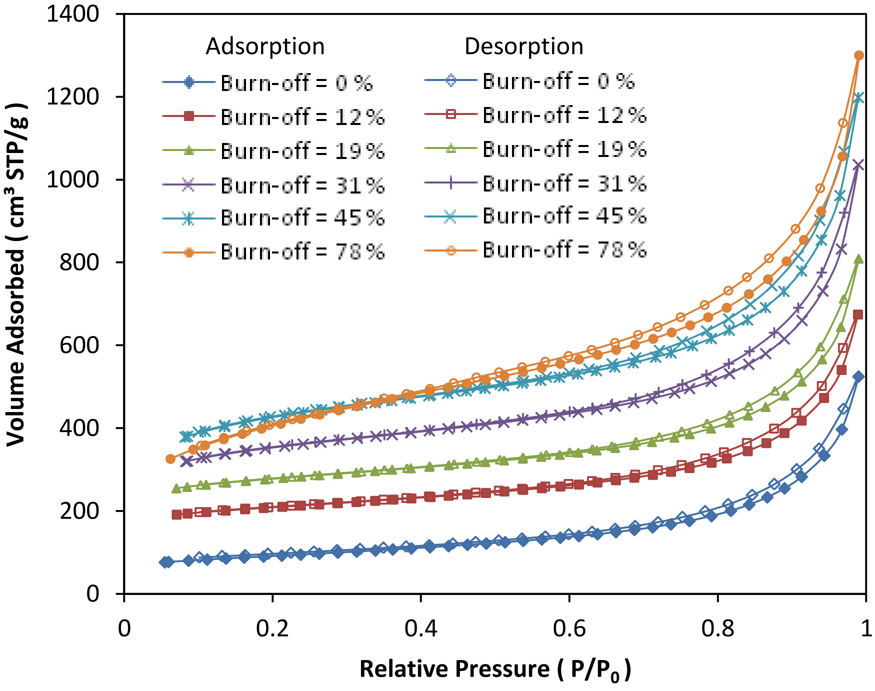

Figure 6.25: N_2 adsorption/desorption isotherms at 77K for CPF9-2 and ACPF9-2-CO_2 based carbons (the description of the activation conditions under CO_2 resulting in the various degrees of burn-off is shown in Table 6.13)

The effect of activation induced porosity can also be seen in the SEM images of the unactivated carbon (CPF) and the activated carbon ACPF9-2-CO_2/800/120, in Figure 6.26a and Figure 6.26b, respectively. The network structure of both samples is evident: however, the surface topography depicted in Figure 6.26b, for the activated sample, appears to reveal a more porous network. This is consistent with the increase in pore volume determined by the nitrogen adsorption/desorption method.

Figure 6.27a shows the PSD curves for CPF9-2 and ACPF9-2-CO_2 based carbons with different degrees of burn-off. The PSD curves for pore diameter in the range of 2 – 5 nm, are magnified and shown in clearly in Figure 6.27b. All PSD curves are identical but with a steady shift upwards on the y - axis both in the small and large pore diameter regions, consistent with an increase in the pore volumes of the carbons with increasing burn-off. The results of the volumetric measurements displayed in Table 6.13 also show that CO_2-activated carbons are predominantly mesoporous. CO_2 activation appears to have a somewhat similar effect on porosity as O_2

activation (Section 6.2.2.1). However, there appears to be a greater volume of micropores generated in the former. This is consistent with similar work carried out by Suuberg *et al*. [178], comparing O_2 and CO_2 activated tyre - derived carbons. Furthermore, a continuous increase in pore volume is observed at higher extents of burn off for the CO_2 activated samples. This shall be explained in the following discussion.

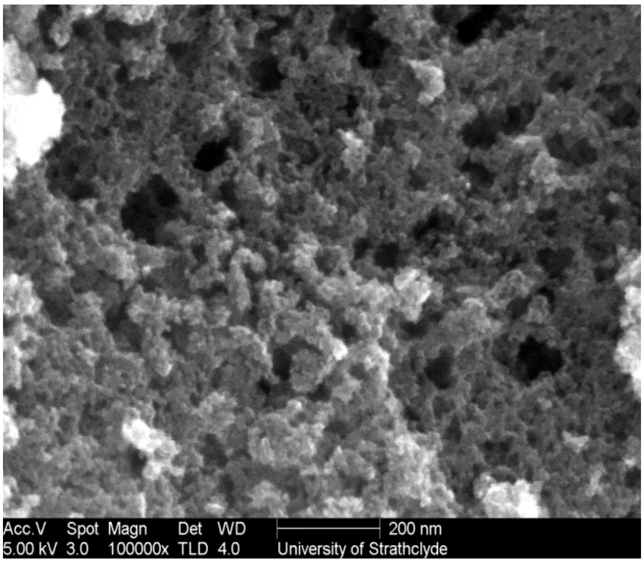

Figure 6.26a: SEM image of CPF9

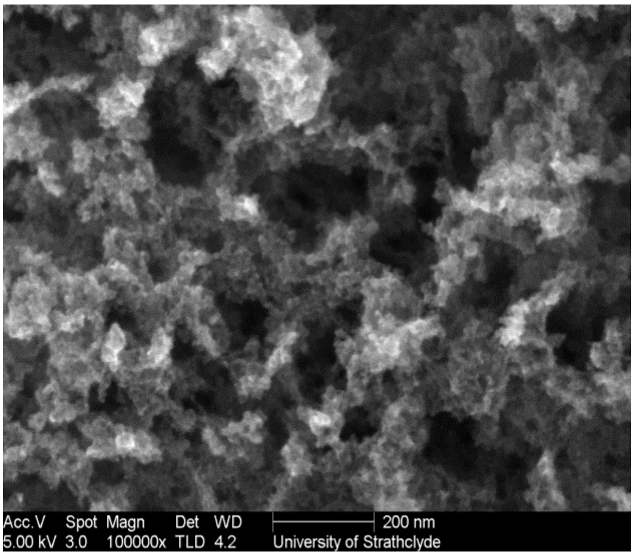

Figure 6.26b: SEM image of ACPF9-2-CO_2/800/120

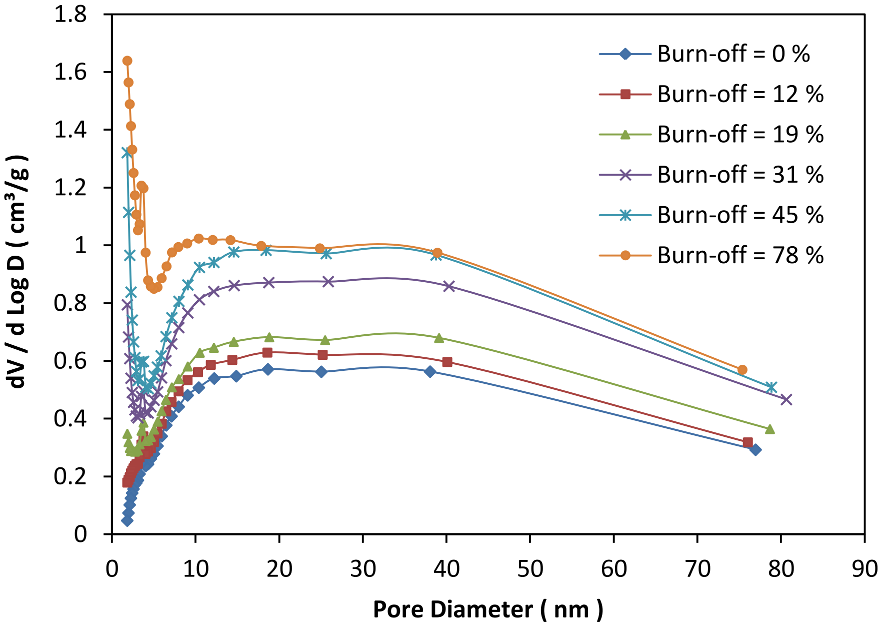

Figure 6.27a: Pore size distribution of CFP9-2 and ACPF9-2-CO_2 based carbons (the description of the activation conditions under CO_2 resulting in the various degrees of burn-off is shown in Table 6.13)

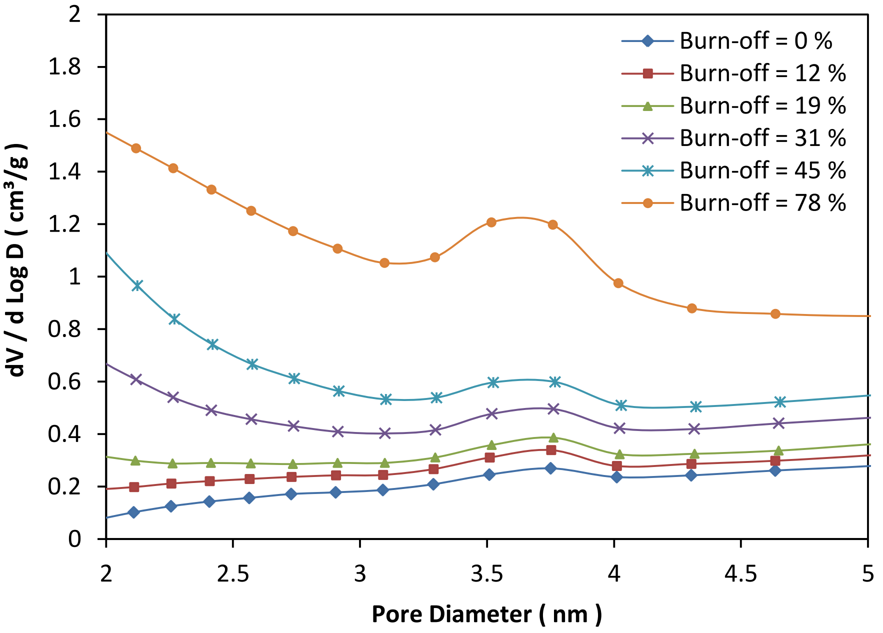

Figure 6.27b: Expanded pore size distribution curves of CFP9-2 and ACPF9-2-CO_2 based carbons (the description of the activation conditions under CO_2 resulting in the various degrees of burn-off is shown in Table 6.13)

***Table 6.13:** Pore characteristics of CPF9-2 and ACPF9-2-CO_2 based carbons

Sample	**Burn off (%)**	**S_{BET} (m^2/g)**	**ΔS_{BET} (m^2/g)**	**V_{total} (cm^3/g)**	**ΔV_{total} (cm^3/g)**	**V_{micro} (cm^3/g)**	**ΔV_{micro} (cm^3/g)**	**V_{meso} (cm^3/g)**	**ΔV_{meso} (cm^3/g)**	**% V_{micro}**	**% V_{meso}**	**D_{avg} (nm)**	**ΔD_{avg} (nm)**	D_{peak} (nm)
CPF9-2	0	310 ± 0.9 %	Av. $S_{BET(CPF9-2)}$ ± 3.4 %	0.8117	Av. $V_{total\ (CPF9-2)}$ ± 5.5 %	0.0450	Av. $V_{micro\ (CPF9-2)}$ ± 7.4 %	0.7667	Av. $V_{meso(CPF9-2)}$ ± 5.9 %	5.50	94.50	10.5	Av. $D_{avg\ (CPF9-2)}$ ± 4.2 %	10≤ D_{peak} ≤40
ACPF9-2-CO_2/800/15	12	668 ± 1.8 %	$S_{BET(ACPF9-2-CO2/800/15)}$ ± 3.4 %	1.0434	$V_{total\ (ACPF9-2-CO2/800/15)}$ ± 5.5 %	0.2000	$V_{micro\ (ACPF9-2-CO2/800/15)}$ ± 7.4 %	0.8434	$V_{meso\ (ACPF9-2-CO2/800/15)}$ ± 5.9 %	19	81	6.3	$D_{avg\ (ACPF9-2-CO2/800/15)}$ ± 4.2 %	10≤ D_{peak} ≤40
ACPF9-2-CO_2/800/30	19	884 ± 1.9 %	$S_{BET(ACPF9-2-CO2/800/30)}$ ± 3.4 %	1.2519	$V_{total\ (ACPF9-2-CO2/800/30)}$ ± 5.5 %	0.2761	$V_{micro\ (ACPF9-2-CO2/800/30)}$ ± 7.4 %	0.9758	$V_{meso\ (ACPF9-2-CO2/800/30)}$ ± 5.9 %	22	78	5.7	$D_{avg\ (ACPF9-2-CO2/800/30)}$ ± 4.2 %	10≤ D_{peak} ≤40
ACPF9-2-CO_2/800/60	31	1133 ± 1.8 %	$S_{BET(ACPF9-2-CO2/800/60)}$ ± 3.4 %	1.6031	$V_{total\ (ACPF9-2-CO2/800/60)}$ ± 5.5 %	0.2960	$V_{micro\ (ACPF9-2-CO2/800/60)}$ ± 7.4 %	1.3071	$V_{meso(ACPF9-2-CO2/800/60)}$ ± 5.9 %	18	82	5.7	$D_{avg\ (ACPF9-2-CO2/800/60)}$ ± 4.2 %	10≤ D_{peak} ≤40
ACPF9-2-CO_2/800/90	45	1383 ± 1.8 %	$S_{BET(ACPF9-2-CO2/800/90)}$ ± 3.4 %	1.8537	$V_{total\ (ACPF9-2-CO2/800/90)}$ ± 5.5 %	0.3106	$V_{micro\ (ACPF9-2-CO2/800/90)}$ ± 7.4 %	1.5431	$V_{meso\ (ACPF9-2-CO2/800/90)}$ ± 5.9 %	17	83	5.4	$D_{avg\ (ACPF9-2-CO2/800/90)}$ ± 4.2 %	10≤ D_{peak} ≤40
ACPF9-2-CO_2/800/120	78	1382 ± 1.2 %	$S_{BET(ACPF9-2-O2/800/120)}$ ± 3.4 %	2.0112	$V_{total\ (ACPF9-2-O2/800/120)}$ ± 5.5 %	0.1395	$V_{micro\ (ACPF9-2-O2/800/120)}$ ± 7.4 %	1.8717	$V_{meso\ (ACPF9-2-O2/800/120)}$ ± 5.9 %	7	93	5.8	$D_{avg\ (ACPF9-2-O2/800/120)}$ ± 4.2 %	10≤ D_{peak} ≤40

*Gas flowrate was 200 ml/min. All parameters are as defined in Appendix B. See caption for Table 6.11 for information about error analysis.

An important difference between the O_2 and CO_2 activation procedures is found in the methods by which increasing burn-off was obtained. In the case of O_2 activation, the carbon samples were subject to an increase in temperature, which not only increased the rate of an intrinsically rapid and exothermic carbon-O_2 reaction, but also led to the accelerated burning and subsequent destruction of the carbon structure. On the other hand, increasing burn-off for the CO_2 activation process, was obtained simply by increasing the duration of activation, and maintaining a fixed temperature for each activation experiment (therefore, keeping the rate of reaction constant): the effect of which, was to allow more time for activation and, therefore, pore formation. This, coupled with a lower flowrate of 200 ml/min for CO_2, in comparison to ~ 370 ml/min for O_2 (indicative of a lower gas diffusion rate), in addition to the intrinsically slower rate of the carbon-CO_2 reaction, in comparison to the carbon-O_2 reaction, allowed for a progressive increase in the porosity of the CO_2 activated samples, even at high extents of burn off. The sample ACPF9-2-CO_2/800/120 possesses the highest total pore and mesopore volumes of ~ 2.01 cm^3/g and 1.87 cm^3/g respectively of all O_2 and CO_2 activated carbons. These also represent the highest pore volumes obtained in this work.

6.3 Fourier Transform Infrared (FTIR) Analysis

Figure 6.28 shows the transmittance IR spectrum for PF9, CPF9, O_2 and CO_2 activated PF carbons. The drastic difference between the peaks in the PF gel spectrum and the carbonised materials is due to the effect of carbonisation, namely, increasing of carbon content at the expense of heteroatoms, such as oxygen and hydrogen, as shall be explain shortly. In relation to the PF gel spectrum, the peaks at 2927 and 2858 correspond to methylene C-H stretching vibrations [179], while the peak at 1483 cm^{-1} can be associated with methylene C-H bending vibrations [77]. This is consistent with the structure of the PF gels (Figure 4.1), which contains methylene bridges linking the phenol molecules. The peaks at 1607 and 3404 cm^{-1} can be linked to aromatic ring (C=C-C) and O-H stretching vibrations respectively [139], [179]. Furthermore, the peaks at 1225 and 1148 cm^{-1} are due to aromatic C-H bending and methylene ether C-O stretching vibrations respectively, while the peak at 1074 cm^{-1} is due to the C-O stretch of the $–CH_2OH$ group. These signals agree well with the PF gel structure depicted in Figure 4.1.

The IR spectra for both carbonised and activated samples, reveal only one peak in the region of approximately 1580 – 1600 cm^{-1}, which corresponds to the presence of carbonyl groups (C=O) in their structures. All other peaks, such as those associated with the methylene and methylene ether bridges associated with the PF gel, do not show up on the spectra for the carbonised and activated samples. In the case of the carbonised sample, CPF9, this is consistent with carbonisation reactions involving the cleavage of the C-O and C-H bonds, and the corresponding disappearance of the associated methylene and methylene ether linkages: an occurrence which is also preserved in the activated carbon samples [110].

In order to investigate the effect of activation on the concentration of surface oxygen groups, the transmittance spectra were converted into absorbance spectra (Figure 6.29). The areas under each of the peaks in Figure 6.29 were obtained using the peak area function of the FTIR equipment. Since the peak areas are linearly proportional to the concentration for the analysed functional group, they are good indicators of concentration and can be used for comparison. The peak areas for both O_2 and CO_2 activated samples ranged between 1.2 – 1.8 AU (absorbance units), while the peak area for the carbonised material, CPF9, was approximately 0.6 AU. This suggests an increase in the concentration of carbonyl groups upon activation, which is greater than twice the concentration in the original unactivated carbon sample.

The origin of the oxygen containing species on the activated carbons can be found in the activation process itself. The same reactions that lead to the formation of gaseous products, also lead to the formation of surface oxygen complexes: the thermal stabilities of which are associated with different environments within the carbon surface [64]. It is this introduction of surface oxygen species that resulted in increased peak areas of the activated samples in comparison the unactivated carbon. The peaks areas and, therefore, concentration of surface oxygen groups in the O_2 and CO_2 activated carbons did not differ significantly, with values ranging between 1.2 – 1.8 AU.

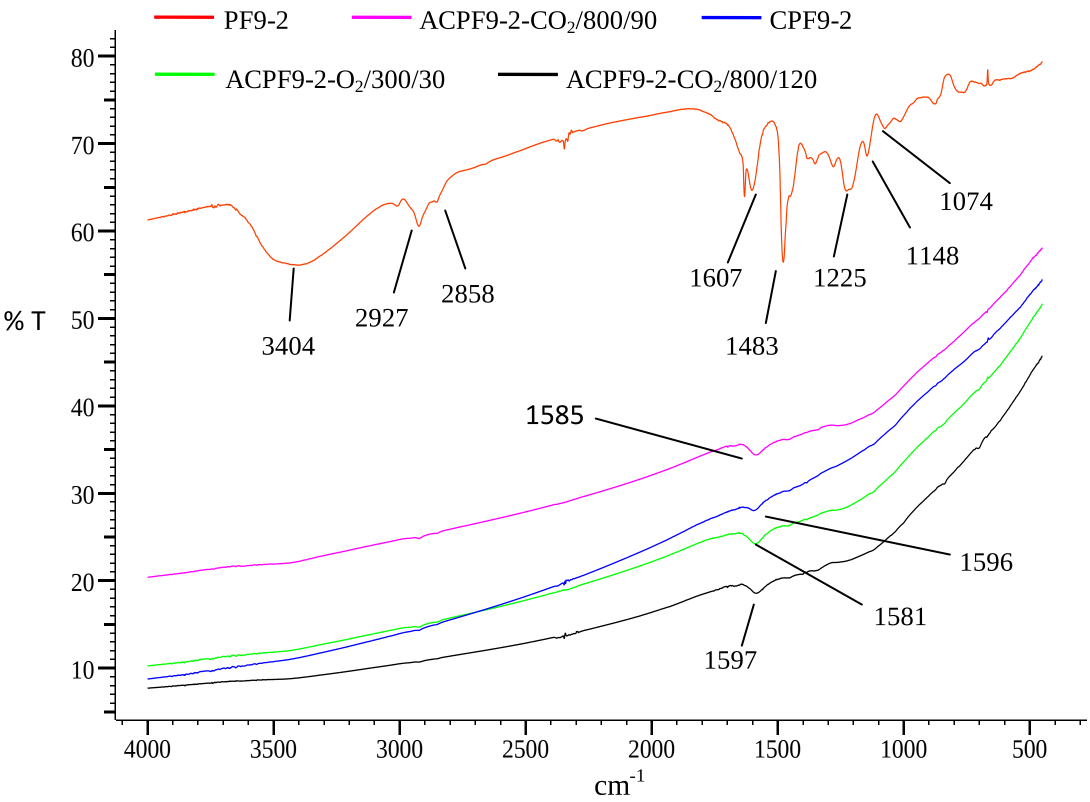

Figure 6.28: Transmittance IR spectra for PF9, CPF9, O_2 and CO_2 activated carbons

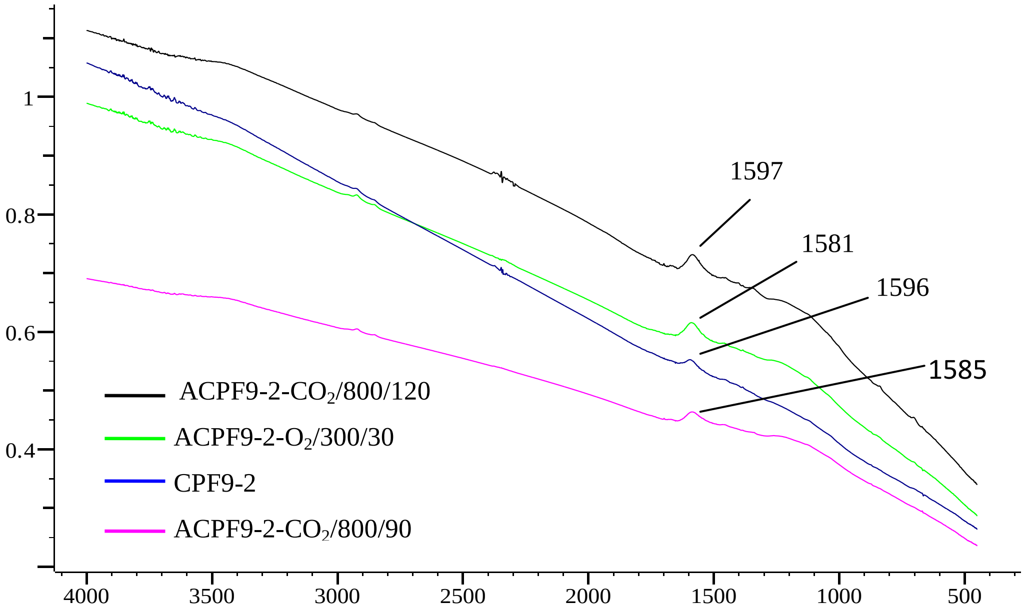

Figure 6.29: Absorbance IR spectra CPF9, O_2 and CO_2 activated carbons (used for comparing the concentrations of surface functional groups)

6.4 Electrochemical Performance

In this section the effect of porous properties, of both O_2 and CO_2 activated carbon electrodes, on the electrochemical performance of the Li/O_2 cells was investigated. The power capability of these batteries was studied by varying the cell discharge rates. All discharge capacities are based on the first discharge/charge cycle of the Li/O_2 cells. The number of cycles quoted in this section, are based on a cut-off discharge capacity of 50 mAh/g i.e. only the cycles that produce a discharge capacity of above 50 mAh/g are counted.

6.4.1 Galvanostatic Measurements

6.4.1.1 Electrochemical Performance of CO_2 Activated Carbons

Figure 6.30 shows the discharge behaviour of Li/O_2 cells using CO_2–activated PF carbon based electrodes with different pore volumes. It shows that the working cell voltage varies between approximately 2.5 – 2.7 V and corresponds well to previous reports published on similar cells discharged in O_2 at atmospheric pressure, involving the formation of Li_2O_2 as discharge product [42], [31]. It can be observed that the initial open circuit voltage is roughly in the range of 3.3 - 3.5 V and is higher than the theoretical potential (2.96 V) based on the thermodynamics of the reaction of Li and O_2 to form Li_2O_2. This is likely due to a mixed potential effect associated with reaction of Li ions with impurities in the electrolyte as well as with the catalyst EMD [12]. Additionally, the cell working voltage is lower than the theoretical standard cell potential by an amount referred to as the discharge overpotential. As the anode reaction involving the dissolution of Li metal into solution to form Li ions is known to be very fast, the observed discharge overpotential is probably the result of a kinetic activation barrier involved in the oxygen reduction process at the cathode [12]. Another contribution could be a result of ohmic polarisation, which refers to resistive losses from various parts of the cell, such as the electrolyte, separator and current collector. Furthermore, since lithium ions travel to the active regions of the cathode from the bulk electrolyte, an electrode with a sufficiently large average pore size would be required to allow quick penetration of the lithium ions into the porous cathode. Therefore, it is likely that a further contribution to the observed drop in voltage could be related to electrode porosity.

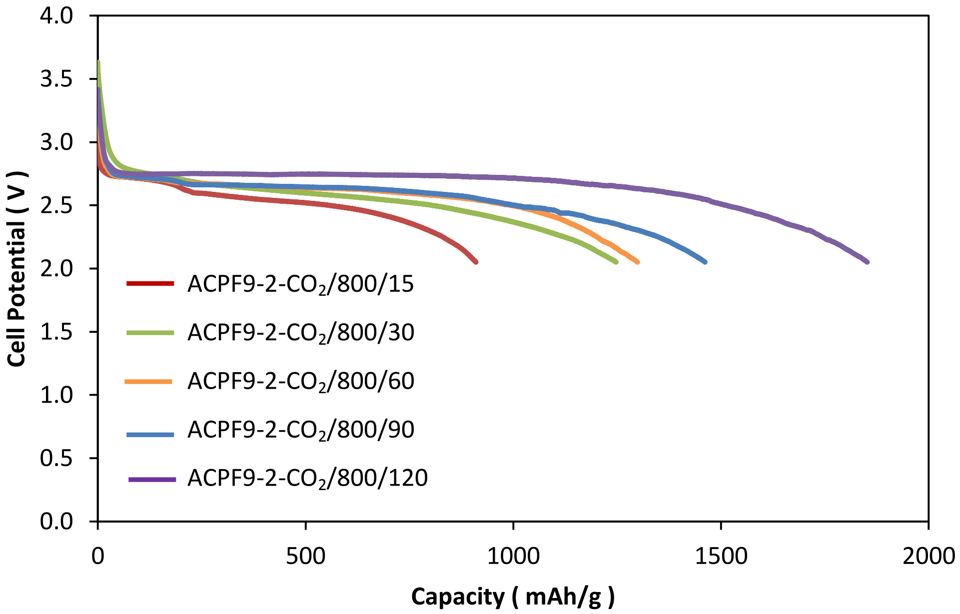

Figure 6.30: Discharge Capacities of CO_2 – activated carbons at 70 mA/g

Table 6.14 shows a correlation between the porous characteristics of the CO_2-activated carbons and the corresponding electrochemical performance of Li/O_2 cells based on electrodes derived from these carbons. Figure 6.30 and Table 6.14 show that the discharge capacity of the cells shows an increase with increasing mesopore volume, with the highest mesopore volume showing the highest storage capacity of 1852 mAh/g. This is likely due to the increase in storage space available for the discharge product Li_2O_2 [42]. The discharge process is thought to cease when the pores are choked with discharge product and, therefore, the relatively lower discharge capacities associated with samples of lower pore volumes are due to a reduced amount of available space for storage of discharge product.

***Table 6.14:** Discharge capacities of CO_2 – activated carbons with various porous characteristics at 70 mA/g

Sample	**V_{total} (cm^3/g)**	**ΔV_{total} (cm^3/g)**	**V_{micro} (cm^3/g)**	**ΔV_{micro} (cm^3/g)**	**V_{meso} (cm^3/g)**	**ΔV_{meso} (cm^3/g)**	**% V_{micro}**	**% V_{meso}**	**D_{avg} (nm)**	**ΔD_{avg} (nm)**	**D_{peak} (nm)**	**DC (mAh/g)**	**ΔDC (mAh/g)**	**CN**	**ΔCN**
ACPF9-2-CO_2/800/15	1.0434	$V_{\text{total (ACPF9-2-CO2/800/15)}}$ ± 5.5 %	0.2000	$V_{\text{micro (ACPF9-2-CO2/800/15)}}$ ± 7.4 %	0.8434	$V_{\text{meso (ACPF9-2-CO2/800/15)}}$ ± 5.9 %	19	81	6.3	$D_{\text{avg (ACPF9-2-CO2/800/15)}}$ ± 4.2 %	$10 \leq D_{peak} \leq 40$	910	$DC_{\text{(ACPF9-2-CO2/800/15)}}$ ± 4.2 %	5	$CN_{\text{(ACPF9-2-CO2/800/15)}}$ ± 1
ACPF9-2-CO_2/800/30	1.2519	$V_{\text{total (ACPF9-2-CO2/800/30)}}$ ± 5.5 %	0.2761	$V_{\text{micro (ACPF9-2-CO2/800/30)}}$ ± 7.4 %	0.9758	$V_{\text{meso (ACPF9-2-CO2/800/30)}}$ ± 5.9 %	22	78	5.7	$D_{\text{avg (ACPF9-2-CO2/800/30)}}$ ± 4.2 %	$10 \leq D_{peak} \leq 40$	1247	$DC_{\text{(ACPF9-2-CO2/800/30)}}$ ± 4.2 %	4	$CN_{\text{(ACPF9-2-CO2/800/30)}}$ ± 1
ACPF9-2-CO_2/800/60	1.6031	$V_{\text{total (ACPF9-2-CO2/800/60)}}$ ± 5.5 %	0.2960	$V_{\text{micro (ACPF9-2-CO2/800/60)}}$ ± 7.4 %	1.3071	$V_{\text{meso(ACPF9-2-CO2/800/60)}}$ ± 5.9 %	18	82	5.7	$D_{\text{avg (ACPF9-2-CO2/800/60)}}$ ± 4.2 %	$10 \leq D_{peak} \leq 40$	1299	$DC_{\text{(ACPF9-2-CO2/800/60)}}$ ± 4.2 %	2	$CN_{\text{(ACPF9-2-CO2/800/60)}}$ ± 1
ACPF9-2-CO_2/800/90	1.8537	$V_{\text{total (ACPF9-2-CO2/800/90)}}$ ± 5.5 %	0.3106	$V_{\text{micro (ACPF9-2-CO2/800/90)}}$ ± 7.4 %	1.5431	$V_{\text{meso (ACPF9-2-CO2/800/90)}}$ ± 5.9 %	17	83	5.4	$D_{\text{avg (ACPF9-2-CO2/800/90)}}$ ± 4.2 %	$10 \leq D_{peak} \leq 40$	1461	$DC_{\text{(ACPF9-2-CO2/800/90)}}$ ± 4.2 %	3	$CN_{\text{(ACPF9-2-CO2/800/90)}}$ ± 1
ACPF9-2-CO_2/800/120	2.0112	$V_{\text{total (ACPF9-2-O2/800/120)}}$ ± 5.5 %	0.1395	$V_{\text{micro (ACPF9-2-O2/800/120)}}$ ± 7.4 %	1.8717	$V_{\text{meso (ACPF9-2-O2/800/120)}}$ ± 5.9 %	7	93	5.8	$D_{\text{avg (ACPF9-2-O2/800/120)}}$ ± 4.2 %	$10 \leq D_{peak} \leq 40$	1852	Av. $DC_{\text{(ACPF9-2-CO2/800/90)}}$ ± 4.2 %	3	Av. $CN_{\text{(ACPF9-2-CO2/800/90)}}$ ± 1

*All parameters are as defined in Appendix B. See caption for Table 6.11 for information about error analysis associated with the column headings ΔV_{total}, ΔV_{micro}, ΔV_{meso}, and $\Delta D_{avg.}$. The errors associated with the column headings, ΔDC, and ΔCN, refer to reproducibility errors calculated using the average deviation method [155]. The average, Av., associated with the aforementioned columns, is based on the preparation of three electrodes using the ACPF9-2-CO_2/800/120, and performing electrochemical measurements (at 70 mA/g) on all three. It is assumed that the deviation from the average of measured parameters would be similar for other activated carbon based electrodes.

Although there is also an increase in micropore volume between ACPF9-2-CO_2/800/15 to ACPF9-2-CO_2/800/90, it is unlikely that these micropore volumes play any significant role in the observed increase in discharge capacity as such pores are easily blocked with discharge product [95].

The variation of discharge capacity and pore size in Table 6.14 does not seem to show any particular trend. A more thorough investigation on relationship between pore size and capacity is included in Section 6.4.1.5. Furthermore, it can be observed, from Table 6.14, that the cycle life of the Li/O_2 cells is quite low, with the highest being 5 cycles. This is representative of capacity fade upon cycling: a topic which will also be further discussed in section 6.4.1.4.

6.4.1.2 Electrochemical Performance of O_2 Activated Carbons

Electrochemical tests were also performed on the ACPF9-2-O_2 carbon based electrodes. Figure 6.31 shows the discharge capacities for Li/O_2 cells using O_2–activated PF carbon based electrodes. Table 6.15 shows the variation of porosity parameters with electrochemical performance. The cycling behaviour of these cells is similar to those based on the CO_2–activated PF carbons discussed in Section 6.4.1.1.

Figure 6.31 and Table 6.15 also show that the discharge capacities increase with increasing mesopore volume, further demonstrating the significant influence of mesopore volume on the electrochemical performance of Li/O_2 cells.

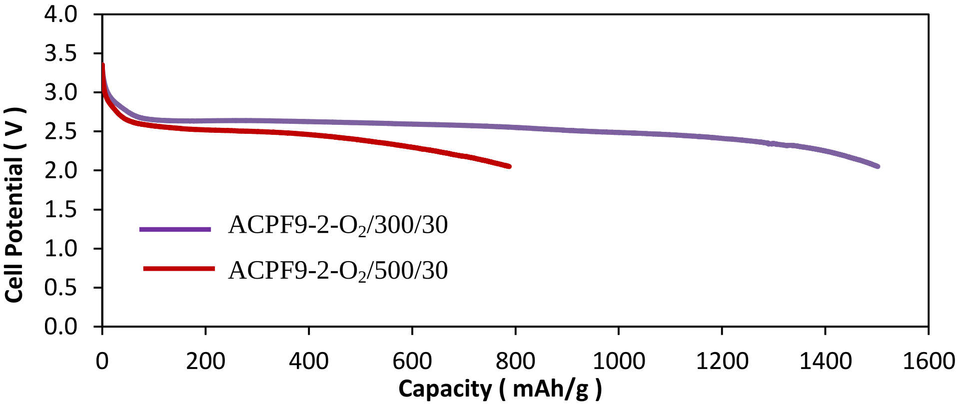

Figure 6.31: Discharge Capacities of ACPF9-2-O_2 based carbons at 70 mA/g

***Table 6.15:** Discharge capacities of ACPF9-2-O_2 based carbons with various porous characteristics at 70 mA/g

Sample	**V_{total} (cm^3/g)**	**ΔV_{total} (cm^3/g)**	**V_{micro} (cm^3/g)**	**ΔV_{micro} (cm^3/g)**	**V_{meso} (cm^3/g)**	**ΔV_{meso} (cm^3/g)**	**% V_{micro}**	**% V_{meso}**	**D_{avg} (nm)**	**ΔD_{avg} (nm)**	D_{peak} (nm)	**DC (mAh/g)**	**ΔDC (mAh/g)**	**CN**	**ΔCN**
ACPF9-2-O_2/300/30	1.2443	$V_{total\ (ACPF9-2-O2/300/30)}$ ± 5.5 %	0.1376	$V_{micro\ (ACPF9-2-O2/300/30)}$ ± 7.4 %	1.1064	$V_{meso\ (ACPF9-2-O2/300/30)}$ ± 5.9 %	11	89	7.0	$D_{avg\ (ACPF9-2-O2/300/30)}$ ± 4.2 %	$20 \leq D_{peak} \leq 40$	1502	$DC_{(ACPF9-2-O2/300/30)}$ ± 4.2 %	3	$CN_{(ACPF9-2-O2/300/30)}$ ± 1
ACPF9-2-O_2/500/30	0.7619	$V_{total\ (ACPF9-2-O2/500/30)}$ ± 5.5 %	0.0799	$V_{micro\ (ACPF9-2-O2/500/30)}$ ± 7.4 %	0.6820	$V_{meso\ (ACPF9-2-O2/500/30)}$ ± 5.9 %	10	90	8.1	$D_{avg\ (ACPF9-2-O2/500/30)}$ ± 4.2 %	$20 \leq D_{peak} \leq 40$	788	$DC_{(ACPF9-2-O2/500/30)}$ ± 4.2 %	5	$CN_{(ACPF9-2-O2/500/30)}$ ± 1

*All parameters are as defined in Appendix B. See caption for Table 6.14 for information about error analysis.

In addition to the above experiments, ACPF9-1-O_2 based carbons were also subject to galvanostatic measurements to examine their discharge performance. The results, which are displayed in Figure 6.32 and Table 6.16, are consistent with the aforementioned variation of discharge capacity with mesopore volume.

Comparing the electrochemical performance of all the activated carbon based electrodes, in the previous section including the present one, the highest storage capacity achieved was 1852 mAh/g, and corresponds to the highest mesopore volume of ~ 1.87 cm^3/g (Section 6.4.1.1). This discharge capacity is also the highest obtained in this work and is comparable to similar cells, using RF based activated carbon electrodes reported in the literature [24]. Although the cycleability still requires much improvement, the aforementioned discharge capacity demonstrates the great potential that Li/O_2 batteries possess, as it represents a value over 10 times the capacity obtained with Li-ion cells [31]. Furthermore, it shows that PF based carbon can attain capacities as high as those of similar RF based carbons, highlighting the potential of these materials [42].

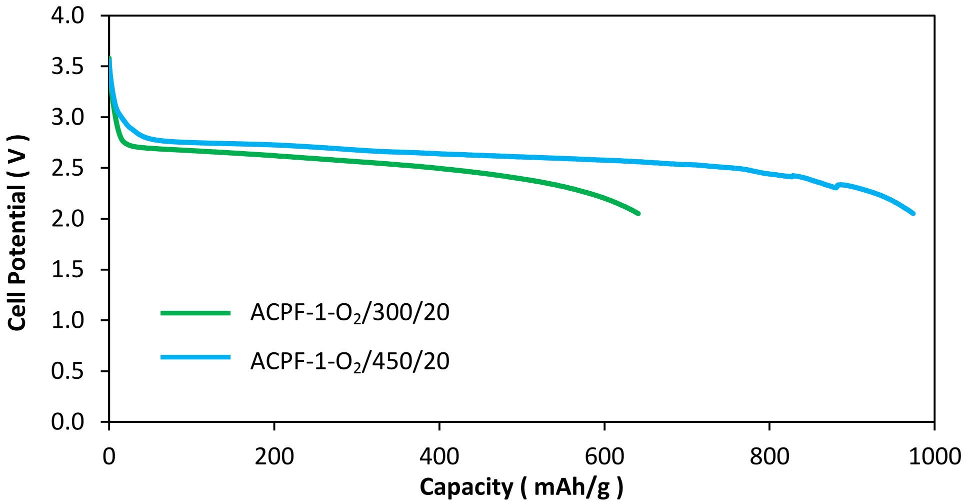

Figure 6.32: Discharge Capacities of ACPF9-1-O_2 based carbons at 70 mA/g

***Table 6.16:** Discharge capacities of ACPF9-1-O_2 based carbons with various porous characteristics at 70 mA/g

Sample	**V_{total} (cm^3/g)**	**ΔV_{total} (cm^3/g)**	**V_{micro} (cm^3/g)**	**ΔV_{micro} (cm^3/g)**	**V_{meso} (cm^3/g)**	**ΔV_{meso} (cm^3/g)**	**% V_{micro}**	**% V_{meso}**	**D_{avg} (nm)**	**ΔD_{avg} (nm)**	**D_{peak} (nm)**	**DC (mAh/g)**	**ΔDC (mAh/g)**	**CN**	**ΔCN**
ACPF9-1-O_2/300/20	0.7856	$V_{total\ (ACPF9\text{-}1\text{-}O2/300/20)}$ ± 5.5 %	0.1047	$V_{micro\ (ACPF9\text{-}1\text{-}O2/300/20)}$ ± 7.4 %	0.6809	$V_{meso\ (ACPF9\text{-}1\text{-}O2/300/20)}$ ± 5.9 %	13	87	6.7	$D_{avg\ (ACPF9\text{-}1\text{-}O2/300/20)}$ ± 4.2 %	$10 \leq D_{peak} \leq 40$	771	$DC_{(ACPF9\text{-}2\text{-}O2/300/20)}$ ± 4.2 %	9	$CN_{(ACPF9\text{-}2\text{-}O2/300/20)}$ ± 1
ACPF9-1-O_2/450/20	0.8968	$V_{total\ (ACPF9\text{-}1\text{-}O2/450/20)}$ ± 5.5 %	0.0851	$V_{micro\ (ACPF9\text{-}1\text{-}O2/450/20)}$ ± 7.4 %	0.8117	$V_{meso\ (ACPF9\text{-}1\text{-}O2/450/20)}$ ± 5.9 %	9	91	8.1	$D_{avg\ (ACPF9\text{-}1\text{-}O2/450/20)}$ ± 4.2 %	$10 \leq D_{peak} \leq 40$	974	$DC_{(ACPF9\text{-}2\text{-}O2/450/30)}$ ± 4.2 %	4	$CN_{(ACPF9\text{-}2\text{-}O2/450/30)}$ ± 1

*All parameters are as defined in Appendix B. See caption for Table 6.14 for information about error analysis.

6.4.1.3 Effect of Discharge Rate on Electrochemical Performance

In order to assess the power capabilities of the Li/O_2 cells in this work, discharge rates were varied and the corresponding electrochemical performance analysed. Figure 6.33 and Table 6.17 show the variation of discharge capacity with discharge rate. It can be observed that there is a decrease in discharge capacity with increasing current density. This is likely due to limited diffusion of O_2 into the active regions of the porous electrode, as well as slower Li ion and charge transfer within the carbon structure, with increasing discharge rate.

At higher discharge rates, pores within the cathode get blocked more rapidly due to quick deposition of discharge product [180]. This limits the flow of reactants (O_2, Li ions) and electrolyte to the inner active regions of the porous electrode [12] more severely than at lower current densities where pore clogging occurs at a slower rate, allowing for better utilization of the electroactive surface area. This illustrates that at high current drain rates, the Li/O_2 cell loses some of its energy and it is, therefore, important to engineer the porous structure of the cathode in such a way as to accommodate more discharge products whilst minimising mass transfer barriers. This would allow for the realisation of high power densities; which means the cell would be capable of maintaining high energy densities at high current drain rates.

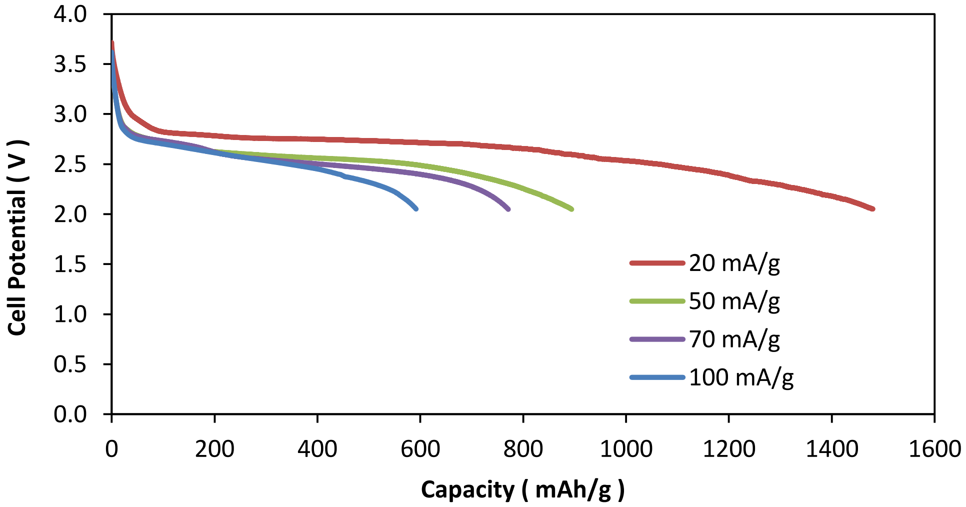

Figure 6.33: Discharge capacities of an activated PF carbon based electrode at different discharge rates

Table 6.17: Variation of discharge capacity with discharge rate for an activated PF carbon based electrode

Discharge rate (mA/g)	**DC (mAh/g)**	**ΔDC (mAh/g)**	**CN**	**ΔCN**
20	1480	DC_{20} ± 4.2 %	7	CN_{20} ± 1
50	894	DC_{50} ± 4.2 %	4	CN_{50} ± 1
70	771	DC_{70} ± 4.2 %	9	CN_{70} ± 1
100	592	DC_{100} ± 4.2 %	4	CN_{100} ± 1

All parameters are as defined in Appendix B. It is assumed that the errors calculated at 70 mA/g, as explained in the caption for Table 6.14, would be similar for other discharge rates.

6.4.1.4 Cycleability and Capacity Fade

Parameters such as mesopore volume and discharge rate, do not seem to have any significant effect on the cycleability of the Li/O_2 cells tested in this work (Tables 6.14 – 6.17). Furthermore, the cycle numbers obtained for the cells are quite low. Figure 6.34, shows the variation of discharge capacity with cycle number for some of the cells prepared in this work.

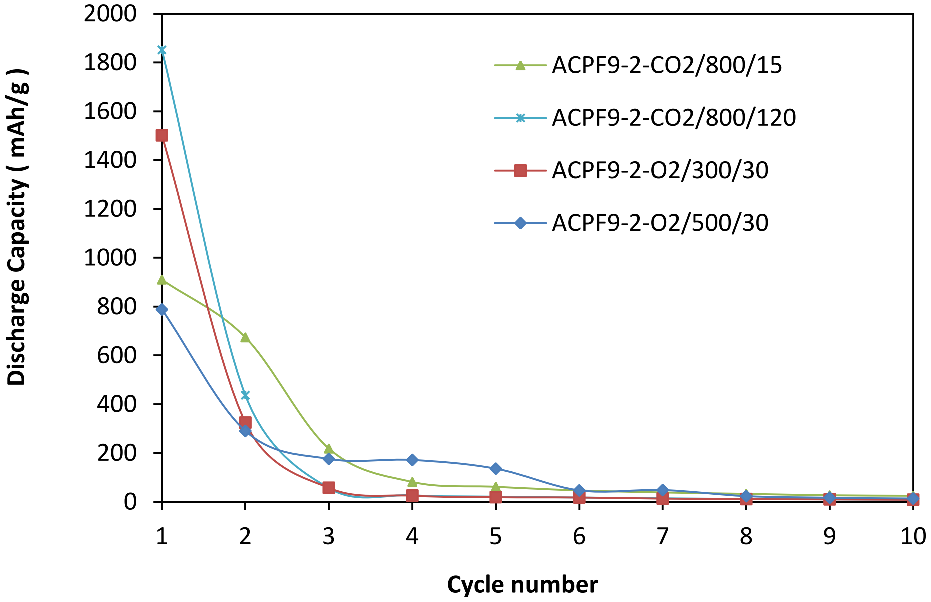

Figure 6.34: Variation of discharge capacity with cycle number for activated carbon based electrodes

It can be observed that there is a rapid drop in capacity over the first few cycles. This is thought to be associated with the pore size distribution of the carbons used in the electrodes. Electrodes synthesised by Mirzaeian *et al.* [24] containing activated carbons, with similar mesopore volumes were able to undergo over 20 discharge-charge cycles. The mesopore size distribution for the carbons used in that study is shown in Figure 6.35, and clearly demonstrates that the mesopore volume is almost exclusively generated from pores of around 40 nm in diameter.

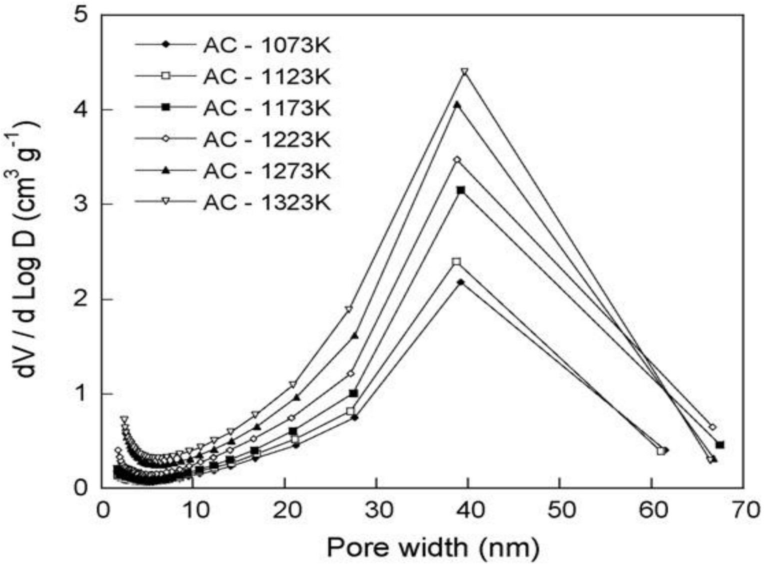

Figure 6.35: Pore size distribution of RF based activated carbons [24]

On the other hand, the pore size distributions for the activated carbons synthesised in this work, show significant contributions from smaller pores in the range of 2 – 20 nm (Figures 6.22a, 6.24 and 6.27a). The likely relationship between pore size and cycling behaviour is discussed as follows.

Figure 6.36 shows the accommodation of Li oxides (discharge product) in pores of different sizes. It suggests that during discharge, the small mesopores are more quickly filled (corresponding to the high density regions) with discharge product and diffusion of O_2 to the reaction zone becomes more difficult than in larger mesopores. Furthermore, the low conductivity of the discharge product, which impedes Li ion transfer and charge transfer, is more pronounced in the high density regions [24]. The slower kinetics of electron transfer in this region in comparison to the supply of Li ions is compensated for by the irreversible reaction of Li ions with certain electrolyte components [24]. This is thought to lead to structural changes of the O_2- electrode, deteriorating cell performance and causing capacity fade upon subsequent cycling.

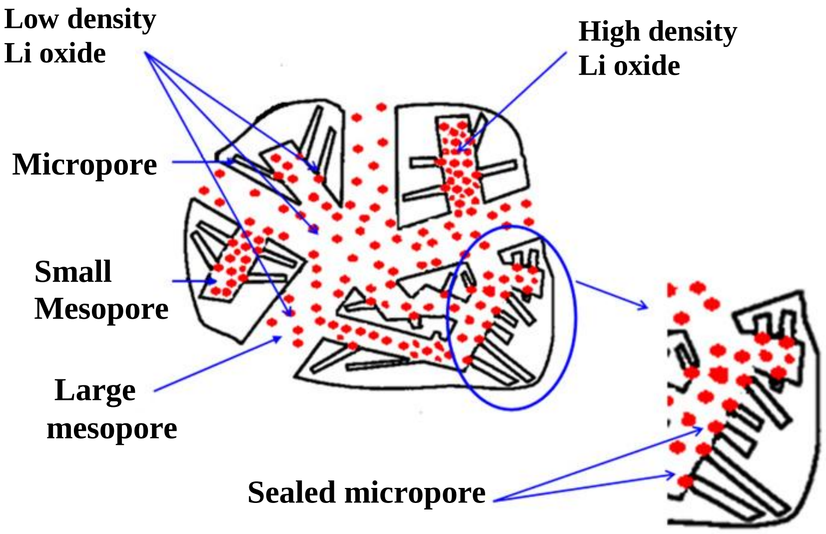

Fig. 6.36 Accommodation of Li oxides in pores of various sizes [95] (although there are different pore models of carbon, such as the branched- tree, norbit and drill-hole models, this model shown here, the branched tree model, is a good representation of the concept of transportation (e.g. of electrolyte) and interconnectivity between pores of various sizes [64])

The aforementioned theory relating to smaller pores being filled more quickly than larger ones, is indeed a probable occurrence during the operation of an Li/O_2 cell, due to a reduced storage space available in such pores. However, probing techniques would be beneficial to verify these suggestions. An ideal method would be to obtain an image of the electrode before and after a short time of discharge. However, trying to identify the location of the pores in the discharged electrode, and comparing with the undischarged electrode, will prove immensely difficult as the discharge product is likely to cover both the surface of the electrode, as well as the pores within it. Therefore the image of the discharge electrode may appear distorted, preventing a clear identification of which pores have been filled with discharge product [94]. Zhang *et al*. obtained SEM images of a carbon based electrode, prior to and after discharge in an Li/O_2 cell. The obtained images did not provide information on specific pore filling. This issue is further complicated by the fact that finding the exact region on a sample that was imaged prior to discharge, on the discharged electrode, is somewhat unlikely, as the electrode will need to be removed from the imaging equipment for discharge, and then returned for further analysis. One possible solution to this might be to employ a ‘live imaging procedure’, whereby the changes occurring in a specific region of the electrode can be monitored during the discharge process. This also poses another problem of its own, as the electrode is enclosed in the cell casing, and any probing technique being used for monitoring the changes in the electrode, will need to penetrate the cell container. A study performed by R. Pynn [181] comparing the penetration depths of various incident probes, such as electrons, X-rays and neutrons, showed that neutrons penetrate matter much more deeply than X-rays or electrons. Therefore, techniques such as neutron scattering, might allow for the investigation of specific pore filling during the discharge of the Li/O_2 cell.

Another possible explanation for capacity fade could be the reaction of electrolyte solvent (PC) with the lithium oxide discharge products to form Li_2CO_3 or lithium alkyl carbonates, XO-O-(C=O)-Li, where X is an alkyl group. [182]. In addition to the formation of Li_2O_2 upon discharge and its decomposition to release O_2 during charge [31], scientists working on Li/O_2 batteries have also confirmed the presence of Li_2CO_3 after discharge [58] as well as the evolution of CO_2 upon charge. In these studies, the compounds Li_2O_2 and Li_2CO_3 were detected using X-ray diffraction techniques [31], [58], whereas the evolved gasses O_2 and CO_2 where detected with mass spectrometry. It is, therefore, likely that the origin of CO_2 is via the decomposition of carbonates formed upon reaction of lithium oxide discharge products and the electrolyte solvent (PC) [183]. This implies that upon subsequent discharge/charge cycles, more electrolyte gets consumed until a point where the discharge reaction can no longer be sustained, therefore, reducing the cycle life of the cell.

A typical discharge/charge curve of Li/O_2 cells in this work is shown in Figure 6.37. The charge potential of 4 V – 4.4 V is consistent with previously reported studies on similar cells [30 - 31]. In comparison to the thermodynamic potential of 2.96 V of the reaction between Li and O_2 forming Li_2O_2, this charging voltage is notably higher and the difference is referred to as the charge overpotential. The high charging voltage required is likely due to the decomposition of the carbonates formed during discharge, as mentioned earlier, which require a charging voltage of over 4 V [175]. It can also be observed that not all the discharge capacity has been regained upon charging. Mirzaeian *et al.* [24] have shown, by impedance spectroscopy, that an increasing amount of discharge product builds up in the cathode upon continuous cycling, indicating that not all discharge product has been decomposed in the reverse reaction occurring during charge. This could be due to the irreversible formation of Li_2O [87]. A further contribution to this could be a result of the irreversible side reactions between Li ions and electrolyte species that occur due to slow kinetics at the cathode side as described earlier, contributing some irreversible capacity to the overall discharge capacity [24]. Both processes also contribute to capacity fade. As explained earlier the irreversible side reaction leads to the deterioration of the cell performance resulting in low cycle life, while the accumulation of low conductive discharge product not only reduces the amount of storage space available, but also allows for progressively slower kinetics of Li ion transfer and charge transfer upon subsequent cycling.

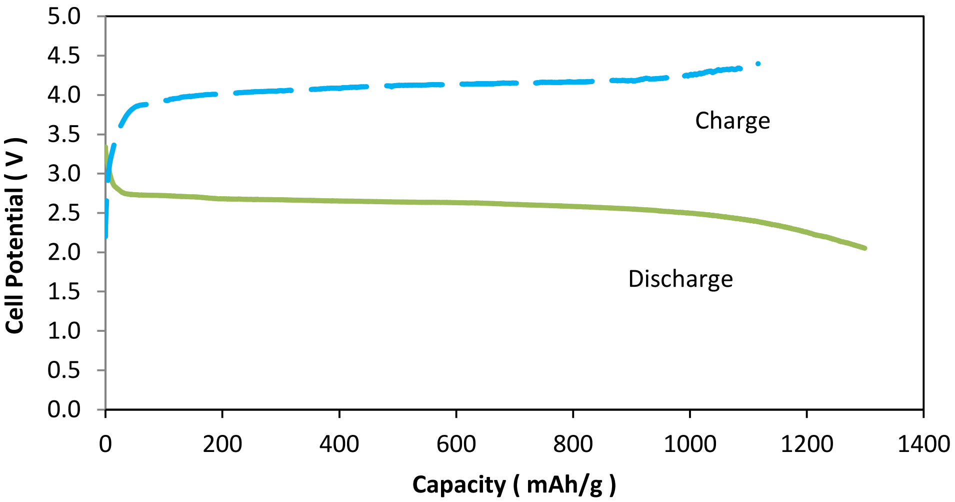

Figure 6.37: Discharge/charge curve for the 1st cycle using ACPF9-2-CO_2/800/60 based electrode

6.4.1.5 Relationships between Porosity and Electrochemical Performance

The galvanostatic discharge/charge measurments carried out on PF based carbon electrodes have shown that the mesopore volume is the major porosity parameter controlling the discharge capacity of Li/O_2 cells. Figures 6.38 and 6.39 show the variation between mesopore volume and discharge capacity for O_2 and CO_2 activated carbon based electrodes, respectively.

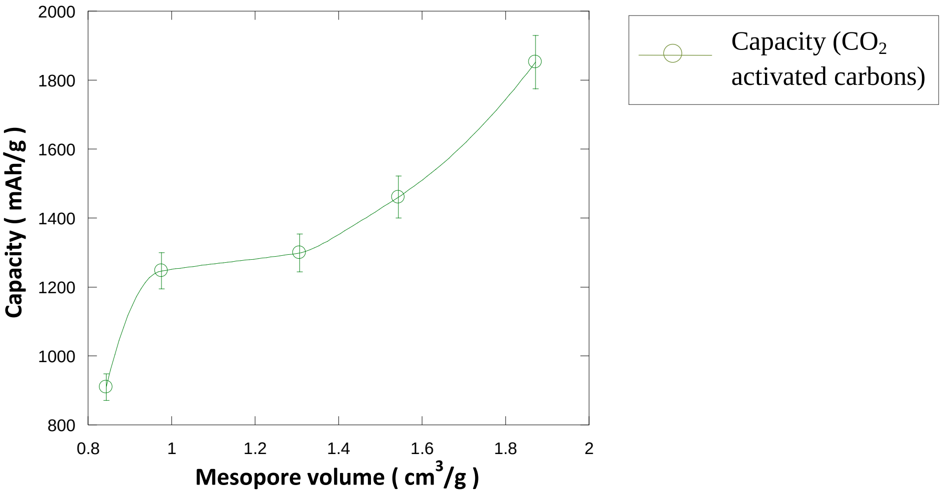

Figure 6.38: Variation of discharge capacity with mesopore volume for CO_2 activated PF carbon based electrodes (the data points are connected by a trend line)

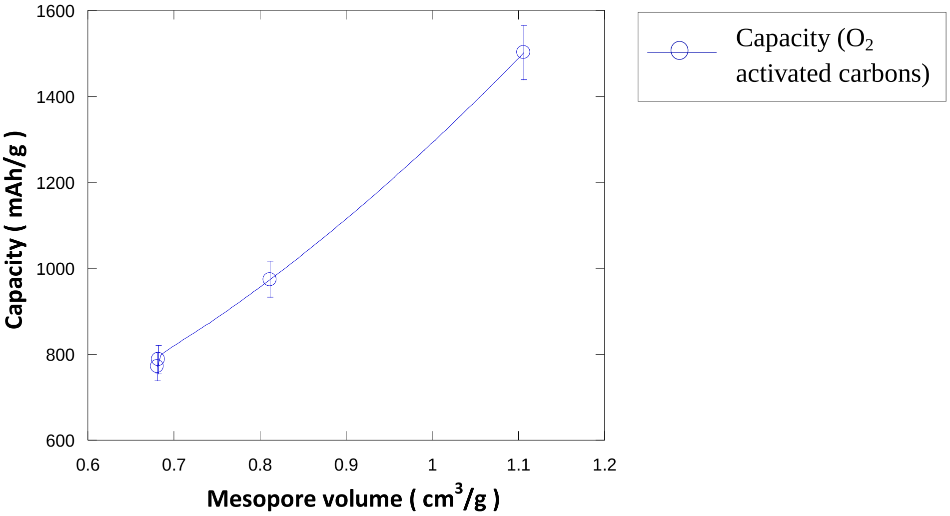

Figure 6.39: Variation of discharge capacity with mesopore volume for O_2 activated PF carbon based electrodes (the data points are connected by a trend line)

***Table 6.18:** Variation in electrochemical performance with porosity for CO_2 activated PF carbon based electrodes (Detailed information regarding these samples are available in Section 6.2)

Sample	**V_{total} (cm^3/g)**	**ΔV_{total} (cm^3/g)**	**V_{micro} (cm^3/g)**	**ΔV_{micro} (cm^3/g)**	**V_{meso} (cm^3/g)**	**ΔV_{meso} (cm^3/g)**	**% V_{micro}**	**% V_{meso}**	**D_{avg} (nm)**	**ΔD_{avg} (nm)**	**DC (mAh/g)**	**ΔDC (mAh/g)**	**NC (mAh/cm^3)**	**ΔNC (mAh/cm^3)**	**CN**	**ΔCN**
ACPF9-2-CO_2/800/15	1.0434	$V_{\text{total (ACPF9-2-CO2/800/15)}}$ ± 5.5 %	0.2000	$V_{\text{micro (ACPF9-2-CO2/800/15)}}$ ± 7.4 %	0.8434	$V_{\text{meso (ACPF9-2-CO2/800/15)}}$ ± 5.9 %	19	81	6.25	$D_{\text{avg (ACPF9-2-CO2/800/15)}}$ ± 4.2 %	910	$DC_{\text{(ACPF9-2-CO2/800/15)}}$ ± 4.2 %	1079	$NC_{\text{(ACPF9-2-CO2/800/15)}}$ ± 7.3 %	5	$CN_{\text{(ACPF9-2-CO2/800/15)}}$ ± 1
ACPF9-2-CO_2/800/30	1.2519	$V_{\text{total (ACPF9-2-CO2/800/30)}}$ ± 5.5 %	0.2761	$V_{\text{micro (ACPF9-2-CO2/800/30)}}$ ± 7.4 %	0.9758	$V_{\text{meso (ACPF9-2-CO2/800/30)}}$ ± 5.9 %	22	78	5.67	$D_{\text{avg (ACPF9-2-CO2/800/30)}}$ ± 4.2 %	1247	$DC_{\text{(ACPF9-2-CO2/800/30)}}$ ± 4.2 %	1278	$NC_{\text{(ACPF9-2-CO2/800/30)}}$ ± 7.3 %	4	$CN_{\text{(ACPF9-2-CO2/800/30)}}$ ± 1
ACPF9-2-CO_2/800/60	1.6031	$V_{\text{total (ACPF9-2-CO2/800/60)}}$ ± 5.5 %	0.296	$V_{\text{micro (ACPF9-2-CO2/800/60)}}$ ± 7.4 %	1.3071	$V_{\text{meso(ACPF9-2-CO2/800/60)}}$ ± 5.9 %	18	82	5.66	$D_{\text{avg (ACPF9-2-CO2/800/60)}}$ ± 4.2 %	1299	$DC_{\text{(ACPF9-2-CO2/800/60)}}$ ± 4.2 %	994	$NC_{\text{(ACPF9-2-CO2/800/60)}}$ ± 7.3 %	2	$CN_{\text{(ACPF9-2-CO2/800/60)}}$ ± 1
ACPF9-2-CO_2/800/90	1.8537	$V_{\text{total (ACPF9-2-CO2/800/90)}}$ ± 5.5 %	0.3106	$V_{\text{micro (ACPF9-2-CO2/800/90)}}$ ± 7.4 %	1.5431	$V_{\text{meso (ACPF9-2-CO2/800/90)}}$ ± 5.9 %	17	83	5.36	$D_{\text{avg (ACPF9-2-CO2/800/90)}}$ ± 4.2 %	1461	$DC_{\text{(ACPF9-2-CO2/800/90)}}$ ± 4.2 %	947	$NC_{\text{(ACPF9-2-CO2/800/90)}}$ ± 7.3 %	3	$CN_{\text{(ACPF9-2-CO2/800/90)}}$ ± 1
ACPF9-2-CO_2/800/120	2.0112	$V_{\text{total (ACPF9-2-O2/800/120)}}$ ± 5.5 %	0.1395	$V_{\text{micro (ACPF9-2-O2/800/120)}}$ ± 7.4 %	1.8717	$V_{\text{meso (ACPF9-2-O2/800/120)}}$ ± 5.9 %	7	93	5.82	$D_{\text{avg (ACPF9-2-O2/800/120)}}$ ± 4.2 %	1852	Av. $DC_{\text{(ACPF9-2-CO2/800/90)}}$ ± 4.2 %	989	Av. $NC_{\text{(ACPF9-2-CO2/800/90)}}$ ± 7.3 %	3	Av. $CN_{\text{(ACPF9-2-CO2/800/90)}}$ ± 1

*All parameters are as defined in Appendix B. See caption for Table 6.11 for information about error analysis associated with the column headings ΔV_{total}, ΔV_{micro}, ΔV_{meso} and $\Delta D_{avg.}$, and the caption for Table 6.14 for the error analysis associated with column headings ΔDC, and ΔCN. The error value relating to the column heading ΔNC was also based on ACPF9-2-CO_2/800/120 and was calculated by combining the reproducibility errors of discharge capacity (Table 6.14) and mesopore volume (Table 6.11), using the quadratic sum method [184 - 185] and was applied to the value of NC for the other electrodes, under the assumption of a similar deviation.

***Table 6.19:** Variation in electrochemical performance with porosity for O_2 activated PF carbon based electrodes (Detailed information regarding these samples are available in Section 6.2)

Sample	**V_{total} (cm^3/g)**	**ΔV_{total} (cm^3/g)**	**V_{micro} (cm^3/g)**	**ΔV_{micro} (cm^3/g)**	**V_{meso} (cm^3/g)**	**ΔV_{meso} (cm^3/g)**	**% V_{micro}**	**% V_{meso}**	**D_{avg} (nm)**	**ΔD_{avg} (nm)**	**DC (mAh/g)**	**ΔDC (mAh/g)**	**NC (mAh/cm^3)**	**ΔNC (mAh/cm^3)**	**CN**	**ΔCN**
ACPF9-1-O_2/300/20	0.7856	$V_{\text{total (ACPF9-1-O2/300/20)}}$ ± 5.5 %	0.1047	$V_{\text{micro (ACPF9-1-O2/300/20)}}$ ± 7.4 %	0.6809	$V_{\text{meso (ACPF9-1-O2/300/20)}}$ ± 5.9 %	13	87	6.66	$D_{\text{avg (ACPF9-1-O2/300/20)}}$ ± 4.2 %	771	$DC_{\text{(ACPF9-2-O2/300/20)}}$ ± 4.2 %	1132	**NC**$_{\text{(ACPF9-2-O2/300/20)}}$ ± 7.3 %	9	$CN_{\text{(ACPF9-2-O2/300/20)}}$ ± 1
ACPF9-2-O_2/500/30	0.7619	$V_{\text{total (ACPF9-2-O2/500/30)}}$ ± 5.5 %	0.0799	$V_{\text{micro (ACPF9-2-O2/500/30)}}$ ± 7.4 %	0.6820	$V_{\text{meso (ACPF9-2-O2/500/30)}}$ ± 5.9 %	10	90	8.1	$D_{\text{avg (ACPF9-2-O2/500/30)}}$ ± 4.2 %	788	$DC_{\text{(ACPF9-2-O2/500/30)}}$ ± 4.2 %	1155	**NC**$_{\text{(ACPF9-2-O2/500/30}}$± 7.3 %	5	$CN_{\text{(ACPF9-2-O2/500/30)}}$ ± 1
ACPF9-1-O_2/450/20	0.8968	$V_{\text{total (ACPF9-1-O2/450/20)}}$ ± 5.5 %	0.0851	$V_{\text{micro (ACPF9-1-O2/450/20)}}$ ± 7.4 %	0.8117	$V_{\text{meso (ACPF9-1-O2/450/20)}}$ ± 5.9 %	9	91	8.11	$D_{\text{avg (ACPF9-1-O2/450/20)}}$ ± 4.2 %	974	$DC_{\text{(ACPF9-2-O2/450/30)}}$ ± 4.2 %	1200	**NC**$_{\text{(ACPF9-2-O2/450/30)}}$ ± 7.3 %	4	$CN_{\text{(ACPF9-2-O2/450/30)}}$ ± 1
ACPF9-2-O_2/300/30	1.2443	$V_{\text{total (ACPF9-2-O2/300/30)}}$ ± 5.5 %	0.1376	$V_{\text{micro (ACPF9-2-O2/300/30)}}$ ± 7.4 %	1.1064	$V_{\text{meso (ACPF9-2-O2/300/30)}}$ ± 5.9 %	11	89	7.0	$D_{\text{avg (ACPF9-2-O2/300/30)}}$ ± 4.2 %	1502	$DC_{\text{(ACPF9-2-O2/300/30)}}$ ± 4.2 %	1358	**NC**$_{\text{(ACPF9-2-O2/300/30)}}$ ± 7.3 %	3	$CN_{\text{(ACPF9-2-O2/500/30)}}$ ± 1

*All parameters are as defined in Appendix B. See caption for Table 6.18 for information about error analysis.

Tables 6.18 and 6.19 show the variation of porosity parameters with electrochemical performance of CO_2 and O_2 activated carbon based electrodes, respectively, (arranged in the order of increasing mesopores volumes). The aforementioned tables also include additional columns for the capacity of the associated Li/O_2 cells normalised to the mesopores volume. The normalised capacity values are indicative of the level of increase in capacity with respect to the mesopore volumes.

Upon initial observation of the normalised capacities, it appears that they vary randomly with increasing mesopore volume, rather than having a constant or even fairly constant value. This could indicate that there are other porosity parameters contributing to the discharge capacity and will be discussed shortly.

Figure 6.40 and table 6.20 show the variation of discharge capacities normalised to mesopore volume with average pore size for both O_2 and CO_2 activated carbon based electrodes. They indicate that there is an overall increase in the normalised capacities with average pore size, although, with slight deviations from this trend. Approximately, however, this shows that the level of increase in discharge capacity with mesopore volume (normalised capacity), becomes more pronounced with increasing pore size. This can be understood from the viewpoint of reduced mass transfer barriers and increased access of reactant (Li-ions and O_2) and electrolyte to the inner active regions of the electrode. In other words, larger average pore sizes mean that the pore volume becomes more accessible resulting in increased storage space for discharge product and subsequently higher discharge capacities [1], [24], [95].

The cycling performance of Li/O_2 cells in this work is in the range of 3 – 9 cycles and seems to vary randomly with mesopore volume and average pore size. Similar behaviour of cycle life with these porosity parameters can be found in the literature [24]. However, a comparison of the results, obtained here, with those in the literature (using polymer derived carbon based electrodes and similar electrode preparation procedures) [24], indicates that low cycle life of these cells may be due to the pore size distriubtion of the carbons used as electrodes, which show a significant contribution of pores with smaller dimensions, as opposed to the ones obtained in the literature, where the total mesopore volume was almost entirely a result of pores of much larger dimensions, with little contribution of smaller pores (section 6.4.1.4). This comparison takes into consideration specific carbons with similar mesopore volumes in both cases, but with a significant differences in PSD profile. The corresponding cycling performance being ~3 cycles, for the cell prepared in this work, and ~20 cycles for that reported in the literature [24]. This could, therefore, imply that the pore size of the cathode is a crucial factor in controlling its cycling performance.

The mesopore volume is also important for the cycling performance in the context of build up and accumulation of discharge product which could lead to a progressive drop in available storage space upon continuous cycling (Section 6.4.1.1). However, a combination of a large mesopore volume and a large average pore size, would be an even better scenario, as both can work syngerstically: where the wide pores allow for increased access of the reactants and electrolyte into the available pore volume.

The electrochemical performance of Li/O_2 cells in this work appear to be mainly controlled by the porosity of the carbons used as the electrodes. The O_2 and CO_2 activation processes yielded similar levels of surface functionality in the ensuing activated carbons, as indicated by the concentrations of carbonyl groups, determined using the absorbance IR spectra of the samples, combined with Beer’s Law. Furthermore, as the results obtained in this work show that porosity has a significant effect on electrochemical performance, it would seem that an investigation of the effect of surface functionality can only be effective when both mesopore volume and pore size are fixed.

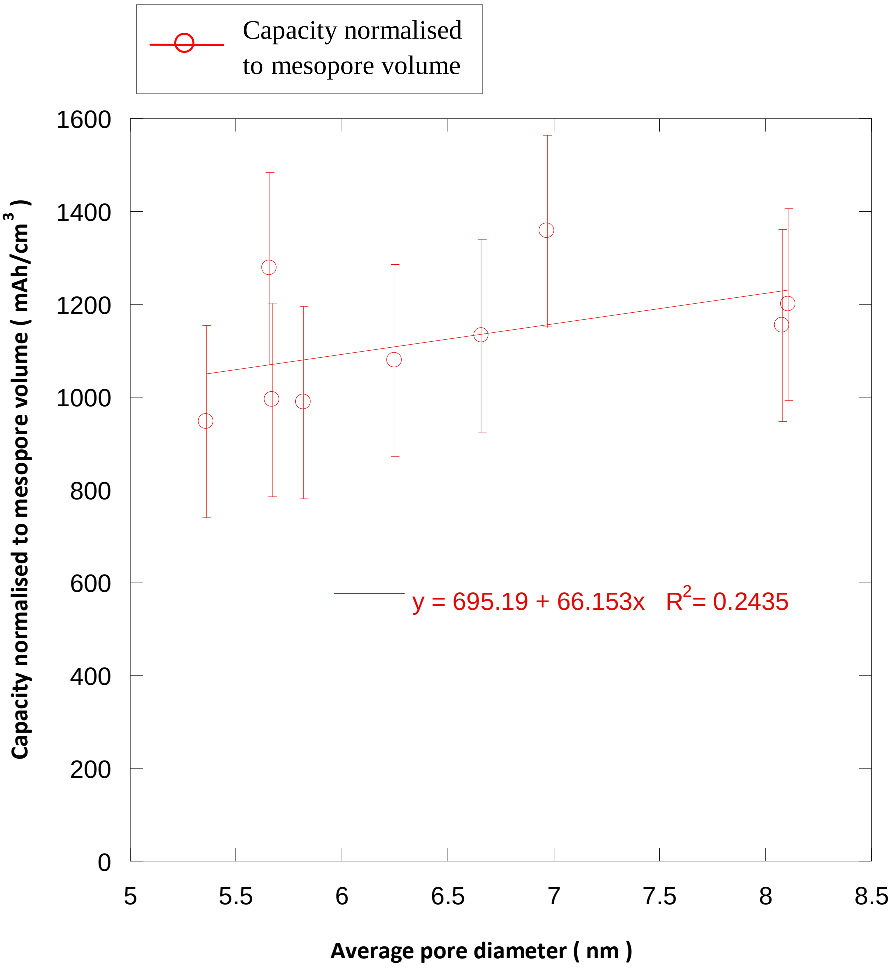

Figure 6.40: Variation of capacity normalised to mesopore volume with average pore size for both CO_2 and O_2 activated PF carbon based electrodes

Table 6.20: Variation of capacity normalised to mesopore volume with average pore size for both CO_2 and O_2 activated PF carbon based electrodes

Sample	**D_{avg} (nm)**	**ΔD_{avg} (nm)**	**D_{peak} (nm)**	**NC (mAh/ cm^3)**	**ΔNC (mAh/ cm^3)**	**CN**	**ΔCN**
ACPF9-2-CO_2/800/90	5.36	D_{avg} (ACPF9-2-CO2/800/90) ± 4.2 %	10≤ Dpeak ≤40	947	NC(ACPF9-2-CO2/800/90) ± 7.3 %	3	CN(ACPF9-2-O2/300/20) ± 1
ACPF9-2-CO_2/800/30	5.66	D_{avg} (ACPF9-2-CO2/800/30) ± 4.2 %	10≤ Dpeak ≤40	1278	NC(ACPF9-2-CO2/800/30) ± 7.3 %	4	CN(ACPF9-2-CO2/800/30) ± 1
ACPF9-2-CO_2/800/60	5.67	D_{avg} (ACPF9-2-CO2/800/60) ± 4.2 %	10≤ Dpeak ≤40	994	NC(ACPF9-2-CO2/800/60) ± 7.3 %	2	CN(ACPF9-2-CO2/800/60) ± 1
ACPF9-2-CO_2/800/120	5.82	D_{avg} (ACPF9-2-CO2/800/120) ± 4.2 %	10≤ Dpeak ≤40	989	NC(ACPF9-2-CO2/800/120) ± 7.3 %	3	CN(ACPF9-2-CO2/800/120) ± 1
ACPF9-2-CO_2/800/15	6.25	D_{avg} (ACPF9-2-CO2/800/15) ± 4.2 %	10≤ Dpeak ≤40	1079	NC(ACPF9-2-CO2/800/15) ± 7.3 %	5	CN(ACPF9-2-CO2/800/15) ± 1
ACPF9-1-O_2/300/20	6.66	D_{avg} (ACPF9-1-O2/300/20) ± 4.2 %	10≤ Dpeak ≤40	1132	NC(ACPF9-1-O2/300/20) ± 7.3 %	9	CN(ACPF9-1-O2/300/20) ± 1
ACPF9-2-O_2/300/30	6.97	D_{avg} (ACPF9-2-O2/300/30) ± 4.2 %	20≤ Dpeak ≤40	1358	NC (ACPF9-2-O2/300/30) ± 7.3 %	3	CN(ACPF9-2-O2/300/30) ± 1
ACPF9-2-O_2/500/30	8.08	D_{avg} (ACPF9-2-O2/500/30) ± 4.2 %	20≤ Dpeak ≤40	1155	NC(ACPF9-2-O2/500/30) ± 7.3 %	5	CN(ACPF9-2-O2/500/30) ± 1
ACPF9-1-O_2/450/20	8.11	D_{avg} (ACPF9-1-O2/450/20) ± 4.2 %	10≤ Dpeak ≤40	1200	NC(ACPF9-1-O2/450/20) ± 7.3 %	4	CN(ACPF9-1-O2/450/20) ± 1

*All parameters are as defined in Appendix B. See caption for Table 6.18 for information about error analysis.

Chapter 7

Conclusions

7.1 General Conclusions

The immense potential for rechargable Li/air batteries has attracted a great deal of attention from researchers worldwide. Much still needs to be understood regarding the fundamental mechanisms governing the operation of these batteries and, as a result, this technology is still at its early stages of development. In addition to trying to determine what processes are actually taking place in these batteries, a significant amount of the work is being dedicated to improving energy densities and power capabilities. Various aspects of this technology, including the battery design, type of electrolytes, electrodes, binders and current collectors, represent avenues for optimisation. In this work, a detailed study of the effect of various parameters, starting from the initial synthesis stages to the electrochemical performance of carbon based air cathodes has been carried out in order to maximise the performance of the Li/air batteries. Additionally, an attempt to reduce raw material costs has prompted the use of phenol-formaldehyde gels as carbon precursors. The price comparison between the raw materials, phenol and resorcinol, showed the lower costs of the former. Furthermore, a comparison between PF and RF based materials (gels, carbons and activated carbons), revealed similar levels of obtainable mesoporosity for the gels and the activated carbons. Additionally, these comparisons showed that although activated PF based carbons are highly mesoporous, the contribution of small mesopores, to the total mesopore volume, is more significant than in RF gels. A comparison between the electrochemical performance of PF and RF based activated carbon electrodes, further illustrated the significance of this difference in pore size distribution. Overall, PF based materials represent a promising alternative to their RF counterparts, in terms of the attainable pore volumes and discharge capacities (similar to those for RF based materials), in addition to the lower cost of phenol relative to resorcinol. However, there are certain issues that need to be addressed in order to make PF based materials much more competitive than RF based materials, as will be discussed in section 7.3. Conclusions from the viewpoint of porosity optimisation of these gels and the corresponding carbons, as well as the electrochemical performance based on these carbons are presented below.

The optimisation of the porous structure of the PF gels began with an investigation of the effect of P/C ratio, keeping the P/F ratio and concentration of phenol in water, constant, at 0.5 and 1.06 mol/l, respectively. The total and mesopore volumes of the gels were found to increase with increasing ratio for P/C $\leq$ 8 and decrease with a further increase in P/C ratio for P/C > 8. It was demonstrated that P/C ratio had a significant effect on the porous structure of PF gels. The sample with P/C ratio of 8 (PF3) exhibited the highest total pore and mesopore volumes of ~ 1.28 cm^3/g, respectively. The PF gels were also found to be predominantly mesoporous. Upon investigation of the effect of solvent exchange liquid and drying method, freeze drying with t-butanol emerged as the preferred route to obtain highly mesoporous gels with maximised pore volumes. However, due to lack of complete uniformity, and subsequent difficulty in reproducing gels with a P/C ratio of 8, a further investigation on the effect of P/F ratio was carried out. It was found that at a P/F ratio of 0.4, which corresponds to an increase in amount of formaldehyde, produced a uniform gel structure that was more easily reproduced, and the corresponding gel (PF9) possessed total pore and mesopore volumes of ~ 1.16 and 1.15 cm^3/g with an average pore size of 11.4 nm. This was attributed to an increase in crosslink density with increasing amount of formaldehyde, which although improved aforementioned characteristics of the gel, resulted in a slight loss of porosity. As it is paramount to produce a gel with a uniform structure that can be easily reproduced, the preferred reactant ratios for gel synthesis with a fixed concentration of phenol in water, emerged as P/C =8 and P/F = 0.4, rather than P/F=0.5. It was assumed that the trend, in terms porosity, observed at P/F = 0.5, would be similar in the case of P/F = 0.4, hence the choice of the reactant ratios. This shall be further discussed in section 7.3.

In the process of converting the gels to carbons, an analysis of the effect of carbonisation temperatures was performed on both PF3 and PF9. In both cases, an increase in micropore volume was observed, as a result of the cleavage of C-O and C-H bonds from the methylene and and methylene ether linkages of the original gel structure, and the removal of gaseous species, leading to significant mass loss and subsequent development of porosity, but there was also a drop in overall pore volume between the gel and the carbons as described in section 6.2.1. However, for the carbons, there seemed to be an overall increase in total pore and mesopore volumes with carbonisation temperature and 1050 °C appeared to be the optimum for maximised porosity for both CPF3 and CPF9 carbons. In the case of the PF9 sample, carbonisation temperatures were restricted to ≥ 1000 °C as temperatures below this led to self heating of the carbon upon exposure to air. Nevertheless, on comparison of the temperatures that could be tested: 1000 °C and 1050 °C, the latter emerged as the preferred temperature in terms of increased porosity. The corresponding carbon, CPF9 – 1050°C, possessed total pore and mesopore volumes of ~ 0.81 and 0.77 cm^3/g, respectively, and an average pore size of 10.5 nm.

Further enhancement of the porous characteristics of the carbons was achieved by physical activation. Fast and mild oxidation in O_2 and CO_2, respectively, was carried out. In both processes, an increase in pore volumes with increasing burn-off was observed although the activated carbons possessed smaller mean pore sizes than the original carbon. Furthermore, with O_2 activation, much higher extents of burn-off led to the collapse of the structure, and this was associated with the intensity of the gasification process resulting from much higher gas flowrates and diffusion of gas into the carbon structure, elevated temperatures, and the stronger reactivity of O_2 with carbon in comparison to CO_2. The CO_2 activated carbon, ACPF9-2-CO_2/800/120, produced the highest total pore and mesopore volumes of ~ 2.01 and 1.87 cm^3/g respectively, and possessed an average pore size of 5.8 nm. The FTIR analysis of the surface functional groups on both O_2 and CO_2 activated carbons showed that both possessed similar levels of surface functionality.

The galvanostatic discharge/charge measurements were carried out on both O_2 and CO_2 activated carbon based electrodes. It was found there was an increase in discharge capacity with mesopore volume in both cases, with the highest discharge capacity of 1852 mAh/g corresponding to the highest mesopore volume of ~ 1.87 cm^3/g. Although low cost PF based carbon electrodes have shown relatively high discharge capacities, the low cycle life of the associated Li/O_2 cells, which ranges from 3 – 9 cycles, is thought to be partly due to the low average pore sizes. However, the important effect of mesopore volumes on increasing the specific energy of Li/air batteries was further demonstrated. By normalising discharge capacity to mesopore volume, it was found that an increase in average pore size also leads to an increase in discharge capacity. Furthermore, the effect of discharge rates performed on the carbon based electrodes showed a decline in discharge performance with increasing rates of discharge.

7.2 Conclusions for Energy Storage

The maximum discharge capacity of 1852 mAh/g obtained in this work represents a value which is over 10 times the energy density of Li-ion batteries. Although this holds great promise for portable electronics and electric vehicles alike, issues relating to the cycleability require much improvement. The cycle life of the aforementioned cell which showed maximum discharge capacity obtained in this work was 3 cycles. Furthermore, the inability of the Li/O_2 cells to provide high energy density at higher discharge rates represents another obstacle in its use for high power applications.

Most of the aforementioned issues originate from the various aspects of the battery, ranging from the properties or type of the electrode, electrolyte or catalyst, to the nature of the battery operation itself. The significant contribution of smaller pores to the overall mesopore volume, for example, is thought to be partly responsible for the low cycle life of the cells, considering that smaller sized pores are choked with discharge product quicker than in larger sized ones. The implication is that upon continuous discharge the accumulation of low conductive discharge product impedes the ability of Li ions to access the pores, leading to adverse reactions of the Li-ions with electrolyte components, which are detrimental to the electrochemical performance of the cell. Evidently this is a direct result of an intrinsic aspect of the non-aqueous Li/air cell, namely the insolubility of discharge product in the electrolyte. In fact the deposition of discharge product in the pores of the electrode is one of the major reasons for termination of the discharge process. This implies that the discharge capacity obtained in this work can still be enhanced, by further porosity control: an approach which could also lead to an increase in the cycle life of the Li/air cells.

Another possible contribution to the capacity fade upon subsequent cycling could be associated with the method by which the catalyst is incorporated into the structure of the carbon electrode. Mechanical mixing of catalyst and carbon might not be the most efficient technique for adequate dispersion of catalyst throughout the structure of the carbon as well as contact between catalyst and carbon as shall be further discussed in section 7.3.

7.3 Recommendations for Further Work

Along with the need to improve the cycle life of Li/air batteries, attention needs to be devoted to improving further the discharge performance to achieve the true potential of this technology. Some of the methods by which this can be achieved shall be discussed in this section.

Templating methods, where an inert component or template (e.g. zeolite and silica spheres) with a specific pore size, is introduced at the initial stages of the gel synthesis procedure i.e. in the initial solution, have been widely applied in the area of nanotechnology, to induce the desired pore size in gel structures [186]. Applying such methods to PF gels could greatly enhance the electrochemical performance of the PF carbon based electrodes. Furthermore, exploring the effect of surface functionalities on electrochemical performance might be an essential tool for enabling strategically tailored surface properties on carbon electrodes, to enhance electrochemical performance [81]. However, this will be most effective once porosity has been optimised, and with the use of oxidation methods that do not alter the porosity to any significant extent. A good area for investigation would be chemical oxidation under mild conditions, controlled by the concentration of the oxidising agent, temperature and duration of activation [187]. In order to make PF gels much more competitive than RF gels, the issue of the higher catalyst content used in the synthesis of the former, will need to be addressed. This might be achieved by considering much cheaper catalysts, which are also more alkaline than sodium carbonate (i.e. with higher pH values). A further investigation into the sodium content of the dried gels, by way of highly sensitive techniques, such as neutron scattering, to detect ‘hidden’ regions containing elevated sodium concentrations, which may not be accessible by techniques such as EDS, would be very useful. Some of the benefits of this could be gaining a better understanding of the self-ignition behaviours of some samples carbonised in a certain range of temperatures, as well as determining the effect of sodium content on the electrochemical performance of Li/O_2 batteries. In addition to this, a further investigation of the effect of P/C ratio on PF gels synthesised with a P/F ratio of 0.4, would provide valuable information on the optimum P/C ratio in terms of maximised porosity, for P/F = 0.4.

An investigation of different electrolyte formulations could also be useful as varied levels of solubility and diffusivity of oxygen in the electrolyte possess significant effects on electrochemical performance of Li/air batteries. The use of mixed solvent to reduce the viscosity of propylene carbonate (PC) represents another approach.

To improve uniform dispersion of manganese oxide based catalyst within the carbon structure and better contact of catalyst with carbon, a different approach can be utilised. This involves the redox reaction between manganese sulphate and potassium permanganate in the presence of the carbon matrix [188]. To compare the extent of catalyst dispersal by mechanical mixing and the redox reaction approach, it is likely that techniques, such as neutron scattering, will be required to get a full picture of the catalytically active areas in the air cathode [189]. This can also be used to determine how pores of different sizes are filled with discharge product [181]. In addition to these methods for enhancing Li/air batteries, other analysis techniques such as electrochemical impedance spectroscopy would prove useful to further investigate the loss of capacity upon continuous cycling [24].

Chapter 8

References

[1] R. Padbury, X. Zhang, *J. Power Sources*, 2011, **196**, 4436 – 4444.

[2] R. Saidur, M. R. Islam, N. A. Rahim and K. H. Solangi, *Renew. Sust. Energ. Rev.*, 2010, **14**, 1744 – 1762.

[3] T. Matsushima, S. Takagi, S. Muroyama, *Renew. Energ.*, 2006, **31**, 1343 - 1354.

[4] R. M. Dell and D. A. J. Rand, *Understanding Batteries*, 2001, RSC Publishing, Cambridge.

[5] J. P. Zheng, R. Y. Liang, M. Hendrickson and E. J. Plichta, *J. Electrochem. Soc.*, 2008, **155**, A432 – A437.

[6] B.E Conway, *Electrochemical supercapacitors*: *Scientific fundamentals and technological applications*, 1999, Kluwer Academic/Plenum Publishers, New York.

[7] P. J. Hall, M. Mirzaeian, S. I. Fletcher, F. B. Sillars, A. J. R. Rennie, G. O. Shitta-Bey, G. Wilson, A. Cruden and R. Carter, *Energy Environ. Sci.*, 2010, **3**, 1238 – 1251.

[8] P. G. Bruce, *Solid State Ionics*, 2008, **179**, 752 – 760.

[9] K. K. Lian, L. Bai, Patent 5563765 (Motorola Inc.), 1996.

[10] Energy chemistry laboratory: Analysis of characteristics for EDLCs using flurohyrogenate ionic liquids, http://www.echem.energy.kyoto-u.ac.jp/research-e.html (accessed January 2012).

[11] R. A. Higgins, *Energy storage*, 2010, Springer, New York.

[12] G. Girishkumar, B. McCloskey, A. C. Luntz, S. Swanson and W. Wilcke, *J. Phys. Chem. Lett.*, 2010, **1**, 2193 – 2203.

[13] M. Winter, R. J. Brodd, *Chem. Rev.*, 2004, **104**, 4245-4269.

[14] D. Linden and T. Reddy, *Handbook of batteries*, 3rd ed., 2001, McGraw Hill, New York.

[15] C.A Vincent, B. Scrosati, *Modern Batteries: An introduction to electrochemical power sources*, 2nd ed., 1997, Butterworth-Heinemann, Oxford.

[16] F. A. Carey, *Organic chemistry*, 4th ed, 2000, McGraw Hill, New York.

[17] S. S. Zumdahl, S. A. Zumdahl, *Chemistry*, 7th ed., 2007, Houghton Mifflin, New York.

[18] A.J. Baird, L. R. Faulkner, *Electrochemical methods: Fundamentals and applications*, 2nd ed., 2001, John Wiley and Sons, New York.

[19] K. M Abraham and Z. Jiang, *J. Electrochem. Soc.*, 1996, **143**, 1 – 5.

[20] M. W. Chase, Jr., *NIST-JANAF thermochemical tables*, 4th ed., American Chemical Society and the American Institute of Physics for the National Institute of Standards and Technology, New York.

[21] J. Chen and F. Cheng, *Accounts. Chem. Res.*, 2009, **42**, 713 – 723.

[22] K. Kinoshita, Carbon: *Electrochemical and Physicochemical Properties*, 1988, John Wiley & Sons, New York.

[23] T. Nagaura and K. Tozawa, *Progress in Batteries and Solar Cells*, 1990, **9**, 209.

[24] M. Mirzaeian and P. J. Hall, *Journal of Power sources*, 2010, **195**, 6817 – 6824.

[25] G. X. Wang, S. Bewlay, M. Lindsay, Z. P. Guo, J. Yao, K. Konstatinov, H. K. Liu and S. X. Dou, *Materials Forum*, 2004, **27**, 33 – 44.

[26] M. Wakihara, Material Science and Engineering: R: Reports, 2001, **33**, 109 – 134.

[27] M. Mirzaeian and P. J. Hall, *Power System Tech.*, 2007, **31**, 90-96.

[28] K. Chung, M. W. Chung, W. S. Kim, S. K. Kim, Y. E. Sung, Y. K. Choi, *Bull. Korean Chem. Soc.*, 2001, **22**, 189 – 193.

[29] EEMB Lithium Battery Manufacturer, www.eemb.com (accessed January 2012).

[30] A. Debart, J. Bao, G. Armstrong and P. G. Bruce, *J. Power Sources*, 2007, **174**, 1177 – 1182.

[31] T. Ogasawara, A. Debart, M. Holzapfel, P. Novak and P. G. Bruce, *J. Am. Chem. Soc.*, 2006, **128**, 1390 – 1393.

[32] A. Debart, A. J. Paterson, J. Bao, and P. G. Bruce, *Angew. Chem. Int. Ed.*, 2008, **47**, 4521 – 4524.

[33] S. Flandrois and B. Simon, *Carbon*, 1999, **37**, 165-180.

[34] C. A. J. Fisher, M. S. Islam and H. Moriwake, *J. Phys. Soc. Jpn.*, 2010, **79**, 59 – 84.

[35] J. P. Schmidt, T. Chrobak, M. Ender, J. Illlig, D. Klotz, E. Ivers-Tiffee, *J. Power Sources*, 2011, **196**, 5342 – 5348.

[36] Z. Stoeva, R. Gomez, A. G. Gordon, M. Allan, D. H. Gregory, G. B. Hix, and J. J. Titman, *J. Am. Chem. Soc.*, 2004, **126**, 4066 -4067.

[37] Y. Takeda, M. Nishijima, M. Yamahata, K. Takeda, N. Imanishi, O. Yamamoto, *Solid State Ionics*, 2000, **130**, 61 – 69.

[38] M. Nishijima, T. Kagohashi, Y. Takeda, M. Imanishi, O. Yamamoto, *J. Power Sources*, 1997, **68**, 510 – 514.

[39] J. L. C. Rowsell, V. Pralong, L. F. Nazar, *J. Am. Chem. Soc.*, 2001, **123**, 8598 – 8599.

[40] B. L. Ellis, K. T. Lee and L. F. Nazar, *Chem. Mater.*, 2010, **22**, 691 – 714.

[41] J. Read, K. Mutolo, M. Ervin, W. Behl, J. Wolfenstine, A. Driedger, and D. Foster, *J. Electrochem. Soc.*, 2003, **150**, A1351 – A1356.

[42] M. Mirzaeian and P. J. Hall., *Electrochim. Acta*, 2009, **54**, 7444 – 7451.

[43] J. K. Ngala, S. Alia, A. Dobley, V. M. B. Crisotomo and S. L. Suib, *Chem. Mater.*, 2007, **19**, 229-234.

[44] L. Mao, D. Zhang, T. Sotomura, K. Nakatsu, N. Koshiba and T. Ohsaka, *Electrochim. Acta*, 2003, **48**, 1015 – 1021.

[45] P. Arora and Z. J. Zhang, *Chem. Rev.*, 2004, **104**, 4419 – 4462.

[46] M. Maja, C. Orecchia, M. Strano, P. Tosco and M. Vanni, *Electrochim. Acta*, 2000, **46**, 423 – 432.

[47] K. Kinoshita, *Electrochemical Oxygen Technology*, 1992, John Wiley & Sons, New York.

[48] S. S. Zhang, D. Foster and J. Read, *J. Power Sources*, 2010, **195**, 1235 – 1240.

[49] C. Chakkaravarthy, A. K. Abdul Waheed and H. V. K. Udupa, *J. Power Sources*, 1981, **6**, 203-228.

[50] Y. Tang, L. Lu, H. W. Roesky, L. Wang and B. Huang, *J. Power Sources*, 2004, **138**, 313-318.

[51] M.L. Doche, F.Novel-Cattin, R. Durand and J. J. Rameau, *J. Power Sources*, 1997, **65**, 197 – 205.

[52] Q. Li and L. J. Bjerrum, *J. Power Sources*, 2002, **110**, 1 – 10.

[53] A. R. Despic, D. M. Drazic, M. M. Purenovic, and N. Cikovic, *J. Appl. Electrochem.*, 1976, **6**, 527 – 542.

[54] C. A. Caldas, M.C. Lopes and I. A. Carlos, *J. Power Sources*, 1998, **74**, 108 – 112.

[55] E. L. Littauer and K. C. Tsai, *J. Electrochem. Soc.*, 1976, **123**, 771 – 776.

[56] J. Read, *J. Electrochem. Soc.*, 2002, **149**, A1190 – A1195.

[57] I. Kowalczk, J. Read and M. Salomon, *Pure Appl. Chem.*, 2007, **79**, 851 – 860.

[58] A. K. Thapa, S. Kazuki, H. Matsumoto and T. Ishihara, 216th ECS Meeting, Vienna, Austria, October 4 – 9, 2009, Abstract 687.

[59] W. Xu, J. Xiao, J. Zhang, D. Wang and J. G Zhang, *J. Electrochem. Soc.*, 2009, **156**, A773 – A779.

[60] O. Crowther, B. Meyer, M. Morgan and M. Salomon, *J. Power Sources*, 2011, **196**, 1498 – 1502.

[61] J. Read, *J. Electrochem. Soc.*, 2006, **153**, A96 – A100.

[62] S. D. Beattie, D. M. Manolescu, and S. L. Blair., *J. Electrochem. Soc.*, 2009, **156**, A44 - A47.

[63] A Kruger, *Carbon materials and nanotechnology*, 2010, Wiley-VCH, Germany.

[64] H. Marsh and F. Rodriguez-Reinoso, *Activated Carbon*, 2006, Elsevier, London.

[65] S. S. Zumdahl, S. A. Zumdahl, *Chemisty*, 8th ed., 2010, Brooks Cole, California.

[66] A. Putrovito, P.Davies, Bonds to Bands: Conduction Properties of Solids, University of Pennsylvannia, www.seas.upenn.edu/~chem101/sschem/conduction.html (accessed May 20120)

[67] H. Marsh, *Introduction to Carbon Science*, 1989, Butterworths, London.

[68] M. S. Dresselhaus, G. Dresselhaus, A. Jorio, *Group theory: Application to the physics of condensed matter*, 2008, Springer, Berlin.

[69] H. Shi, J. Barker, M. Y. Saidi, R. Koksbang and L. Morris, *J. Power Sources*, 1997, 68, 291 – 295.

[70] M. Fan, C. P. Huang, A. E. Bland, Z. Wang, R. Slimane, I. G. Wright, *Environanotechnology*, 2010, Elsevier, Oxford.

[71] K. Kinoshita, *Carbon: Electrochemical and Physicochemical Properties*, 1988, John Wiley & Sons, New York.

[72] F. Schuth, K. Sing, J. Weitkamp, *Handbook of porous solids*, Vol. 1, 2002 Wiley-VCH, Germany.

[73] J. R. Dahn, T. Zheng, Y. Liu and J. S. Xue, *Science*, 1995, **270**, 590 – 593.

[74] J. Li, X. Wang, Q. Huang, S. Gamboa and P. J. Sebastian, *J. Power Sources*, 2006, **158**, 784 – 788.

[75] B. Fang and L. Binder, *J. Power Sources*, 2006, **163**, 616 – 622.

[76] S. R. Mukai, C. Tamitsuji, H. Nishihara and H. Tamon, *Carbon*, 2005, **43**, 2618 – 2641.

[77] D. Wu, R. Fu, Z. Sun and Z. Yu, *J. Non-Cryst. Solids*, 2005, **351**, 915 – 921.

[78] www.sigma-aldrich.com (accessed May 2011).

[79] Y. Guo and D. A. Rockstraw, *Carbon*, 2006, **44**, 1464 – 1475.

[80] T. J. Bandosz, *Activated carbon surfaces in environmental remediation*, 2006, Elseiver, Oxford.

[81] S. W. Lee, N. Yabuuchi, B. M. Gallant, S. Chen, B. S. Kim, P. T. Hammond and Y. Shao-Horn, *Nat. Nanotechnol.*, 2010, **5**, 531 – 537.

[82] B. Kumar, J. Kumar, R. Leese, J. P. Fellner, S. J. Rodrigues and K. M. Abraham, *J. Electrochem. Soc.*, 2010, **157**, A50 - A54.

[83] Y. Wang and H. Zhou, *J. Power Sources*, 2010, **195**, 358 – 361.

[84] W. Xu, J. Xiao, D. Wang, J. Zhang, J-G Zhang, *J. Electrochem. Soc.*, 2010, **157**, A219 – A224.

[85] G. Q. Zhang, J. P. Zheng, R. Liang, M. Hendrickson and E. J. Plitcha, 217th ECS Meeting, Vancouver, Canada, April 25 – 30, 2010, Abstract 751.

[86] M. Eswaran, N. Munichandraiah and L. G. Scanlon, *Electrochem. Solid. St.*, 2010, **13**, A121-A124.

[87] A. Kraytsberg and Y. Ein-Eli, J. Power Sources, 2011, **196**, 886 – 893.

[88] T. Kuboki, T. Okuyama, T. Ohsaki and N. Takami, *J. Power Sources*, 2005, **146**, 766 – 769.

[89] H. Ye, J. Huang, J. J. Xu, A. Khalfan and S. G. Greenbaum, *J. Electrochem. Soc.*, 2007, **154**, A1048 – A1057.

[90] M. Armand and J. M. Tarascon, *Nature*, 2008, **451**, 652 – 657.

[91] W. Xiao, D. Wang and X. W. Lou, *J. Phys. Chem. C*, 2010, **114**, 1694 – 1700.

[92] J. G. Zhang, D. Wang, W. Xu, J. Xiao and R. E. Williford, *J. Power. Sources*, 2010, **195**, 4332 – 4337.

[93] S. S. Sandhu, J. P. Fellner and G. W. Brutchen, *J. Power. Sources*, 2007, **164**, 365 – 371.

[94] D. Zhang, Z. Fu, Z. Wei and T. Huang, *J. Electrochem. Soc.*, 2010, **157**, A362 – A365.

[95] C. Tran, X. Q. Yang and D. Qu, *J. Power Sources*, 2010, **195**, 2057 – 2063.

[96] S. J. Visco, B. D. Katz, Y. S. Nimon and L. C. Dejonghe, U. S. Patent 7282295 (Polyplus Battery Company), 2007.

[97] P. Stevens, G. Toussaint, G. Caillon, P. Viaud, P. Vinatier, C. Cantau, O. Fichet, C. Sarrazin, M. Mallouki, ECS Transactions, 2010, **28**, 1 – 13.

[98] M. T. Gilbert, J. H. Knox and B. Kaur, *Chromatographia*, 1982, **16**, 138 – 146.

[99] M. Weiner, G. Reichenauer, S. Braxmeier, F. Hemberger and H. P. Elbert, *Int. J. Thermophys*, 2009, **30**, 1372 – 1385.

[100] N. Job, B. Heinrichs, S. Lambert, J. P. Pirard, J. F. Colomer, B. Vertruyen and J. Marien, *AIChE. J.*, 2006, **52**, 2663 – 2676.

[101] T. Yamamoto, A. Endo, T. Ohmori and M. Nakaiwa, *Carbon*, 2004, **42**, 1671 – 1676.

[102] R. B. Durairaj, *Resorcinol: Chemistry, Technology and Applications*, 2005, Springer, Berlin.

[103] A. Knop, L. A. Pilato, *Phenolic resins: Chemistry applications and performance, future directions*, 1985, Springer, Berlin.

[104] M.F. Grenier – Loustalot, S. Larroque, D. Grande, P. Grenier, *Polymer*, 1996, **37**, 1363 – 136.

[105] D. Fairen-Jimenez, F. Carrasco-Maarin, C. Moreno-Castilla, *Carbon*, 2006, 44, 2301 – 2307.

[106] N. Husing and U. Schubert, 2006. *Aerogels. Ullmann's Encyclopedia of Industrial Chemistry*.

[107] S. A. Al-Muhtaseb and J. A. Ritter, *Adv. Mater.*, 2003, **15**, 101-114.

[108] G. Reichenauer, 2008. *Aerogels. Kirk-Othmer Encyclopedia of Chemical technology*.

[109] A. C. Pierre, 2007. *Sol-Gel Technology. Kirk-Othmer Encyclopedia of Chemical Technology*.

[110] M. Mirzaeian and P. J. Hall, *J. Mater. Sci.*, 2009, **44**, 2705 – 2713.

[111] H. Tamon, H. Ishizaka, T. Yamamoto and T.Suzuki, *Carbon*, 1999, **37**, 2049 – 2055.

[112] IUPAC. Compendium of Chemical Technology, 2nd ed. (the "Gold Book"). Compiled by A. D. McNaught and A. Wilkinson. Blackwell Scientific Publications, Oxford (1997). XML on-line correct version: http://goldbook.iupac.org (2006-) created by M. Nic, J. Jirat, B. Kosata; updates compiled by A. Jenkins.

[113] D. Sangeeta, J. R. LaGraf, *Inorganic materials chemistry: Desk reference*, 2nd Ed. 2005, CRC Press Florida.

[114] G. O. Shitta-Bey, M. Mirzaeian, P. J. Hall, *J. Sol-Gel Sci. Techn.*, 2011, **57**, 178 – 184.

[115] Asbury Carbons, www.asbury.com (accessed February 2010).

[116] P. V. Samant, F. Goncalves, M. M. A. Freitas, M. F. R. Pereira and J. L. Figueiredo, *Carbon*, 2004, **42**, 1321 – 1325.

[117] H. Teng, S. C. Wang, *Carbon*, 2000, **38**, 817 – 824.

[118] S. J. Gregg and K. S. W. Sing, *Adsorption, surface area and porosity*, 1967, Academic Press, New York.

[119] K. S. W. Sing, D. H. Everett, R. A. W. Haul, L. Moscou, R. A. Pierotti, J. Rouquerol and T. Siemieniewska, *Pure. Appl. Chem.*, 1985, **57**, 603 – 619.

[120] S. Brunauer, P. H. Emmett and E. Teller, *J. Am. Chem. Soc.*, 1938, **60**, 309 – 319.

[121] Y. Quanhong, L. Chang, L. Min, F. Yanzhen, C. Hiuming, W. Maozhng, *Sci. China Ser. E*, 2002, **45**, 561 – 568.

[122] H. Y. Erbil, *Surface chemistry of solid and liquid interfaces*, 2006, Blackwell Pubishing, Oxford.

[123] K. K. Aligizaki, *Pore structure of cement-based materials: Testing, interpretation and requirements*, 2006, Taylor and Francis, Abingdon.

[124] I. Langmuir, *J. Am. Chem. Soc.*, 1918, **40**, 1361 – 1403.

[125] S. Lowell and J. E. Shields, *Powder Surface Area and Porosity,* 3rd ed., 1991, Chapman and Hall, London.

[126] R. C. Bansal, M. Goyal, *Activated carbon adsorption*, 2005, Taylor and Francis, Abingdon.

[127] F. Rouquerol, J. Rouquerol, and K. Sing, *Adsorption by Powders and Porous Solids: Principles, Methodology, and Applications*, 1999, Academic Press, San Diego.

[128] E. P. Barrett, L. G. Joyner and P. P. Halenda, *J. Am. Chem. Soc.*, 1951, **73**, 373 – 380.

[129] T. Allen, *Particle Size Measurement: Surface Area and Pore Size Determination*, Vol. 2, 5th ed., 1997, Chapman and Hall, London.

[130] S. Brunauer, *Pure Appl. Chem.*, 1976, **48**, 401 – 405.

[131] J. H. De Boer, B. C. Lippens, B. G. Linsen, J. C. P. Broekhoff, A. V. Heuvel and T. J. Osinga, *J. Colloid Interf. Sci.*, 1966, **21**, 405 – 414.

[132] Micrometrics ASAP 2420 Operator’s Manual V2.01, June 2007.

[133] S. R. Sandler, W. Karo, J. A. Bonesteel and E. M. Pearce, *Polymer Synthesis and Characterization, A Laboratory Manual*, 1998, Academic Press, San Diego.

[134] P. J. Haines, *Principles of thermal analysis and calorimetry,* 2002, Royal Society of Chemistry, Cambridge.

[135] Introduction to thermogravimetry, www.anasys.co.uk (accessed January 2012).

[136] B. C. Smith, *Fundamentals of fourier transform infrared spectroscopy,* 2nd Ed., 2011, Taylor and Francis, New York.

[137] Introduction to fourier transform spectroscopy. Molecular materials research centre website, http://mmrc.caltech.edu/FTIR/FTIR.html (accessed November 2010).

[138] J. P. Sibilia, *A Guide to Materials Characterization and Chemical Analysis*, 2nd ed, 1996, John Wiley & Sons, New York.

[139] R. W. Pekala, *J. Mater. Sci.,* 1989, **24**, 3221-3227.

[140] J. P. Cain, P. L. Gassman, H. Wang, A. Laskin, *Phys. Chem. Chem. Phys.,* 2012, **12**, 5206 – 5218.

[141] D. J. O' Connor, B.A. Sexton, R. St. C. Smart, *Surface analysis methods in materials science,* 2nd ed., 2003, Springer, Berlin.

[142] D. Brune, R. Hellborg, H. J. Whitlow, O. Honderic, *Surface characterization: A user's source book*, 1997, Wiley-VCH, Berlin.

[143] American Society For Mass Spectrometry, www.asms.org (accessed January 2012).

[144] J. Goldstein, D. Newbury, D. Joy, C. Lyman, P. Echlin, E. Lifshin, L. Sawyer, J. Michael, *Scanning electron microscopy and x-ray microanalysis*, 3rd ed., 2002, Kluwer Academic/Plenum Publishers, New York.

[145] N. Yao, Z. L. Wang, *Handbook of microscopy for nanotechnology*, 2005, Kluwer Academic Publishers, New York.

[146] R.M. Weinbrandt, I. Fatt, *J. Petrol. Technol.*, 1969, **21**, 543 – 548.

[147] Solatron User Guide, Solatron Analytical Ltd, 2005.

[148] D. Berndt, D. Spahrbier, 2001. *Batteries. Ullmann's Encyclopedia of industrial chemistry*.

[149] R. K. Sinnot, *Coulson and Richardson's Chemical Engineering*, Vol. 6, 3rd ed., 1999, Butterworth-Heinemann, Oxford, 947 – 967.

[150] V.Ruiz, C. Blanco, M. Granda, R. Menendez and R. Santamaria, *J. Appl. Electrochem.*, 2007, **37**, 717 – 721.

[151] FTIR sample preparation, University of Illinois, http://www.niu.edu/analyticallab/ftir/sample preparation, (accessed February 2010).

[152] F. W. Langkilde, A. Svantesson, *J. Pharmaceut. Biomed.*, 1995, **13**, 409 – 414.

[153] Saffron Scientific Equipment Ltd, www.saffron-uk.com (accessed December 2010)

[154] M. A. Aegerter, N. Leventis, M. M. Koebel, *Aerogels Handbook*, 2011, Springer, Newyork.

[155] D. E. Simaneck, Lock Haven University, Error analysis, http://www.lhup.edu (accessed February 2012).

[156] M. Weiner, G. Reichenauer, F. Hemberger, H. P. Ebert, *Int. J. Thermophys.*, 2006, **27**, 1826 – 1843.

[157] D. R. Lide, *CRC Handbook of chemistry and physics*, 89th Ed., 2008, CRC Press, Florida.

[158] T. Yamamoto, T. Nishimura, T. Suzuki and H. Tamon, *J. Non-cryst. Solids*, 2001, **288**, 46 – 55.

[159] T. Yamamoto, T. Nishimura, T. Suzuki and H. Tamon, *Carbon*, 2001, **39**, 2374 – 2376.

[160] H. Tamon, H. Ishizaka, T. Yamamoto and T.Suzuki, *Carbon*, 2000, **38**, 1099 – 1105.

[161] M. Weiner, G. Reichenauer, T. Scherb, J. Fricke, *J. Non-Cryst. Solids*, 2004, **350**, 126 – 130.

[162] S. R. Kumar, P. K. Pillai, K. G. K. Warrier, *Polyhedron*, 1998, **17**, 1699 – 1703.

[163] K. B. Ameen, K. Rajasekar, T. Rajasekharan, M.V. Rajasekaran, *J. Sol – Gel Sci. Technol.*, 2008, **45**, 9 – 15.

[164] C. Scherdel, G. Reichenauer, *Micropor. Mesopor. Mat.*, 2009, **126**, 133 – 142.

[165] C. Scherdel, R. Gayer and T. Slawik, *J. Porous. Mater.*, DOI: 10.1007/s10934-010-9396-y.

[166] M. J. Mosquera, D. M. del los Santos, L. Valdez-Castro and L. Esquivias, *J. Non- cryst. Solids*, 2008, **354**, 645 – 65.

[167] G. W. Scherer, *J. Non-Cryst. Solids*, 1988, **100**, 77 – 92.

[168] N. Job, A. Thery, R. Pirard, J. Marien, L. Kocon, J. N. Rouzaud, F. Beguin and J. P. Pirard, *Carbon*, 2005, **43**, 2481 – 2494.

[169] H. Tamon, H. Ishizaka, M. Mikami and M. Okazaki, *Carbon*, 1997, **35**, 791-796.

[170] W. C. Li, A. H. Lu, S. C. Guo, *Carbon*, 2001, **39**, 1989 – 1994.

[171] J. Kuhn, R. Brandt, H. Mehling, R. Petricevic and J. Fricke, *J. Non-Cryst Solids*, 1998, **225**, 58 – 63.

[172] C. Darne, F. Terzetti, C. Coulais, J. Fournier, Y. Guichard, L. Gate, S. Binet, *Ann. Occup. Hyg*., 2010, **54**, 532 – 544.

[173] S. Q. Zhang, J. Wang, J. Shen, Z. S. Deng, Z. Q. Lai, B. Zhou, S. M. Attia and L. Y. Chen, *Nanostruct. Mater.*, 1999, **11**, 375 – 381.

[174] T. Wigmans, J. V. Doorn and J. A. Moulijn, Fuel, 1983, **62**, 190 – 195.

[175] S. Yuasa, *Proc. Combust. Inst.*, 1985, **20**, 1869 – 1876.

[176] S. R. Tennison, *Appl. Catal. A – Gen.*, 1998, **173**, 289 – 311.

[177] P. Davini, *Carbon*, 2001, **39**, 1387 – 1393.

[178] E. M. Suuberg, I. Aarna, *Carbon*, 2007, **45**, 1719 - 1726.

[179] J. Coates, *Interpretation of Infrared Spectra, A practical Approach, Encyclopedia of Analytical Chemistry,* (ed. R. A. Meyers), 2000, John Wiley & Sons, Chichester, 10815 – 10837.

[180] J. Xiao, D. Wang, W. Xu, D. Wang, R. E. Williford, J. Liu and J. G. Zhang, *J. Electrochem. Soc.*, 2010, **157**, A487 – A492.

[181] R. Pynn, *Los Alamos Science*, 1990, **19**, 1 - 32.

[182] F. Mizuno, S. Nakanishi and H. Iba, The 15th International Meeting on Lithium Batteries, June 27 – July 2, 2010, Montreal, Quebec, Canada Abstract 819.

[183] K. Takechi, E. Sudo, T. Inaba, F. Mizuno, H. Nishikoori and T. Shiga, 218th ECS Meeting, Oct 10 – 15, 2010, Las Vegas, Nevada, Abstract 586.

[184] J. R. Taylor, *An introduction to error analysis: The study of uncertainties in physical measurements*, 2nd Ed. University Science Books, 1997.

[185] D. M. Harrison, Error analysis in experimental physical science, http://www.upscale.utoronto.ca/PVB/PVB.html, (accessed June 2011).

[186] S. Han, K. T. Lee, S. M. Oh and T. Hyeon, *Carbon*, 2003, **41**, 1049 – 1056.

[187] G. Soto-Garrido, C. Aguilar, R. Garcia, Renan Arriagada, *J. Chil. Chem. Soc.*, 2003, **48**, doi:10.4067/S0717-97072003000300013.

[188] H. Cheng and K. Scott, *J. Power Sources*, 2010, **195**, 1370 – 1374.

[189] R. A. Pethrick and J. V. Dawkins, *Modern Techniques for Polymer Characterisation*, 1999, John Wiley & Sons, Chichester.

APPENDICES

APPENDIX A

TGA Measurement of CPF9 under Oxygen

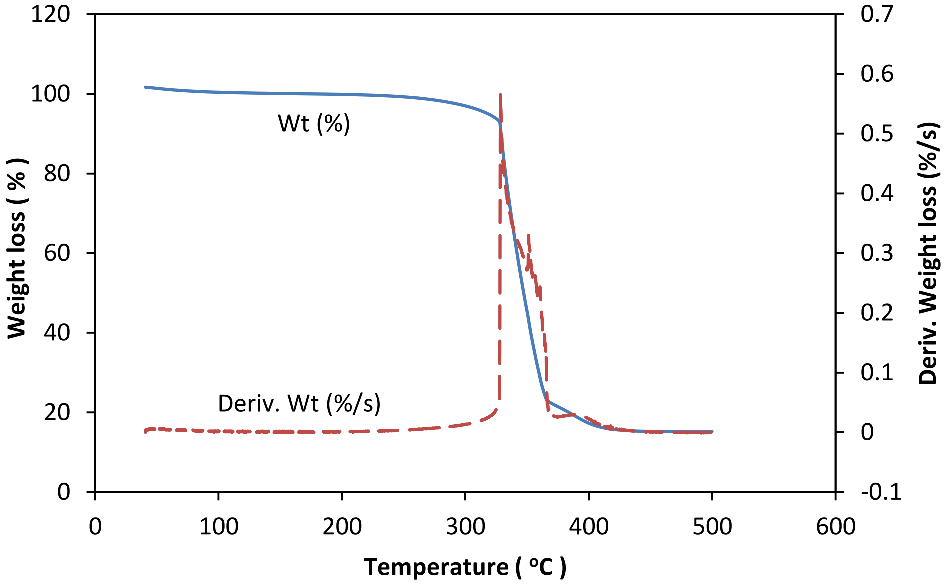

Figure A1.1: TGA measurement for CPF9 under O_2, which was used as the basis for the temperature range chosen for O_2 activation experiments described in Section 5.3.1 (wt (%) refers to the weight loss curve and Deriv. Wt (%/s) refers to the derivative weight loss curve)

APPENDIX B

Acronyms and Abbreviations

ACPF	Activated carbonised phenol-formaldehyde gel
Acet.	Acetone
Av	Average of three measurements
BDG	Butyl diglyme (diethylene-glycol-ether)
BEE	1-tert-butoxy-2-ethoxyethane
BET	Brunauer-Emmett-Teller
BJH	Barret-Joyner-Halenda
C	Catalyst (sodium carbonate)
CPF	Carbonised phenol-formaldehyde gel
Cycl. No	Cycle number
D. Met.	Drying method
$\mathbf{D_{avg}}$	Average pore diamter
DEC	Diethyl carbonate
DEE	1,2-diethoxy/ethane
DG	Diglyme (diethylene-glycol-dimethyl-ether)
DC	Discharge capacity
DME	1,2-dimethoxy/ethane
$\mathbf{D_{peak}}$	Peak diameter corresponding to the largest pore size
DPG	Diproglyme (dipropylene-glycol-dimethyl-ether)
EC	Ethylene carbonate
EDG	Ethyl diglyme (diethylene-glycol-diethyl-ether)
EDLC	Electrochemical double layer capacitor
EDS	Energy Dispersive X-ray Spectroscopy
EMD	Electrolytic manganese dioxide
EV	Electric vehicle
F	Formaldehyde
F.D.	Freeze drying
FTIR	Fourier Transform Infrared
HEV	Hybrid electric vehicle
IR	Infrared
m/z	Mass to charge ratio
nA	Nanoamps
NC	Capacity normalised to mesopore volume
ND	Not detected
NMR	Nuclear Magnetic Resonance

P	Phenol
P/C	Phenol to catalyst ratio
P/F	Phenol to formaldehyde ratio
P/W	Concentration of phenol in water
pA	Picoamps
PC	Propylene carbonate
PF	Phenol-formaldehyde
PVDF/HFP	Polyvinyl-lidene difluoride/hexafluoropropylene
RF	Resorcinol-formaldehyde
r_{peak}	Peak radius
RTIL	Room temperature ionic liquid
S. E. Liq.	Solvent exchange liquid
S_{BET}	BET surface area
SEI	Solid electrolyte interface
SEM	Scanning Electron Microscopy
t-but	Tertiary butanol
TGA	Thermogravimetric Analysis
UV-VIS	Ultraviolet-Visible
V. D.	Vacuum drying
V_{meso}	Mesopore volume
V_{micro}	Micropore volume
V_{total}	Total pore volume
W	Water (deionised)
XPS	X-ray Photoelectron Spectroscopy
ΔCN	Average deviation for cycle number
ΔDC	Average deviation for discharge capacity
ΔNC	Average deviation for capacity normalised to mesopore volume
ΔS_{BET}	Average deviation for BET surface area
ΔV_{meso}	Average deviation for mesopore volume
ΔV_{micro}	Average deviation for micropore volume
ΔV_{total}	Average deviation of total pore volume

APPENDIX C

Sample nomenclature, synthesis parameters and treatment

C1 Gels

Table C1.1: Gel nomenclature, synthesis parameters and treatment

Sample	**P/C**	**P/F**	**P/W (mol/l)**	**Drying method**	**Solvent exchange liquid**
PF1	3	0.5	1.06	Freeze drying at -30 ^{o}C	t-butanol
PF2	6	0.5	1.06	Freeze drying at -30 ^{o}C	t-butanol
PF3	8	0.5	1.06	Freeze drying at -30 ^{o}C	t-butanol
PF4	10	0.5	1.06	Freeze drying at -30 ^{o}C	t-butanol
PF5	12	0.5	1.06	Freeze drying at -30 ^{o}C	t-butanol
PF6	8	0.5	1.06	Vacuum drying at 40 ^{o}C	t-butanol
PF7	8	0.5	1.06	Vacuum drying at 40 ^{o}C	Acetone
PF8	8	0.5	1.06	Vacuum drying at 70 ^{o}C	t-butanol
PF9	8	0.4	1.06	Freeze drying at -30 ^{o}C	t-butanol
PF10	8	0.6	1.06	Freeze drying at -30 ^{o}C	t-butanol

C2 Carbons

Table C2.1: Carbon nomenclature, synthesis parameters and treatment

Sample	**Carbonisation temperature (^{o}C)**	**Duration of carbonisation at stated temperature (mins)**	**Argon flowrate (ml/min)**
CPF3-600 ^{o}C	600 ^{o}C	180	200
CPF3-700 ^{o}C	700 ^{o}C	180	200
CPF3 -800 ^{o}C	800 ^{o}C	180	200
CPF3-900 ^{o}C	900 ^{o}C	180	200
CPF3-1000 ^{o}C	1000 ^{o}C	180	200
CPF3-1050 ^{o}C	1050 ^{o}C	180	200
CPF9-1000 ^{o}C (or CPF9-1)	1000 ^{o}C	180	200
CPF9-1050 ^{o}C (or CPF9-2)	1050 ^{o}C	180	200

C3 Activated carbons

Table C3.1: Activated carbon nomenclature, synthesis parameters and treatment

Sample	**Activating temperature (^oC)**	**Duration of activation at stated temperature (mins)**	**Activating reagent (gas)**	**Activating gas flowrate (ml/min)**
ACPF9-1-O_2/300/20	300	20	O_2	100
ACPF9-1-O_2/450/20	450	20	O_2	100
ACPF9-2-O_2/300/30	300	30	O_2	370
ACPF9-2-O_2/500/30	500	30	O_2	370
ACPF9-2-CO_2/800/15	800	15	CO_2	200
ACPF9-2-CO_2/800/30	800	30	CO_2	200
ACPF9-2-CO_2/800/60	800	60	CO_2	200
ACPF9-2-CO_2/800/90	800	90	CO_2	200
ACPF9-2-CO_2/800/120	800	120	CO_2	200

APPENDIX D

Publications

J Sol-Gel Sci Technol (2011) 57:178–184
DOI 10.1007/s10971-010-2339-x

ORIGINAL PAPER

Effect of composition, solvent exchange liquid and drying method on the porous structure of phenol–formaldehyde gels

Gbolahan O. Shitta-Bey · Mojtaba Mirzaeian · Peter J. Hall

Received: 1 September 2010 / Accepted: 25 September 2010 / Published online: 14 October 2010

Abstract Organic gels have been synthesized by sol–gel polycondensation of phenol (P) and formaldehyde (F) catalyzed by sodium carbonate (C). The effect of synthesis parameters such as phenol/catalyst ratio (P/C), solvent exchange liquid and drying method, on the porous structure of the gels have been investigated. The total and mesopore volumes of the PF gels increased with increasing P/C ratio in the range of P/C $\leq$ 8, after this both properties started to decrease with P/C ratio for P/C > 8 and the gel with P/C = 8 showed the highest total and mesopore volumes of 1.281 and 1.279 cm^3 g^{-1} respectively. The gels prepared by freeze drying possessed significantly higher porosities than the vacuum dried gels. The pore volume and average pore diameter of the freeze dried gels were significantly higher than those of the vacuum dried gels. T-butanol emerged as the preferred solvent for the removal of water from the PF hydrogel prior to drying, as significantly higher pore volumes and specific surface areas were obtained in the corresponding dried gels. The results showed that freeze drying with t-butanol and lower P/C ratios were favourable conditions for the synthesis of highly mesoporous phenol–formaldehyde gels.

Keywords Phenol–formaldehyde gels · Synthesis parameters · Porosity · Production

1 Introduction

Organic gels with controlled porous structures can be synthesized via the sol–gel polycondensation of resorcinol and formaldehyde (F) using sodium carbonate as the catalyst (C) [1]. Pyrolysis of these gels under inert atmosphere produces carbon gels with porous properties similar to the porosity parameters of the original gel precursors [2, 3]. These materials can be used for a variety of applications such as adsorbents for gas separation [4], catalyst supports [5], electrodes for energy storage devices [6–8], packing materials for chromatography [9] and thermal insulators [10].

In the attempt to reduce the raw materials costs in the gel synthesis, resorcinol can be replaced with a cheaper alternative such as phenol [11, 12]. Phenol (P) has a negative charge in its 2, 4, 6 ring positions and therefore undergoes a similar sol–gel polycondensation reaction to resorcinol [13]. However, the lack of one OH group in phenol compared to resorcinol results in a lower electron density leading to a lower solubility in water [13] and lower reactivity [14] for phenol. This leads to a slower reaction rate for the polycondensation of PF gels [12]. As a result, the P/C ratio for the synthesis of PF gels is much lower than the resorcinol/catalyst (R/C) ratio used for the synthesis of resorcinol–formaldehyde (RF) gels [12], to prevent segregation and increase reaction rate [13]. As PF gels possess a high level of mesoporosity [11], they are suitable organic precursors for the preparation of highly mesoporous carbons which can be used for a wide variety of applications. Wu et al. [11] have synthesized PF gels with densities in the range of 0.22–0.37 g cm $^{-3}$, specific surface areas of up to 522 m^2 g^{-1} and with mesopore volumes up to 1.43 cm^3 g^{-1}.

Although PF gels have been used for the preparation of highly mesoporous carbons [11, 12], there have been only

---

G. O. Shitta-Bey · M. Mirzaeian (✉) · P. J. Hall (✉)
Department of Chemical and Process Engineering,
University of Strathclyde, Glasgow G1 1XJ, UK
e-mail: mojtaba.mirzaeian@strath.ac.uk

P. J. Hall
e-mail: p.j.hall@strath.ac.uk

limited studies on the effect of synthesis parameters such as gelation temperature, PF content, phenol/formaldehyde ratio and phenol/catalyst ratio on the porous structure of PF gels [11, 12], and less is known about the effect of drying methods on the porosity of the PF dried gels. In the aforementioned studies of the effect of P/C ratio on the porous structure of PF gels, the gels were synthesized at P/C ratios of 8.5 and 10 [11]. This work however investigates the effect of P/C ratios over a wider range, in addition to the effect of solvent exchange liquids such as acetone and t-butanol, and also effect of drying methods such as vacuum drying for acetone exchanged; and both freeze drying and vacuum drying for t-butanol exchanged gels, on the porous structure of the PF gels.

2 Experimental

The following materials were used in the PF gel production: Phenol [C_6H_50H, Sigma-Aldrich, 99%], formaldehyde [(HCHO), Sigma-Aldrich, a solution of 37% in water containing 10–15% methanol as stabilizer], sodium carbonate anhydrous [Na_2CO_3, Sigma-Aldrich, $\geq$99.5%], Tertiary –butyl alcohol (t-butanol) [Sigma-Aldrich, 99.5%], acetone [Sigma-Aldrich, 99.5%].

The PF gels were synthesized by the sol–gel polycondensation of phenol (P) and formaldehyde (F), using sodium carbonate (C) as the catalyst, according to a procedure described elsewhere [12]. P, C and F, were mixed in water under vigorous stirring to form homogeneous PF solutions. The molar ratio of phenol to formaldehyde, P/F, and phenol to water, P/W (g mol^{-1}), were kept constant and the ratio of phenol to catalyst, P/C, was varied during the synthesis of the gels. The PF solutions were transferred to sealable flasks and gelled by curing for 4 days at 90 °C at atmospheric pressure. The hydrogels were then solvent exchanged with t-butanol or acetone for 3 days to replace residual water in the sample prior to the drying process. PF aerogels were prepared by drying in a vacuum oven at 70 °C for 2 days (high temperature) or 40 °C for 3 days (low temperature), while PF cryogels were prepared by freeze drying under vacuum at −40 °C for 3 days.

The porous structure of the PF gels were determined by the analysis of nitrogen adsorption/desorption isotherms measured by ASAP 2420 adsorption analyzer (Micrometrics) at 77 K. The samples were degassed at 90 °C for 3 h prior to adsorption measurements. BET method was used to determine the surface areas of the samples and t-plot method was used for micropore analysis. The mesoporosity was analysed by the BJH method. The total pore volumes were calculated based on the adsorbed volume of nitrogen at $P/P_0 = 0.99$ [1]. Pore size distributions were determined by applying BJH method to the desorption isotherms [15].

3 Results and discussion

To identify the production conditions that maximized porosity levels, the first step was to identify the optimal P/C ratio. Figure 1 shows the nitrogen adsorption/desorption isotherms at 77 K for PF gels with different P/C ratios that had been freeze-dried at −40 °C. For clarity only three isotherms are shown in Fig. 1. The isotherms are typical of type IV isotherms with hysteresis loops indicating the presence of mesopores [16]. This is consistent with previous work carried out on this type of gels [12]. The lower and upper parts of the hysteresis loop represent capillary condensation and evaporation in the mesopores respectively [16].

The porosity parameters of the gels are given in Table 1. Figure 1 shows that for $P/C > 8$, the quantity of gas adsorbed starts to decrease with P/C ratio, indicating a decrease in the level of porosity of the gels. It can be seen that the total pore and mesopore volumes of the gels increase with P/C ratio for $P/C \leq 8$ indicating development of mesoporosity in the gel structure. The gel with P/C ratio of 8 shows the highest mesopore volume of 1.279 $cm^3\ g^{-1}$.

Table 1 shows a decrease in pore volumes for $P/C > 8$. These results show that the P/C ratio is one of the main parameters to control the porosity of PF gels, as catalyst instigates the formation of initial nuclei in the polycondensation reaction between phenol and formaldehyde [11]. An increase in P/C ratio (decrease in the catalyst concentration) in the range of 3–8 lead to a decrease in the amount of initial nuclei, allowing for greater particle growth that leads to the formation of larger pore size and results in an increase in pore volume [11, 17]. It is believed that for $P/C > 8$ a further increase in P/C ratio (a decrease in catalyst concentration) results in the collapse of the porous structure of the gel and decrease in the pore volume during

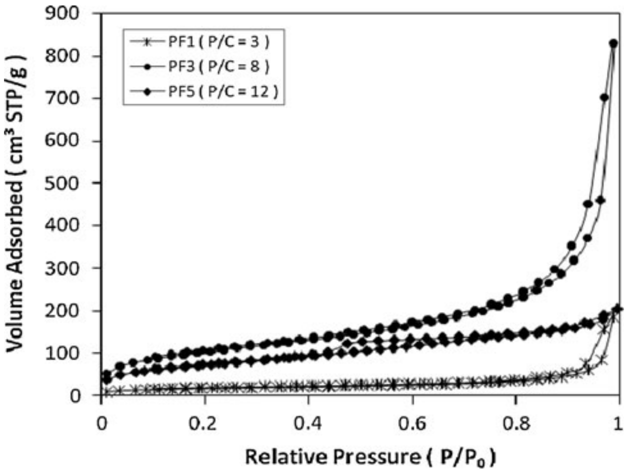

Fig. 1 N_2 adsorption/desorption isotherms at 77 K for PF gels with different P/C ratios freeze dried at −40 °C

Table 1 Pore characteristics of PF gels freeze dried at −40 °C

Sample	P/C	S_{BET} (m^2 g^{-1})	V_{total} (cm^3 g^{-1})	V_{micro} (cm^3 g^{-1})	V_{meso} (cm^3 g^{-1})	%V_{micro}	%V_{meso}	D_{avg} (nm)
PF1	3	58	0.284	0.0029	0.281	1.02	98.98	19.4
PF2	6	380	0.761	0.0115	0.749	1.51	98.49	8.0
PF3	8	369	1.281	0.0023	1.279	0.18	99.82	13.9
PF4	10	249	0.355	0.0034	0.352	0.96	99.04	5.7
PF5	12	258	0.316	ND	N/A	N/A	N/A	4.9

S_{BET} BET surface area, V_{total} total pore volume, V_{micro} micropore volume, V_{meso} mesopore volume (V_{total}–V_{micro}), *ND* not detectable, *N/A* not applicable

the gelation, due to the lack of sufficient catalyst to enable formation of a completely three dimensional cross-linked structure.

Figure 2a shows the pore size distribution (PSD) curves of freeze-dried PF gels with different P/C ratios. The PSD curves for pore diameter in the range of 2–5 nm are magnified and shown in Fig. 2b clearly. The PSD curves shown in Fig. 2a for PF gels synthesized with P/C ratios above 8 (PC; 10 and 12) show peaks in the range of 3.5–4.5 nm indicating the presence of small mesopores in the gel structure.

In the case of PF gels synthesized with P/C ratios ≤8, gels with P/C ratio of 6 and 8 shows PSD curves with two peaks in small and large pore diameter regions. The first peak (shown in Fig. 2b) shows the contribution of small mesopores and the second peak (shown in Fig. 2a) shows the contribution of large mesopores to the gel structure. The results of volumetric measurements on these two gels given in Table 1 show that their structure is predominantly mesoporous with higher pore volume compared to all PF gels shown in Fig. 2a. PF gel with P/C = 8 possesses the highest mesopore volume of 1.279 cm^3 g^{-1} and average pore size of 13.9 nm.

For the gel prepared with P/C ratio of 3, the PSD curve in Fig. 2a shows that the gel structure consists entirely of large mesoporous with average pore size of 19.4 nm given in Table 1. This gel has a mesopore volume of 0.281 cm^3 g^{-1}, which is much lower that the mesopore volume of gel prepared with P/C ratio of 8. These results show that P/C ratio plays an important role in the control of the porous structure of PF gels, and that a P/C ratio of 8 is optimum for the synthesis of highly mesoporous PF gels to maximise pore volume.

The next step in determining optimal porosity production conditions was to identify the best solvent exchange liquid. Although a number of possible candidates were tested, for brevity only two will be compared here to illustrate the importance of the exchange liquid, the lower boiling acetone and the higher boiling t-butanol. Figure 3 shows the adsorption/desorption isotherms for acetone and t-butanol exchanged PF gels prepared with P/C ratio of 8. The pore characteristics of the samples are given in Table 2.

There is a significant difference in nitrogen adsorption/desorption isotherms when acetone and t-butanol were used as solvents to remove water from the hydrogel structure. Data given in Table 2 shows that the t-butanol exchanged samples contain much higher specific surface areas and larger pore volumes. Figures 4a shows the PSD curves for t-butanol and acetone exchanged PF gels prepared with P/C ratio of 8. The PSD curves for pore diameter in the range of 2–20 nm are magnified and shown in Fig. 4b clearly. The PSD curves in Fig. 4a and b show that the acetone exchanged sample (PF8) exhibits almost a non-porous structure with a very low pore volume of 0.0034 cm^3 g^{-1} (see Table 2) indicating acetone does not help to maintain

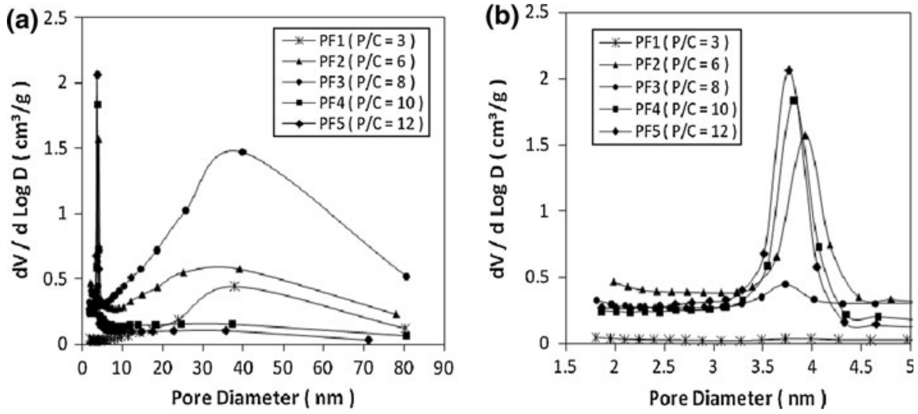

Fig. 2 Pore size distribution of freeze dried PF gels with different P/C ratios

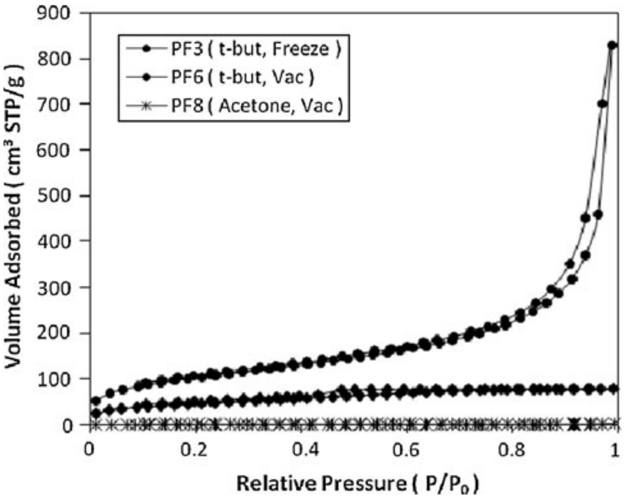

Fig. 3 N_2 adsorption/desorption isotherms of t-butanol and acetone exchanged PF gels prepared with P/C ratio of 8

the porosity of PF hydrogels during the drying process and cannot be considered as a solvent exchange liquid for this type of gels. It is believed that the higher extent of capillary forces exerted on the walls of the pores in the gel structure leads to the collapse of the porous structure for the vacuum dried acetone exchanged gel. There are two possible explanations for this given as follow.

The first possible explanation is that: the vapor pressure of solvent within the porous structure of the gel depends on the pore diameter, the liquid–vapor interfacial energy and the wetting angle (Kelvin–Helmholtz equation). In pores with a small diameter the vapor pressure is smaller than in very fine pores and therefore the capillary force exerted on a wall is inversely proportional to the pore diameter. On drying, the fluid in the pore space is stressed, while the solid network is in compression, leading to the contraction of the solid network. The stresses in the pore liquid and the solid balance each other almost [18, 19], however as the wet gel has a spectrum of pore diameters, there is a spectrum of capillary forces acting on the gel network, meaning the contraction stresses are different and stress gradients exist. In fact these differential capillary forces exerted onto the gel network, but not their absolute value, lead to the collapse of the gel network.

The rate of evaporation is directly proportional to the evaporation pressure. Due to the low boiling point of acetone its rate of evaporation during the vacuum drying process is high. Faster evaporation with acetone then only means that the rate of stress change exerted on the network is larger [19]. The experimental results suggest that the gel-network is not able to withstand this higher stress rate compared to that if a slow evaporation with t-butanol applies and thus it is compressed leading to a collapse of the porous network.

There is, however also another possible explanation that: the solid network is continuously ageing during drying. Slow evaporation gives more time for aging and thus for stiffening of the network compared to fast evaporation. But the aging rate depends on the solubility of the chemical constituents in the pore fluid. The larger the solubility, the faster the aging (this is a variant of Ostwald ripening).

Table 2 Porous characteristics of PF gels with P/C ratio of 8 prepared by different solvent exchange liquids

Sample	Solvent exchange liquid	S_{BET} (m^2 g^{-1})	V_{total} (cm^3 g^{-1})	V_{micro} (cm^3 g^{-1})	V_{meso} (cm^3 g^{-1})	$\%V_{micro}$	$\%V_{meso}$	D_{avg} (nm)
PF3	t-butanol	369	1.2813	0.0023	1.2790	0.18	99.82	13.9
PF6	t-butanol	159	0.1211	0.0057	0.1154	4.71	95.29	3.0
PF8	Acetone	0.97	0.0034	0.0002	0.0032	5.88	94.12	13.9

PF3: Freeze dried at −40 °C, PF6: Vacuum dried at 40 °C and PF8: Vacuum dried at 40 °C

Fig. 4 Pore size distribution of gels prepared by different solvent exchange liquids (P/C = 8)

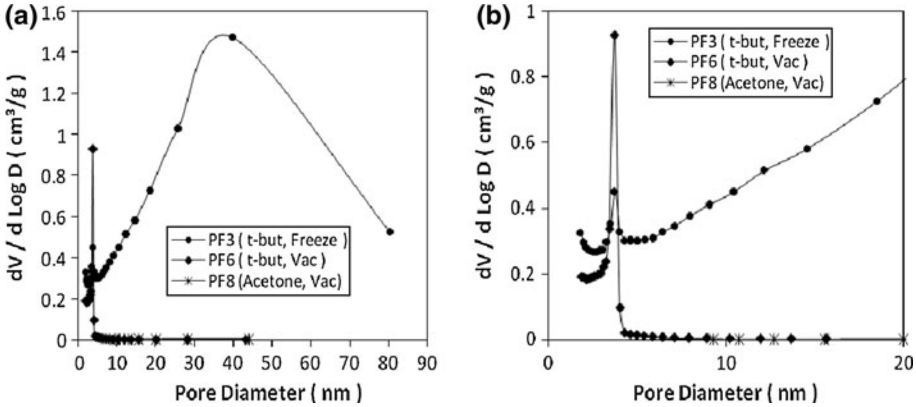

Thus, provided a similar solubility of phenol in acetone and t-butanol, the slower evaporation rate in t-butanol would lead to more time for aging and thus less crack susceptibility and of course less compaction and the wet gel structure would be better preserved.

The PSD curves for t-butanol exchanged PF gels (PF3 and PF6) in Fig. 4a show a narrow distribution for vacuum dried gel (PF6) with a pore volume of 0.1211 cm^3 g^{-1} and average pore diameter of 3 nm; and a wider distribution for freeze dried gel (PF3) with a pore volume of 1.2813 cm^3 g^{-1} which is the highest pore volume of all dried samples and average pore diameter of 13.9 nm. These results show that the level of porosity in both t- butanol exchanged gels is much higher than that in acetone exchanged gel indicating t-butanol as solvent exchange fluid is the most effective solvent for the synthesis of mesoporous PF gels.

Slower evaporation of t-butanol at 40 °C and consequently a smaller rate of stress change exerted on the network [19] compared to that during the evaporation of acetone, lead to a higher pore volume for vacuum dried t-butanol exchanged gel compared to a very low pore volume for the vacuum dried acetone exchanged gel at 40 °C.

In the case of the freeze dried t-butanol exchanged sample, the drying temperature in the freeze dryer was chosen at −40 °C, well below the freezing point of t-butanol, 25 °C [20]. This avoids vapour-liquid interface on pore walls during the removal of the solvent which maintains the original porous characteristics of the hydrogel and results in a highly mesoporous structure.

Since the freezing point of acetone is −95 °C [20] and the substantial amount of energy and subsequently costs involved for gel production at such a low temperature are too high, freeze drying was not carried out on the acetone exchanged samples. A more in-depth look at different drying methods is discussed in the following section.

Having determined optimal P/C ratios and solvent exchange liquids this final section presents data on the effects of drying conditions on the pore structure of the gels. Figure 5 shows the nitrogen adsorption/desorption isotherms at 77 K for PF gels prepared with different drying methods. The drying methods that correspond to each sample are described in Table 3.

The adsorption–desorption isotherms in Fig. 5 show that a significantly greater amount of nitrogen is adsorbed by the cryogel PF3, in comparison to the aerogels PF6 and PF7. This is suggestive of a much greater level of porosity in the cryogel. Data given in Table 3 shows that the cryogel PF3 exhibits a significantly greater specific surface area, total pore volume, mesopore volume and average pore size.

Figures 6a shows the PSD curves for freeze dried and both low and high temperature vacuum dried PF gels. A clearer representation of the PSD curves for the low pore diameter range is depicted in Fig. 6b. The porous characteristics of the gels are given in Table 3. The PSD curves magnified in Fig. 6b show that the low and high temperature vacuum dried gels possess low level of porosities with total pore volumes of 0.1211 and 0.0497 cm^3 g^{-1} and mean pore sizes of around 3 nm, respectively. The PSD curve for the cryogel in Fig. 6a, shows a highly mesoporous structure, with total pore volumes of 1.2813 cm^3 g^{-1} which is the highest pore volume of all gels and an average pore size of 13.9 nm. These results show that freeze drying is the preferred drying method for the preparation of highly mesoporous PF gels.

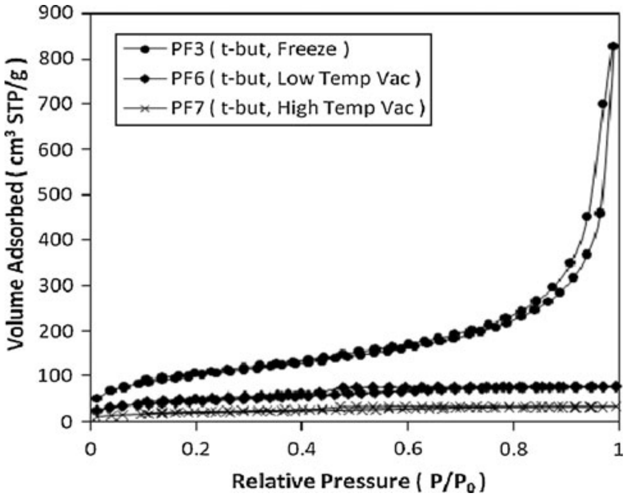

Fig. 5 N_2 adsorption/desorption isotherms at 77 K for PF gels with P/C ratio of 8 prepared by different drying methods

Vacuum drying involves the formation of a vapour-liquid interface as the liquid in the pores of the gel is removed by evaporation. The differences in the surface tension between the vapour and the liquid at the interface could induce a mechanical stress on the pores of the gel, thereby leading to the collapse of the porous structure [21]. However, in the freeze drying technique, the residual liquid in the wet gel is frozen and then removed directly as vapour [21–23]. Therefore the vapour-liquid interface is avoided [22] and the original porous structure of solvent exchanged gel is better maintained compared to the vacuum drying method [24].

A comparison between adsorption/desorption isotherms for vacuum dried gels at low and high temperatures (PF6 and PF7) in Fig. 5 shows that decrease in drying temperature results in higher level of porosity probably due to a decrease in the rate of evaporation [19]. This avoids the collapse of the porous structure to some extent due to less shrinkage which maintains the porous structure of the gel better. The PSD curves in Fig. 6b and data given in Table 3 also show that PF6 possesses a greater pore volume than PF7.

Table 3 Porous characteristics of PF gels with P/C ratio of 8 prepared by different drying methods

Sample	Drying method	S_{BET} (m^2 g^{-1})	V_{total} (cm^3 g)$^{-1}$	V_{micro} (cm^3 g^{-1})	V_{meso} (cm^3 g^{-1})	%V_{micro}	%V_{meso}	D_{avg} (nm)
PF3	Freeze drying at −40 °C	369	1.2813	0.0023	1.2790	0.18	99.82	13.9
PF6	vacuum drying at 40 °C	159	0.1211	0.0057	0.1154	4.71	95.29	3.0
PF7	vacuum drying at 70 °C	65	0.0497	0.0030	0.0467	6.04	93.96	3.1

Solvent exchange liquid for all samples was t-butanol

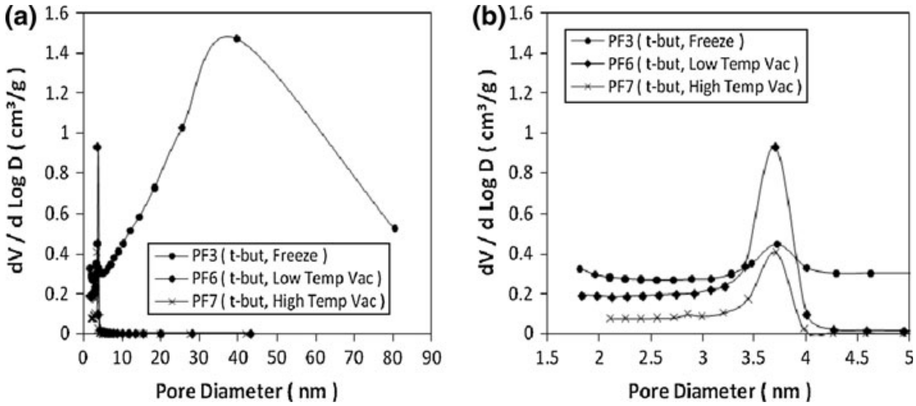

Fig. 6 PSD of PF gels prepared with different drying methods (P/C = 8)

4 Conclusions

PF gels can be used as organic precursors in the preparation of carbons [11, 12] which have a variety of applications including electrodes for energy storage, adsorbents for gas separation and packing materials for chromatography. As the porous properties of these carbons are closely associated to those of their organic precursors [11], the control of the porous structure of PF gels is highly important. The ability to understand the effect of synthesis parameters on the porous properties of the gel is paramount to a more effective tailoring of these properties to suit the required application.

Highly mesoporous phenol formaldehyde gels can be synthesized via sol–gel polycondensation of inexpensive phenol and formaldehyde under alkaline conditions. Synthesis parameters such as P/C ratio, solvent exchange liquids and drying methods including freeze drying and vacuum drying have a significant effect on the porous structure of the gels. In this work it is shown that there is an increase in total pore and mesopore volumes of the gels with increasing P/C ratio for $P/C \leq 8$ and after this these properties start to decrease with P/C ratio for $P/C > 8$. The gel prepared with $P/C = 8$ shows the highest total pore and mesopore volumes of 1.281 and 1.2790 cm^3 g^{-1} respectively. Tertiary–butyl alcohol as a solvent used for the removal of water from the aqua gel combined with freeze drying technique also emerged as the preferred method for the preparation of the gels as the porous properties in the wet gel are better inherited by the final gel.

Acknowledgments We are grateful to the EPSRC for funding this work (grant code EP/D031672/1).

References

1. Mirzaeian M, Hall PJ (2009) J Mater Sci 144:2705–2712
2. Tamon H, Ishizaka H, Mikami M, Okazaki M (1997) Carbon 35:791
3. Fung AWP, Wang ZH, Lu K, Dresselhaus MS, Pekala RW (1993) J Mater Res 8:1875
4. Yamamoto T, Endo A, Ohmori T, Nakaiwa M (2004) Carbon 42:1671
5. Job N, Heinrichs B, Lambert S, Pirard JP, Colomer JF, Vertruyen B, Marien J (2006) AIChE J 52:2663
6. Pekala RW, Farmer JC, Alviso CT, Tran TD, Mayer ST, Miller JM, Dunn B (1998) J Non-Cryst Solids 225:74
7. Mirzaeian M, Hall PJ (2009) J Electrochim Acta 54:7444
8. Fischer U, Saliger R, Bock V, Petricevic R, Fricke J (1997) J Porous Mat 4:281
9. Gilbert MT, Knox JH, Kaur B (1982) Chromatographia 16:138
10. Weiner M, Reichenauer G, Braxmeier S, Hemberger F, Elbert HP (2009) Int J Thermophys 30:1372
11. Wu D, Fu R, Sun Z, Yu Z (2005) J Non-Cryst Solids 351:915
12. Mukai SR, Tamitsuji C, Nishihara H, Tamon H (2005) Carbon 43:2628
13. Scherdel C, Reichenauer G (2009) J Microporous Mesoporous Mater 126:133
14. Durairaj RB (2005) Resorcinol: chemistry, technology and applications. Springer, Berlin
15. Barrett EP, Joyner LG, Halenda PP (1951) J Am Chem Soc 73:373
16. Gregg SJ, Sing KSW (1967) Adsorption, surface area and porosity. Academic Press, New York
17. Yamamoto T, Nishimura T, Suzuki T, Tamon H (2001) J Non-Cryst Solids 288:46
18. Smith DM, Scherer GW, Anderson JM (1995) J Non-Cryst Solids 188:191

19. Mosquera MJ et al (2008) J Non-Cryst Solids 354:645
20. Sinnott RK (1999) Coulson and Richardson's chemical engineering, vol 6, 3rd edn. Butterworth-Heinemann, Oxford, pp 947–967
21. Al-Muhtaseb SA, Ritter JA (2003) J Adv Mater 15:101
22. Job N, Thery A, Pirard R, Marien J, Kocon L, Rouzaud JN, Beguin F, Pirard JP (2005) Carbon 43:2481
23. Yamamoto T, Nishimura T, Suzuki T, Tamon H (2001) Carbon 39:2374
24. Tamon H, Ishizaka H, Yamamoto T, Suzuki T (1999) Carbon 37:2049

Journal of The Electrochemical Society, **159** (3) A315-A320 (2012)
0013-4651/2012/159(3)/A315/6/$28.00 © The Electrochemical Society

The Electrochemical Performance of Phenol-Formaldehyde Based Activated Carbon Electrodes for Lithium/Oxygen Batteries

Gbolahan O. Shitta-Bey,[a] Mojtaba Mirzaeian,[b,z] and Peter J. Hall[a,z]

[a]*Department of Chemical and Process Engineering, University of Strathclyde, Glasgow G1 1XJ, United Kingdom*
[b]*School of Chemistry and Chemical Engineering, Queen's University Belfast, Belfast BT9 5AG, United Kingdom*

Here we demonstrate the use of polymer derived activated carbons as the potential electrode material for Li/O_2 batteries. The activated carbons were synthesized by sol-gel polycondensation of low cost phenol and formaldehyde followed by carbonization at 1050°C in an inert atmosphere and activation under CO_2 to different degrees of burn off. Galvanostatic charge/discharge measurements performed on the activated carbon based electrodes show that discharge capacity increases with mesopore volume, with the highest discharge capacity of 1852 mAh/g obtained for the carbon having the highest mesopore volume of 1.8717 cm^3/g. Galvanostatic rate capability tests show that discharge capacity of the cell decreases with increasing discharge rates significantly.

Manuscript submitted November 9, 2011; revised manuscript received December 15, 2011. Published January 10, 2012.

Fossil fuel (coal, oil, natural gas) based energy is fast becoming out of date due to the associated environmental concerns along with the requirements to meet CO_2 emissions reduction targets.[1,2] Furthermore, as the ever increasing world demand for energy is placing increased pressure on fossil fuel reserves, with energy demand forecasted to be doubled by the year 2050 and tripled by the end of the century, renewable energies such as solar, wind and tidal are gaining more attention.[3] However, due to the intermittent nature of such renewable energy sources, effective energy storage systems need to be in place, to ensure continuity of supply to meet an ever growing consumer demand.

Reducing the dependency on fossil fuels can also be achieved by switching to electric vehicles (EVs) especially if they are used in conjunction with renewable energies as key energy supplies. Furthermore, as consumer electronics continue to become more portable, concurrent with increasingly modern lifestyles, there is a greater demand from power sources in terms of being more light weight and compact while still being able to provide considerable amounts of energy. Electrochemical energy storage devices possessing high energy densities are very attractive in this respect.

Li/O_2 batteries in particular are potentially capable of meeting the energy storage demands of the various applications discussed above. The battery combines lithium as anode electrochemically with oxygen accessed from the environment on a porous composite electrode through a non-aqueous electrolyte. During discharge, oxygen from air is reduced catalytically on the surface of the cathode to form oxide/peroxide anions. The Li^+ cations delivered by the electrolyte along with electrons from the external circuit, combine with catalytically reduced oxygen anions to form Li_2O_2 within the pores of the porous O_2 cathode.[4] Since lithium is the least electronegative metal with ability to donate electrons most easily[5] and oxygen as the active cathode material does not need to be carried on-board the cell, the battery provides a theoretical energy density of over 11000 Wh/kg (on the bases the weight of lithium) at a voltage range of 2.9–3.1 V. This is considerably higher than the energy density of any advanced rechargeable battery technology.[6] The recent works[4,5] on these batteries has revealed that the energy density of a Li/O_2 cell exceeds the energy density of current Li-ion batteries even more than 10 times which was previously predicted by Ogasawara et al.[7]

The end of discharge in a Li/O_2 cell occurs when the cathode is choked with discharge products.[8] Therefore a highly mesoporous cathode material with appropriate pore size and pore volume is essential to facilitate electrolyte diffusion onto the porous electrode as well as provide enough space for accommodation of discharge products, leading to a high discharge capacity.[9] Design and engineering of the porous carbon used as the cathode electroactive material is one of the key challenges for enhanced capacity and better cyclability of the cell.[5,10] Since the porous carbon used in the composite electrode is mixed with binder and catalyst, the choice and characteristics of the binder[11] and the catalyst[12] play a vital role in determining the electrochemical performance of the cathode in a Li/O_2 cell. It has also been discussed that characteristics of separator[13] and type of electrolyte[14] are important for the electrochemical performance of the cell. This work aims to use phenol-formaldehyde based activated carbons as electrode material in the cathode for Li/O_2 cells and study the effect of their porosity parameters on the cells' electrochemical performance.

Different types of carbons have been used as electrode materials in Li/O_2 cells.[4,9,11] In comparison to the more widely resorcinol-formaldehyde based carbons used in electrodes for electrochemical energy storage devices[9,15,16] phenol-formaldehyde (PF) carbons with controlled porosity have been utilized as cost effective electrode materials in this study since phenol represents a cheaper alternative to resorcinol, and therefore contributes toward the cost reduction of raw materials. Furthermore, these gels can be readily synthesized with over 90% mesoporosity in their structure.[17–19] The role of physical activation in controlling the porosity of the carbon and its performance in the Li/O_2 cell is explored. Power capabilities are also investigated by analyzing cell performance at different discharge rates.

Experimental

PF solutions were prepared by mixing phenol, sodium carbonate, formaldehyde and water to form homogeneous solutions. These were then poured into glass vials, sealed and cured at elevated temperatures. Based on our previous studies,[17] the gels were synthesized at an optimal phenol/catalyst ratio of 8 for maximized porosity. After curing, the gels were solvent exchanged by immersing in t-butanol to replace any residual water. The t-butanol exchanged gels were then freeze dried under vacuum at −40°C for 3 days to obtain dried cryogels. The PF cryogels were subsequently carbonized in a tubular furnace under argon at 1050°C. Activated carbon gels were prepared by activation of the resultant carbons under CO_2 at 800°C for varying times. The preparation of phenol-formaldehyde (PF) gels and carbons has been described elsewhere.[17]

The porosity of the PF gels and carbon gels were characterized by analysis of nitrogen adsorption/desorption isotherms measured by an ASAP 2420 adsorption analyzer (Micrometrics) at 77 K. The samples were degassed at 90°C for 3 hours prior to the adsorption measurements. BJH method was used for mesoporosity analysis, t-plot method for micropore analysis, and BET method for determination of surface area. The calculations for total pore volumes were based on the adsorbed volume of nitrogen at $P/P_0 = 0.99$.[20,21] Pore size distributions were determined by applying the BJH method to the desorption isotherms.[22]

[z] E-mail: m.mirzaeian@qub.ac.uk; p.j.hall@strath.ac.uk

SEM images of the carbon samples were obtained using a FEI Sirion 200 field-emission gun scanning electron microscope (FEG-SEM) operated at 5 kV accelerating voltage and a beam current of approximately 100 pA.

The cathode electrode was prepared by mixing the porous carbon as active material, electrolytic manganese dioxide (EMD) as catalyst, Kynar Flex 2801 binder (polyvinylidene difluoride/hexafluoropropylene; PVDF/HFP; 88/12 by weight) and propylene carbonate (PC) as wetting agent, in a weight ratio of 11/19/15/55 respectively[7,23] with acetone in a small glass bottle under magnetic stirring for 4 hours into a slurry mixture. The slurry was then cast into a 200 μm thick film using an applicator and the film was left unaltered to allow for evaporation of acetone. Following this, the thin film was then cut into 1.3 cm diameter circular disk-like electrodes. The electrode fabrication procedure is described elsewhere.[23]

Construction of the electrochemical cell was carried out in an argon atmosphere glove box. The cell components consisted of a stainless steel bar which functions as the anode current collector, a lithium metal foil (also in circular disk form) as anode, a glass micro-fiber separator soaked with electrolyte (1 M $LiPF_6$ in propylene carbonate), a cathode electrode (carbon composite cathode) and an aluminum mesh, with a spring and a hollow aluminum bar on top of it, functioning as the cathode current collector. Good contact between the various components of the cell was attained by compressing all cell components together. The cell was then sealed completely, apart from the aluminum mesh window in order to allow for exposure of the cathode to O_2 atmosphere.

Prior to electrochemical tests, the cell was exposed to an O_2 atmosphere supplied by an O_2 cylinder at room temperature for 30 minutes and then sealed tightly. Galvanostatic charge/discharge measurements were then carried out on the cell using a Solartron 1470E potentiostat, by applying a constant current at a charge/discharge rate of 70 mA/g in the potential range between 2 and 4.5 V. For the analysis of the effect of discharge rate, the cells were discharged at rates of 20, 50, 70 and 100 mA/g in the same potential range.

Results and Discussion

The N_2 adsorption/desorption isotherms at 77 K for activated carbons with different degrees of burn-off are shown in Figure 1. All isotherms are of type IV with hysteresis loops indicating the presence of mesopores.[24] The lower and upper parts of the hysteresis loop are representative of capillary condensation and evaporation in the mesopores of the carbon structure respectively.[24] The starting carbon is referred to as CPF and the activated carbons are named as ACPFx - y, where x is the activation temperature in °C, and y is the time in minutes. The porosity parameters of the carbons and the description of activation conditions under CO_2, resulting in various degrees of burn off are shown in Table I. Figure 1 shows a steady increase in the amount of gas adsorbed with an increase in the extent of burn-off, indicative of the development of porosity in the porous structure of the carbon. Table I shows that there is an increase in total pore and mesopore volumes with increasing degree of burn off. This is consistent with previous work reported on similar carbon gels.[5] The rise in pore volumes could be due to the creation of new pores and by selective gasification of certain structural components, widening of existing pores, or by opening of previously inaccessible pores.[5,25] In the case of ACPF800 – 120, the drop in micropore volume and increase in mesopore volume with increasing burn off could be due to the widening of micropores to form mesopores. Data given in Table I show that the BET surface area of the carbon increases from 310 m^2/g for CPF to 1382 m^2/g ACPF800–120 indicating that activation produces a significant increase in the BET surface area of the carbon. These results show that longer periods of activation under CO_2 at fixed temperature leads to further porosity development resulting in larger pore volumes and surface areas. However activation longer than 120 minutes under CO_2 will lead to a very high degree of carbon loss (>80%), which is not energy/cost effective due to the significant difference in the amount of starting material and the final activated sample. Therefore the maximum duration for CO_2 activation used was 120 minutes and production of carbon materials at activation times longer than 120 min has not been continued.

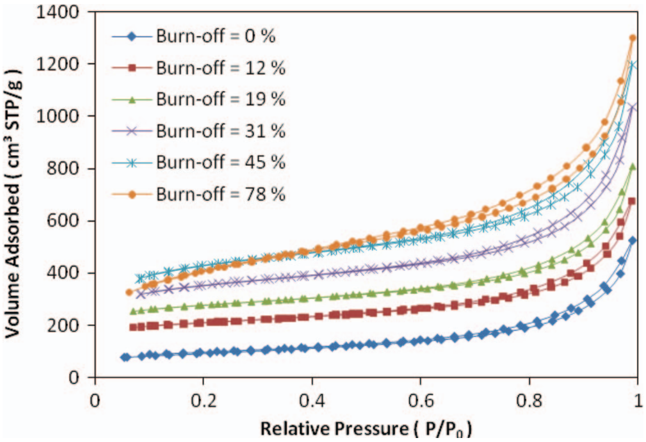

Figure 1. N_2 adsorption/desorption isotherms at 77K for the CPF carbon activated to different degrees of burn off.

Figure 2a shows the PSD curves for the activated carbons with different degrees of burn-off. The PSD curves for pore diameter in the range of 2–5 nm are magnified and shown clearly in Figure 2b. All PSD curves are similar but with a steady shift upwards on the pore volume axis both in the small and large pore diameter regions, indicating increase in the pore volumes of the carbons with increasing burn-off.

Additionally, the results of the porosity measurements displayed in Table I show that the activated carbons are predominantly mesoporous with pore sizes ranging between 5.4–6.3 nm. The sample ACPF800–120 possesses the highest total pore and mesopore volumes of 2.0112 cm^3/g and 1.8717 cm^3/g respectively. The effect of activation on the structure of the carbon can be seen in the SEM images shown in Figure 3. The network structure of both samples is evident; however, the surface topography depicted in Figure 3b for the activated carbon sample appears to reveal a more porous network. This is consistent with the porosity parameters (increase in pore volume) obtained by the nitrogen adsorption/desorption method.

Table I. Pore characteristics of CPF carbon activated to different degrees of burn off.

Sample	Burn off (%)	S_{BET} (m^2/g)	V_{total} (cm^3/g)	V_{micro} (cm^3/g)	V_{meso} (cm^3/g)	$\%V_{micro}$	$\%V_{meso}$	D_{avg} (nm)
CPF	0	310	0.8117	0.0450	0.7667	6	95	10.5
ACPF800-15	12	668	1.0434	0.2000	0.8434	19	81	6.3
ACPF800-30	19	884	1.2519	0.2761	0.9758	22	78	5.7
ACPF800-60	31	1133	1.6031	0.2960	1.3071	18	82	5.7
ACPF800-90	45	1383	1.8537	0.3106	1.5431	17	83	5.4
ACPF800-120	78	1382	2.0112	0.1395	1.8717	7	93	5.8

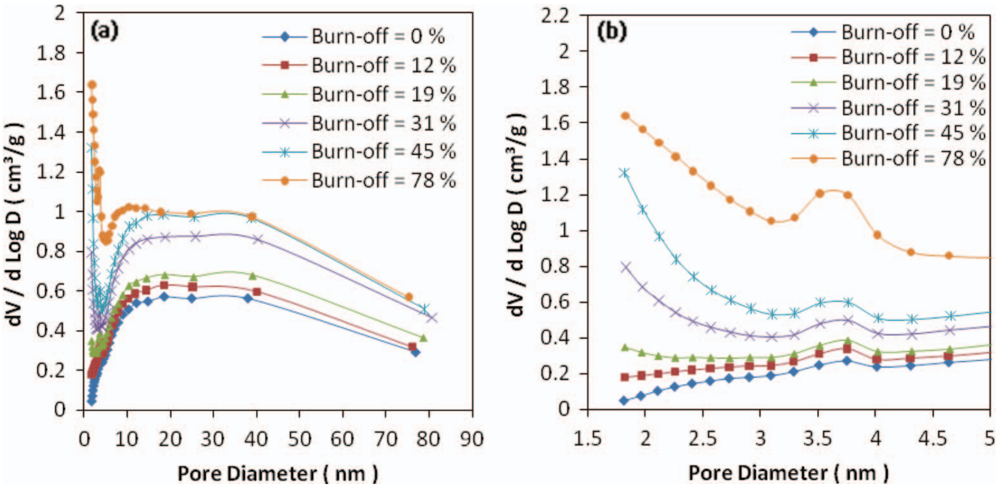

Figure 2. (a) Pore size distribution of CPF carbon activated to different degrees of burn off, (b) Expanded region for pore size distribution curves in the range of 2–5 nm.

The electrochemical performance of the activated carbons as electrode materials was investigated in Li/O_2 cells. Figure 4 shows the discharge behavior of the cells using activated PF carbons with different pore volumes as electrode active materials. The cell potential variation with discharge capacity curves show flat discharge profiles at approximately 2.5–2.8 V which is in good agreement with previous reports published on similar cells discharged in O_2 at atmospheric pressure, involving the formation of Li_2O_2 as discharge product.[5,7]

Increase in cell potential with increasing degree of burn-off might be due to the change in surface characteristics of the carbon used in electrode.[9] The initial open circuit voltage of the cell for different activated carbons as electrode materials, varies in the range of 3.3–3.5 V (Fig. 4). These values are higher than the theoretical potential of 3.1 V calculated by the thermodynamics of the reaction of Li and O_2 to form Li_2O_2.[26] Higher open circuit voltage of the cell compared to the theoretical potential might be due to a mixed potential effect associated with reaction of Li ions with impurities in the electrolyte as well as Li intercalation into the catalyst EMD.[27] The difference between the theoretical open circuit voltage of the cell and the working discharge potential of the cell is known as the discharge overpotential. The significant potential drop in the first stage of discharge, shown on discharge curves in Figure 4 is probably a result of a kinetic activation barrier involved in the cathode chemistry[27] in addition to the series resistances between cell components, since Ohmic losses

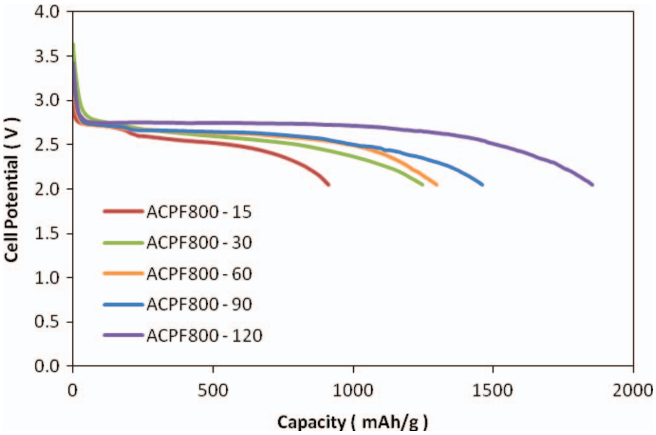

Figure 4. Discharge capacities of activated carbons at discharge rate of 70 mA/g.

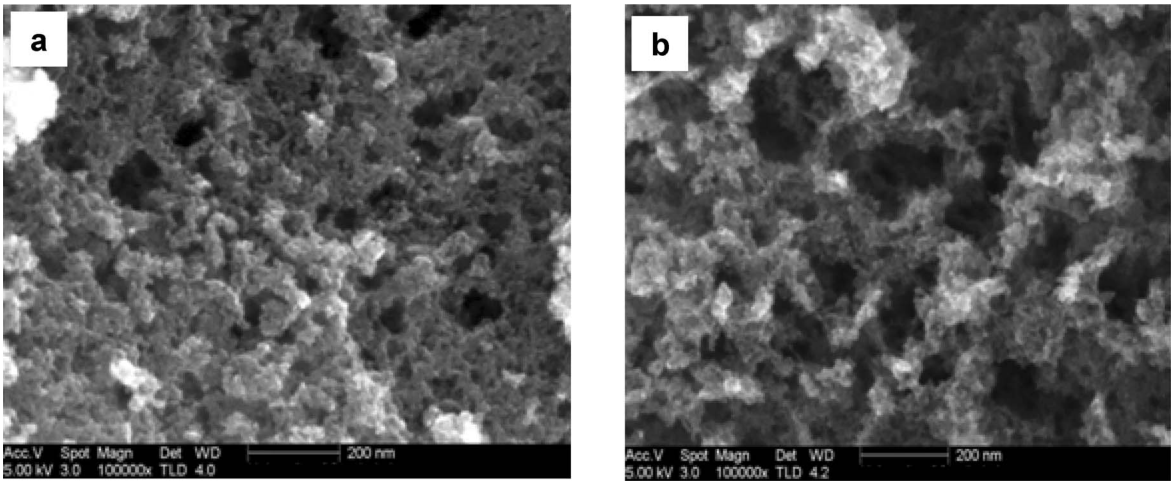

Figure 3. SEM images of carbon samples. (a) CPF and (b) ACPF800-120.

Table II. Discharge characteristics of activated carbons based electrodes with varying porosity.

Sample	Cell Voltage (V)	Discharge Capacity (mAh/g)	Number of cycles
ACPF800-15	2.51	910	5
ACPF800-30	2.59	1247	4
ACPF800-60	2.63	1299	2
ACPF800-90	2.64	1461	3
ACPF800-120	2.75	1852	3

from different parts of the cell such as current collectors, electrolyte and separator have a contribution to the overall internal resistance of the cell which leads to the observed voltage drop. Dell and Rand have argued that a slow diffusion from the bulk solution to the electrode as a result of the electrode's porosity and electrode's thickness might also shift the potential of the cell away from the theoretical potential.[28]

Table II shows the variation of electrochemical performance of Li/O_2 cells based on electrodes derived from carbons with different porous parameters. The discharge capacities are based on the first cycle for all electrodes and are normalized to the weight of carbon in the electrode. The cycling data refers to all cycles with a discharge capacity greater than 50 mAh/g. Figure 4 and Table II show an increase in the discharge capacity of the cells with increasing mesopore volume. ACPF800-120 carbon with the highest mesopore volume shows the highest storage capacity of 1852 mAh/g. This is likely due to the increase in storage space available for the accommodation of discharge product Li_2O_2.[5] The discharge process is thought to cease when the pores are choked with discharge product and therefore the relatively lower discharge capacities associated with samples of lower pore volumes are due to a reduced amount of available space for storage of discharge product.

Although there is also an increase in micropore volume between ACPF800-15 to ACPF800-90, it is unlikely that these micropore volumes play any significant role in the observed increase in discharge capacity as such pores are easily blocked with discharge product[29] or are not wetted by the electrolyte during the cell operation. Furthermore the pore size distribution of the samples is similar and therefore the effect of the pore size on discharge capacity cannot easily be determined. Although the surface area of the carbon material increases with degree of burn off during activation process, however since this increased surface area is mostly due to the development of micropores in the carbon structure, it has no significant effect on the electrochemical performance of the porous electrode in Li/O_2 cells.[14,30,31] A study carried out by Kuboki et al[31] compares the effect of surface area and pore volume on electrochemical performance. It is shown that the pore volume has a more marked effect on specific capacity than the surface area. Another study carried out by X. H Yang et al shows that a carbon material with a significantly lower surface area but a much larger pore size displayed much better electrochemical performance than one with higher surface area but smaller pore size.[30]

The limited cyclability of the cell, with the highest being 5 cycles shown in Table II is representative of significant capacity fade upon cycling and might be associated with the relatively low pore sizes of the carbon used in the electrode. It has been argued that carbons with wider pores and larger pore volumes result in larger discharge capacities due to the higher diffusivity of the electrolyte and better accessibility of the oxygen and lithium ions to the carbon structure and also larger space for accommodation of the discharge products within the electrode.[5]

Tran et al[29] suggested that pores of different sizes are filled with discharge product at different rates. It is believed that during discharge smaller mesopores are more quickly filled with discharge product, and diffusion of O_2 to the reaction zone becomes more difficult than in larger mesopores. Therefore as discharge proceeds, the smaller pores will be more densely populated with discharge product. Subsequently the low conductivity of the discharge product which impedes Li ion transfer and charge transfer would be more pronounced in these high density regions.[9] The slower kinetics of electron transfer in this region in comparison to the supply of Li ions is compensated for by the irreversible reaction of Li ions with certain electrolyte components.[9] This is thought to lead to structural changes of the O_2-electrode, deteriorating cell performance and causing capacity fade upon subsequent cycling.

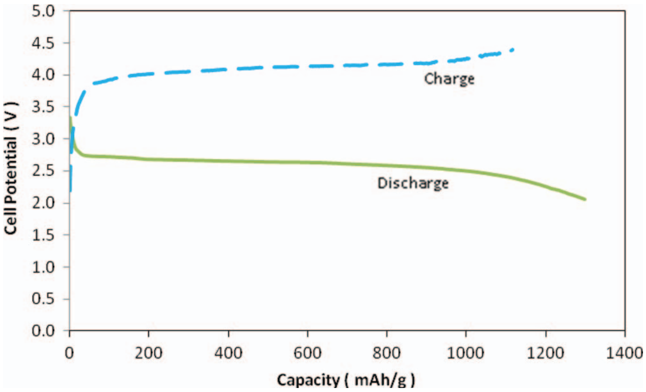

Figure 5. Typical charge/discharge curve for electrode using ACPF800-60 carbon as active material.

Another class of thought could be the reaction of electrolyte solvent (PC) with the lithium oxide discharge products to form Li_2CO_3 or lithium alkyl carbonates, XO-O-(C=O)-Li, where X is an alkyl group.[32] In addition to the formation of Li_2O_2 upon discharge and its decomposition to release O_2 during charge,[7] scientists working on Li/O_2 batteries have also confirmed the presence of Li_2CO_3 after discharge[33] as well as the evolution of CO_2 upon charge. It is therefore likely that origin of CO_2 is via the decomposition of the carbonates formed upon reaction of lithium oxide discharge products and the electrolyte solvent (PC).[34] This implies that upon subsequent charge/discharge cycles, more electrolyte gets consumed, causing a depletion in the amount of available electrolyte, until a point is reached where the discharge reaction can no longer be sustained, therefore reducing the cycle life of the cell.

A typical charge/discharge curve of Li/O_2 cells in this work is shown in Figure 5. The charge potential of 4 V–4.4 V is consistent with previously reported studies on similar cells.[7,12] In comparison to the thermodynamic potential of 3.1 V of the reaction between Li and O_2 forming Li_2O_2, this charging voltage is notably higher and the difference is referred to as the charge overpotential. The high charging voltage required is likely due to the decomposition of the carbonates formed during discharge as mentioned earlier, which require a charging voltage of over 4 V.[32] It can also be observed that not all the discharge capacity has been regained upon charging. Mirzaeian et al[9] has shown by impedance spectroscopy that an increasing amount of discharge product builds up in the cathode upon continuous cycling, indicating that not all discharge product has been decomposed in the reverse reaction during charge. This could be either due to the irreversible formation of Li_2O [35] or buildup of Li_2O_2 within pores due to poor dispersion of the catalyst within the carbon's pores. A further contribution to this could be a result of the irreversible side reactions between Li ions and electrolyte species that occur due to slow kinetics at the cathode side as described earlier, contributing some irreversible capacity to the overall discharge capacity.[9]

In order to assess the power capabilities of the Li/O_2 cells, the electrochemical performance of the cells was analyzed at different discharge rates. Figure 6 and Table III show the variation of discharge capacity with discharge rate for an activated PF carbon with average pore size of 6.7 nm used in electrode's formulation. It can be observed that there is a decrease in discharge capacity with increasing current density. This is likely due to limited diffusion of O_2 and slower Li

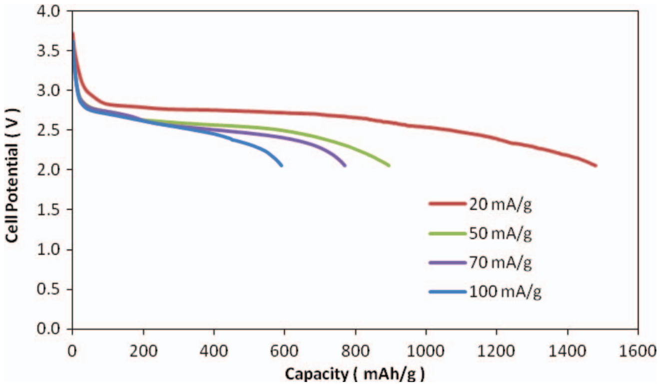

Figure 6. Discharge capacities of an activated PF carbon based electrode at different discharge rates.

ion and charge transfer within the carbon structure at higher discharge rates.

Xiao et al have argued that at higher discharge rates, pores within the cathode get blocked more rapidly due to quick deposition of discharge product.[36] This limits the flow of reactants (O_2, Li ions) and electrolyte to the inner active regions of the porous electrode[27] more compared with that at lower current densities. At lower discharge rates the electroactive surface area of the electrode is better utilized since pore clogging occurs at a slower rate. This illustrates that at high current rates the cell loses some of its energy and it is important to balance the energy and power densities of the battery by controlling its cathode's porous structure in such a way as to accommodate more discharge products and at the same time minimize mass transfer barriers for oxygen and lithium ion transfer.

It has been argued that mesopores are important for improving the energy and power capabilities of Li/O_2 cells.[5] They lead the electrolyte ions transport into the bulk of material quickly and also provide larger space for formation of discharge products. Therefore a sample with wider pores and larger pore volume might result in: i) higher diffusivity of the electrolyte into the carbon structure and better accessibility of lithium ions to the carbon surface (reaction zone). ii) larger space for the storage of discharge products as larger pore volume is available in the porous structure, and finally iii) better diffusion of oxygen to the carbon-electrolyte interface.

Since the cost of electrode material has a significant impact on the allowable costs of energy storage systems, an alternative basis for comparing different materials for energy storage is based on their cost-to-performance ratios. Therefore a portfolio of storage options that meet the cost, performance and durability requirements for the use of phenol -formaldehyde based activated carbon as an alternative electroactive material in Li/O_2 butteries will be needed. The highest discharge capacity of 1852 mAh/g obtained in this work is comparable with the capacity of a Li/O_2 cell using resorcinol-formaldehyde based activated carbon electrodes.[5] However, the phenol-formaldehyde based cells possess lower cycle life, attributed to their relatively smaller average pore sizes. Therefore, the issue relating to the pore size of phenol -formaldehyde based activated carbon electrodes will need to be worked on.

Table III. Variation of discharge capacity with discharge rate for an activated PF carbon based electrode.

Discharge rate (mA/g)	Discharge Capacity (mAh/g)
20	1480
50	894
70	771
100	592

Table IV. Price comparison of phenol and resorcinol.[38]

Raw Material	Cost ($ / kg)
Phenol	109.2
Resorcinol	264

One of the operational requirements of energy storage systems is to maximize their storage cost-effectiveness through the use of materials and production methods which are both relatively inexpensive and inherently scalable. A comparison in the cost of PF and RF based electrodes can be seen in the sigma-aldrich prices of phenol and resorcinol[38] shown in Table IV.

In comparison to the more widely resorcinol- formaldehyde based carbons used in electrodes for electrochemical energy storage devices[9,15,16] phenol-formaldehyde (PF) carbons with controlled porosity have been utilized as cost effective electrode materials in this study since phenol represents a cheaper alternative to resorcinol, and therefore contributes toward the cost reduction of raw materials. Much larger quantities of these materials will inevitably be required for large scale fabrication of electrodes, and therefore these price differences will be even more pronounced.

Conclusions

Activated carbons have been prepared by sol-gel polymerization of low cost phenol and formaldehyde followed by carbonization of the corresponding gels at 1050°C under Ar atmosphere and activation in CO_2 to different degrees of burn-off. A steady increase in total and mesopores volumes with increasing burn-off was observed with a relatively similar pore size distribution for all carbon samples. The corresponding activated carbons were used in the preparation of composite electrodes for Li/O_2 batteries.

The galvanostatic charge/discharge measurements carried out on the activated carbon based electrodes showed an increase in discharge capacity with mesopore volume, with the highest discharge capacity of 1852 mAh/g corresponding to the carbon with the highest mesopore volume of 1.8717 cm^3/g. The discharge capacity obtained in this work represents a value roughly 10 times the energy density of current Li-ion batteries.[37] Although this further highlights the immense potential of Li/O_2 cells, issues relating to the cyclability require much improvement. Furthermore the effect of discharge rates performed on carbon based electrodes, showed a decline in discharge capacity with increasing rates of discharge. This therefore highlights the need to engineer the porous structure of the cathode so as to maintain a fine balance between energy and power densities where required. Furthermore, the significant effect of mesopore volume on improving the specific energy of Li/O_2 batteries has been demonstrated.

Acknowledgment

We thank the EPSRC for funding as part of the Supergen Energy Storage Consortium (grant code EP/H019596/1).

References

1. C. Liu, F. Li, L. P. Ma, and H. M Cheng, *Adv. Mater.*, **22**, E28 (2010).
2. P. G. Bruce, *Solid State Ionics*, **179**, 752 (2008).
3. R. Padbury and X. Zhang, *J. Power Sources*, **196**, 4436 (2011).
4. A. Debart, A. J. Paterson, J. Bao, and P. G. Bruce, *Angew. Chem. Int. Ed.*, **47**, 4521 (2008).
5. M. Mirzaeian and P. J. Hall, *Electrochim. Acta*, **54**, 7444 (2009).
6. J. P. Zheng, R. Y. Liang, M. Hendrickson, and E. J. Plichta, *J. Electrochem. Soc.*, **155**, A432 (2008).
7. T. Ogasawara, A. Debart, M. Holzapfel, P. Novak, and P. G. Bruce, *J. Am. Chem. Soc.*, **128**, 1390 (2006).
8. J. Read, *J. Electrochem. Soc.*, **153**, A96 (2006).

9. M. Mirzaeian and P. J. Hall, *J. Power sources*, **195**, 6817 (2010).
10. K. Kinoshita, *Carbon: Electrochemical and Physicochemical Properties*, John Wiley & Sons, New York, 1988.
11. S. D. Beattie, D. M. Manolescu, and S. L. Blair, *J. Electrochem. Soc.*, **156**, A44 (2009).
12. A. Debart, J. Bao, G. Armstrong, and P. G. Bruce, *J. Power Sources*, **174**, 1177 (2007).
13. P. Arora and Z. J. Zhang, *Chem. Rev.*, **104**, 4419 (2004).
14. J. Read, *J. Electrochem. Soc.*, **149**, A1190 (2004).
15. S. J. Kim, S. W. Hwang, and S. H. Hyun, *J. Mater. Sci.*, **40**, 725 (2005).
16. Y. Zhu, H. Hu, W. Li, and X. Zhang, *Carbon*, **45**, 160 (2007).
17. G. O. Shitta-Bey, M. Mirzaeian, and P. J. Hall, *J. Sol-Gel Sci. Techn.*, **57**, 178 (2011).
18. S. R. Mukai, C. Tamitsuji, H. Nishihara, and H. Tamon, *Carbon*, **43**, 2628 (2005).
19. D. Wu, R. Fu, Z. Sun, and Z. Yu, *J. Non-Cryst. Solids*, **351**, 915 (2005).
20. M. Mirzaeian and P. J. Hall, *J. Mater. Sci.*, **44**, 2705 (2009).
21. V. Ruiz, C. Blanco, M. Granda, R. Menendez, and R. Santamaria, *J. Appl. Electrochem.*, **37**, 717 (2007).
22. E. P. Barrett, L. G. Joyner, and P. P. Halenda, *J. Am. Chem. Soc.*, **73**, 373 (1951).
23. M. Mirzaeian and P. J. Hall, *Power System Techhnolgy*, **31**(20), 90 (2007).
24. S. J. Gregg and K. S. W. Sing, *Adsorption, surface area and porosity*, Academic Press, New York, 1967.
25. H. Marsh and B. Rand, *Carbon*, **9**, 47 (1971).
26. D. Linden and T. Reddy, *Handbook of batteries*, 3rd ed., McGraw Hill, New York, 2001.
27. G. Girishkumar, B. McCloskey, A. C. Luntz, S. Swanson, and W. Wilcke, *J. Phys. Chem. Lett.*, **1**, 2193 (2010).
28. R. M. Dell and D. A. J. Rand, *Understanding Batteries*, RSC Publishing, Cambridge, 2001.
29. C. Tran, X. Q. Yang, and D. Qu, *J. Power Sources*, **195**, 2057 (2010).
30. X. H Yang, P. He, and Y. Y. Xia, *Electrochem. Commun.*, **11**, 1127 (2009).
31. T. Kuboki, T. Okuyama, T. Ohsaki, and N. Takami, *J. Power Sources*, **146**, 766 (2005).
32. F. Mizuno, S. Nakanishi, and H. Iba, *The 15th International Meeting on Lithium Batteries*, June 27–July 2, Montreal, Quebec, Canada Abstract 819 (2010).
33. A. K. Thapa, S. Kazuki, H. Matsumoto, and T. Ishihara, *216th ECS Meeting*, Vienna, Austria, October 4–9 (2009) Abstract 687.
34. K. Takechi, E. Sudo, T. Inaba, F. Mizuno, H. Nishikoori, and T. Shiga, *218th ECS Meeting*, Las Vegas, Nevada, Oct 10–15 (2010) Abstract 586.
35. A. Kraytsberg and Y. Ein-Eli, *J. Power Sources*, **196**, 886 (2011).
36. J. Xiao, D. Wang, W. Xu, D. Wang, R. E. Williford, J. Liu, and J. G. Zhang, *J. Electrochem. Soc.*, **157**, A487 (2010).
37. J. P. Schmidt, T. Chrobak, M. Ender, J. Illig, D. Klotz, and E. Ivers-Tiffee, *J. Power Sources*, **196**, 5342 (2011).
38. Sigma-Aldrich Company Ltd, Gillingham, UK. www.sigmaaldrich.com. (2011).

PERSPECTIVE www.rsc.org/ees | Energy & Environmental Science

Energy storage in electrochemical capacitors: designing functional materials to improve performance

Peter J. Hall,*[a] Mojtaba Mirzaeian,[a] S. Isobel Fletcher,[a] Fiona B. Sillars,[a] Anthony J. R. Rennie,[a] Gbolahan. O. Shitta-Bey,[a] Grant Wilson,[a] Andrew Cruden[b] and Rebecca Carter[b]

Received 24th March 2010, Accepted 21st June 2010
DOI: 10.1039/c0ee00004c

Electrochemical capacitors, also known as supercapacitors, are becoming increasingly important components in energy storage, although their widespread use has not been attained due to a high cost/performance ratio. Fundamental research is contributing to lowered costs through the engineering of new materials. Currently the most viable materials used in electrochemical capacitors are biomass-derived and polymer-derived activated carbons, although other carbon materials are useful research tools. Metal oxides could result in a step change for electrochemical capacitor technology and is an exciting area of research. The selection of an appropriate electrolyte and electrode structure is fundamental in determining device performance. Although there are still many uncertainties in understanding the underlying mechanisms involved in electrochemical capacitors, genuine progress continues to be made. It is argued that a large, collaborative international research programme is necessary to fully develop the potential of electrochemical capacitors.

1. Introduction

Electrochemical capacitors are devices that are capable of storing electrical charge but are distinguished from electrochemical cells as they can absorb and release charge much more quickly; they are an increasingly important class of energy storage devices.[1,2] Although frequently referred to as "supercapacitors" or "ultracapacitors" these names convey little scientific information and are herein referred to as electrochemical capacitors (ECs). This is itself a generic name for two main subdivisions—Electrochemical Double Layer Capacitors (EDLCs) and pseudocapacitors, both of which will be described in Section 2. The term "supercapacitor" does, however, convey one essential feature of these devices, namely their specific capacitance is six to nine orders of magnitude larger than conventional dielectric capacitors. This can be seen from a simple order of magnitude calculation. The specific capacitance, C (F g^{-1}), of a capacitor is given by:[2]

$$C = \varepsilon_0 \varepsilon_r \frac{S}{D} \tag{1}$$

where ε_0 is the electric constant (8.854×10^{-12} F m^{-1}), ε_r the relative dielectric constant of the interface (whether liquid or solid), S is the specific surface area of the electrodes (m^2 g^{-1}), and $D(m)$ is the separation of the electrode plates. Firstly, consider a conventional dielectric capacitor. Assuming $\varepsilon_r \approx 10^3$, $S \approx 1$ m^2, and $D \approx 10^{-6}$ m then $C \approx 8 \times 10^{-3}$ F (in fact most capacitors used in electronic circuits are pF to μF). ECs are based around materials with $S \approx 10^3$ m^2 g^{-1} and the formation of an electrochemical double layer on the electrode surface during polarisation for which $D \approx 10^{-9}$ m. Assuming $\varepsilon_r \approx 10$ then $C \approx 80$ F g^{-1}. Clearly, this is several orders of magnitude greater than conventional capacitors.

Broader context

The age of low-cost energy is ending, and the world is preparing for an era of massively increased energy costs. The reasons for this expected increase are varied: the decarbonisation of energy, the greater use of more expensive energy generating technology (such as nuclear and renewable), and fossil-fuels which require increasing amounts of energy for extraction and utilisation. This will create new, growing markets for technologies that utilise energy more efficiently. As energy becomes more valuable, storage technologies can improve efficiencies in supply systems, by storing energy when in excess and releasing at times of high demand. This occurs over a variety of timescales encompassing inter-seasonal fluctuations to pulsed power lasting milliseconds. The excellent power handling characteristics of electrochemical capacitors over the timescale 0.1–100 s allow engineers to match the specification of the primary energy sources closer to that of the average power demand. Electrochemical capacitors provide additional peak power demands as and when required. In the short to medium term, hybrid systems combining electrochemical capacitors with various primary energy sources (such as internal combustion engines, batteries and fuel cells) are expected to be increasingly important. To fully exploit the potential of electrochemical capacitors in the field of energy storage, further advances in the engineering of materials are required.

---

[a] *Department of Chemical & Process Engineering, University of Strathclyde, James Weir Building, 75 Montrose Street, Glasgow, G1 1XJ, Scotland, UK. E-mail: p.j.hall@strath.ac.uk*
[b] *Department of Electronic & Electrical Engineering, University of Strathclyde, Royal College Building, 204 George Street, Glasgow, G1 1XW, Scotland, UK*

There are many ways of defining specific capacitance, such as normalisation to unit surface area, volume or mass of the device. However, since the focus of this perspective is materials, capacitance is normalised to unit mass of active material, which simplifies comparisons between materials.

Since the energy stored in a capacitor is given by:[2]

$$E = \frac{1}{2}C(\Delta V)^2 \qquad (2)$$

it becomes possible to store enough energy for many practical purposes. For example, a 10 μF capacitor operating at 50 V can store 1.25×10^{-3} J whereas a 3000 F capacitor operating at 2.7 V can store approximately 11×10^3 J. To give this number a practical context, this is the equivalent kinetic energy of a 1000 kg vehicle moving at 16 km h^{-1} (10 mph). It is important to emphasise that since EC voltage decreases linearly with state of charge, not all of the stored energy can generally be used.

The factors influencing energy density are summarised in eqn (1) but the factors determining power density are much more complex. The power density, P, is inversely proportional to the resistance of the device, R, as illustrated by:

$$P = \frac{1}{4}\frac{(\Delta V)^2}{R} \qquad (3)$$

R is the equivalent series resistance (ESR) which is comprised of the electrode resistance, electrolyte resistance and resistance due to the diffusion of ions in the electrode porosity.

The rationale behind this perspective acknowledges the fact that ECs can store sufficient energy for a variety of applications and they outperform batteries in terms of power handling. Also, it is recognised that they are far from achieving their true commercial potential. In order to realise this potential, significant improvements are required to enhance the cost/performance ratio. Improvements in manufacturing and materials engineering are needed.

This perspective commences with a comparison of different types of capacitor with electrochemical cells. This leads to an outline of the applications of EC devices. Since progress and wider adoption will rely on materials development, the perspective provides an overview of the main classes of materials (electrodes and electrolytes) used in ECs.

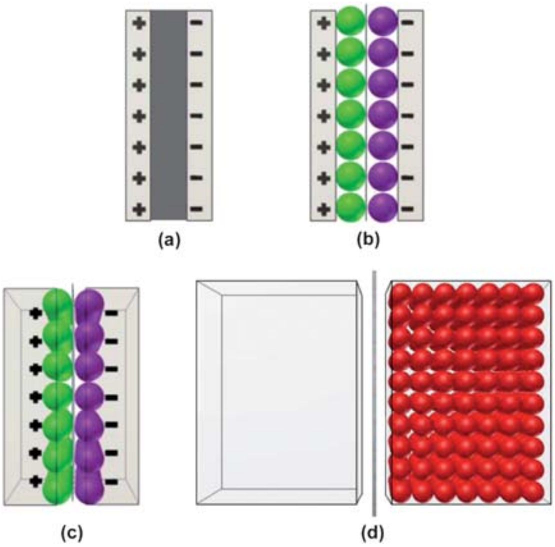

Fig. 1 Representations of electrical energy storage in charged devices: (a) a traditional capacitor where charges are physically separated by a dielectric material, (b) an EDLC where charge separation occurs at the electrode/electrolyte interface, (c) a pseudocapacitor where charge transfer reactions occur at the electrode *surface* and (d) a generic battery where energy is stored as chemical potential by the change in oxidation state of the *bulk* electrode material.

2. Batteries and electrochemical capacitors for electrical energy storage

Although batteries and ECs are normally regarded as separate technologies, it is much more illuminating to regard them as different points on a continuum of electron transfer between electrolyte and electrode (Fig. 1). At one end of the continuum are dielectric capacitors which store energy directly as electrostatic charges on two opposing electrodes. Batteries are at the other end of the continuum where energy is stored through electrochemical reactions.

ECs (patented by Becker in 1957[3] and commercialised by SOHIO in 1978[2,4,5]) differ from electrostatic capacitors by storing charge as an electrical double layer at the interface between electrode and electrolyte. Solvated ions in the electrolyte are

Pictured are members of the consortium from the University of Strathclyde (l–r): Dr A. Cruden, Prof. P. J. Hall, R. Carter, G. Wilson, Dr M. Mirzaeian, A. J. R. Rennie, G. O. Shitta-Bey and F. B. Sillars

The UK Energy Storage Consortium was launched in 2006 by the Engineering and Physical Sciences Research Council (EPSRC) as part of the SUPERGEN initiative. The consortium aims to accelerate the development of energy storage systems, and to provide strategies for their rapid implementation in the UK energy sector. The University of Strathclyde focuses on the development of electrode materials for electrochemical capacitors and lithium–oxygen batteries and the application of these devices in the field of transportation. More information can be found at www.energystorage.org.uk.

attracted to the electrode surface by equal but opposite charges on the electrode effectively creating two capacitors in series connected by electrolyte. As a result of the high internal surface area of the electrodes and the nanometre scale thickness of the double layer, the capacitance and the energy density of an EDLC are several orders of magnitude higher than those of electrostatic capacitors, as described in Section 1. A further step in the continuum shows a transitional state with electrochemical processes involving Faradaic and non-Faradaic energy storage simultaneously. Conway[2] refers to this as pseudocapacitance which is observed when fast, potential-dependent reactions result in Faradaic charge transfer across the double-layer. These reactions become thermodynamically favourable in certain ranges of potential and produce capacitive charge/discharge characteristics. This occurs due to the appearance of a derivative (dq/dV), equivalent to a capacitance, realised by a change in the rate of charge acceptance with changes in potential.[2] Pseudocapacitive behaviour is identified using cyclic voltammetry. Materials exhibiting pure double-layer capacitance produce parallelogram-shaped voltammograms whereas irregular peaks are generated by pseudocapacitive materials. Reactions that result in Faradaic charge transfer are mainly of the redox type where changes in the oxidation state of the materials occur which is analogous to battery systems.

However, reactions do not propagate into the bulk material, and occur only at the electrode/electrolyte interface. For example, ruthenium dioxide (RuO_2) can participate in redox reactions with a very high degree of reversibility and consequently charge/discharge lifetimes in excess of 10^6 cycles are possible.[5] Intercalation of a guest species, such as Li^+, into the electrode material can also produce a pseudocapacitive response.[6] For this reason, ECs utilising pseudocapacitance can be considered as a transition between EDLCs and intercalation batteries. It is important to note that although EDLCs and pseudocapacitors are differentiated on the basis of the predominant charge storage mechanism, all EC devices exhibit both mechanisms to some extent. The process shown in Fig. 1c represents pseudocapacitance. This is similar to the redox reactions that occur in batteries, however, the charge/discharge behaviour is capacitative in nature.

Completing the continuum are batteries which, as mentioned previously, store energy indirectly using Faradaic oxidation and reduction of electroactive reagents capable of generating charge, and bulk-phase transformations achieving high energy density and high voltage at the expense of slower transport and reduced cycle life.[7]

Conway[2] quantified the degree of electron transfer in different devices as: 0.17–0.20 e^- per atom of accessible surface in a double-layer capacitor, 1–2.5 e^- per atom of accessible surface of electroactive material in a pseudocapacitor and 1–3 e^- per atom or molecule of *bulk* phase for a battery. Although it has been argued that capacitors and batteries effectively lie on a continuum of electron transfer, this should not mask essential differences in their characteristics and performance. For example, the reversibility of the chemical and capacitive energy storage systems is substantially different. In batteries, charge transfer across the electrode/electrolyte interface leads to changes in the molecular structure of the electrode by redox reactions and restricts cycle life to $\sim10^3$ charge/discharge cycles.[7] Conversely, physical charge storage in EDLCs has no associated chemical and phase changes during cycling. This results in a highly reversible storage mechanism where cycle lifetimes greater than 10^6 are frequently obtained which, in turn, leads to important differences in the energy and power handling of capacitors and batteries. This is usually summarised in a Ragone plot which compares energy density ((W h) kg^{-1}) and power density (W kg^{-1}). Fig. 2 shows a Ragone plot comparing the energy and power densities of Li-ion batteries with those of ECs at different discharge rates. Li/O_2 technology is projected to produce energy densities of several times the values attained using current Li-ion technology.[8,9] ECs have the ability to produce much higher power densities in comparison with batteries and exhibit considerably fewer material stability problems. Based on such comparisons ECs and batteries should be regarded as complementary technologies, each providing a unique solution to energy storage.

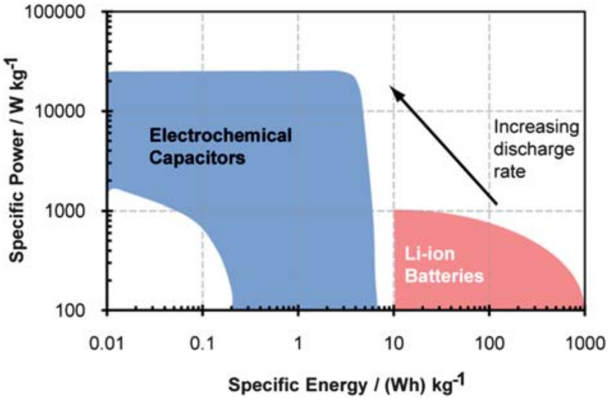

Fig. 2 Specific power against specific energy for ECs and high-power Li-ion batteries.

3. Applications of electrochemical capacitors

It is expected that ECs will be used for a variety of applications, most of which can be grouped into one or more of the following three categories:

1. Power capture and supply
2. Power quality applications
3. Backup, safety and low maintenance applications

ECs are particularly appropriate in certain applications due to their high power capability, high efficiency and long life span.

3.1 Power capture and supply

Future hybrid energy systems will couple the high energy density of batteries, fuel cells or internal combustion engines (ICEs) combined with the rapid charge/discharge and power capabilities of ECs.

In such hybrids, batteries could provide an average power output, while ECs provide additional peak power when required.[10] In this way, batteries are not pushed to the limit of their power capabilities, resulting in longer battery lifetimes. ECs allow a more flexible approach in the design of energy systems, and as further performance improvements in areas such as energy density are made, this design flexibility for systems should increase.

A passenger car driven in an urban or suburban setting will accelerate and decelerate frequently as the driver encounters traffic lights, turns and obstacles. The resultant drive cycle has power spikes due to the acceleration of the vehicle, and contains a significant amount of potentially recoverable energy from braking. An example of a real-life drive cycle showing the speed and power required by a small passenger car during a standard urban journey is given in Fig. 3.[10,11] Note that the peak power required by the vehicle is 17 kW, but the average power indicated by the dashed line is just 2.5 kW. Furthermore, a peak power of 15 kW is available from regenerative braking. The large disparity between peak and average power indicates that ECs could be very useful in passenger vehicles.

ECs may therefore be used to improve the efficiency of vehicles, although the metric defining 'efficiency' depends on the type of vehicle being discussed. If the ECs are used with an ICE or fuel cell, then fuel efficiency is the most important factor. If the ECs are used with batteries, then the efficiency would typically be measured in the yield: km $(\mathrm{kW\ h})^{-1}$. In either case a greater efficiency should mean a greater range or a smaller size for the primary energy source (fuel tank or battery pack). Efficiency may also be measured in total emissions from the vehicle; although this is a considerably more complex calculation, it does indicate the direct environmental benefits.

ECs may also be used to reduce maintenance and running costs for vehicles. For an ICE vehicle this will primarily mean reducing fuel consumption. For a battery-powered vehicle, it means extending the life of the batteries. In both cases the ECs can also extend the life of the friction brakes, as their ability to accept high power bursts means that the friction brakes will be used less frequently. In turn this creates a reduction in pollutants, in this case particulate matter from the brake pads. The benefits of ECs for passenger cars are also applicable to heavier hybrid vehicles such as urban buses, urban delivery vehicles and refuse collectors that have a high number of acceleration and deceleration cycles throughout their working day.[12]

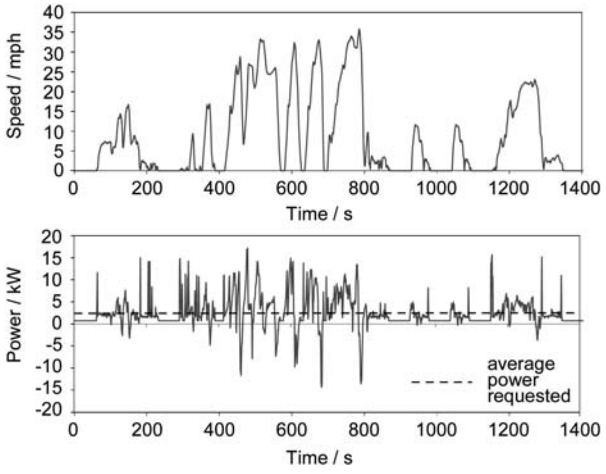

Fig. 3 A typical urban driving cycle created at West Virginia University.[10,11] The upper plot shows the speed of the vehicle and the lower plot shows the power required for a small passenger car.

EC applications for trams, trains and trolleybuses allow for energy recovery in either a mobile form (onboard the vehicle) or in a static form (at a station or specific route stop).[13] EC energy recovery systems for these vehicles may also allow infrastructure costs to be reduced *e.g.* overhead lines and third lines may not be required along the full route.

ECs have also found an application in starting diesel locomotives. They are less susceptible to degradation than batteries at lower temperatures, in terms of both performance and lifespan. In addition to the advantages previously mentioned, including increasing the lifespan of the batteries, and allowing for a smaller bank of batteries to be used, they also improve the fuel consumption of diesel engines, as the operator has the option to turn the engine off in the knowledge that it will start again.

Industrial applications that require power recovery and/or high power bursts are also well suited to energy systems incorporating ECs.[14] Some load lifting equipments such as forklift trucks and seaport cargo cranes use hybrid power systems that include ECs to reduce the size of the primary energy source.

In smaller products such as mobile phones, ECs can provide a pulse of energy to meet the needs of high current LED flash devices. Enhanced battery performance can be obtained using LEDs rather than current xenon technology. There is also interest in using ECs to provide higher quality audio from mobile phone speakers by providing better power management to the audio circuits. In cameras, ECs are utilised to extend the life of the battery by providing some of the peak power required to power intensive areas such as the optical zoom and flash.

3.2 Power quality applications

Uninterruptible power supplies (UPS) have protected the power quality in industrial and commercial applications for many years. In sectors such as pharmaceuticals, biotech, paper and semiconductor production the cost implications of a poor quality power supply necessitate some form of voltage protection. Even if there is no damage to critical equipment, the loss of stock or manufacturing capacity can be prohibitive. The effects of loss of service in telecommunications or data storage centres also mean that power quality is viewed as a critical issue. UPS systems typically provide bridging power support until an auxiliary power supply can be brought on line or delicate equipment is shut down in a controlled manner. Dependent on the type of UPS system, it can also provide protection against voltage spikes and undesired harmonics in the power supply. If, as expected, there will be more decentralised generation coupled with a higher dependence on variable renewable energy generation, localised power quality management products will have a greater role to play. The role of ECs within UPS systems is seen as being favourable.[15]

ECs are also currently used to stabilise dc bus voltages in vehicles, in order to protect the delicate electronics of engine control and other electronic equipment from sudden variations in voltage, and provide power to energy intensive auxiliary equipment.[16]

3.3 Backup, safety and low maintenance applications

In many consumer electronic devices, *e.g.* laptops, cameras, and mobile phones, smaller ECs provide backup energy storage when the primary energy source is being changed; this allows basic information such as date and time information to be stored. The widespread use of smaller ECs in this field has shown that they are a cost effective way to provide this service.

A newer market is found in cordless hand tools that use ECs as the energy store. These tools are characterised by smaller amounts of energy stored in comparison to batteries, but with the benefit of longer lifetime, less temperature-dependent loss of performance, and a much shorter charging time (typically under 3 minutes). Screwdrivers, pipe cutters and torches are commercially available but more energy intensive tools such as drills require the energy density provided by lithium ion batteries.

Some fail-safe actuators use ECs to power the actuator to a predetermined "safe" position in the event of a power failure. Using energy stored in ECs rather than in springs allows the actuator motor to be reduced in capacity, as it no longer has to overcome the force of the spring.

Rigorous performance testing of EDLCs concluded that these devices are reliable over hundreds of thousands of cycles. Their robust design and long cycle life result in the requirement for little maintenance, and they offer a significant weight reduction in comparison with batteries for some applications. For these reasons, EDLCs are used as an integrated power source in the emergency door and slide management system on the Airbus A380.†

ECs are increasingly used in wind turbine blade pitching systems to provide emergency power backup and peak power to provide the energy to the blade pitching motors.[17] This not only increases the efficiency of the wind turbine, but is also critical in terms of safety as the blades can be pitched to reduce damage associated with high wind speeds. Lower maintenance components are a critical design consideration for offshore wind turbines due to the increased costs of repair/replacing components.

Overall, ECs will continue to find growth markets as components in hybrid energy systems for energy capture and/or provision of peak power, power quality, and to a much lesser degree as a primary energy source in their own right. The penetration into these markets will be driven by improvements in the performance of ECs, which continues as research progresses. As with other products, the limits to market penetration will be governed by future performance/cost improvements of ECs in relation to other technologies, but the expected growth in electrical systems coupled with changes of electrical generation and supply should mean that ECs have growing markets in which to compete.

4. Materials

Although ECs are designed to outperform batteries in terms of power density, it may be necessary in some applications to sacrifice power density performance to increase energy density. Other applications, such as power quality management, place a greater emphasis on power density. For some applications self-discharge may be crucial whereas for others this may only be a relatively minor inconvenience. This suggests that one single EC design will not suffice and that the appropriate selection of materials is crucial.

4.1 Carbon electrode materials

From the considerable amount of literature available on carbon electrode materials,[2,18–20] four major requirements for EC electrode carbons can be identified as: high surface area, low electrical resistance, good polarisability and controllable pore size. The following subsections give a brief outline of the various carbon materials that meet these requirements.

A substantial fraction of the research carried out on ECs has depended, and continues to do so, on an understanding of the properties of carbon. Carbon is an element almost uniquely suited to EDLC production due to the existence of several allotropic forms (fullerenes, graphite and nanotubes), various microtextures owing to the degree of graphitisation, a rich variety of dimensionality from 0 to 3D and the ability to exist in different forms (powders, fibres, foams and composites). They are also easy to process, relatively low cost, chemically stable in different solutions (from strongly acidic to basic), possess very high surface areas and are stable over a wide range of temperatures.[18]

4.1.1 Activated carbons. Activated carbons are generally produced from the pyrolysis of biomass precursors such as wood, coal, peat, coconut and other agricultural waste products. The specific surface area and porosity of carbons are then significantly increased by an activation process which removes disordered carbon from the structure in an oxidising atmosphere. A large variety of carbonaceous materials can be converted into activated carbon, although the properties of the final product and the ease with which it can be produced will be dependent on: the nature of the raw material used, the nature of the activating agent, and the conditions of the activation process. There are two methods for activation: physical and chemical. In the chemical activation process, carbonisation and activation are carried out by thermal decomposition of the precursor impregnated with a chemical activating agent, such as KOH, HNO_3 or H_3PO_4. Physical activation involves gasification of the carbon produced from carbonisation with an oxidising gas at elevated temperatures.

As capacitance is theoretically related to the surface area of the electrode (eqn (1)), activated carbons are commonly used for EDLC production with surface areas over 2000 $m^2\ g^{-1}$ possible. *Inter alia* Shi,[18] Qu and Shi,[19] and Frackowiak and Béguin[20] have carried out comprehensive studies on activated carbons to determine the correlation between porous structure and the performance in EDLCs. The specific capacitance was observed to vary over the range 94–413 F g^{-1}, however, it was found that the specific capacitance was not proportional to total surface area as predicted by eqn (1) (see Section 4.5).

4.1.2 Carbon nanotubes. Since the late 1990s there has been a large volume of research carried out on the applicability of

---

† Maxwell Technologies Press Release, 14 April 2005, http://www.maxwell.com/news-events/release.asp?PRID = 162.

carbon nanotubes (CNTs) as EDLC electrodes. CNTs have a narrow pore size distribution (PSD), highly accessible surface area, low resistivity, and high stability.[21]

The basic structure of a CNT is a single seamless cylinder of crystalline graphite, with a well-defined central core, whose end can be capped by a fullerene-type structure. This type of CNT is known as a Single Walled Carbon Nanotube (SWCNT). The more common form of CNTs is as Multi-Wall Carbon Nanotubes (MWCNTs), which consist of several graphene cylinders, arranged concentrically around a common axis. CNTs are composed of mesopores and exhibit surface areas $\sim 10^2$ m^2 g^{-1} (surface areas up to 475 m^2 g^{-1} have been reported for activated MWCNTs).[20] Their accessible pore network combined with low resistivity and high stability has led to CNTs being extensively researched as materials for EC electrodes. Specific capacitances of between 15 and 300 F g^{-1} have been reported using different configurations of CNTs.[22]

Due to high production costs, it is not considered viable to use CNTs as the bulk active material in electrodes. Therefore, the most recent developments for the use of CNTs in the manufacture of EDLCs are as conductivity enhancers replacing carbon blacks. They have several advantages over carbon or acetylene blacks as they have an electrical conductivity exceeding 5×10^5 S m^{-1} at room temperature for purified materials.[21] The high aspect ratio of CNTs compared to other carbon additives allows for lower weight doping levels to obtain comparable conductivity enhancement. One investigation by Chen *et al.*[23] noted that by changing acetylene black to CNTs in electrode manufacture resulted in a 90% reduction in ESR. To reduce inter-particle resistance in carbon aerogel electrodes, CNTs were grown directly onto microfibrous carbon paper, and then dipped into polyacrylonitrile and dimethylformamide aquagel. Subsequent carbonisation and activation produced binderless composite electrodes that exhibited a specific capacitance of 524 F g^{-1} (four times that of the pristine carbon aerogel electrode).[24]

4.1.3 Carbon nanofibres.

Carbon nanofibres (CNFs) were first synthesised in the 1990s and differ from the better-known carbon fibres in that their diameters are much smaller and are more difficult to produce in a well-aligned manner.[25] CNFs in many ways represent an ideal material for application in EDLCs; they generally exhibit an open, mesoporous structure and good conductivity (only along the fibre axis). If they are produced from electrospun polymers, compared to CNTs, they are relatively cheap and easy to manufacture and are therefore an attractive alternative to CNTs. Binderless web structures can also be produced *via* electrospinning. CNFs can also be produced by chemical vapour deposition, although this increases costs *vis-a-vis* CNTs.

CNFs have diameters between 50 and 500 nm with an average pore size (d_{av}) of 3–20 nm, and activation can lead to the opening of smaller pores. Due to the morphology of activated CNFs most of the porosity is situated on the surface of the fibres leading to more easily accessible active sites.[25–28] Activated CNFs have been noted to possess BET surface areas of up to 1200 m^2 g^{-1} with specific capacitances in the range of 60–175 F g^{-1}.[26,27] Newer multi-branched CNFs exhibited a specific capacitance of 300 F g^{-1}.[28]

Presently, CNFs are not considered to be an ideal material for ECs due to their high cost and high ESR arising from poor inter-fibre conductivity.

4.1.4 Carbide-derived carbons.

The unique nanoporous structure of carbide-derived carbon (CDC) together with the narrow pore size distribution and the possibility to fine-tune the pore size has lead to a large volume of research being carried out to study these materials as electrodes for electrochemical capacitors.

Carbide derived carbons are manufactured by the chlorination of metallic carbides (*e.g.* TiC, B_4C, ZrC, Ti_3SiC_2, Ti_2AlC, and SiC) at elevated temperatures (800–1200 °C; high enough to facilitate the reaction, but lower than that required for graphitisation). The resulting carbons exhibit a high specific surface area with a pore size that can be controlled by choice of starting material and chlorination temperature.[29]

Unlike other materials research for ECs, the research into the use of CDCs has been concentrated on the development of microporous carbon materials for improving performance. All results below are for microporous carbon materials with average pore widths below 2 nm.

So far, the best CDC materials for ECs are derived from TiC. TiC-derived CDC at 800 °C with BET surface area of over 1600 m^2 g^{-1} and average micropore width of 0.7 nm have shown specific capacitances of between 130 and 190 F g^{-1}.[30,31]

Recently a new method was developed, which improves the pore size distribution in CDCs, using the chlorination of carbide/oxide mixture, due to which the carbothermal reduction of TiO_2 in chlorine atmosphere gives the possibility to oxidise *in situ* the desired part of carbon during its formation from the carbide.[32] This method produced microporous carbons with surface areas of up to 1600 m^2 g^{-1} and specific capacitance of 120 F g^{-1}.

This class of carbons are important from a research point of view but have limited commercial potential due to their high cost, as well as safety and environmental concerns associated with production.

4.1.5 Template-derived carbons.

Template-derived carbons are produced by filling the porous structure of an inorganic matrix with a carbon precursor (*e.g.* sucrose, propylene, pitch, or polymer solutions) followed by carbonisation. The inorganic template is then completely removed by hydrofluoric acid. The use of a template allows for the production of porous carbons with well-defined pore characteristics such as surface area, pore volume and PSD.

Activated carbons can exhibit very wide PSDs with pores randomly connected, leading to poor conductivity and ionic transport for use as electrodes. Template-derived carbons have an advantage over activated carbons as they produce high-surface area materials with regularly interconnected pores that allow for improved ionic transport and improved power density. The pore size of the template can be engineered to match pore width to electrolyte properties to improve performance. Xing *et al.*[33] have shown that template-derived carbons produced a 10% reduction in capacitance with increasing discharge rate compared with Maxsorb® activated carbon's 80% reduction under the same conditions. Specific capacitances of 220 F g^{-1}

have been reported for template-derived carbons with surface areas of 1500–1600 m^2 g^{-1}.[34]

As with carbide-derived carbons, high production costs and safety considerations (particularly with the use of hydrofluoric acid) have limited their use for potential commercial development, although they are useful materials for fundamental research.

4.1.6 Polymer-derived carbons. Polymer derived carbons are highly promising for EC applications due to their low cost and the fact that it is possible to control the pore structure of the precursor.[35–38] Organic gels such as resorcinol formaldehyde (RF),[39] polyvinyl chloride,[40] phenol–melamine formaldehyde,[41] phenolic novolac furfural[42] and phenol formaldehyde (PF)[43,44] have been used as carbon precursors.

RF gels have been the most commonly utilised polymer gel for the production of carbon electrodes in ECs.[39,45,46] Zhu *et al.*[46] reported that an activated carbon xerogel (with surface area, pore size and pore volume of 1500 m^2 g^{-1}, 3.2 nm, and 0.67 cm^3 g^{-1} respectively) produced a specific capacitance of 295 F g^{-1} using aqueous electrolyte (6 M KOH). Other studies[47,48] have investigated the use of room temperature ionic liquid (RTIL) electrolytes with a commercially available activated carbon material and carbon xerogels, aerogels and cryogels. After normalisation to surface area, the specific capacitance of gel-derived carbons outperformed the activated carbon electrodes. Section 4.5 provides a more in depth discussion on the effect of pore size in electrode carbons. The relationship between pore size and capacitive performance with RTIL electrolytes has been investigated by Sillars *et al.*[49]

Carbons based on phenol formaldehyde (PF) gels have emerged as particularly interesting due to their low cost and density.[43] They undergo a similar sol gel polymerisation process to that of RF gels.[40,43] Work is currently being undertaken with the aim of porosity control at the nanoscale in PF gel-derived carbons.

4.1.7 Carbon perspective. Section 3 has shown that ECs are likely to have widespread applications and, as such, reduced costs and ease of production are paramount, apart from in a few niche applications. This excludes more specialised carbons, such as carbide-derived and template-derived materials, because they involve complex and potentially hazardous production methods. This is not to lessen their importance in fundamental studies, or to overlook the fact that they can frequently outperform cheaper and commercially available materials. Currently carbon nanotubes and nanofibres are economically uncompetitive with biomass or polymer derived carbons. Therefore, the mass commercial development of ECs is likely to be based around the latter forms. Of these, biomass derived carbons have the advantage of being significantly cheaper but have the disadvantage that their PSD is difficult to control. Polymer derived carbons have the advantage that is it is possible to engineer PSDs more precisely but, of course, are more costly. The fundamental importance of PSD is discussed in Section 4.5. However, carbon nanotubes and nanofibres may prove to be useful in small concentrations, as conductivity enhancers.

4.2 Heteroatoms and surface functionalities

Carbons used in ECs contain markedly variable amounts of other elements: retained through incomplete carbonisation of the precursor or added during preparation. Typically, heteroatoms present in appreciable quantities (up to 10 wt%)[50] include oxygen, hydrogen and nitrogen. To a lesser extent, residual catalyst particles, such as iron or sodium, are also found. These different atoms can affect the capacitive behaviour of the carbon materials through their participation in Faradaic reactions, changing the electronic conductivity of the bulk material,[51] or by influencing wettability, and consequently affecting the electroactive surface area. For example, in devices that use an aqueous electrolyte, the presence of hydrophilic surface groups is desirable to maximise the amount of electrode porosity filled with electrolyte. However, increases in specific capacitance due to the incorporation of heteroatoms can be accompanied by increases in ESR (with a resultant decrease in power density) and self-discharge rate.[52]

4.2.1 Oxygen. The presence of oxygen-containing functional groups on carbons is almost unavoidable, as empty valencies remaining from high-temperature treatment are highly reactive. Atmospheric oxygen is reversibly physisorbed, as well as being irreversibly chemisorbed, by carbons on exposure to air yielding reactive surface functional groups such as phenol, carbonyl, carboxyl, quinone and lactone groups.[50,53] The activation process usually results in the addition of acidic oxygen functionalities to the carbon surface.[50] On the other hand, basic oxygen groups are formed when a carbon subjected to high-temperature treatment in an inert environment is cooled and subsequently exposed to atmospheric oxygen.

Self-discharge characteristics are known to be influenced by the oxygen content of the carbon. Specifically, carbons with acidic surface character exhibit comparatively high rates of self-discharge.[54] This is usually accompanied by an increase in the ESR and decrease in electrode stability. Furthermore the presence of oxide groups can cause gas to be evolved on charge/discharge.

4.2.2 Nitrogen. Ammoxidation of carbonaceous materials (a process similar to gas-phase activation using a fraction of ammonia in the feed stream) has been studied as a way of adding nitrogen to electrode carbons.[55,56] It was found that the addition of nitrogen in this manner caused a decrease in surface area, but resulted in a threefold increase in specific capacitance.[55]

The chosen precursor affects the elemental make up of the resultant carbon. The polymers discussed in Section 4.1.6 contain oxygen and hydrogen atoms in the final carbon. To increase residual nitrogen-content, the carbonisation of melamine–formaldehyde resins (and their composites),[57–60] polyacrylonitrile composites[61,62] and the impregnation of urea and melamine in activated carbon precursors[63,64] have been studied. The carbonisation of nitrogenous fibres[65] and organic liquids in mica templates[66] has also been investigated as possible precursors for the production of nitrogen-enriched carbons for EC electrodes.

However, the relationship between heteroatom content, surface area and capacitance is not fully understood. Jurewicz *et al.*[55,56] have reported that an increase in nitrogen content does not always result in an increase in capacitance as the incorporation of heteroatoms is usually at the expense of surface area, further highlighting the importance of porosity in EC electrodes.

Elsayed[67] recently investigated the production of nitrogen-enriched carbons for CO_2 capture, where co-pyrolysis mechanisms, as well as amine 'catalysed' polymerisation, were investigated. Controlled addition of nitrogen to the carbon surface was achieved, while retaining a significant degree of porosity and surface area. The application of similar materials in ECs is currently being explored.

4.2.3 Hydrophobic surface functionality. When organic electrolytes are used, a hydrophobic electrode surface is desirable to maximise electroactive surface area. To increase hydrophobicity, physical and chemical methods have been investigated.[68] Physical methods involve the use of elevated temperatures (under hydrogen or an inert atmosphere) to remove hydrophilic functional groups. Chemical modification can be carried out by the addition of an organosilicon compound or gas phase fluorination. The most effective surface modification technique for hydrophobisation has been found to be treatment with a surfactant.[69,70] Fang and Binder[69] produced activated carbon aerogels modified with sodium oleate and vinyltrimethoxysilane (vtmos). Both surfactants added hydrophobic functional groups to the carbon surface with no significant effect on the surface area. The addition of the vtmos functional groups increased specific capacitance by 10 F g^{-1} with no pseudocapacitive behaviour being observed, and reduced the ESR from 5 to 1.8 Ω cm^{-2}. Capacitance decay over 20 000 cycles is comparable with an untreated surface, showing that vtmos surface groups do not significantly affect the cycling life of the EDLC.[70]

4.3.1 Metal oxides. Many metal oxides exhibit pseudocapacitive behaviour over small ranges of potential. Ruthenium dioxide, RuO_2, exhibits the highest reported specific capacitance (*ca.* 850 F g^{-1})[71] over a relatively wide potential range, and has been the subject of extensive research. The pseudocapacitive behaviour of RuO_2 was identified in 1971 when the Galvanostatic charge/discharge curve was identified as being that of an 'electric condenser'.[72]

The unique properties of RuO_2 that result in significant pseudocapacitive behaviour are that the material exhibits a metallic electronic conductivity[73,74] and that several voltage-dependent redox processes overlap in the operating range of potential.[2] This overlap of the redox reactions results in a fairly constant capacitance.

The morphology and hydration state of RuO_2 are of great importance in determining the level of protonic conductivity exhibited by the material. Zheng *et al.*[75,76] found that the amorphous, hydrated form of RuO_2 produced using a sol–gel process, resulted in a specific capacitance of 720 F g^{-1}. Systematic studies by Dmowski *et al.*[71] revealed that electronic conductivity of RuO_2 nanocrystals is balanced with the protonic conductivity of the surrounding structural water when one mole of RuO_2 is hydrated by 0.58 mole of water ($RuO_2 \cdot 0.58H_2O$), resulting in a maximum capacitance of 850 F g^{-1}. Electrolytic production methods have also been found to yield hydrous forms of RuO_2.[77] This has enabled increased electrochemical utilisation of the metal oxide by forming thin layers (*ca.* 3 nm thick) on high surface area substrates. Electrodes based on high surface area conductive substrates (such as CNT film[77] or activated carbon[78]) result in more efficient use of RuO_2. From a practical point of view, RuO_2 is prohibitively expensive for transport applications and has mainly been used in small-scale military devices.

For a metal oxide to be of use in a pseudocapacitor, the following characteristics are desirable: chemical and structural reversibility of reactions occurring in the charge/discharge process, high electrical conductivity, and both electron and proton hopping in the oxide lattice.

Less expensive alternatives to RuO_2 have been explored over the past decade and a wide-ranging report on recent studies into the capacitive behaviour of metal oxides can be found in the review article by Jayalakshmi and Balasubramanian.[79] Pseudocapacitive behaviour is displayed to some extent by many metal oxides (such as nickel, cobalt, iron and tin oxides) with the majority of current research being concentrated on manganese, vanadium and iron oxides. These compounds have shown promise as electrode materials[80–82] and various synthesis methods have been used to produce materials with different morphologies and pore characteristics.[83–86] Since the electrical conductivity of these alternatives is drastically lower than that of RuO_2, maximising the electrochemical utilisation of the metal oxide is essential. Materials with increased surface area have been developed with this aim, and electrodes employing conductive substrates covered with a thin layer of pseudocapacitive metal oxide show particular promise.[82,87,88]

4.3.2 Lithium intercalation capacitors. Asymmetric cells, where a porous carbon electrode is paired with a doped lithium intercalation compound, are devices that combine the charge storage mechanism of an EDLC with that seen in Li-ion batteries. Referred to as lithium intercalation capacitors (LICs), these devices produce a higher specific energy than other ECs and deliver a higher specific peak power than Li-ion batteries. LICs exploit the reduction in open circuit voltage caused by lithium doping to produce devices with higher output voltages in comparison with symmetric ECs.

This technology was first realised using nanostructured $Li_4Ti_5O_{12}$ combined with activated carbon in an organic electrolyte to construct a device that produced a specific energy five times that of EDLCs available at the time.[89] Subsequent to this study, advances in this system and different materials combinations in LICs were explored.[90–97] Devices using $Li_4Ti_5O_{12}$ have been shown to exhibit long cycle lives, as this compound does not exhibit a great degree of expansion or contraction during Li^+ intercalation,[89–91] a problem observed with other hybrid devices. Graphite has also been investigated as an intercalation host in LICs with increased specific energy due to a larger operating voltage.[92,93] However, LICs, especially those using a graphite electrode, have the disadvantage that excessive discharge rates can result in solid lithium forming on the electrode surface which significantly reduces cycle life and is a potential hazard. Also, the intercalation electrode can limit the power of these devices as the solid state diffusion of lithium ions is a slow process in comparison with the EDLC mechanism.[91–93]

To be competitive with established devices, LICs need to exhibit a specific power and cycle life comparable with that of non-aqueous EDLCs[98,99] as the increased energy density can be met with available battery technology.

4.3.3 Electroconductive polymers. Another possible electrode material for ECs appeared with the development of electrically conductive polymers (ECPs). These polymers possess π–orbital conjugation which, as well as resulting in electronic conductivity, gives compounds the ability to be oxidised or reduced at an electrode interface.[2,100]

ECPs that have been considered as electrode materials for ECs include polymethyl methacrylate,[101] *p*-phenylenevinylene,[102] polypyrrole,[103] polythiophenes[104] and polyaniline (PANI).[105] Of these polymers PANI has produced the most promising results as it has an easy polymerisation process, good capacitance performance, low cost, and is considered environmentally friendly.[106] The drawback of these materials is the high ESR associated with the random deposition method utilised in manufacturing. To overcome this, ECPs are usually found in composite electrodes with fillers that exhibit high conductivity, and have specific surface areas in the region of 1000 m^2 g^{-1}. Also, the long-term stability has proved to be a problem due to the repeated swelling and shrinking of ECPs during charge/discharge.[107] The use of activated carbon (AC) as a substrate allows for an enlarged active surface area of conductive polymer. Wang *et al.*[108] coated AC with PANI with the aim of increasing the specific capacitance of the electrodes while retaining a good cycle life. The study found that the PANI/AC composite exhibited a specific capacitance of 587 F g^{-1} in comparison to 140 F g^{-1} for the pristine AC due to the introduction of pseudocapacitance. It was also found that the capacitance retention after 50 cycles for the PANI/AC composite was 92%, significantly greater than the value of 65% obtained for pure PANI. Particular interest has been paid to CNTs due to their high conductivity, which greatly reduces the resistivity of PANI composites.[109–111] Gupta and Miura[111] observed an increase in specific capacitance to 485 F g^{-1} for a PANI(73%)/SWCNT composite by comparison to specific capacitances of 34 and 234 F g^{-1} for pure SWCNTs and PANI respectively.

4.4 Electrolytes

The type of electrolyte employed in ECs has a marked effect on the amount of energy stored in the cell, and how quickly this energy can be released. Due to the relationship governing the amount of energy stored in EDLCs (eqn (2)) it is evident that the operating voltage is of importance in the determination of energy density. In ECs, the decomposition voltage of the electrolyte determines the operating voltage of the cell.

4.4.1 Aqueous-based electrolytes. For aqueous electrolytes, the maximum operating voltage is theoretically limited by the electrolysis of water to 1.229 V (at 25 °C). Larger amounts of energy can be stored in ECs when using an organic electrolyte, where the operating voltage is limited to roughly 2.7 V (for propylene carbonate solvent), and wider operating ranges are attainable when using ionic liquid electrolytes (*ca.* 3.5 V). Electrolyte conductivity has a significant effect on the equivalent series resistance of the cell, which in turn determines power output. Aqueous electrolytes tend to produce faster rates of charge/discharge due to the relatively high conductivity and low viscosity of concentrated solutions. The conductivity of 6 M KOH at 25 °C is in excess of 600 mS cm^{-1} and this compares to 20 mS cm^{-1} for tetraethylammonium tetrafluoroborate in propylene carbonate and in the region of 10 mS cm^{-1} for typical room temperature ionic liquids (original data). The viscosity of aqueous solutions is significantly lower than that of alternative EC electrolytes.[112] Further advantages associated with aqueous electrolytes are their low cost and ease of manufacture in comparison with hygroscopic organic based and RTIL electrolytes. The most commonly employed aqueous electrolytes are 1 M H_2SO_4 and 6 M KOH,[113] although neutral electrolytes, such as NaCl[57] and KCl[81] have been investigated.

Relatively concentrated electrolytes are required to minimise the ESR and maximise power output. However, strong acids and bases determine materials selection for cell manufacture. The use of concentrated electrolytes also increases the rate of self-discharge displayed by the capacitor.[2]

4.4.2 Organic-based electrolytes. Organic electrolytes allow for increased operating voltages of up to 3 V and a consequent increase in energy density (according to eqn (2)). Typically, the operating voltage is set to 2.5 V to prevent oxidation of the electrolyte through over-charging. To ensure that these electrolytes can operate at the higher voltages they must be handled in an atmosphere free of water and oxygen. This ensures that the evolution of H_2 and O_2 gases at potential differences above 1.23 V does not occur.[107]

Salts are added to organic solvents to provide mobile ions for transport to the electrode surface. This provides a wider variety of electrolyte–solvent systems *vis-a-vis* aqueous electrolytes.[2] The two most common organic solvents used are propylene carbonate (PC) and acetonitrile (AN). AN was often preferred, as its ESR is a factor of three lower than that of PC. However, there is continuing controversy over the safety of AN (the use of which is prohibited in Japan), in particular in vehicles, due to its high toxicity and flammability. Research aimed at developing a non-toxic electrolyte with low resistivity has proven unsuccessful.[98] Most organic electrolyte based ECs available commercially utilise PC as the solvent. Tetraalkylammonium salts of anions PF_6^- and BF_4^- are preferred for the production of organic electrolytes due to their high solubility, higher dielectric conductivity, and good conductivity (relative to other organic solutions).

A major disadvantage of organic electrolytes is that they exhibit a significantly higher ESR (typical increase by a factor of 50–100 *cf.* aqueous electrolytes),[114] due to lower conductivity and higher viscosity. The increased viscosity also results in reduced wettability, further increasing the ESR and lowering the capacitance due to under-utilised surface area. This increase has a detrimental effect on the power capability of the EC devices, according to eqn (3). However, the increased operating voltage compensates in part for the reduction in power density.[107]

4.4.3 Room temperature ionic liquid electrolytes. Room temperature ionic liquids (RTILs) are essentially molten salts with melting temperatures at or below room temperature and consist of highly asymmetric combinations of anion and cation. Some typical examples of cations are given in Fig. 4 where R_1 to

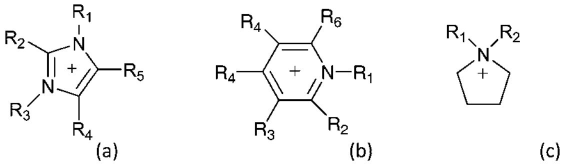

Fig. 4 Structures of cations found in RTILs: (a) imidazolium, (b) pyridinium and (c) pyrrolidinium.

R_6 represent locations of alkyl groups or hydrogen atoms. Other examples of cations include ammonium and phosphonium based ions.[115–121]

Typical examples of anions include simple halides, *e.g.* Cl^-, I^-, and Br^-, larger more complex ions, *e.g.* BF_4^- and PF_6^-, and larger and even more complex ions, examples of which are shown in Fig. 5.

This is by no means an exhaustive list, allowing for different anion–cation combinations and for different types, numbers and chain lengths of attached groups; there are a vast number of possible ionic liquids although not all will be liquid at room temperature. Currently one of the most popular RTILs for electrolyte use is 1-ethyl-3-methylimidazolium bis(trifluoromethylsulfonyl)imide and new RTILs are appearing on the market on a regular basis.

The main advantage of using RTIL electrolytes is their stability over a wide range of potential. Anodic voltages of up to 4.2 V have been reported.[122,123] This equates to a sixteen-fold increase in energy storage compared to an aqueous electrolyte. Other advantages include low volatility and some RTILs are non-flammable. There are, however, some disadvantages. RTILs have relatively high viscosities[112,124–128] and much lower ionic conductivities than aqueous electrolytes.[121,128–135] Not all RTILs have particularly large anodic windows, some no larger than an aqueous electrolyte. Operation at low temperatures may be difficult as many RTILs have melting temperatures just above 273 K.[125] Some RTILs, notably those containing BF_4^- and PF_6^-, are known to produce hydrofluoric acid posing potential safety and disposal hazards. RTILs are hygroscopic which reduces the operating potential range, and have to be handled in an inert atmosphere. A major disadvantage of using RTILs is their high cost, although larger scale production may reduce the price in future.

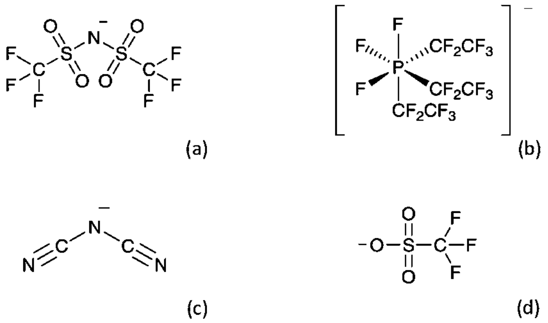

Fig. 5 Structures of anions found in RTILs: (a) bis(trifluoromethylsulfonyl)imide, (b) tris(pentafluoroethyl)trifluorophosphate, (c) dicyanamide and (d) trifluoromethylmethane sulfonate.

A highly promising area of interest in the application of RTILs as EC electrolytes is in the use of protic ionic liquids (PILs). A typical PIL consists of a Brønsted acid–base mixture such as α-picoline with trifluoroacetic acid. Xu and Angell[136] have reported that the conductivity of these proton transfer salts can be an order of magnitude higher than that for the aforementioned RTILs. Rochefort and Pont[137] identified that these salts could be applied to pseudocapacitive systems, coupling the benefits of a wider potential range with the high specific capacitance available using RuO_2. The use of carbon electrodes containing surface functionalities, as a lower cost alternative to RuO_2, with PIL electrolytes has been recently investigated by Mysyk *et al.*[138] Although the operating potentials associated with PILs are not as wide as other RTILs, the development of these electrolytes has allowed the operating voltage of pseudocapacitor devices (which usually operate with aqueous electrolytes) to be increased by a factor of 2. The major research challenges in this field are to reduce the costs associated with production and to obtain a greater understanding of the fundamental mechanisms of operation.

4.4.4 Solid electrolytes. Choudhury *et al.*[139] provide a comprehensive review of the application of the most studied category of solid electrolytes, hydrogel-polymers, and as such this topic will not be discussed here. These systems are being explored to address the safety concerns with liquid electrolytes, particularly in the area of transport applications.

4.5 Porosity in EDLC electrodes‡

An ongoing area of debate in the study of ECs is the influence of electrode porosity on capacitance. Recent research has focussed on tailoring the PSD of nanoporous carbon materials, in order to maximise the accessible surface area for charge storage.[30,140–143]

As previously mentioned in Section 4.1.1, Shi and Qu,[18,19] found that the relationship between surface area and specific capacitance did not follow eqn (1). Two reasons were offered to explain this behaviour. Firstly, all surface area accessed by N_2 at 77 K (used to determine surface area) may not be accessible to the electrolyte and secondly that the local electroadsorption properties are dependent on pore size. Shi[18] proposed that instead of using one value of C/S in eqn (1), this parameter should vary with pore size. This new model provided a better fit for the experimental data and suggested that micropores play an important part in double-layer capacitance. Qu and Shi[19] discussed the effect of pore size on the high power capability of the microporous ACs. They found that the ACs that performed best at higher current densities had mean pore sizes (d_{av}) of 1.5 nm for aqueous electrolytes.

A number of research groups have attempted to determine the importance of mesoporosity in carbon electrode materials. Some investigations[47,48] suggest that micropores are not accessible to electrolyte solution, because solvated ions are too large, and ionic liquids too viscous, to enter micropores. In contrast, other

---

‡ IUPAC recommendations for porosity characterisation: micropores have a width smaller than 2 nm, mesopores have widths in the region 2–50 nm, and macropores have a width larger than 50 nm.

studies[30,141–143] stress the importance of microporosity in maximising specific capacitance.

Raymundo-Piñero *et al.*[141] investigated biomass-derived activated carbons and concluded that mean pore size was more important than surface area for enhancing specific capacitance. The optimum pore sizes for aqueous and organic electrolytes were found to be 0.7 and 0.8 nm, respectively. Further studies determined the mechanism by which micropores become accessible to ions.[30,141–145] Chmiola *et al.*[30] used CDCs with a unimodal pore size distribution ($d_{av} \approx 1$ nm) and reported an anomalous increase in specific capacitance in an organic electrolyte, when compared with other CDCs possessing mean pore widths greater than 2 nm. This was attributed to the desolvation of ions upon entering the micropores. To confirm this supposition, RTIL electrolyte at 333 K was combined with microporous CDCs and studied in an attempt to match pore size to ion size.[144] When d_{av} was matched to ion size, maximum specific capacitance of 160 F g^{-1} (40 F g^{-1} higher than for an equivalent mesoporous material) was obtained. This indicated that ion adsorption is achieved in the most efficient way. It was established that as d_{av} increased above the optimum, specific capacitance decreased and below the optimum pore width ions became sterically hindered from entering the pores. Largeot *et al.*[144] argued that because the larger pore widths could still only accommodate one ion, the decrease in capacitance was attributed to an increase in double-layer thickness.

Ania *et al.*[145] utilised solvent free ionic liquids as *in situ* probes to determine the effect of ion size on EC performance. Microporous activated carbon was used with four RTIL electrolytes of varying cation size (0.8–2 nm). It was observed that specific capacitance decreased with increasing ion size, confirming the importance of the relationship between pore size and ion size for enhancing capacitor performance. Since ion size determines the "accessible volume",[145] this study showed that the optimum pore size of the carbon electrode is dependent on the ion size of the electrolyte used.

Other studies have investigated the effect of mesoporosity on specific capacitance, and seem to contradict the original belief that such pores are necessary to facilitate electrolyte diffusion into smaller pores.[146,147] Fernández *et al.*[146] studied a variety of phenolic resin derived activated carbons, five were exclusively microporous, the remaining samples exhibited a bimodal PSD. Comparisons were made between samples possessing the same micropore structure, but variable mesopore volumes. Increasing levels of mesoporosity appeared to have a detrimental effect on the *volumetric* capacitance of the ECs, reducing from 60 F cm^{-3} to 47 F cm^{-3} in an aqueous electrolyte, and 46 F cm^{-3} to 26 F cm^{-3} in an organic electrolyte.

The same study also investigated whether mesoporosity was necessary for fast diffusion of ions at high charge rates. The ratio of the fastest rate capacitance to the slowest rate capacitance was compared with average micropore size. For aqueous electrolytes the ratio was found to be independent of pore size, since the small ions of the aqueous electrolyte were able to access the smallest pores. In the organic electrolyte it was observed that ion diffusion became increasingly hindered by the decrease in average micropore width. A pore width of 1.2 nm optimised the rate capability of the organic electrolyte, in contrast to the optimum observed by Chmiola *et al.*[30,142–144]

Aurbach *et al.*[148] studied the effect of ion desolvation on charge/discharge behaviour. It was found that ions become trapped inside small pores, which then require a large potential to release them. This reduces the effective specific capacitance and cycle lifetime.

Traditionally, the most widely accepted EDLC model is based on the double-layer formation between planar electrodes and an electrolyte.[149] However, this model seems insufficient where three-dimensional networks of interconnected pores are involved in the charge storage mechanism. Huang *et al.*[150] proposed a heuristic model that incorporates the effect of pore curvature on capacitance. This model assumes that in the macroporous region, curvature has negligible effect on the specific capacitance and the planar electrode model remains valid. Conversely, in the mesopore region a different model is appropriate that of an electric double-cylinder. For micropores, it was proposed that the ions are aligned along the pore axis when charged, producing an electric wire-in-cylinder capacitor (a reduction of the double cylinder model, where the inner cylinder diameter is defined by the ion size). These models were successfully applied to carbons with unimodal PSDs.

Other groups are of the view that mesopores are essential for the full surface area of the porous carbons to be utilised in double-layer formation. Arbizzani *et al.*[47] and Lazzari *et al.*[48] investigated the use of an activated carbon that exhibited an average pore diameter of 3 nm with 50% of the structure being microporous, and compared the results to that of carbon xerogels and cryogels that possessed mesopores of average width 9, 15 and 20 nm. On normalising capacitance to mesopore surface area the carbon xerogels and cryogels outperformed the activated carbon. The mesoporous carbons displayed normalised capacitances comparable to that of a clean graphite electrode, *i.e.* 20–30 μF cm^{-2},[50] showing that most of the surface area of the carbon xerogels and cryogels was accessible to the RTIL electrolyte. Kim and Yang[151] produced similar results using activated carbon nanofibres.

Porosity is not only an issue in defining capacitance but has ramifications for the power densities displayed by ECs. This is investigated by comparing specific capacitance values obtained at high discharge rates with values measured at low discharge rates. Mesoporous carbons are considered essential for high power applications such as electric vehicles (EVs). Fernández *et al.*[152] worked with porous carbons derived from PVA and magnesium citrate with surface area of 1300 m^2 g^{-1}, a PSD centred between 5 and 15 nm. At a high current density (100 mA cm^{-2}) these carbons were found to maintain 85% of the specific capacitance in comparison with the capacitance obtained at a low discharge rate (1 mA cm^{-2}).

Fuertes *et al.*[153] carried out a study on three templated carbons each exhibiting a distinct pore regime; one carbon was exclusively microporous, another displayed small mesopores (~3 nm) and the third large mesopores (~16 nm). They assessed the effect of current density on specific capacitance for each carbon. At low rates (*ca.* 1 mA cm^{-2}) all carbon samples had a specific capacitance of 200 F g^{-1}. However, as the rate increased, specific capacitance decreased in a different manner for each carbon. The microporous carbon showed a decrease in capacitance of 75%. For the carbon with small mesopores, the reduction in capacitance was lower but showed a continual decrease in capacitance with increasing current density. The carbon with larger mesopores reached a minimum value of 100 F g^{-1} at much lower current densities, and would continue to allow for higher discharge rates with no further deleterious effect on capacitance.

This discussion highlights the complex relationship between PSD and the energy/power densities of EC devices which, despite considerable advances, remains to be fully elucidated. It is known that micropores are electronically complex in nature,[154] which should be incorporated into our understanding of charge storage mechanisms where micropores are involved. The effect of PSD on self-discharge through charge redistribution in pore networks is emerging as an important area of research with work currently being undertaken on this topic.

5. Conclusions

Capacitive devices are traditionally considered as the converse of batteries in that they are high power, low energy density devices. Although EDLCs may be thought of in this context, pseudocapacitors have many of the characteristics of both batteries and capacitors and there exists a continuum of electrochemical storage mechanisms between these extremes. As the awareness of the benefits of ECs is increasing, their range of commercial applications is growing and becoming technologically more diverse. Some applications require enhancement of their energy handling capabilities, others require improved power handling, and still others may require very low self-discharge rates. It is certain that each application will require a specific EC design. The advancement of future ECs depends critically on the development and deployment of new materials.

The main research challenges associated with ECs are to develop new electrode materials, to enhance specific capacitance by surface modification and to match electrode structure with electrolyte.

The most common form of electrode material is carbon and a wide variety of forms have been tested and commercialised. More exotic forms (such as nanofibres, nanotubes, template-derived and carbide-derived carbons) have been very important from a fundamental research point of view. However, it is unlikely that they will be developed commercially in the short or medium term due to prohibitive costs and often production methods. Research for commercial development should focus on biomass-derived and polymer-derived activated carbons. Of these biomass-derived activated carbons are cheaper but result in lower performance devices. Since it is possible to control and engineer the porosity of polymer-derived carbons, these can deliver improved performance but at a higher cost.

Surface modification of carbons can enhance capacitance although a thorough understanding of these mechanisms, their stability and influence on self-discharge has not been fully explained.

Many metal oxides exhibit pseudocapacitative behaviour, but the only truly effective material is still RuO_2, which is prohibitively expensive for widespread usage. Research is being undertaken on most viable alternatives, such as manganese, vanadium and iron oxides. Commercial pseudocapacitors based on these alternative materials are very much the Holy Grail of this subject. A breakthrough would constitute a step change in energy storage technology and therefore for clean energy in general.

Electrolyte selection is critical to device performance because energy density is proportional to the square of the electrolyte decomposition potential. Three main classes, in order of increasing decomposition potential, exist: aqueous-based, organic-based and RTIL. Most commercially available devices use organic liquids but they need to be manufactured in inert atmospheres, which increases production costs. *Ceteris paribus*, aqueous electrolyte devices are cheaper to produce and offer higher power densities, while RTILs offer higher energy densities, but at higher cost. Future applications will rely on systems based on all three electrolyte classes. Solid electrolytes are likely to have important applications in transportation where safety is of utmost concern.

A major research topic is to understand the relationship between electrode porosity and electrolyte. In particular, the importance of micro- and mesoporosity is still to be resolved. The literature is riddled with apparent contradictions and workers new to the subject may well find this topic daunting.

A large-scale and coherent research programme is needed to resolve these difficulties involving a wide array of materials and experimental techniques.

Acknowledgements

This work was funded by the Supergen Energy Storage Consortium (grant code EP/D031672/1).

References

1 P. J. Hall and E. J. Bain, *Energy Policy*, 2008, **12**, 4352–4355.
2 B. E. Conway, *Electrochemical Supercapacitors: Scientific Fundamentals and Technological Applications*, Kluwer Academic/Plenum Publishers, New York, 2nd edn, 1999.
3 H. I. Becker, General Electric Company, *US Pat.*, 2 800 616, 1957.
4 J. R. Miller and A. F. Burke, *Electrochem. Soc. Interface*, 2008, 53–57, Spring.
5 S. Trasatti and P. Kurzweil, *Platinum Met. Rev.*, 1994, **38**, 46–56.
6 K. West, B. Zachau-Christiansen and T. Jacobsen, *J. Power Sources*, 1993, **43–44**, 127–134.
7 A. K. Shukla, S. Sampath and K. Vijayamohanan, *Curr. Sci.*, 2000, **79**, 1656–1661.
8 S. S. Sandhu, J. P. Fellner and G. W. Brutchen, *J. Power Sources*, 2007, **164**, 365–371.
9 M. Mirzaeian and P. J. Hall, *Electrochim. Acta*, 2009, **54**, 7444–7451.
10 R. Carter and A. Cruden, *IEEE International Symposium on Power Electronics, Electrical Drives, Automation and Motion*, 2008, vol. 1–3, pp. 727–732.
11 T. Markel, A. Brooker, T. Hendricks, V. Johnson, K. Kelly, B. Kramer, M. O'Keefe, S. Sprik and K. Wipke, *J. Power Sources*, 2002, **110**, 255–266.
12 W. Lhomme, P. Delarue, P. Barrade, A. Bouscayrol and A. Rufer, *Conference Record of the 2005 IEEE Industry Applications Conference*, 2005, vol. 1–4, pp. 2013–2020.
13 Z. Gizinski, M. Gasiewski, I. Mascibrodzki, M. Zych, K. Zymmer and M. Zulawnik, *13th International Power Electronics and Motion Control Conference*, 2008, vol. 1–5, pp. 1562–1567.
14 S. M. Kim and S. K. Sul, *IEEE Transactions on Power Electronics*, 2006, vol.21, pp. 1420–1427.
15 I. Galkin, A. Stepanov and J. Laugis, *International Baltic Electronics Conference, Proceedings*, 2006, pp. 237–240.
16 J. M. Miller and M. Everett, *Power Electronics in Transportation*, 2004, pp. 19–26.
17 T. Z. Wei, S. Wang and Z. P. Qi, *2007 International Conference on Electrical Machines and Systems*, 2007, vol. 1–4, pp. 1524–1527.
18 H. Shi, *Electrochim. Acta*, 1995, **41**, 1633–1639.
19 D. Qu and H. Shi, *J. Power Sources*, 1998, **74**, 99–107.
20 E. Frackowiak and F. Béguin, *Carbon*, 2001, **39**, 937–950.

21 S. Wen, M. Jung, O.-S. Joo and S. Mho, *Curr. Appl. Phys.*, 2005, **6**, 1012–1015.
22 E. Frackowiak, K. Metenier, V. Bertagna and F. Béguin, *Appl. Phys. Lett.*, 2000, **77**, 2421–2423.
23 Q. L. Chen, K. H. Xue, W. Shen, F. F. Tao, S. Y. Yin and W. Xu, *Electrochim. Acta*, 2004, **49**, 4157–4161.
24 S. B. Sinnott and R. Andrews, *Crit. Rev. Solid State Mater. Sci.*, 2001, **26**, 145–249.
25 W. Lu and D. D. L. Chung, *Carbon*, 1997, **35**, 427–435.
26 T. Bordjiba, M. Mohamedi and L. H. Dao, *Adv. Mater.*, 2008, **20**, 815–819.
27 C. Merino, P. Sato, E. Vilaplana-Ortego, J. M. Gomez de Salazar, F. Pico and J. M. Rojo, *Carbon*, 2004, **43**, 551–557.
28 X. Y. Tao, X. B. Zhang, L. Zhang, J. P. Cheng, F. Liu, J. H. Luo, Z. Q. Luo and H. J. Heise, *Carbon*, 2004, **44**, 1425–1428.
29 J. Leis, A. Perkson, M. Arulepp, P. Nigu and G. Svenson, *Carbon*, 2002, **40**, 1559–1564.
30 J. Chmiola, G. Yushin, R. Dash and Y. Gogotsi, *J. Power Sources*, 2006, **158**, 765–772.
31 A. Janes, L. Permann, M. Arulepp and E. Lust, *Electrochem. Commun.*, 2004, **6**, 313–318.
32 M. Arulepp, J. Leis, M. Latt, F. Miller, K. Rumma, E. Lust and A. F. Burke, *J. Power Sources*, 2006, **146**, 1460–1466.
33 W. Xing, S. Z. Qiao, R. G. Ding, F. Li, G. Q. Lu, Z. F. Yan and H. M. Cheng, *Carbon*, 2006, **44**, 216–224.
34 M. Sevilla, S. Alvarez, T. A. Centeno, A. B. Fuertes and F. Stoeckli, *Electrochim. Acta*, 2007, **52**, 3207–3215.
35 R. W. Pekala, *J. Mater. Sci.*, 1989, **24**, 3221–3227.
36 W. Li, G. Reichenauer and J. Fricke, *Carbon*, 2002, **40**, 2955–2959.
37 H. Tamon, H. Ishizaka, T. Araki and M. Okazaki, *Carbon*, 1998, **36**, 1257–1262.
38 M. Mirzaeian and P. J. Hall, *J. Mater. Sci.*, 2009, **44**, 2705–2713.
39 R. W. Pekala, J. C. Farmer, C. T. Alviso, T. D. Tran, S. T. Mayer, J. M. Miller and B. Dunn, *J. Non-Cryst. Solids*, 1998, **225**, 74–80.
40 J. Yamashita, T. Ojima, M. Shioya, H. Hatori and Y. Yamada, *Carbon*, 2003, **41**, 285–294.
41 D. Long, J. Zhang, J. Yang, Z. Hu, G. Cheng, X. Liu, R. Zhang, L. Zhan, W. Qiao and L. Ling, *Carbon*, 2008, **46**, 1259–1262.
42 R. W. Pekala, C. T. Alviso, X. Lu, J. Gross and J. Fricke, *J. Non-Cryst. Solids*, 1995, **188**, 34–40.
43 D. Wu, R. Fu, Z. Sun and Z. Yu, *J. Non-Cryst. Solids*, 2005, **351**, 915–921.
44 S. R. Mukai, C. Tamitsuji, H. Nishihara and H. Tamon, *Carbon*, 2005, **43**, 2618–2641.
45 S. J. Kim, S. W. Hwang and S. H. Hyun, *J. Mater. Sci.*, 2005, **40**, 725–731.
46 Y. Zhu, H. Hu, W. Li and X. Zhang, *Carbon*, 2007, **45**, 160–165.
47 C. Arbizzani, S. Beninati, M. Lazzari, F. Soavi and M. Mastragostino, *J. Power Sources*, 2007, **174**, 648–652.
48 M. Lazzari, M. Mastragostino and F. Soavi, *Electrochem. Commun.*, 2007, **9**, 1567–1572.
49 F. B. Sillars, S. I. Fletcher, M. Mirzaeian and P. J. Hall, submitted.
50 K. Kinoshita, *Carbon: Electrochemical and Physicochemical Properties*, Wiley Interscience, New York, 1988.
51 Y. P. Wu, E. Rahm and R. Holze, *Electrochim. Acta*, 2002, **47**, 3491–3507.
52 C. H. Hsieh and H. Teng, *Carbon*, 2002, **40**, 667.
53 H. P. Boehm, *Carbon*, 1994, **32**, 759–769.
54 A. G. Pandolfo and A. F. Hollenkamp, *J. Power Sources*, 2006, **157**, 11–27.
55 K. Jurewicz, K. Babeł, A. Źiółkowski, H. Wachowska and M. Kozłowski, *Fuel Process. Technol.*, 2002, **77–78**, 191–198.
56 K. Jurewicz, K. Babeł, A. Źiółkowski and H. Wachowska, *Electrochim. Acta*, 2003, **48**, 1491–1498.
57 D. Hulicova, J. Yamashita, Y. Soneda, H. Hatori and M. Kodama, *Chem. Mater.*, 2005, **17**, 1241–1247.
58 D. Hulicova, M. Kodama and H. Hatori, *Chem. Mater.*, 2006, **18**, 2318–2326.
59 W. Li, D. Chen, Z. Li, Y. Shi, Y. Wan, J. Huang, J. Yang, D. Zhao and Z. Jiang, *Electrochem. Commun.*, 2007, **9**, 569–573.
60 G. Lota, K. Lota and E. Frackowiak, *Electrochem. Commun.*, 2007, **9**, 1828–1832.
61 G. Lota, B. Grzyb, H. Machnikowska, J. Machnikowski and E. Frackowiak, *Chem. Phys. Lett.*, 2005, **404**, 53–58.
62 F. Béguin, G. Lota, K. Szostak and E. Frackowiak, *Adv. Mater.*, 2005, **17**, 2380–2384.
63 M. Seredych, D. Hulicova-Jurcakova, G. Q. Lu and T. J. Bandosz, *Carbon*, 2008, **46**, 1475–1488.
64 D. Hulicova-Jurcakova, M. Seredych, G. Q. Lu and T. J. Bandosz, *Adv. Funct. Mater.*, 2009, **19**, 438–447.
65 K. Leitner, A. Lerf, M. Winter, J. O. Besenhard, S. Villar-Rodil, F. Suarez-Garcıa, A. Martinez-Alonso and J. M. D. Tascon, *J. Power Sources*, 2006, **153**, 419–423.
66 M. Kodama, J. Yamashita, Y. Soneda, H. Hatori, S. Nishimura and K. Kamegawa, *Mater. Sci. Eng., B*, 2004, **108**, 156–161.
67 M. A. M. Elsayed, PhD thesis, University of Strathclyde, 2007.
68 T. J. Bandosz and C. O. Ania, *Activated Carbon Surfaces in Environmental Remediation, Chapter 4—Surface Chemistry of Activated Carbon and It Characterisation*, Elsevier, 2006.
69 B. Fang and L. Binder, *J. Power Sources*, 2006, **163**, 616–622.
70 D. Lozano-Castelló, D. Cazorla-Amorós, A. Linares-Solano, S. Shiraishi, H. Kurihara and A. Oya, *Carbon*, 2003, **41**, 1765–1775.
71 W. Dmowski, T. Egami, K. E. Swider-Lyons, C. T. Love and D. R. Rolison, *J. Phys. Chem. B*, 2002, **106**, 12677–12683.
72 S. Trasatti and G. Buzzanca, *J. Electroanal. Chem. Interfacial Electrochem.*, 1971, **29**, App. 1–5.
73 J. M. Fletcher, W. E. Gardner, B. F. Greenfield, M. J. Holdoway and M. H. Rand, *J. Chem. Soc. A*, 1968, 653–657.
74 J. B. Goodenough, in *Progress in Solid-State Chemistry*, ed. N. Reiss, Elsevier, vol. 5, 1971.
75 J. P. Zheng and T. R. Jow, *J. Electrochem. Soc.*, 1995, **142**, L6–L8.
76 J. P. Zheng, P. J. Cygan and T. R. Jow, *J. Electrochem. Soc.*, 1995, **142**, 2699–2703.
77 I.-H. Kim, J.-H. Kim, Y.-H. Lee and K.-B. Kim, *J. Electrochem. Soc.*, 2005, **152**, A2170–A2178.
78 C.-C. Hu, W.-C. Chen and K.-H. Chang, *J. Electrochem. Soc.*, 2004, **151**, A281–A290.
79 M. Jayalakshmi and K. Balasubramanian, *Int. J. Electrochem. Sci.*, 2008, **3**, 1196–1217.
80 H. Y. Lee and J. B. Goodenough, *J. Solid State Chem.*, 1999, **144**, 220–223.
81 H. Y. Lee and J. B. Goodenough, *J. Solid State Chem.*, 1999, **148**, 81–84.
82 X. Zhao, C. Johnston and P. S. Grant, *J. Mater. Chem.*, 2009, **19**, 8755–8760.
83 A. Chandra, A. J. Roberts and R. C. T. Slade, *Solid State Commun.*, 2008, **147**, 83–87.
84 A. Chandra, A. J. Roberts, E. Lam How Yee and R. C. T. Slade, *Pure Appl. Chem.*, 2009, **81**, 1489–1498.
85 Z. J. Lao, K. Konstantinov, Y. Tournaire, S. H. Ng, G. X. Wang and H. K. Liu, *J. Power Sources*, 2006, **162**, 1451–1454.
86 R. N. Reddy and R. G. Reddy, *J. Power Sources*, 2006, **156**, 700–704.
87 I.-H. Kim, J.-H. Kim, B.-W. Cho, Y.-H. Lee and K.-B. Kim, *J. Electrochem. Soc.*, 2006, **153**, A989–A996.
88 I.-H. Kim, J.-H. Kim, B.-W. Cho and K.-B. Kim, *J. Electrochem. Soc.*, 2006, **153**, A1451–A1458.
89 G. G. Amatucci, F. Badway, A. Du Pasquier and T. Zheng, *J. Electrochem. Soc.*, 2001, **148**, A930–A939.
90 A. Du Pasquier, A. Laforgue, P. Simon, G. G. Amatucci and J.-F. Fauvarque, *J. Electrochem. Soc.*, 2002, **149**, A302–A306.
91 A. Du Pasquier, I. Plitz, S. Menocal and G. Amatucci, *J. Power Sources*, 2003, **115**, 171–178.
92 V. Khomenko, E. Raymundo-Piñero and F. Béguin, *J. Power Sources*, 2008, **177**, 643–651.
93 S. R. Sivakkumar, J. Y. Nerkar and A. G. Pandolfo, *Electrochim. Acta*, 2010, **55**, 3330–3335.
94 A. Yoshino, T. Tsubata, M. Shimoyamada, H. Satake, Y. Okano, S. Mori and S. Yatab, *J. Electrochem. Soc.*, 2004, **151**, A2180–A2182.
95 Y.-g. Wang and Y.-y. Xia, *Electrochem. Commun.*, 2005, **7**, 1138–1142.
96 Y.-g. Wang and Y.-y. Xia, *J. Electrochem. Soc.*, 2006, **153**, A450–A454.
97 Y.-g. Wang, J.-y. Luo, C.-x. Wang and Y.-y. Xia, *J. Electrochem. Soc.*, 2006, **153**, A1425–A1431.
98 A. Burke, *Electrochim. Acta*, 2007, **53**, 1083–1091.
99 K. Naoi and P. Simon, *Electrochem. Soc. Interface*, 2008, 34–37, Spring.

100 A. Rudge, J. Davey, I. Raistrick and S. Gottesfeld, *J. Power Sources*, 1994, **47**, 89–107.

101 C. C. Hu and T. W. Tsou, *J. Power Sources*, 2003, **115**, 179–186.

102 K. W. Nam, W. S. Yoon and K. B. Kim, *Electrochim. Acta*, 2002, **47**, 3201–3209.

103 C. C. Hu and C. C. Wang, *J. Electrochem. Soc.*, 2003, **150**, A1079–A1084.

104 R. N. Reddy and R. G. Reddy, *J. Power Sources*, 2003, **124**, 330–337.

105 J. K. Chang, Y. L. Chen and W. T. Tasai, *J. Power Sources*, 2004, **135**, 344–353.

106 J. Deng, X. Xing, W. Zhang, Y. Peng, J. Wang, X. Long, P. Li and A. S. C. Chan, *Eur. Polym. J.*, 2002, **38**, 2497–2501.

107 R. Kötz and M. Carlen, *Electrochim. Acta*, 2000, **45**, 2482–2498.

108 Q. Wang, J. Li, W. Gao, K. Wu and X. Wang, *New Carbon Mater.*, 2008, **23**, 275–280.

109 T. Shinomiya, V. Gupta and N. Miura, *Electrochim. Acta*, 2004, **51**, 4412–4419.

110 V. Gupta and N. Miura, *J. Power Sources*, 2006, **157**, 616–620.

111 V. Gupta and N. Miura, *Electrochim. Acta*, 2006, **52**, 1721–1726.

112 S. I. Fletcher, F. B. Sillars, N. E. Hudson and P. J. Hall, *J. Chem. Eng. Data*, 2010, **55**, 778–782.

113 Y. Zhang, H. Feng, X. Wu, L. Wang, A. Zhang, T. Xia, H. Dong, X. Li and L. Zhang, *Int. J. Hydrogen Energy*, 2009, **34**, 4889–4899.

114 F. B. Sillars, A. J. R. Rennie and P. J. Hall, unpublished data.

115 P. Kilaru, G. A. Baker and P. Scovazzo, *J. Chem. Eng. Data*, 2007, **52**, 2306–2314.

116 K. Kim, C. Lang, R. Moulton and P. A. Kohl, *J. Electrochem. Soc.*, 2004, **151**, A1168–A1172.

117 Y.-J. Kim, Y. Matsuzawa, S. Ozaki, K. C. Park, C. Kim, M. Endo, H. Yoshida, G. Masuda, T. Sato and M. S. Dresselhaus, *J. Electrochem. Soc.*, 2005, **152**, A710–A715.

118 D. R. MacFarlane, J. Sun, J. Golding, P. Meakin and M. Forsyth, *Electrochim. Acta*, 2000, **45**, 1271–1278.

119 H. Matsumoto, M. Yanagida, M. K.TanimotoNomura, Y. Kitagawa and Y. Miyazaki, *Chem. Lett.*, 2000, 922–932.

120 H. Matsumoto, H. Kageyama and Y. Miyazaki, *Chem. Lett.*, 2001, 182–183.

121 J. Sun, M. Forsyth and D. R. MacFarlane, *J. Phys. Chem. B*, 1998, **102**, 8858–8864.

122 W. Lu, K. Henry, C. Turchi and J. Pellegrino, *J. Electrochem. Soc.*, 2008, **155**, A361–A367.

123 Merck KGaA, Darmstadt, Germany, www.merck-chemicals.com, 2008.

124 J. M. Crosthwaite, M. J. Muldoon, J. K. Dixon, J. L. Anderson and J. F. Brennecke, *J. Chem. Thermodyn.*, 2005, **37**, 559–568.

125 M. Galínski, A. Lewandowski and I. Stepniak, *Electrochim. Acta*, 2006, **51**, 5567–5580.

126 K. R. Harris and L. A. Woolf, *J. Chem. Eng. Data*, 2005, **50**, 1777–1782.

127 D. R. MacFarlane, P. Meakin, J. Sun, N. Amini and M. Forsyth, *J. Phys. Chem. B*, 1999, **103**, 4164–4170.

128 A. B. McEwen, H. L. Ngo, K. LeCompte and J. Goldman, *J. Electrochem. Soc.*, 1999, **146**, 1687–1695.

129 M. E. Kandil and K. N. Marsh, *J. Chem. Eng. Data*, 2007, **52**, 2382–2387.

130 A. Noda, K. Hayamizu and M. Watanabe, *J. Phys. Chem. B*, 2001, **105**, 4603–4610.

131 H. Ohno and M. Yoshizawa, *Solid State Ionics*, 2002, 303–309.

132 H. Tokuda, K. Hayamizu, K. Ishii, M. A. B. H. Susan and M. Watanabe, *J. Phys. Chem. B*, 2004, **108**, 16593–16600.

133 H. Tokuda, K. Hayamizu, K. Ishii, M. A. B. H. Susan and M. Watanabe, *J. Phys. Chem. B*, 2005, **109**, 6103–6110.

134 H. Tokuda, K. Ishii, M. A. B. H. Susan, S. Tsuzuki, K. Hayamizu and M. Watanabe, *J. Phys. Chem. B*, 2006, **110**, 2833–2839.

135 J. A. Widegren, E. M. Saurer, K. M. Marsh and J. W. Magee, *J. Chem. Thermodyn.*, 2005, **37**, 569–575.

136 W. Xu and C. A. Angell, *Science*, 2003, **302**, 422–425.

137 D. Rochefort and A.-L. Pont, *Electrochem. Commun.*, 2006, **8**, 1539–1543.

138 R. Mysyk, E. Raymundo-Piñero, M. Anouti, D. Lemordant and F. Béguin, *Electrochem. Commun.*, 2010, **12**, 414–417.

139 N. A. Choudhury, S. Sampath and A. K. Shukla, *Energy Environ. Sci.*, 2009, **2**, 55–67.

140 V. V. N. Obreja, *Phys. E.*, 2008, **40**, 2596–2605.

141 E. Raymundo-Piñero, K. Kierzek, J. Machnikowski and F. Béguin, *Carbon*, 2006, **44**, 2498–2507.

142 J. Chmiola, G. Yushin, Y. Gogotsi, C. Portet, P. Simon and P. L. Taberna, *Science*, 2006, **313**, 1760–1763.

143 J. Chmiola, C. Largeot, P. L. Taberna, P. Simon and Y. Gogotsi, *Angew. Chem., Int. Ed.*, 2008, **47**, 3392–3395.

144 C. Largeot, C. Portet, J. Chmiola, P. L. Taberna, Y. Gogotsi and P. Simon, *J. Am. Chem. Soc.*, 2008, **130**, 2730–2731.

145 C. O. Ania, J. Pernak, F. Stefaniak, E. Raymuñdo-Pinero and F. Béguin, *Carbon*, 2006, **44**, 3126–3130.

146 J. A. Fernández, S. Tennison, O. Kozynchenko, F. Rubiera, F. Stoeckli and T. A. Centeno, *Carbon*, 2009, **47**, 1598–1604.

147 A. Balducci, R. Dugas, P. L. Taberna, P. Simon, D. Plée, M. Mastragostino and S. Passerini, *J. Power Sources*, 2007, **165**, 922–927.

148 D. Aurbach, M. D. Levi, G. Salitra, N. Levy, E. Pollak and J. Muthu, *J. Electrochem. Soc.*, 2008, **155**, A745–A753.

149 P. Delahay, *Double-Layer and Electrode Kinetics*, Interscience Publishers, New York, 1965.

150 J. Huang, B. Sumpter and V. Meunier, *Chem.–Eur. J.*, 2008, **14**, 6614–6626.

151 C. Kim and K. S. Yang, *Appl. Phys. Lett.*, 2003, **83**, 1216–1218.

152 J. A. Fernández, T. Morishita, M. Toyoda, M. Inagaki, F. Stoeckli and T. A. Centeno, *J. Power Sources*, 2007, **175**, 675–679.

153 A. Fuertes, F. Pico and J. M. Rojo, *J. Power Sources*, 2004, **133**, 329–336.

154 P. J. Hall, S. Brown, J. Fernandez and J. M. Calo, *Carbon*, 2000, **38**, 1257–1259.